16 May 2008 | $10

Science

AAAS

COVER

Male flowers of *Guronia makoyana*, a Central American plant in the cucumber family, harbor larvae (not visible) of two species of fly; a third fly species infests female flowers of the same species of plant. Some plant species in this family can host as many as 13 different fly species. See page 928.

Photo: Marty Condon

DEPARTMENTS

EDITORIAL

NEWS OF THE WEEK

NEWS FOCUS

864

LETTERS

BOOKS *ET AL.*

875

POLICY FORUM

PERSPECTIVES

CONTENTS continued >>

SCIENCE EXPRESS

www.sciencexpress.org

MOLECULAR BIOLOGY

Activation of the Cellular DNA Damage Response in the Absence of DNA Lesions

E. Soutoglou and T. Misteli

Protein complexes that usually assemble on and repair damaged DNA can form at undamaged sites to halt the cell cycle if several of the proteins are first tethered there.

10.1126/science.1159051

ASTRONOMY

An Eccentric Binary Millisecond Pulsar in the Galactic Plane

D. J. Champion et al.

A rapidly rotating pulsar has a highly eccentric orbit about its companion star, not the usual circular orbit, challenging ideas on how such binary systems form.

>> Science Express Perspective by E. P. J. van den Heuvel

10.1126/science.1157580

PERSPECTIVE: An Eccentric Pulsar: Result of a Threesome?

E. P. J. van den Heuvel

>> Science Express Research Article by D. J. Champion et al.

10.1126/science.1158738

MOLECULAR BIOLOGY

Widespread Translational Inhibition by Plant miRNAs and siRNAs

P. Brodersen et al.

Plant microRNAs and small interfering RNAs, thought to inhibit gene expression by cleavage of their RNA targets, also interfere with the translation of these RNAs into protein.

10.1126/science.1159151

PLANETARY SCIENCE

Mars North Polar Deposits: Stratigraphy, Age, and Geodynamical Response

R. J. Phillips et al.

Radar mapping shows that Mars' thick north polar ice cap contains four dust-rich layers recording variation in the planet's orbit and only slightly depresses the underlying crust.

>> News story p. 867

10.1126/science.1157546

TECHNICAL COMMENT ABSTRACTS

ECOLOGY

Comment on "Habitat Split and the Global Decline of Amphibians" 874

D. C. Cannatella

full text at www.sciencemag.org/cgi/content/full/320/5878/874c

Response to Comment on "Habitat Split and the Global Decline of Amphibians"

C. R. Fonseca, C. G. Becker, C. F. B. Haddad, P. I. Prado

full text at www.sciencemag.org/cgi/content/full/320/5878/874d

CREDIT (BOTTOM): MARIUS S. SCHÖPFLER

REVIEWS

GEOCHEMISTRY

Transformation of the Nitrogen Cycle: Recent Trends, Questions, and Potential Solutions 889

J. N. Galloway et al.

>> Review p. 893

GEOCHEMISTRY

Impacts of Atmospheric Anthropogenic Nitrogen on the Open Ocean 893

R. A. Duce et al.

>> Review p. 889

BREVIA

PHYSIOLOGY

The Energetic Cost of Climbing in Primates 898

J. B. Hanna, D. Schmitt, T. M. Griffin

Large primates expend less energy walking than climbing, but smaller ones walk and climb with similar efficiencies, possibly facilitating an evolutionary shift into trees.

RESEARCH ARTICLES

PHYSICS

Quasi-Particle Properties from Tunneling in the $\nu = 5/2$ Fractional Quantum Hall State 899

I. P. Radu et al.

Tunneling measurements between the conduction channels in the fractional quantum Hall effect confirm that the charge is quantized in units of ⅖ of an electron charge.

CELL BIOLOGY

Design Logic of a Cannabinoid Receptor Signaling Network That Triggers Neurite Outgrowth 903

K. D. Bromberg, A. Ma'ayan, S. R. Neves, R. Iyengar

Analysis of transcription data and known signaling networks predict two previously unrecognized regulators of neuronal growth, which were experimentally confirmed.

CONTENTS continued >>

REPORTS

ADVANCING SCIENCE, SERVING SOCIETY

SCIENCE (ISSN 0036-8075) is published weekly on Friday, except the last week in December, by the American Association for the Advancement of Science, 1200 New York Avenue, NW, Washington, DC 20005. Periodicals Mail postage (publication No. 484460) paid at Washington, DC, and additional mailing offices. Copyright © 2008 by the American Association for the Advancement of Science. The title SCIENCE is a registered trademark of the AAAS. Domestic individual membership and subscription (51 issues): $144 ($74 allocated to subscription). Domestic institutional subscription (51 issues): $770; Foreign postage extra: Mexico, Caribbean (surface mail) $55; other countries (air assist delivery) $85. First class, airmail, student, and emeritus rates on request. Canadian rates with GST available upon request, GST #125439322. Publications Mail Agreement Number 1069624. **Printed in the U.S.A.**

Change of address: Allow 4 weeks, giving old and new addresses and 8-digit account number. **Postmaster:** Send change of address to AAAS, P.O. Box 96178, Washington, DC 20090–6178. **Single-copy sales:** $10.00 current issue, $15.00 back issue prepaid (includes surface postage; bulk rates on request). **Authorization to photocopy** material for internal or personal use under circumstances not falling within the fair use provisions of the Copyright Act is granted by AAAS to libraries and other users registered with the Copyright Clearance Center (CCC) Transactional Reporting Service, provided that $20.00 per article is paid directly to CCC, 222 Rosewood Drive, Danvers, MA 01923. The identification code for Science is 0036-8075. Science is indexed in the *Reader's Guide to Periodical Literature* and in several specialized indexes.

CONTENTS continued >>

Captive cheetahs are being besieged.

SCIENCENOW

www.sciencenow.org

HIGHLIGHTS FROM OUR DAILY NEWS COVERAGE

The Mystery of the Dying Cheetahs
Researchers are closing in on how a version of mad cow disease is decimating captive cheetah populations.

Taking the Young Universe's Temperature
Gas molecules from across the cosmos help to underpin the big bang.

Blame It on the Beetles
Voracious insects ruined a whole lot of dinosaur fossils.

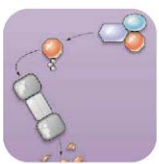

FAK targets p53 for degradation.

SCIENCE SIGNALING

www.sciencesignaling.org

THE SIGNAL TRANSDUCTION KNOWLEDGE ENVIRONMENT

PERSPECTIVE: Focal Adhesion Kinase Versus p53—Apoptosis or Survival?
W. G. Cance and V. M. Golubovskaya
Focal adhesion kinase acts as a scaffold protein to target p53 for degradation in the nucleus, leading to cell proliferation.

ST NETWATCH: Technical Information
Read entries in a new section that features online information about experimental design, methods, reagents, and data analysis.

GLOSSARY
Find out what BDNF, NICD, and PARL mean in the world of cell signaling.

Maintaining an interest in science.

SCIENCE CAREERS

www.sciencecareers.org/career_development

FREE CAREER RESOURCES FOR SCIENTISTS

MiSciNet: African Americans in the Scientific Workforce
A. Sasso
Many African American freshmen hope to become science majors, but their numbers decline in subsequent years.

MiSciNet: Betty Mbom
A. Sasso
As an undergraduate, Stanford-bound Betty Mbom started a minority mentoring program at her university.

Coming to Europe
A. Swarup
New policies aim to improve international scientists' mobility into and within Europe.

***Science* Careers Podcast: European Visa Issues**
K. Travis
A European policy official talks about coming to Europe to do science.

SCIENCEPODCAST

www.sciencemag.org/about/podcast.dtl

FREE WEEKLY SHOW

Download the 16 May *Science* Podcast to hear about the the metabolic cost of climbing in primates, how shorebirds use surface tension to eat, rampant tiger mosquitoes, and more.

CREDITS: (SCIENCENOW) YURI LINE/NATIONAL ACADEMY OF SCIENCES, PNAS (2008); (SCIENCE CAREERS) NANCY ARMSTRONG/PROCTER & GAMBLE; (SCIENCE SIGNALING) C. BICKEL

Separate individual or institutional subscriptions to these products may be required for full-text access.

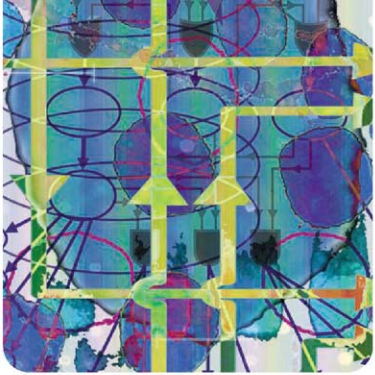

CREDITS (TOP TO BOTTOM): PAULA HARRISON/UNIVERSITY OF DUNDEE; T. A. MILLER

<< The Logic of Neurite Outgrowth

Cannabinoid receptor 1 (CB1R) regulates neurite outgrowth, has important functions in central nervous system development, and is a drug target for several diseases. **Bromberg *et al.*** (p. 903) combined transcriptional profiling on DNA arrays with graph theory analysis of known signaling networks to explore the effects of signaling by the CB1R. Unexpectedly, the analysis predicted that the product of the breast cancer susceptibility gene BRCA1 was likely to regulate transcription factors activated during CB1R-stimulated neurite outgrowth. Furthermore, depletion of BRCA1 did indeed inhibit CB1R-stimulated neurite outgrowth. The transcription factor PAX6 was also regulated in response to cannabinoid signaling. This type of network analysis is useful to define the logic of complex signaling decision processes.

Manmade Sources of Nitrogen

Manmade sources of biologically available nitrogen may enhance the capacity of the ocean to assimilate carbon dioxide. However, this assimilation capacity is likely to be offset by the production of nitrous oxide, itself a potent greenhouse gas. **Duce *et al.*** (p. 893) review the current status of atmospheric emission and deposition of nitrogen species and its impact on the biological nitrogen cycle. As anthropogenic mobilization of nitrogen increases in many areas of the world, negative environmental impacts are becoming apparent. The distressing paradox is that parts of the world still do not receive enough nitrogen to sustain food production. The N-related issues facing society are numerous, complex, and interrelated. **Galloway *et al.*** (p. 889) review some of the most critical factors and propose a strategy for how society might manage nitrogen.

From Folds to Wrinkles

Thin films on fluid or elastic substrates occur in many situations on many length scales and will deform from their flat geometries when compressed. Both wrinkled and folded states can occur, but the transition between them is not well understood. **Pocivavsek *et al.*** (p. 912) examine the compression of a set of supported membranes that span a range of length scales and stiffness and find a universal transition from wrinkling to localized folds when the compression exceeds one-third of the length of the membrane.

Cosmic Shock Waves

Intergalactic space is filled with magnetic fields, cosmic rays, and wisps of turbulent plasma. How these magnetic fields arose during the evolution of the universe is not well understood. **Ryu *et al.*** (p. 909) have conducted computer simulations showing that during the formation of the large-scale structures in the cosmos, shock waves created swirling regions that led to turbulent mixing. Very weak magnetic fields in the early universe could have been amplified by this turbulence, leading to the fields and structures we see today. These predictions should be testable using the new generation of radio telescopes such as the Square Kilometer Array.

Melting and Mixing the Mantle

The geochemistry of many types of basalt rich in sodium and potassium and relatively poor in calcium has been thought to imply derivation from the Earth's mantle containing some recycled oceanic crust. **Pilet *et al.*** (p. 916; see the Perspective by **Niu**) show experimentally, however, that many of the same signatures—both the compositions of the basalts and trends with time—can be produced by melting mantle that has previously interacted with a hydrous melt or fluid, forming veins of hydrous minerals. These hydrous phases dominate the composition of early melts and also buffer mantle melting temperatures.

Two Places at Once

Molecules heavier than H_2 have an inner layer, or core, of electrons that are held more tightly to individual nuclei than the constantly rearranging outer-valence electrons. What happens to the vacancy created when one such core electron is expelled by a high-energy photon? Does the hole remain localized beside one nucleus until a valence electron drops down to fill it, or does it spread out along the molecular axis? **Schöffler *et al.*** (p. 920; see the Perspective by **Ueda**) use ion imaging to probe this question in N_2, deriving the symmetry of the hole state based on the trajectory of an Auger electron emitted after relaxation. Depending on the angle of the Auger electron detected, the state could be described as either localized or delocalized, a consequence of quantum entanglement.

Microwaves in a Hurry

Rotational spectroscopy is widely used to characterize molecular structures in the gas phase. However, bandwidth limitations have generally restricted the technique to characterization of stable ground state geometries. **Dian *et al.*** (p. 924; see the Perspective by **Melnik and Miller**) have devised a Fourier Transform Microwave Spectrometer that uses an amplified chirped pulse to acquire data over an 11-GHz spectral range in a single burst. As a result, they can acquire spectra rapidly enough to probe the rotational dynamics of vibrationally excited molecules. Specifically, they examine the rotational isomerization of cyclopropane carboxaldehyde about a carbon-carbon single bond after exciting the aldehyde C-H stretch and using lineshape analysis, extract-mode–specific rates less than a tenth as rapid as statistical theory predicts.

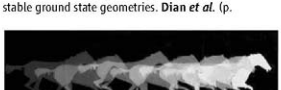

Continued on page 847

Continued from page 845

Similar But Not the Same

The level of species diversity in the tropics—especially among so-called cryptic species, which are genetically distinct but resemble other closely related species—is unclear. By sampling all morphologically similar larvae found on plants in the cucumber family across the New World tropics with molecular markers, **Condon *et al.*** (p. 928; cover) demonstrate a much higher than expected insect diversity on these plants: The insects tend to be specific not only to a single plant species but within that species to a single part of the plant.

Sipping with Tweezers

The surface of water in a pipette is higher at the edges than in the center, due to the relatively stronger attraction of a water molecule for glass in comparison to other molecules of water. **Prakash *et al.*** (p. 931; see the Perspective by **Denny**) demonstrate how surface tension and cycles of opening and closing its beak allow the shorebird *Phalaropes* to transport droplets of water uphill into its mouth. A droplet of water, suspended between the upper and lower mandibles of a tweezers-like model of the *Phalaropes* beak, moves toward the hinged end as the mandibles are brought closer together; it slips back slightly as the tweezers are opened, but the net motion is still forward. Closing and opening its beak several times thus enables the bird to ingest the droplet of water, along with the small invertebrates contained therein.

Keeping Foreign DNA Silent

Bacterial genomes are densely packed, so it is critical that transcription of operons is precisely terminated to prevent transcription of downstream genes. Regulation of many *Escherichia coli* genes uses three factors—Rho, NusA, and NusG—that work together to promote accurate transcription termination. **Cardinale *et al.*** (p. 935) now show that this termination is required to suppress expression of toxic genes from cryptic prophages. The *E. coli* derivative strain MDS42 lacking these prophages and other phylogenetically unique genes is highly resistant to a Rho inhibitor and can sustain deletions of the essential nusA and nusG genes. Thus Rho acts globally to prevent read-through of downstream operons, to match transcriptional yield to translational needs, and to suppress expression of foreign DNA.

Improving Imperfect Predictions

Although the genome encodes the proteins, there is variety in the regulatory choices available in translating the genome into the proteome. **Baerenfaller *et al.*** (p. 938, published online 24 April) analyzed the proteome of *Arabidopsis* and compared it to the known genome. As expected, proteins were identified from many of the genes predicted from genome. However, some proteins highlighted the presence of genes not yet predicted, for example, from sequences thought to be introns or pseudogenes. Further analysis of different organs and developmental stages confirms that, while the genome remains constant, the proteome shifts with development.

Plant Responses to Salt Stress

Detrimental levels of salt can result when agriculture is extended to marginal lands or relies on irrigation. Using the *Arabidopsis* root tip, **Dinneny *et al.*** (p. 942, published online 24 April; see the Perspective by **Voesenek and Pierik**) examined how different cells within a tissue respond to the physiological stresses due to salinity. Different layers of cells, whether at the surface of the root or more internal, responded differently to the environmental stress of too much salt. Furthermore, stressed cells could influence their neighbors, and gene expression patterns changed over the duration of the stress.

Cadherins and Guidepost Neurons

The *Celsr3* gene, which encodes a cell-surface cadherin molecule, is widely expressed in neurons of the developing brain after they have migrated when they are refining their connections. **Zhou *et al.*** (p. 946) prevented *Celsr3* expression in a variety of specific regions of the developing mouse brain. *Celsr3* expression was critical to the function of guidepost neurons—cells that developing axons use as flags to find their way. In particular, the axon tracts that connect thalamus and cortex depend upon Celsr3 interactions as they develop.

CREDIT: RAINEY SHULER

Alan I. Leshner is the chief executive officer of the American Association for the Advancement of Science and executive publisher of *Science*.

Just Give Them Grants

THE INTERDEPENDENT GOLD STANDARDS OF A SUCCESSFUL CAREER IN ACADEMIC RESEARCH are publication in prestigious journals and securing funding for one's independent research. There has been much discussion among scientists and funders about how best to launch such a career and how to fill the pipeline of young scientists to sustain the momentum of science (see also discussions at www.sciencecareers.org).

A major problem is that in many countries, research funding is quite constrained, so it's getting increasingly difficult for new investigators to secure their first grants. As a result, investigators are older and older when they finally begin independent work. On average, a recipient of a Starting Independent Researcher Grant from the European Research Council (ERC) is 35.6 years old and about 6 years past earning the Ph.D. New investigators supported by the U.S. National Science Foundation are also typically 6 to 7 years post-Ph.D. In the biomedical sciences, the average age at which an investigator first obtains a regular research grant from the U.S. National Institutes of Health (NIH) is 42 for a Ph.D. and 44 for MDs. No wonder there is concern about filling the pipeline of scientists. One has to wait until near middle age before getting one's own research program in full gear. (Next month, the American Academy of Arts and Sciences will release a report on supporting young investigators and high-risk–high-reward research.)

This prolonged wait for a grant is not the only problem. A new investigator often has to have completed two or three postdoctoral training periods before securing a tenure-track position. As emphasized in the U.S. National Research Council's 2005 report, *Bridges to Independence,* this extensive post-Ph.D. training, in which one often focuses on a mentor's research agenda rather than one's own, may stifle innovation and overly narrow young scientists' interests. If this is true, our models for postdoctoral training need revision.

Virtually every research funding agency has experimented with approaches to recruiting and funding young scientists, and many have been abandoned. Some small seed-grant programs were discarded because they didn't provide enough resources. Some special programs have included mentoring components on the basis of the argument that even after substantial postdoctoral training, young investigators would benefit from even more lab leadership training. And some special programs have been abandoned because their awards were more stigmatizing than beneficial. One such example is the FIRST Award (R-29) from the NIH, given up in part because many universities treated it as funding for those who could not get a "real" regular research grant, and thus it was not credited toward getting tenure. This argues for uniformity in how we support new investigators, instead of mounting special programs. One possibility is to review new investigators as a group, rather than having them compete with more seasoned investigators with established track records and extensive preliminary data.

What should we do? If the consensus is that young scientists really need a regular research grant to launch their careers, why not simply tilt funding decisions more toward new investigators? After all, there are many more meritorious proposals from junior investigators—which have passed muster through peer review—than can be funded. The tilt would, of course, result in fewer senior investigators getting funded or receiving multiple grants, but if we are genuinely concerned about the pipeline, we will need to make this tradeoff.

Some such initiatives have begun. Last year, the proportion of NIH research grants going to new investigators was over 25% for the first time in nearly a decade. The ERC plans to award about one-third of its frontier research funding as Starting Grants. And the United Kingdom's Medical Research Council is providing protected research time for younger faculty through New Investigator Research Grants.

These endeavors are clearly a start, but the number of young investigators being funded is still relatively small. More such efforts are needed to encourage young scientists who are contemplating research careers and to foster innovation and creativity while they are at their peak. This would demonstrate a real commitment of the scientific enterprise to ensuring its own continuity.

– Alan I. Leshner

10.1126/science.1159794

CLIMATE SCIENCE

Wetter or Drier?

One expected result of global climate warming is an overall increase in precipitation. Not every place will receive more rain—some will receive less, even though the average should increase. Certain changes are already apparent in various regions, such as a greater frequency of extreme rainfall events and a higher number of rainy days. Another potential change that could have important effects is an increase in prolonged dry spells. Groisman and Knight have compiled rainfall data covering the last 40 years from more than 4000 carefully selected stations across the conterminous United States, in order to determine if this pattern already has begun there. They find that it has. More precisely, they show that the mean duration of prolonged dry spells in the warm season has increased significantly, and that the return period of 1-month-long dry episodes over the eastern United States has decreased from 15 years to between 6 and 7 years. This pattern could be hazardous for terrestrial ecosystems and agriculture. — HJS

J. Climate **21**, 1850 (2008).

VIROLOGY

Leave It to Mimi

Acanthamoeba polyphaga mimivirus is a very large double-stranded DNA virus (genome size of 1.2 megabase pairs). By examining images of infected amoebae with electron tomography and cryo-scanning electron microscopy, Zuberman *et al.* have deduced how the genome is released from and packaged into the icosahedral viral capsid. Other DNA viruses have been observed to use a single icosahedral vertex both for loading DNA during viral biogenesis and for releasing it upon entering the host cell. In contrast, mimivirus appears to use two distinct portals. When feeding its genome into newly assembled viral capsids, a passageway at the center of an icosahedral face is used; when releasing its DNA, the mimivirus capsid undergoes a large conformational opening of five icosahedral faces around a single vertex. This so-called stargate serves as a membrane-lined sleeve through which the whole viral genome can escape promptly after infection. These entry and exit strategies may also be used by other large DNA-containing viruses, especially those that, like mimivirus, contain an internal membrane and encode proteins related to the DNA-packaging ATPases that are involved in bacterial DNA segregation, another process during which a large amount of DNA passes through a membrane portal. — SMH

PLOS Biol. **6**, e114 (2008).

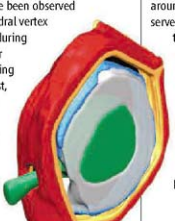

DNA (green) entering through the viral capsid (red/orange) and membrane (blue).

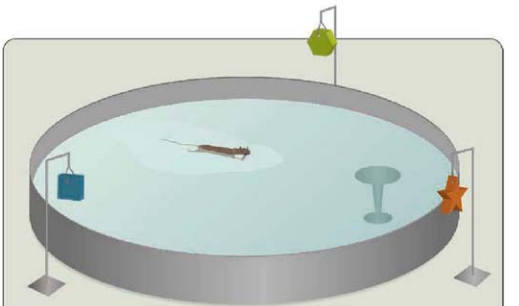

NEUROSCIENCE

Neurogenesis and Navigation

One of the old dogmas in neuroscience is that neurons in the adult mammalian brain do not divide and hence that their number cannot increase. Recent discoveries, however, show that in some areas of the adult mammalian brain, new neurons are being generated throughout the life span of the organism. This revisionist view has led to the speculation that some kinds of information encoding may require adult neurogenesis. Adult-born neurons have been hypothesized to play a role in spatial memory formation in the dentate gyrus of the hippocampus, but a causal relation between neurogenesis and spatial memory has not been unequivocally documented.

Dupret *et al.* generated transgenic mice that selectively overexpressed the pro-apoptotic protein Bax in neural precursor cells in an inducible manner. Overexpression of Bax removed newly born cells in the adult dentate gyrus and caused a strong deterioration in the relational processing of spatial information in the Morris water maze. Animals were unaffected when tested on simpler forms of spatial knowledge; nor were they affected in tasks where memory could be acquired without the hippocampus. — PRS

PLoS One **3**, e1959 (2008).

CHEMISTRY

Start Smart

Palladium(0) complexes are widely used as homogeneous catalysts for formation of carbon-carbon, carbon-oxygen, and carbon-nitrogen bonds. In general, the active catalysts are too unstable to store, and so precursors (often in the Pd(II) oxidation state) are prepared with stabilizing ligands that dissociate under the reaction conditions. However, the mechanisms and efficiency whereby these precursors transform into active catalysts have largely gone unaddressed, as has the potentially inhibitory effect of the stabilizing ligands left behind in the reaction solution. Biscoe *et al.* undertook a more careful approach by synthesizing a stable Pd(II) precursor complex resembling a reaction intermediate along the catalytic cycle. In three efficient steps, they appended a cyclometalated phenyl ring with a tethered chelating amine group to the Pd center. Exposure of this precatalyst to basic reaction conditions in the presence of aryl chlorides and amines led to rapid liberation of the protective ligand as an inert dihydroindole, leaving the resultant Pd(0)

CREDITS: (TOP TO BOTTOM) N. KENTMANN/AAAS/SCIENCE; ZUBERMAN *ET AL.*, *PLOS BIOL.* 6, E114 (2008)

complex free to proceed with a similar C-N coupling cycle of the bulk reagents. In comparison with traditional precatalysts, these complexes dramatically accelerated coupling reactions (in one case from 4 days to 4 hours), allowing loadings below 1 mol % and reaction temperatures at or below 25°C for sensitive substrates. The absence of interfering precatalyst ligands also facilitated clear mechanistic studies. — JSY

J. Am. Chem Soc. **130**, 10.1021/ja801137k (2008).

ECOLOGY

Deterministic Competition

The neutral theory of ecological community composition, which holds that species are interchangeable, has in recent years become a benchmark against which to test ecological data for signs of more niche-based mechanisms of species coexistence. Using data on tree species abundance in a Mexican tropical deciduous forest, Kelly *et al.* show that closely related pairs of species are more similar in abundance to each other than would be expected by chance, and also more similar in abundance than more distantly related species. This analysis suggests that closely related species interact with each other in different ways than do more distantly related or unrelated pairs—and hence argues against an important tenet of neutral theory. — AMS

Ecology **89**, 962 (2008).

BIOMATERIALS

Bridging the Gap

Peripheral nerves can be severed by injury or surgical procedures. For large gaps, the only clinical route to repair is through the use of autografts. However, this option requires a second surgical procedure with potential complications at the donor site and there is a limit on the number of suitable donor sites, as only motor or mixed nerves make suitable donors, whereas purely sensory nerves do not. Kim *et al.* fabricated films of an electrospun polymer, with either aligned or randomly distributed fibers that were stacked into thicker constructs. Studies were conducted on rats with 17-mm nerve gaps using both constructs, as well as autografts and saline injections as controls. The polymer films with randomly oriented fibers showed poor axon growth. In contrast, the aligned fibers helped facilitate nerve regeneration with the propagation of Schwann cells from both nerve stumps. Axons were found to grow from the proximal stump, but only in places where the Schwann cells had migrated. The aligned constructs were almost as effective as the autografts in restoring muscle functionality, but the pattern of nerve regeneration differed between those grown on the polymer and the autografts or normal nerves, and there was greater electrical signal latency. Overall, the work shows that topography of a graft, without the addition of neurotrophic factors or cell transplants, may be enough to induce nerve regeneration. — MSL

CREDIT: KIM ET AL., BIOMATERIALS 29, 10.1016/J.BIOMATERIALS.2008.03.042 (2008)

Biomaterials **29**, 10.1016/j.biomaterials.2008.03.042 (2008).

IMMUNOLOGY

Another Twist in the Extrathymic Tale

αβ T cells are descended from progenitors within the thymus, yet additional sites of lymphogenesis may also exist, most notably the mucosa of the gut. A decade ago, compelling evidence for intestinal extrathymic αβ T cell development appeared with the report of small gut lymphoid aggregates called cryptopatches (CPs) that contained progenitors able to repopulate the T cell compartments of a mouse. Then, a few years ago, controversy was ignited by an elaborate fate-mapping study that concluded that all intestinal αβ T cells are thymus-derived after all. In that study, the transcription factor retinoic acid–related orphan receptor γt (RORγt) was required for both gut and thymic T cell development, but this could be uncoupled from CP development and function. Thus, it was concluded that CPs are not genuine sites of lymphocyte development, but rather are lymphoid aggregates, induced by lymphoid tissue–inducing (LTi) cells and required for intestinal immune responses.

Naito *et al.* have performed further detailed analyses of the same engineered mouse strains used in the second study and find that CPs harbor a more complex mix of cells than was originally apparent, of which only a minority are actually LTi-like. Indeed, many CP cells with absent or minimal RORγt expression displayed the telltale signs of differentiating T cells, even in animals that did not possess a thymus. The case for extrathymic αβ T cell development may now be re-reinforced, but we still remain some way from understanding the function of these unusual T cells. — SJS

Mucosal Immunol. **1**, 198 (2008).

www.sciencemag.org

Science

1200 New York Avenue, NW
Washington, DC 20005
Editorial: 202-326-6550, FAX 202-289-7562
News: 202-326-6581, FAX 202-371-9227
Bateman House, 82-88 Hills Road
Cambridge, UK CB2 1LQ
+44 (0) 1223 326500, FAX +44 (0) 1223 326501

Subscription Services For change of address, missing issues, new orders and renewals, and payment questions: 866-434-AAAS (2227) or 202-326-6417, FAX 202-842-1065. Mailing addresses: AAAS, P.O. Box 96178, Washington, DC 20090-6178 or AAAS Member Services, 1200 New York Avenue, NW, Washington, DC 20005

Institutional Site Licenses please call 202-326-6755 for any questions or information

Reprints: Author Inquiries 800-635-7181
Commercial Inquiries 803-359-4578

Permissions 202-326-7074, FAX 202-682-0816

Member Benefits AAAS/Barnes&Noble.com bookstore www.aaas.org/bn; AAAS Online Store http://www.apisource.com/aaas/ code MKB6; AAAS Travels: Betchart Expeditions 800-252-4910; Apple Store www.apple/eppstore/aaas; Bank of America MasterCard 1-800-833-6262 priority code FAA3YU; Cold Spring Harbor Laboratory Press Publications www.cshlpress.com/affiliates/aaas.htm; GEICO Auto Insurance www.geico.com/landingpage/go51.htm?logo=17624; Hertz 800-654-2200 CDP#343457; Office Depot https://bsd.officedepot.com/portalLogin.do; Seabury & Smith Life Insurance 800-424-9883; Subaru VIP Program 202-326-6417; VIP Moving Services http://www.vipmayflower.com/domestic/index.html; Other Benefits: AAAS Member Services 202-326-6417 or www.aaasmember.org.

science_editors@aaas.org	(for general editorial queries)
science_letters@aaas.org	(for queries about letters)
science_reviews@aaas.org	(for returning manuscript reviews)
science_bookrevs@aaas.org	(for book review queries)

Published by the American Association for the Advancement of Science (AAAS), *Science* serves its readers as a forum for the presentation and discussion of important issues related to the advancement of science, including the presentation of minority or conflicting points of view, rather than by publishing only material on which a consensus has been reached. Accordingly, all articles published in *Science*—including editorials, news and comment, and book reviews—are signed and reflect the individual views of the authors and not official points of view adopted by AAAS or the institutions with which the authors are affiliated.

AAAS was founded in 1848 and incorporated in 1874. Its mission is to advance science and innovation throughout the world for the benefit of all people. The goals of the association are to: foster communication among scientists, engineers and the public; enhance international cooperation in science and its applications; promote the responsible conduct and use of science and technology; foster education in science and technology for everyone; enhance the science and technology workforce and infrastructure; increase public understanding and appreciation of science and technology; and strengthen support for the science and technology enterprise.

Information for Authors

See pages 634 and 635 of the 1 February 2008 issue or access www.sciencemag.org/about/authors

Editor-in-Chief **Bruce Alberts**
Executive Editor **Monica M. Bradford**
Deputy Editors **R. Brooks Hanson, Barbara R. Jasny, Katrina L. Kelner**
News Editor **Colin Norman**

Editorial supervisory senior editor Phillip D. Szuromi; senior editor/perspectives Lisa D. Chong; senior editors Gilbert J. Chin, Pamela J. Hines, Paula A. Kiberstis (Boston), Marc S. Lavine (Toronto), Beverly A. Purnell, L. Bryan Ray, Guy Riddihough, H. Jesse Smith, Valda Vinson; associate editors Jake S. Yeston, Laura M. Zahn; online editor Stewart Wills; associate online editors Robert Frederick, Tara S. Marathe; web content developer Martyn Green; book review editor Sherman J. Suter; associate letters editor Jennifer Sills; editorial manager Cara Tate; senior copy editors Jeffrey E. Cook, Cynthia Howe, Harry Jach, Barbara P. Ordway, Trista Wagoner; copy editors Chris Filiatreau, Lauren Kmec, Peter Mooreside; editorial coordinators Carolyn Kyle, Beverly Shields; publications assistants Ramatoulaye Diop, Joi S. Granger, Jeffrey Hearn, Lisa Johnson, Scott Miller, Jerry Richardson, Jennifer A. Seibert, Brian White, Anita Wynn; editorial assistants Carlos L. Durham, Emily Guise, Patricia M. Moore; executive assistant Sylvia S. Kihara; administrative support Maryrose Madrid

News deputy news editors Robert Coontz, Eliot Marshall, Jeffrey Mervis, Leslie Roberts; contributing editors Elizabeth Culotta, Polly Shulman; news writers Yudhijit Bhattacharjee, Adrian Cho, Jennifer Couzin, David Grimm, Constance Holden, Jocelyn Kaiser, Richard A. Kerr, Eli Kintisch, Andrew Lawler (New England), Greg Miller, Elizabeth Pennisi, Robert F. Service (Pacific NW), Erik Stokstad; intern Elsa Youngsteadt; contributing correspondents Jon Cohen (San Diego, CA), Daniel Ferber, Ann Gibbons, Mitch Leslie, Charles C. Mann, Virginia Morell, Evelyn Strauss, Gary Taubes; copy editors Rachel Curran, Linda B. Felaco, Melvin Gatling; administrative support Scherraine Mack, Fannie Groom; bureaus New England: 207-549-7755, San Diego, CA: 760-942-3252, FAX 760-942-4979, Pacific Northwest: 503-963-1940

Production director James Landry; senior manager Wendy K. Shank; assistant manager Rebecca Doshi; senior specialist Chris Redwood; specialist Steve Forrester; **Preflight** director David M. Tompkins; manager Marcus Spiegler; specialist Jessie Mudjitaba

Art director Kelly Buckheit Krause; associate art director Aaron Morales; illustrators Chris Bickel, Katharine Sutliff; senior art associates Holly Bishop, Laura Creveling, Preston Huey, Nayomi Kevitiyagala; associate Jessica Newfield; photo editor Leslie Blizard

Science International

Europe (science@science-int.co.uk) editorial: international managing editor Andrew M. Sugden; senior editor/perspectives Julia Fahrenkamp-Uppenbrink; senior editors Caroline Ash, Stella M. Hurtley, Ian S. Osborne, Stephen J. Simpson, Peter Stern; editorial support Deborah Dennison, Rachel Roberts, Alice Whaley; administrative support John Cannell, Janet Clements, Louise Smith; news: europe news editor John Travis; deputy news editor Daniel Clery; contributing correspondents Michael Balter (Paris), John Bohannon (Vienna), Martin Enserink (Amsterdam and Paris), Gretchen Vogel (Berlin); intern Laura Cahoon

Asia Japan Office: Asca Corporation, Eiko Ishioka, Fusako Tamura, 1-8-13, Hirano-cho, Chuo-ku, Osaka-shi, Osaka, 541-0046 Japan; +81 (0) 6 6202 6272, FAX +81 (0) 6 6202 6271; asca@os.gulf.or.jp; asia news editor Richard Stone (Beijing: rstone@aaas.org); contributing correspondents Dennis Normile (Japan: +81 (0) 3 3391 0630, FAX 81 (0) 3 5936 3531; dnormile@gol.com); Hao Xin (China: + 86 (0) 10 6307 4439 or 6307 3676, FAX +86 (0) 10 6307 4358; cindyhao@gmail.com); Pallava Bagla (South Asia: +91 (0) 11 2271 2896; pbagla@vsnl.com)

Africa Robert Koenig (contributing correspondent, rob.koenig@gmail.com)

Executive Publisher **Alan I. Leshner**
Publisher **Beth Rosner**

Fulfillment Systems and Operations (membership@aaas.org); director Waylon Butler; customer service supervisor Pat Butler; specialists Laurie Baker, Latoya Casteel, LaVonda Crawford, Vicki Linton; data entry supervisor Cynthia Johnson; specialist Tarrika Hill

Business Operations and Administration director Deborah Rivera-Wienhold; assistant director, business operations Randy Yi; senior financial analysts Michael LoBue, Jessica Tierney; financial analysts Benjamin Aronin, Priti Pamnani; rights and permissions: administrator Emilie David; associate Elizabeth Sandler; marketing director John Meyers; marketing managers Allison Pritchard, Darryl Walter; marketing associates Aimee Aponte, Alison Chandler, Mary Ellen Crowley, Marcia Leach, Julianne Wielga, Wendy Wise; international marketing manager Wendy Sturley; marketing executive Jennifer Reeves; marketing/member services executive Linda Rusk; site license sales director Tom Ryan; sales manager Russ Edra; sales and customer service Iquo Edim, Kiki Forsythe, Catherine Holland, Phillip Smith, Philip Tsolakidis; electronic media: manager Lizabeth Harman; project manager Trista Snyder; assistant manager Lisa Stanford; senior production specialists Christopher Coleman, Walter Jones; production specialists Nichele Johnston, Kimberly Oster

Advertising director worldwide ad sales Bill Moran

Product (science_advertising@aaas.org); midwest Rick Bongiovanni: 330-405-7080, FAX 330-405-7081; west coast/w. canada Teola Young: 650-964-2266; east coast/e. canada Christopher Breslin: 443-512-0330, FAX 443-512-0331; uk/europe/asia Michelle Field: +44 (0) 1223 326524, FAX +44 (0) 1223 326532; japan Mashy Yoshikawa: +81 (0) 33235 5961, FAX +81 (0) 33235 5852; senior traffic associate Delandra Simms

Commercial Editor Sean Sanders: 202-326-6430

Classified (advertise@sciencecareers.org); us: recruitment sales manager Ian King: 202-326-6528, FAX 202-289-6742; inside sales manager: midwest/canada Daryl Anderson: 202-326-6543; inside sales representative Karen Foote: 202-326-6740; key account manager Joribah Able; northeast Alexis Fleming: 202-326-6578; southeast Tina Burks: 202-326-6577; west Nicholas Hintibidze: 202-326-6533; sales coordinators Erika Foard, Rohan Edmonson, Shirley Young; international: sales manager Tracy Holmes: +44 (0) 1223 326525, FAX +44 (0) 1223 326532; sales Marium Hudda, Alex Palmer, Alessandra Sorgente; sales assistant Louise Moore; japan Mashy Yoshikawa: +81 (0)3 3235 5961, FAX +81 (0)3 3235 5852; advertising production operations manager Deborah Tompkins; senior production specialists Robert Buck, Amy Hardcastle; senior traffic associate Christine Hall; publications assistant Mary Lagnaoui

AAAS Board of Directors retiring president, chair David Baltimore; president James J. McCarthy; president-elect Peter C. Agre; treasurer David E. Shaw; chief executive officer Alan I. Leshner; board Lynn W. Enquist, Susan M. Fitzpatrick, Alice Gast, Linda P. B. Katehi, Nancy Knowlton, Cherry A. Murray, Thomas D. Pollard, Thomas A. Woolsey

AAAS
ADVANCING SCIENCE, SERVING SOCIETY

Tones From Ancient Greece

The strings of a helikon, a gadget invented by Ptolemy to probe musical scales, sounded last week for the first time in almost 2 millennia at the University of Cambridge in the U.K.

Andrew Barker, a musicologist at the University of Birmingham, U.K., built the instrument from a description in *Harmonics*, Ptolemy's 2nd century treatise on the mathematics of music. Ancient scholars considered the study of harmonics vital in understanding the mathematical rules that they believed governed the universe. He unveiled it as part of Cambridge's Science of Musical Sound Project.

Barker says the 1-meter-long wooden instrument with eight metal strings allows scientists to test "complete scales constructed on the basis of mathematical principles." The helikon creates different pitches with a calibrated sliding bridge, which can be inserted diagonally to shorten strings to different lengths. Strings can also be moved crosswise to raise or lower the range of pitches. Barker, who showed how the adjustments produce different intervals when the gadget is plucked, admits that it's not designed for musicmaking. Still, he says he was delighted that it worked at all.

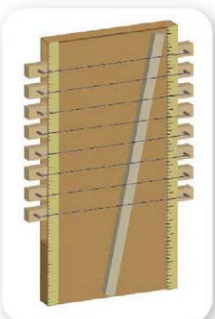

Cambridge historian Torben Rees, a professional jazz singer, called Barker's presentation "a fascinating account of ancient thinking concerning harmonics." Music, he says, was regarded as "the sensible expression of the order of the cosmos. This conception of the universe … was essentially the birth of mathematical physics."

CREDITS: (TOP TO BOTTOM) WIKIPEDIA; J. NEWFIELD/SCIENCE; J. NEWFIELD/SCIENCE; MICHAELA FRYE/WELLCOME TRUST CENTRE FOR STEM CELL RESEARCH

Magellan and El Niño

Ever since Ferdinand Magellan's fleet sailed around the world, historians have wondered why the great navigator took such an inefficient route across the Pacific. Two anthropologists have combined history, oceanography, and computer modeling to lay the blame on El Niño.

After passing through the Strait of Magellan at the tip of South America in late November 1520, Magellan planned to sail to the Moluccas, the equatorial "Spice Islands" west of New Guinea. Instead, he made landfall on Guam, more than 1500 kilometers to the northeast.

Why the detour? Scott M. Fitzpatrick of North Carolina State University in Raleigh and Richard Callaghan of the University of Calgary in Canada say computer simulations and historical accounts suggest that unusually calm weather, brought on by an El Niño event, allowed the ships to sail northward up the coast of Chile before heading west. Magellan had heard reports of a lack of food in the Moluccas—possibly due to drought and famines associated with El Niño—and may have wanted to reprovision the ship farther north before heading there, the authors suggest in an article in press in the *Journal of Pacific History*. "This could be the earliest historical record of an [El Niño] event," Fitzpatrick says.

"None of us could understand how [Magellan] managed to sail so far north, unless he simply had no idea where the Moluccas were," says Micronesian historian Francis Hezel, director of the Micronesian Seminar in Micronesia. "This article at least furnishes us with a coherent explanation for what always seemed to me to be not much more than a drift voyage across the Pacific."

Cosmic Strangeglove

A keratinocyte (*left*) inspired the red hand shape of the *Red Hole* (*right*), one of 300 works displayed at the Royal Albert Hall this month. The painting, by two 9-year-olds at St. Godric's RCVA Primary School in Durham, U.K., was a runner-up in Scopic, a contest for schoolchildren in London and County Durham to create art based on a favorite scientific image. "The *Red Hole* will consume anything, including satellites and novas, although its main meal is stars," say its creators, Lakshmi Piette and Catherine Duffell. The project was cosponsored by the Medical Research Council, Royal Albert Hall, and Durham University.

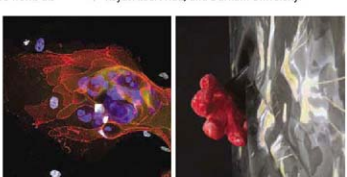

Pioneers

HAT TRICK. When Frances Arnold was growing up, her parents told her that she could achieve whatever she set her mind to. Last week, the 51-year-old chemical engineer and biochemist proved them right by becoming the first woman, and eighth living scientist, to be elected to all three of the U.S. National Academies.

A professor at the California Institute of Technology in Pasadena, Arnold helped develop a technique called "directed evolution" in which promising strands of parent proteins are either mutated or recombined to create new proteins. "[I had] to make better proteins in tenure-clock time," she explains. Arnold has engineered bacterial proteins that mimic human proteins for use in drug development and is working on enzymes that break down cellulose for use in biofuels. "I can alter anything that's encoded in DNA," she says. "The algorithm of evolution fits everything in biology; there is no such algorithm in other fields."

Arnold's induction last week into the National Academy of Sciences was preceded by her joining the National Academy of Engineering (NAE) in 2000 and the Institute of Medicine in 2004. Her father, nuclear physicist and NAE member William Howard Arnold, "was the most excited of all," she says. "He thinks it's great that I have so much fun with science."

FACT AND FICTION

A MATTER OF DEGREES. One of the most telling statistics cited in an influential 2005 National Academies report to argue for an increased federal investment in U.S. science is that "there were almost twice as many U.S. physics bachelor's degrees awarded in 1956 [pre-Sputnik] than in 2004." The decline is evidence that U.S. students are abandoning science, say policymakers including Tom Luce, head of the National Math and Science Initiative. NMSI sponsored a meeting last month in Washington, D.C., to take stock of how well the country has done since the 2005 report. But those data, it turns out, are dead wrong.

In reality, U.S. colleges and universities awarded 72% *more* undergraduate physics degrees in 2004 than in 1956—4965 versus 2883. Sliced another way, degree production has risen by 40% since hitting a post-Sputnik low in 1998 and is approaching levels not seen since the late 1960s, when a series of large graduating classes triggered a serious job crunch.

Academy officials say they don't know how the error occurred, but it's not the first time that *Rising Above the Gathering Storm* has sounded a false note in its scientific call to arms: Its first edition, since corrected, greatly inflated how many engineers graduate each year from Chinese and Indian schools.

MOVERS

THEORISTS' ENCLAVE. University of Cambridge cosmologist Neil Turok has agreed to head the Perimeter Institute for Theoretical Physics (PI) in Waterloo, Canada, which has been leaderless for nearly a year. "The combination of Neil and PI is brilliant and holds great promise," says Stephen Hawking, one of Turok's Cambridge colleagues. Turok succeeds theoretical physicist Howard Burton, who stepped down in June 2007 after failing to agree to the terms of a new contract.

"PI can be like a magnet to the brightest people in the world; … you have to make space and encourage people to tackle hard questions," says Turok, who in 2003 founded the African Institute for Mathematical Sciences (AIMS) in Cape Town, South Africa, to train the continent's best math students (*Science*, 2 May, p. 604). AIMS and PI "are similar in many ways," he says. "They are small, dynamic institutes with an international outlook."

Turok wants to triple the size of the institute, created with a $75 million gift from Mihal "Mike" Lazaridis, whose company makes the BlackBerry, from its current faculty of seven and encourage more visiting researchers with an associates program. "It's not obvious that it's going to work, but that's what makes it interesting," says Turok.

NONPROFIT WORLD >>

SHEPHERDING CATS. Alan Rabinowitz is leading a migration of experts on big cats from the Wildlife Conservation Society (WCS) to Panthera, a New York City–based nonprofit that promotes the conservation of all 36 species of wild cats.

Rabinowitz, 54, has spent his entire career at WCS, where he ran the society's science and exploration division. But he became frustrated by the bureaucracy at the $185 million nonprofit, which runs four New York zoos and works in 53 countries. "I'm completely free to play to my passions," Rabinowitz says about his new job, which he began last month. He's now overseeing Panthera's budget of $6.4 million, including $400,000 in grants for wild cat research.

As part of his move, Rabinowitz has hired Luke Hunter, a specialist in African cats, and famed mammalogist George Schaller from WCS. But he hasn't severed all ties with his former employer: One of his goals is to help WCS and other large organizations work together on cat conservation.

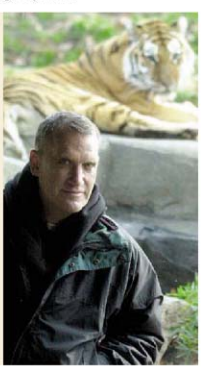

CREDITS: (TOP TO BOTTOM) CARTOON: EDAN WILLEY PHOTOGRAPHY; WILDLIFE CONSERVATION SOCIETY

Got a tip for this page? E-mail people@aaas.org

A cancer vaccine where it's needed most 860

WHO hits the bottle 862

PHYSICS

Fermilab Sends Energy Department Final Plan to Lay Off 7% of Staff

BATAVIA, ILLINOIS—The uncertainty has been the worst part, says Rick Tesarek, a physicist here at Fermi National Accelerator Laboratory (Fermilab). He and his 1950 fellow employees have been wondering who among them will lose their jobs in layoffs forced by budget cuts late last year (*Science*, 11 January, p. 142). "This has been hanging over us for so long now that morale around the lab is starting to plummet," Tesarek says. "We've been waiting since December."

The wait is nearly over. On 25 April, officials at the particle physics lab submitted their final plans for the layoffs to the U.S. Department of Energy (DOE) for approval. About 140 scientists, engineers, technicians, and other staff will receive pink slips in a 3-day process that could begin as early as next week. Roughly 60 more employees have accepted retirement or left because their term positions were not renewed. "We have to do what we have to do to ensure the health of the institution," says Fermilab Director Piermaria Oddone. "I feel terrible about it. … There is no choice."

Regretful. Fermilab's director, Piermaria Oddone, says budget cuts leave the lab "no choice" but to lay off employees.

Fermilab officials have been hoping for an 11th-hour reprieve from the U.S. Congress. As *Science* went to press, the Senate version of a bill to fund the war in Iraq also contained $45 million for DOE particle physics that could be spent this year to avert the layoffs. But the House version of the bill provides no money for the lab, and it's not clear what version will finally prevail. Given that uncertainty, Oddone says that he must proceed with the layoffs.

The cuts were forced when, in December, Congress passed a budget for fiscal year 2008 that slashed the lab's funding from a requested $372 million to $320 million, $22 million less than it had received the year before. The budget cuts specifically targeted funding for research and development on the proposed multibillion-dollar International Linear Collider; research on a superconducting accelerator technology known as SRF; and a proposed neutrino experiment called NOvA, which would have been the lab's biggest experiment once its Tevatron collider shuts down by the end of the decade. The staff cuts, however, will be spread across the lab, Oddone says.

In addition to the layoffs, in February, Fermilab instituted a rolling furlough that requires salaried employees to take 1 week out of every 2 months as unpaid leave. (Hourly employees take their furloughs a few hours at a time.) The scheme, which ▸

ANTHROPOLOGY

Chinese Cancel International Meeting

The Chinese government last week canceled a major anthropology meeting scheduled for July in what appears to be a case of pre-Olympics jitters.

More than 4000 anthropologists had signed up to attend the World Congress of the International Union of Anthropological and Ethnological Sciences (IUAES) in July in the southwestern Chinese city of Kunming. But on 6 May, the Chinese group hosting the conference told organizers it had encountered "complex difficulties" that would necessitate postponing the meeting. The next day, the group issued a letter saying that those difficulties had proven to be "unconquerable."

The sudden cancellation was "a huge surprise," says sociologist Peter Nas of Leiden University in the Netherlands, secretary-general of IUAES. "Nobody expected this. Everything was going very smoothly." He says that the Chinese officials said that there were "economic reasons" for the decision but would not elaborate. An official at the Chinese Academy of Social Sciences, which is serving as the host, told *Science* that "we are not well prepared."

Nas says he hopes the executive committee will discuss the problem in August at a European anthropology convocation in Slovenia. The union's Web site mentions July 2009 as a possible date.

The meeting is held every 5 years at a different location. Some scientists have speculated that Chinese officials were worried that planned discussions about minority ethnic groups and issues relating to human rights could spark further unrest over Tibet, especially because there is a Tibetan enclave in Yunnan Province near Kunming. Travel to Tibet has been sharply restricted, and last month new visa rules were tightened. However, two international scientific meetings planned for just before the Olympics—on rangelands and on the solar eclipse—are going ahead as planned.

–CONSTANCE HOLDEN

CREDIT: FERMILAB PHOTO

The mosquito that's conquering the world
864

Synthetic chemistry clicks
868

will continue until the end of the year, has enabled the lab to keep the Tevatron running. But it has also made work much more difficult, says physicist William Wester. "The furlough is 10% of your time, but efficiency has gone down way more than 10% because you're gone one week and then the next week the person you're working with is gone," he says.

Many researchers say they'll be relieved when the cuts are finally done. But Stephen Pordes, a physicist at the lab, warns that those who elude the ax should not underestimate the impact of watching friends and colleagues lose their jobs. "It's going to be painful to be here even if one survives," he says. Those laid off receive 2 weeks of paid leave with which to start hunting for another job. Those who remain face the task of rebuilding the lab's future.

–ADRIAN CHO

SCIENTIFIC HONORS

The Cost of a Genuine Collaboration

Most scientists would be thrilled to hear from the U.S. National Academy of Sciences (NAS) that they had just been elected to the prestigious organization. But when geneticist Nancy Jenkins got the call on 29 April, her reaction was more circumspect than jubilant. "What about Neal?" she asked. Chagrined to find that her husband and longtime scientific partner, geneticist Neal Copeland, was not on the list, Jenkins decided to strike a blow for true scientific coupledom and turn down the invitation.

"The problem for me is that my husband and I run the lab together as a husband-and-wife team," she explained in a 4 May letter to the academy's home secretary, John Brauman. "It is impossible to separate my contributions from Neal's as we did everything together on an equal basis. … Someday, if both of us have a chance to accept this honor together, it would be the highlight of our scientific careers."

Jenkins and Copeland are specialists in developing mouse models of human disease. They have followed identical scientific paths: After meeting 30 years ago as postdocs at Harvard University, they shared a lab at the U.S. National Cancer Institute for 22 years before moving together in 2006 to the Institute of Molecular and Cell Biology in Singapore. The two say that the academy should change its rules to recognize scientific couples and, more generally, research teams, as appropriate. "If somebody has worked their whole career side by side with another person, it doesn't make sense not to honor them together," says Jenkins.

Brauman says that the current standard of electing only individuals works well, adding that it is not impossible to separate the achievements of two partners. "Everybody recognizes that [Jenkins and Copeland] have made equally important contributions," he says. "But they are not clones. They don't do exactly the same thing." Brauman also says it's extremely difficult to find room in each annual class of 72 to honor scientists from the same field.

This year was not the first time the academy has faced this situation. Neurobiologist Lily Jan delayed accepting her 1995 election because her husband and lab partner, Yuh Nung Jan, had not been chosen. "I was told that I [would] have 1 year to make the decision … and that there [was] a good chance that Yuh Nung [would] be elected by then," says Jan, who is a professor at the University of California, San Francisco. He was, she adds, "and so we both joined NAS that year."

Some NAS colleagues counseled Jenkins to take a similar tack. "They said, 'Oh, don't be silly, Neal will get in, be a good sport,'" she says. But she felt a larger principle was at stake. "The face of science has changed. … There are more women today and more husband-wife teams like us," she says. "This kind of thing is going to happen more often in the future."

More important, Jenkins says, accepting the honor solo would have betrayed a tacit agreement the two struck before they were married and got their first academic jobs at the Jackson Laboratory in Bar Harbor, Maine. "We had to decide: Are we going to have separate labs and compete, or are we going to collaborate?" says Copeland. "We realized that if we competed even the slightest bit, we wouldn't stay married for long."

The two decided to become a team, alternating as last author on every one of their more than 750 papers. "It's a constant give and take," says Jenkins. "We wouldn't have it any other way."

–YUDHIJIT BHATTACHARJEE

CREDIT: Y. BHATTACHARJEE/SCIENCE

Teammates. Nancy Jenkins and Neal Copeland take a stand for science couples.

Anticancer shot. Health experts hope that the HPV vaccine, given routinely in the United States, will become affordable for Latin American countries.

LATIN AMERICA

Price Is the Main Barrier to Wider Use of Papillomavirus Vaccine

At its debut 2 years ago, a vaccine that prevents cervical cancer was heralded as a public health breakthrough that could potentially save millions of women's lives. Yet although the vaccine is now given routinely to young girls in the United States and Europe, it hasn't been deployed in poorer countries, where it could make a bigger difference. This week at a meeting* in Mexico City, health officials and researchers are launching a campaign to introduce the vaccine in Latin America, the first region in the developing world likely to benefit.

Many issues are unresolved, including whether health care systems are ready for the vaccine and whether conservative groups will oppose it. The biggest hurdle, however, is cost. Conference organizers hope that with new data on human papillomavirus infection and the vaccine's potential benefits, Latin American health officials can persuade their governments to negotiate with the two companies that manufacture HPV vaccines to lower the price, now $360 for three doses. The meeting will "send a strong message" about demand, says epidemiologist Jon Andrus of the Pan American Health Organization (PAHO) in Washington, D.C., a cosponsor.

Cervical cancer is associated with HPV, the most common sexually transmitted disease. Clinical trials have shown that two HPV vaccines, made by Merck and GlaxoSmithKline (GSK), are at least 95% effective in preventing persistent HPV infection by the two main types that cause cervical cancer (HPV-16 and HPV-18) (*Science*, 29 April 2005, p. 618). Because screening—using Pap smears—catches most cervical cancer in industrialized countries, the HPV vaccines won't make much of a dent in cancer cases. But disease is much more common in the developing world, where screening often falls short. About 85% of the 270,000 deaths from cervical cancer each year occur in these countries.

To prepare for the Mexico meeting, an international team of researchers pooled data from 15 years' worth of studies on HPV in Latin America and the Caribbean. Their meta-analysis of 118 studies, including data on 33,000 healthy women, found that the HPV infection rate averages 19%, with wide variation—from 13% in Mexico to twice that in Costa Rica. (Prevalence is 27% in the United States.) Women with cervical cancer were almost invariably infected with HPV; HPV-16 and HPV-18 accounted for 59% of cases in the region. That means that the Merck and GSK vaccines could prevent 500,000 deaths if given over 10 years to 70% of 12-year-old girls, the researchers found.

Health officials in the developing world are questioning whether they can afford the price. HPV vaccination would reduce the burden of cancer treatment and cut back on screening—a woman might need to be tested three times in her lifetime, the analysis by the international team notes. Even so, the benefits would be worth the costs only if the vaccine's price comes down. Even at $25 for the three doses, adding HPV vaccine to the standard inoculation regime would cost $290 million over 5 years.

Health experts expect that the companies will offer a discount, as they did in 2005 when they agreed to bulk sales of a new rotavirus vaccine aimed at preventing childhood diarrhea (*Science*, 24 September 2004, p. 1890). First, the World Health Organization (WHO) would need to prequalify the vaccines based on information submitted last year by the manufacturers. Then PAHO could begin negotiating.

If Latin American countries buy the vaccine, they will move on to the challenge of getting it to young girls. This group is older than the one that receives traditional childhood vaccines, so health officials will likely introduce the HPV vaccine in schools. Latin America is up to the challenge, says Ciro de Quadros, executive vice president of the Sabin Vaccine Institute in Washington, D.C., and one of the meeting organizers. He points to the region's success with other vaccines, including nearly eradicating rubella since 1998 by vaccinating people up to 40 years old. "We hope HPV will be the same," he says.

It's still unknown whether the HPV vaccine will draw opposition, as it did in the United States. Some U.S. religious groups initially opposed it as condoning sexual activity by girls. But once the vaccine was widely introduced, notes Scott Wittet of the Seattle, Washington–based Program for Appropriate Technology in Health, those opponents had little influence. In a pilot project to explore introducing the HPV vaccine in Vietnam, Uganda, India, and Peru, this form of opposition has not been a problem so far, says Wittet. "Once people understand the issues, it's not a hard sell."

WHO will likely issue its decision on prequalifying the two vaccines within a few months, Andrus says. Also later this year, WHO and PAHO advisory councils will discuss guidelines on administering HPV vaccines. Assuming that they issue strong recommendations, Andrus says, price negotiations should soon follow. **–JOCELYN KAISER**

CREDIT: JESSICA RINALDI/REUTERS/LANDOV

*Towards Comprehensive Cervical Cancer Prevention and Control, Region of the Americas, 12–13 May 2008, Mexico City, Mexico.

ITALY

A Plea for 'Transparent' Funding

A furor over political meddling in grants for stem cell research in Italy has erupted into a broad protest about favoritism and the lack of peer review in deciding who receives national science funding. Researchers in fields from astrophysics to oncology have endorsed a petition, written by Italian scientists and published in March in a national newspaper, that asks the government to authorize a new agency to allocate research funds independently and transparently. "In Italy, only a small proportion of the funds for scientific research is assigned according to a peer-review process. … It is high time that an evaluation system which assures science's success is translated into state laws and regulations," the petition declares.

A new plea from the petition's authors appeared in the same newspaper on 11 May; over the past few weeks, more than 1500 Italian researchers have signed the appeal, which was addressed to Italy's president, Giorgio Napolitano. He has publicly endorsed their request but has little authority to advance it within the government. The petition may also hit a dead end, as newly elected Prime Minister Silvio Berlusconi barely mentioned science in his campaign.

The furor started last year when some prominent scientists were outraged to learn that the €3 million for stem cell research budgeted in Italy's 2007 national finance act had already been allocated; an unofficial list of awardees was leaked to the scientific community, although it has yet to be released by the Italian Institute for Health Research, which oversees the funds (*Science*, 30 November 2007, p. 1359). "We never saw a call for application or any other official, public announcement of the initiative and of how it would be managed," says stem cell researcher Paolo Bianco of the University of Rome "La Sapienza."

Denying that the stem cell money has already been awarded, Italy's minister of health, Livia Turco, has promised that the funds would not be assigned without public competition and peer review. But no calls for grant applications have been announced.

Disappointment with Italy's distribution of research funds extends beyond stem cell science. Two weeks ago, economist Andrea Ichino of the University of Bologna penned an editorial in the newspaper *Il Sole 24 Ore* saying that his field of statistical and economic public research suffered from a similar lack of transparency. Jobs and grants, he claimed, are awarded mainly without peer evaluation.

Some scientists are now concerned that a new law designed to centralize university grants distribution, scheduled to go into force this year, may further increase favoritism and politicians' influence. "I fear this is the way research will be managed from now on," says stem cell researcher Ranieri Cancedda of the University of Genova.

Part of the concern about the new law is that Fabio Mussi, the minister of universities and research, has not yet provided rules governing allocations and public competitions for the so-called FIRST fund, which totals €300 million for 2008 and €360 million for 2009. An online document attributed to Italy's Ministry of Research also worries some researchers. It says that 70% of the newly created fund will be for strategic

Pleas. Scientists are petitioning Italian President Giorgio Napolitano (*left*) and Prime Minister Silvio Berlusconi (*right*).

research on topics decided by government officials rather than projects submitted by scientists and chosen through peer review.

Yet Francesco Beltrame, head of one of the scientific commissions of the Ministry of Research, tells *Science* that the online document does not reflect how the ministry plans to distribute FIRST funds, which he says will be distributed both by public competitions and "negotiation" between government and research institutions. As Italy waits to see how Berlusconi reshuffles government ministries, the country's scientists say they will continue to demand more transparency in how research money is awarded. "Every time public funds for scientific research are assigned by the national or regional government without a formal and regulated peer-review process," says Elena Cattaneo of the University of Milan, trust in the system is "undermined."

–LAURA MARGOTTINI

Laura Margottini is a freelance writer based in London, U.K.

CREDIT: CHRIS HELGREN/REUTERS/LANDOV

Testing Stem Cell Waters

Proposed legislation to overturn federal restrictions on embryonic stem cell research would give the National Institutes of Health (NIH) authority to ensure the ethical conduct of all U.S. stem cell research, regardless of its funding source. Representative Diana DeGette (D–CO) announced last week at a hearing of the House Energy and Commerce health subcommittee that she plans to include this feature when she reintroduces a bill this summer to expand the number of human embryonic stem cell lines available to federally funded researchers. A previous measure was twice passed by Congress and vetoed by President George W. Bush.

Her idea won the support of NIH Director Elias Zerhouni, who testified at the hearing. "It would be shortsighted not to oversee [stem cell science] at a federal level," Zerhouni said, citing existing NIH guidelines for the use of recombinant DNA and gene therapy as a model. DeGette and cosponsor Michael Castle (R–DE) are still drafting the House bill.

–ELSA YOUNGSTEADT

NASA Calls Back Weiler

In the midst of a budget crisis, NASA has turned to an experienced insider. Last week, NASA Administrator Michael Griffin named Edward Weiler as the associate administrator of the Science Mission Directorate. Weiler was made acting chief 6 weeks ago after S. Alan Stern resigned.

Weiler most recently served as head of NASA's Goddard Space Flight Center in Greenbelt, Maryland, after spending 6 years running the science program at headquarters. The blunt-speaking astrophysicist faces rising costs in a host of missions, a flat budget, and a fight among scientists over whether NASA should focus on Mars or outer planet exploration.

Senator Barbara Mikulski (D–MD) is hoping to make Weiler's job a little bit easier with a $200 million addition to NASA's 2008 budget that would pay back science and other programs tapped after the 2003 Columbia disaster. Her proposal is part of a Senate spending measure to fund the Iraq war that was expected to be voted out of committee this week. Its House counterpart contains no money for the space agency, however, meaning that the boost may not materialize.

The Senate bill also contains $400 million for the National Institutes of Health and $200 million for the National Science Foundation. Legislators have calculated that the additional funds could support 700 and 500 more grants, respectively. But once again, the money's not in the House version **–ANDREW LAWLER**

Health hazard. San people buy alcohol in a Namibian trading store. Harmful drinking is especially dangerous in poorer countries.

PUBLIC HEALTH

Staggering Toward a Global Strategy on Alcohol Abuse

Alcohol is about to get the type of attention usually reserved for AIDS and malaria. Next week, the World Health Organization (WHO) in Geneva, Switzerland, will take steps toward launching the first global assault on the harms associated with drinking. It's a bold move, but it may not be bold enough. Although recent data indicate that alcohol abuse is a major killer worldwide, some experts feel that objections from member states and the involvement of the alcohol industry have weakened a resolution intended to kick-start a WHO-led offensive. Others wonder whether WHO has the resources to make such a strategy effective—or whether the agency should be focusing on other problems.

"A resolution is all very well, but it still takes a substantial commitment … for this to be translated into a substantial and lasting program of work," says Robin Room, an alcohol policy expert at the University of Melbourne in Australia and a long-term observer of WHO.

This isn't the first time WHO has flirted with an alcohol strategy. In 1983, the agency called on member states to strengthen their national alcohol policies—emphasizing a regional rather than global approach to the problem—but the words "fell on stony ground," says Room. "Alcohol has been a politically touchy thing for WHO to deal with," Room notes, saying that the United States threatened to withhold funds from WHO in the 1980s if it pursued policies hostile to private enterprise. For a time, alcohol "dropped off WHO's agenda."

Then came WHO's *World Health Report 2002*. Drawing on various studies, including WHO's Global Burden of Disease project, the report concluded that alcohol was the fifth leading cause of death and disability worldwide. It beat out sanitation problems and high cholesterol and ranked just behind malnutrition and unsafe sex. Alcohol was as dangerous as tobacco, the report found—the source of up to 30% of various cancers and neurological disorders, and it had significant secondary dangers as well, leading to high rates of spousal abuse and homicide. Most devastating, however, was the conclusion that alcohol was the top cause of ill health and premature death in several developing countries, such as Brazil and Indonesia, and that—thanks to rising incomes—things were only going to get worse. "It was a significant wake-up call," says Peter Anderson, a public health expert previously with WHO, who currently advises the European Commission and other agencies on alcohol policy.

The report was the final straw for Finland. Having reduced liquor taxes to stay competitive with cheap Estonian imports, the country had seen a spike in alcohol-related deaths. In 2005, Finland banded together with other Nordic countries, including Sweden and Norway, and presented a resolution to the World Health Assembly, WHO's governing body, calling for a united effort to reduce alcohol-related health problems. "We wanted to see if a global strategy was possible," says Bernt Bull, senior adviser at the Ministry of Health and Care Services in Norway and a member of the Norwegian delegation.

The resolution passed but quickly ran into trouble. The United States favored a voluntary strategy and called for more input from the alcohol industry. Thailand objected that the resolution didn't go far enough and opposed industry involvement. And when WHO reconvened on the issue in May 2007, the drink trade had a new champion: Cuba. "The alcohol

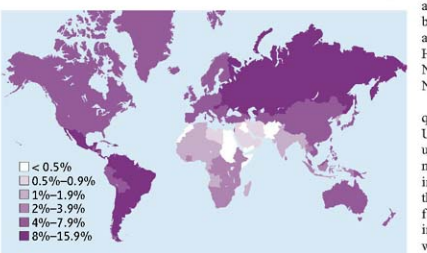

Global toll. As a percentage of all risk factors that cause ill health, alcohol ranks high in many parts of the world, with developing countries bearing much of the burden.

CREDIT: ANTHONY BANNISTER/GALLO IMAGES/CORBIS; SOURCE: WHO

industry gives work and contributes to economic growth," Oscar León Gonzalez of Cuba's foreign affairs department told the Swedish newspaper *Svenska Dagbladet* at the time. He also said poorer countries had bigger problems: "Many countries cannot understand why [the Nordic countries] push the alcohol question so hard when people lie dying of AIDS, tuberculosis, and malaria."

The resolution died, but a few months later two of these poorer countries, Rwanda and Kenya, resurrected it in the form of a similarly worded resolution, effectively deflating León Gonzalez's argument. "Alcohol causes a disproportionate burden of harm in poorer countries," says Anderson, noting that people in these regions are likely to have more serious health risks and have less access to treatment. At the same time, the potential for harm is on the rise in countries like India as people get a bit more money in their pockets. "They're going to start developing the same [alcohol-related] problems we had 50 years ago," notes Ralph Hingson of the U.S. National Institute on Alcohol Abuse and Alcoholism in Bethesda, Maryland. Hingson argues that WHO could help prevent a tragic repetition of this experience.

Buoyed by Africa's involvement, the resolution won wide support from WHO's executive board. Next week, member states are scheduled to vote at the World Health Assembly, and the measure is expected to pass. As written, the resolution directs the WHO director general to formulate a global alcohol strategy within 2 years. WHO's final plan would not be legally binding but could include recommendations such as increasing alcohol taxes and banning certain types of liquor advertisements, as well as helping developed countries implement prevention strategies. A global approach is needed, says Anderson, because the alcohol trade crosses borders and because nations can learn from each other's efforts. "You can't just rely on a single country's response."

Despite its new momentum, however, the plan could run aground. Changes to the resolution, introduced recently by Mexico—and supported by Cuba and the United States—compel WHO's director general to collaborate with the alcohol industry in shaping its strategy. And that could produce a "weak and feckless policy," says Derek Rutherford, chair of the London-based Global Alcohol Policy Alliance. "The industry tries to play down evidence-based factors that reduce alcohol consumption, such as taxes and advertising bans, and instead focuses on education, even though there's no proof that education works," he says.

On the contrary, taxes are often ineffective and can even backfire, driving consumers to dangerous home brews, especially in poorer countries, says Phil Lynch of the U.S.–based spirits company Brown-Forman, a member of the Global Alcohol Producers Group, which is consulting with WHO. The industry is not opposed to regulation, he says, it just wants to see a comprehensive approach. "We understand the products better than everyone else, ... and we deserve a seat at the table."

"Alcohol has been a politically touchy thing for WHO to deal with."

—ROBIN ROOM, UNIVERSITY OF MELBOURNE

WHO also must contend with limited resources. "WHO has a lot of irons in the fire," says Room, noting that WHO's investment in alcohol programs has been "extremely small in comparison with the size of the problems." And Ramanan Laxminarayan, an expert on global disease priorities at the Washington, D.C.– based think tank Resources for the Future, says it may be hard for WHO—and poorer countries—to justify interventions aimed at curbing dangerous drinking. Such interventions "are not good value for the money," says Laxminarayan, noting that malaria interventions are up to 100 times more cost effective.

Laxminarayan agrees with other global disease experts, however, that WHO is doing the right thing. "Developing countries don't always have the foresight to see that alcohol will be a big issue for them," he says. "WHO can be very influential in this regard." Hingson says developed countries could benefit as well. He notes, for example, that the U.S. Surgeon General has released more than 30 reports on tobacco but only two on the harms of alcohol. "We may think we're way ahead, but there are a lot of lessons we can learn."

–DAVID GRIMM

CREDIT: SANDRA BULLOCK

ARISE, Young Scientists

Young scientists in academia are most likely to feel the pain when money is tight. A blue-ribbon committee of U.S. scientists, academic leaders, and policy wonks has come up with a list of steps that the federal government and universities can take to make the system work better for that important population—even without the lubricant of additional cash.

Titled *ARISE—Advancing Research in Science and Engineering*, their report calls for universities to lessen the burden on young faculty members by shouldering a bigger share of salaries and lab costs. It cautions agencies not to run programs with low success rates and to improve monitoring of how their practices affect researchers. And it urges both groups to pay greater attention to the needs of early-career scientists by providing seed money, tenure timeouts, and more support for high-risk, high-reward proposals.

The report, due out early next month (www.amacad.org/arise), was written by a panel of the American Academy of Arts and Sciences chaired by Thomas Cech, head of the Howard Hughes Medical Institute. It was previewed last week in Washington, D.C., at the annual policy forum of the "other" AAAS (which publishes *Science*). –JEFFREY MERVIS

Winds of Change at DOE

The U.S. Department of Energy (DOE) is considering a new focus for its $50-million-a-year wind research program. The goal would be to derive 20% of the country's electricity from wind power by 2030, up from 1% in 2007. "We are moving beyond incrementalism," DOE's Alexander Karsner told reporters in presenting a new report on wind power by a panel of DOE and industry officials.

The report calls for new types of financing, better designs and windmill monitoring, and big changes to the electrical grid to bring electricity from windy areas to population centers. DOE has yet to allocate $10 million for wind research this year at the National Renewable Energy Laboratory in Colorado, as it considers a shift away from new kinds of windmills and toward extending the life of existing units. A decision is expected next month.

One element the wind report did not include in its modeling assumptions was a cap-and-trade system to reduce carbon emissions. But speaking on 12 May at a windmill manufacturer in Portland, Oregon, presumptive Republican presidential candidate John McCain said such a scheme is needed "to assure an energy supply that is safe, secure, diverse, and domestic." –ELI KINTISCH

A Mosquito Goes Global

The Asian tiger mosquito is on a rampage. Entomologists are impressed, public health officials are nervous, and many of the rest of us are swatting furiously. How did *Aedes albopictus* become such a scourge?

CREDIT: DEVON BOWMAN

When entomologist Paul Reiter made an odd discovery at a leafy old cemetery in Memphis, Tennessee, few people thought it was a big deal. At the graveyard's refuse dump, where he was studying mosquito behavior and ecology, Reiter, then with the U.S. Centers for Disease Control and Prevention, had caught a bug seen only a few times before in the Western Hemisphere: an Asian tiger mosquito (*Aedes albopictus*). "How the heck did it get here?" was his first thought. When he reported the find to the local health department, the official was nonplussed. "You better not find another one of those, or people may think you put it there!" he joked. Whatever it was, it wasn't cause for alarm.

The year was 1983, and nobody knew that the Asian tiger mosquito was about to go on a global rampage. Within a few years, it was found in several southeastern states of the United States, in numbers so great that nobody could suspect Reiter—who's now at the Pasteur Institute in Paris—of planting them.

Twenty-five years later, the mosquito has invaded 36 U.S. states, as well as many countries in South and Central America. It's on the march in Africa and the Middle East, has exploded in Italy, and seems set to conquer large swaths of Europe. Greenhouses in the Netherlands have been its latest and northernmost outpost. A worldwide trade in second-hand tires—which often contain water—has been the key to its wide-scale conquest. Lately, an exotic plant called Lucky bamboo has also given it a free ride.

An aggressive daytime biter, *Ae. albopictus* is making life hell for gardeners and ruining picnics and wedding receptions. But the 2005–06 outbreak of an obscure disease called chikungunya in the Indian Ocean as well as a smaller one last summer in Italy have shown that it could also threaten human health—although how much is still fiercely debated among medical entomologists. Some take heart from the fact that although *Ae. albopictus* can be infected with a dizzying variety of viruses in the lab, so far in the real world it has been a rather wimpy disease vector. But others warn that its rise could confront Europe and the United States with serious outbreaks of diseases now restricted to the tropics.

Stowaways

The Asian tiger mosquito, so called because of its bright white stripes, hails from East and Southeast Asia, where it originally lived at the edges of forests, breeding in tree holes and other small natural reservoirs. It has adapted easily to human settlements, where pots, vases, and buckets can replace tree holes, provided there's a bit of vegetation nearby. The mosquito is believed to have spread along with humans to Madagascar and the smaller Indian Ocean islands centuries ago.

But its big break came with the advent of modern shipping. After World War II, when huge amounts of military equipment were sent back to the United States from war zones, inspectors from the U.S. Public Health Service discovered that *Ae. albopictus* had traveled along as a stowaway in used tires, as had six other exotic mosquito species. Radical control measures helped prevent it from establishing itself. *Ae. albopictus* was also found in tires reimported from Vietnam in 1972, but again, it didn't gain a foothold.

In 1985, officials at the Harris County Mosquito Control District in Texas found an *Ae. albopictus* population near a roadside tire dump in Houston. Reiter, who helped investigate its source, soon became an expert in the

thriving international trade in used tires. Millions of tires are shipped each year from countries such as Japan and Germany, which impose strict rules on their wear and on the use of "recaps," to those that are more lenient, such as the United States; for various reasons, tires are also shipped from the United States to Europe and South America.

The water the used tires hold is an ideal place for eggs and larvae, Reiter says; and even if it evaporates, the Asian tiger mosquito's eggs are so drought-resistant that they can survive until the tires reach their destination. (Mosquito species like *Anopheles gambiae*, a malaria vector, could never pull this off.) Meanwhile, the containers in which the tires are shipped ensure a comfy, sheltered journey.

The mosquitoes imported into the United States probably came from Japan, Reiter and others wrote in a 1987 *Science* paper. Like their Japanese counterparts, Asian tiger mosquitoes were able to survive cold winters because their eggs respond to shortening days by going into a state of dormancy called diapause. That capacity, which many other tropical mosquitoes lack, is another key to the tiger's successful spread and explains why it can survive even Chicago's harsh winters.

Its invasion of Latin America lagged behind by a few years, but it proved just as unstoppable. The mosquito was first found in São Paulo, Brazil, in 1986 and soon spread farther in southeastern Brazil. It popped up in Mexico in 1993, in Guatemala, Honduras, and El Salvador in 1995, and in Paraguay, Colombia, and Argentina in 1998. Panama and Nicaragua joined the club in 2002 and 2003, respectively. Good data are lacking for most parts of Africa, but the mosquito has already been found in Nigeria, Cameroon, Equatorial Guinea, and, last year, in Gabon.

In Europe, Albania was the first to find *Ae. albopictus* within its borders, in 1979. The country was still an isolated Stalinist stronghold, and the news reached few scientists elsewhere. When Reiter teamed up with Albanian entomologist Jorgji Adhami to document the outbreak in the 1980s, they concluded that the mosquito may have first entered the country in 1975; the most likely source was China, one of Albania's few trading partners at the time.

By far the hardest hit European country to date is Italy, which blew its chance to quash the nascent invasion, says Romeo Bellini, an entomologist at the Centro Agricoltura Ambiente "Giorgio Nicoli" (CAA) in Baricella. The first few tiger mosquitoes were found in a kindergarten classroom in the port city of Genoa in 1990, and other hot spots soon followed, but the government didn't act quickly or aggressively enough to kill adults and larvae. "They didn't understand what was going on; it wasn't a priority," says Bellini. Eighteen years later, the mosquito is driving people nuts and chipping away at tourism revenue in towns and cities across northern Italy, where the climate is particularly favorable.

In many other places, too, the tiger mosquito is a terrible nuisance. "It's really a horrible pest," says Duane Gubler of the University of Hawaii, Honolulu. That may seem strange, because human blood isn't always its meal of choice. The mosquito is what entomologists call a "catholic," or general, feeder: It can bite a wide variety of mammals, including cows and rats, as well as birds and reptiles. But what the tiger mosquito lacks in host specificity, it seems to make up for in aggression and its sheer numbers. And when other host species are scarce—as they likely are in many cities—the mosquito may have little choice but to bite humans.

A health threat?

The mosquito's impact on health is potentially more serious but also much less clear. In lab studies, researchers have shown that more than two dozen viruses can reproduce in *Ae. albopictus*. The most prominent is dengue, a viral disease that causes severe muscle and joint pains and can also lead to dengue hemorrhagic fever, a rare and often fatal disease. And now that *Ae. albopictus* has become so ubiquitous, "widespread … dengue in the continental United States is a real possibility," Anthony Fauci and David Morens of the U.S. National Institute of Allergy and Infectious Diseases wrote in the *Journal of the American Medical Association* in January.

But whether a mosquito actually spreads disease in the real world depends on many factors: its numbers, how often it bites humans, whether it takes blood meals from multiple people, and how effectively the virus makes it from the mosquito's gut to its salivary glands, and from there, to its victim's veins. So far, there's solid evidence for the tiger mosquito's role in the transmission of only two diseases: dengue and chikungunya. The latter is prominent in Africa and Asia, and its symptoms resemble those of dengue. And even for those two, the mosquito isn't historically known to be a very efficient vector, says Gubler.

The reason appears to be its wide host range. If a mosquito bites a dengue-infected child only to move on to a lizard, the virus goes nowhere because it infects only primates. By contrast, a species called *Ae. aegypti*—also known as the yellow fever mosquito—dines almost exclusively on humans, which is why it has caused an explosive rise in dengue cases in the tropics the past 2 decades. Dengue outbreaks in places that have only *Ae. albopictus* tend to be mild, Gubler says; a 2001–02 outbreak in Hawaii infected only 122 people, for instance.

In fact, Gubler predicts that the spread of *Ae. albopictus* will actually result in a net gain for public health because in many places, it is pushing out *Ae. aegypti* populations. (The species' larvae compete for food when they share water containers, and the tiger mosquito appears to win often.) That's why Gubler dismisses gloomy scenarios like that published by Fauci and Morens. "I couldn't believe they wrote that," he says.

Didier Fontenille of the Institute of Research for Development in Montpellier, France, says he once agreed with Gubler but no longer does. The massive chikungunya outbreak in the Indian Ocean islands, which sickened more than a third of the population in a few months in La Réunion, was caused by

Breeding ground. An entomologist finds mosquito larvae in a discarded tire.

CREDIT: DAVID MCNEW/GETTY IMAGES

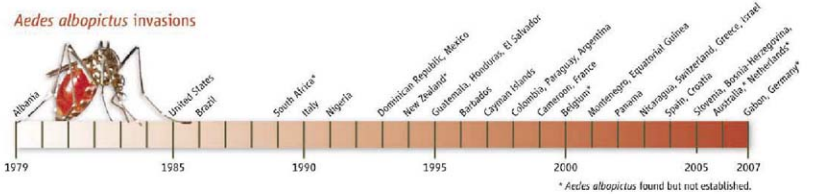

Ae. albopictus. The small outbreak in Italy's Ravenna province last summer sickened more than 200 and killed one older woman. As-yet-unpublished work by Fontenille and his colleagues shows that the mosquito population in La Réunion strongly prefers humans. If that pattern holds true in other countries, the tiger mosquito may be a much more dangerous vector than people assume, he says.

Two studies have also suggested that the chikungunya virus underwent a single-nucleotide mutation during the Indian Ocean outbreak that made it more able to use *Ae. albopictus* as a vehicle (*Science*, 21 December 2007, p. 1860). Nobody can rule out that something similar could happen with dengue, he warns, or with any of the other viruses it was shown to transmit in the lab. Even if *Ae. albopictus* pushes out its main competitor, "there's no reason to be happy," says Fontenille.

Tough fight

Can the tiger mosquito be stopped? Experience to date suggests that once it's become established, it's almost impossible to get rid of, says Francis Schaffner of the University of Zürich, Switzerland. At that point, the only option is suppressing its numbers—and even that is difficult and costly.

Eliminating breeding sites, such as flowerpots and vases, is effective, but it requires the public's participation, which is hard to sustain. Even in Italy, where the public has been bombarded with educational materials—including posters, mugs, and screensavers—larval control is falling short, says Bellini. Spraying insecticides is another widely employed tactic, but its effectiveness is probably limited, says Reiter. Hiding in vegetation, the mosquitoes are much harder to reach with aerosol droplets than are *Ae. aegypti*, which tend to stay inside or close to houses.

Italy is betting on a new weapon: the so-called sterile insect technology (SIT), which aims to drive down the population by releasing massive numbers of sterile males. SIT has been used successfully to battle agricultural pests (*Science*, 20 July 2007, p. 312), but its use with mosquitoes is limited. Bellini's group at CAA has a facility to rear some 100,000 male mosquitoes a week and blast them with infertility-inducing gamma rays. It has studied the mosquitoes' viability and attractiveness to wild females, and a field trial to see whether they can reduce a population is slated for the summer.

Bellini is under no illusion that SIT can eradicate the mosquito from Italy—that would require an immense investment—but it could help drive down populations in an environmentally benign way, he says. But so far, the budget for a rearing facility able to churn out the millions of males that would be needed weekly is still lacking.

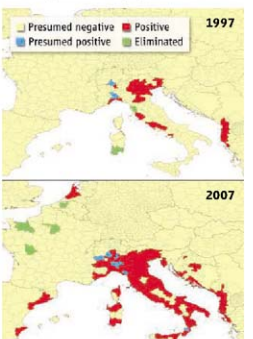

On the march. After becoming established in Albania and Italy, the Asian tiger mosquito started spreading to other European countries.

Countries that have not yet seen the tiger mosquito can hope to prevent it from entering and can hit hard if it does. But again, the options are limited. For its medium-distance travel, the mosquito has been known to hitch a ride in automobiles and trucks—that's how it appears to have spread from Italy to Spain, France, Croatia, Slovenia, Switzerland, and Germany. There's simply no way to stop this type of spread, says Willem Takken of Wageningen University in the Netherlands.

To prevent long-distance infestations, governments would have to regulate the international tire trade. But so far, few governments have been willing to clamp down on that economic sector to thwart an uncertain public health risk. Besides, there are other routes as well. In the summer of 2005, greenhouse workers in the Netherlands started complaining about aggressive mosquitoes. This time, researchers found, the mosquito had hitched a ride in shipments of Lucky bamboo (*Dracaena sanderiana*), a popular decorative plant imported from China.

A major horticultural hub, the Netherlands exports Lucky bamboo widely, which has triggered fears that it might seed new infestations. Horticultural companies have taken steps to reduce the risk, for instance, by treating shipments before they leave China, and no new tiger mosquitoes have been found in the past 6 months—but this may also be due to natural fluctuations, says Ernst-Jan Scholte of the Dutch Plant Protection Service. Wouter van der Weijden of the Centre for Agriculture and Environment, a lobby group, says the Dutch government isn't tough enough and warns that it risks dropping the ball, just like Italy did 18 years ago.

Whether the mosquito could become established this far north—or indeed, how much farther it can push its worldwide range—is anyone's guess. The European Centre for Disease Control and Prevention in Stockholm has charged a group of European scientists to come up with some predictions. The group's map, published in the 2007 book *Emerging Pests and Vector-Borne Diseases in Europe*, shows that France, Belgium, and the Netherlands are at risk of being colonized, as well as the United Kingdom, Ireland, and even the coastal areas of Scandinavian countries. Other models have come up with different ranges, but they agree that the end is not in sight.

Reiter predicts that at best the countries at risk can postpone becoming colonized. Whatever the natural boundaries of its potential habitat are, the tiger mosquito seems determined to reach them. **–MARTIN ENSERINK**

CREDITS: (TOP TO BOTTOM) JAMES GATHANY/CDC; SOURCE: E. J. SCHOLTE AND F. SCHAFFNER, MAPS IN E. J. SCHOLTE, F. SCHAFFNER, P. SCAMPILLA, *EMERGING PESTS AND VECTOR-BORNE DISEASES IN EUROPE*

PLANETARY SCIENCE

Layers Within Layers Hint at a Wobbly Martian Climate

Like Earth, Mars has a layered geology, but the martian version can have a particularly rhythmic regularity; scientists are finally getting a handle on the mechanism driving it

For decades, planetary scientists assumed that the stunning layering of Mars goes back to the planet's innate unsteadiness. The planet wobbles and wanders in its orbit, changing the climate rhythmically. What else could shape the cyclic-looking layering in everything from icy polar deposits to crater fill? But without a time scale, researchers were long stymied in linking particular layering to any particular orbital variation. That left the door open for nonorbital explanations.

Now, new studies are tentatively tying layering to orbital variations. Across the polar caps of Mars and in impact craters, within the past few million years and several billion years ago, new observations and analyses are revealing periodic groupings of layers of the sort that orbitally driven climate change could have laid down. Martian layer counting is all the rage now, says planetary scientist Oded Aharonson of the California Institute of Technology (Caltech) in Pasadena. "That's a good sign."

Just identifying martian layering as periodic and not a random jumble has been controversial. On Earth, paleoceanographers can do hands-on work on sediment cores, analyzing them from the meter scale down to the atomic scale to date the layers precisely. On Mars, researchers must work from images taken from hundreds of kilometers up. They know that younger layers pile up on top of older ones, but they have no idea how long a given set of layers took to form. In the North Polar Layered Deposits (NPLD), for example, alternating dark and light layers exposed in cliff faces presumably reflect dust-darkened ice versus bright, nearly dust-free ice, but it gets more complicated. Dark stripes can be shadows, not dirty ice; frost can mask truly dark layers; and less-than-vertical outcrops can distort the apparent thickness of layers.

To avoid at least some of these problems, geophysicists J. Taylor Perron and Peter Huybers of Harvard University combined images and topography returned from 23 strips across the NPLD by the now-defunct Mars Global Surveyor orbiter. Knowing the slope across layers let them correct apparent thickness to true thickness. As they reported at the Lunar and Planetary Science Conference (LPSC) in March in League City, Texas, most of the surveyed terrains did show—within a lot of climatic noise—periodic layering with a layer thickness of roughly 1.6 meters, although the periodicity waxed and waned with time. A layer in such cyclic bedding may have formed as the planet rhythmically nodded over on its side to 45° or even more—pouring more summer sun on the poles and sending polar ice to the equator. Then Mars would have righted itself and returned to its initial climate, forming a contrasting layer, all in one 120,000-year cycle. If so, the researchers calculate, the upper kilometer or so of the NPLD would have formed over tens of millions of years.

But Perron and Huybers are quick to point out that other, nonorbital processes could be modulating martian climate on a roughly periodic schedule, as El Niño does on Earth. To link layering to changes in orbit, they say, researchers must find a section of ice or rock in which layers change steadily if subtly in thickness or color in step with a longer term rhythm. For example, a series of thin layers might decrease in thickness in a rhythmic pattern that makes them stand out as a single packet. Such bundling could reflect the interaction between two orbital variations—for example, planetary tilt and the shape of Mars's orbit. Such an interaction would create a unique ratio of packet thickness to thin-layer thickness.

Such bundling ratios are starting to show up. As they report online this week in *Science* (www.sciencemag.org/cgi/content/abstract/1157546), planetary geophysicist Roger Phillips of the Southwest Research Institute in Boulder, Colorado, and colleagues analyzed data from SHARAD (SHAllow RADar) onboard the Mars Reconnaissance Orbiter. They found periodic layering on two scales within broad reaches of the NPLD. SHARAD bombards the martian surface with high-frequency radio waves that easily penetrate pure ice but reflect back off dirty ice. The radar sounded out 45 to 50 thin layers beneath the ice's surface, divided into four packets by distinctive zones of low reflection.

So far, the group has two possible interpretations. The low-reflection regions could represent times when Mars's orbit grew rounder and less elliptical, causing storms loading the ice with dust to become less common. Or they could mark times of relatively small axial tilt over many tilt cycles. In either case, the researchers say, the entire NPLD probably formed over roughly the past 5 million years.

LPSC attendees also heard the first quantitative evidence that orbital variations drove climate and geology much earlier in martian history. Planetary scientists Kevin Lewis of Caltech and Aharonson reported their analysis of layering in the low-latitude Arabia Terra region of Mars. They found rhythmic bedding at several locations, all dating to roughly 4 billion years ago. In Becquerel crater, 3.5-meter layers were bundled into packets that average 36 meters in thickness. Lewis and Aharonson have not publicly linked that 10:1 bedding ratio to any particular orbital variations, but they noted in their LPSC talk that Mars's thin atmosphere and lack of oceans make cyclic climate change driven by internal, El Niño–like processes much less likely there than it is on Earth. Nailing down periodic layering on Mars will no doubt require a lot more layer counting and perhaps a better sense of martian time. **–RICHARD A. KERR**

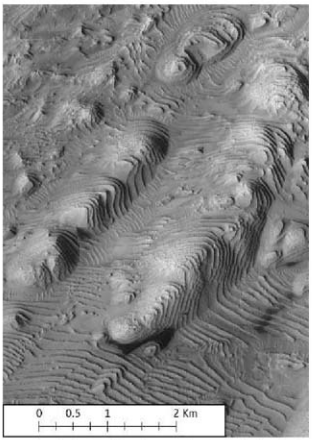

CREDIT: NASA/JPL/UNIVERSITY OF ARIZONA

Mars has rhythm. Evidence is mounting that variations in the orbit of Mars drive cyclic climate changes that layer the planet.

CHEMISTRY

Click Chemistry Clicks Along

Researchers seeking new ways to forge molecules are saving steps and effort by adapting high-yield reactions to fill a variety of needs

NEW ORLEANS, LOUISIANA—Halfway into a talk at a meeting* here last month, Charles Hoyle, a chemist at the University of Southern Mississippi, Hattiesburg, whipped out a clear plastic disk a few centimeters thick and about the size of a small Frisbee. Lodged in the disk were two bullets—one .22 caliber and one .38—fired by one of his colleagues in the lab.

The disc, Hoyle explained, is a laminate of two materials, one a rigid plastic, the other a new rubbery, highly efficient, energy-absorbing material. Putting the two materials together allowed the disk to absorb the energy of the speeding bullets and dissipate it without shattering. What's more, the bullet-stopping armor was made of cheap, everyday starting materials. In addition to armor, such laminates may one day find use in impact-resistant windshields for cars and airplanes, Hoyle says. "That was the most exciting thing I've seen in a couple of months," says K. Barry Sharpless, a Nobel Prize–winning chemist at the Scripps Research Institute in San Diego, California.

For many of the chemists in Hoyle's audience, the excitement lay as much in the way the new laminate was produced as in its impressive capabilities. It is a product of "click chemistry," a term Sharpless coined in 2001 for an approach to synthesis that prizes the use of a few key chemical reactions to link together compounds that contain particular chemical groups. The reactions have a strong energetic driving force that ensures that the starting compounds react every time, quickly, efficiently, and without creating unwanted byproducts. Click chemistry, says chemist Craig Hawker of the University of California, Santa Barbara (UCSB), "is a philosophy about not falling in love with complexity." And, as Hoyle's talk and others at a symposium at the American Chemical Society meeting here revealed, the philosophy is rapidly expanding throughout the world of polymers, materials science, drug delivery, and even biological imaging. "It has just exploded," Hawker says.

Sharpless says the goal of click chemistry is to synthesize materials the way nature does: by starting with a small set of building blocks and then linking them with just a handful of different reactions, as living organisms do in linking amino acids together with peptide bonds to forge proteins.

By contrast, much of modern organic synthesis—such as the medicinal chemistry used to craft many drug molecules—uses a wide variety of less efficient reactions. After going through perhaps dozens of these inefficient reactions, researchers typically wind up with only a minute amount of their desired molecule. Sharpless argues that chemists need to spend more time adapting efficient reactions to suit their needs.

Sharpless and his colleagues at Scripps kicked off the effort earlier this decade when they improved a well-known chemical reaction called the Huisgen reaction, in which chemical groups with carbon-carbon triple bonds called alkynes are linked with azides, which harbor N_3 groups with two nitrogen-nitrogen double bonds. Once the reaction starts, the alkyne and azide building blocks quickly and reliably form ring-containing compounds called 1,2,3-triazoles. But the reaction normally proceeds slowly because a high energy barrier keeps it from getting started. In 2002, Sharpless's team, along with a separate team led by Morten Meldal at the Carlsberg Laboratory in Valby, Denmark, reported that a simple copper salt catalyst dramatically speeds up the reaction. Even better, the catalyst is highly specific, which meant that the alkynes and azides reacted readily with one another but with essentially nothing else, no matter what chemical bath they were stewing in.

See here. Clicked-on fluorescent tags reveal newly synthesized DNA in tissues.

That selectivity spawned an explosion of click chemistry, as researchers around the globe have attached alkynes and azides to all kinds of materials and used the reaction to click them together. In hundreds of papers in recent years, researchers have described novel ways to make materials with new functions. Popular techniques include tacking sugars or peptides onto polymers to make them more biocompatible and clicking new chemical functional groups onto proteins, nanoparticles, and fluorescent compounds. "This stuff has taken on a life of its own," Sharpless says.

As the session at the meeting made clear, the copper-catalyzed alkyne-azide reaction remains the gold standard of click chemistry. Scripps chemist M. G. Finn, for example, reported that his group has recently used the reaction to create metal-binding adhesives twice as strong as any on the market. David Haddleton, a chemist at the University of Warwick in the United Kingdom, also reported using the technique to link azide-containing sugar groups to alkyne-rich polymers to create precisely controlled mimics of glycoproteins that represent a key part of the way the immune

*American Chemical Society Spring 2008 National Meeting, 6–10 April.

CREDITS: (TOP TO BOTTOM) C. HOYLE, UNIVERSITY OF SOUTHERN MISSISSIPPI; A. SALIC, PROCEEDINGS OF THE NATIONAL ACADEMY OF SCIENCES, 19 FEBRUARY 2008

Big impact. Products of click chemistry include this bullet-stopping plastic.

system prevents infections from parasites. Down the road, Haddleton says, he hopes that such mimics could offer a new strategy for preventing infection from organisms that cause dysentery, a disease that hits 40 million people a year worldwide.

The alkyne-azide reaction, however, is not the only game in town. "Click chemistry is no longer about a single reaction," Hawker says. One new reaction developed recently links compounds with thiol and ene functional groups. Thiols are compounds with a sulfur-hydrogen group, and enes are compounds with double bonds between two carbon atoms. When triggered by the absorption of energy-rich ultraviolet photons or other initiators, the sulfur atom in the thiol group readily attaches to one of those carbons while the thiol's hydrogen atom links up with the ene's other carbon. And the reaction is so fast that vast numbers of thiols and enes can be linked up in just minutes.

Progress in linking thiols and enes is taking off, Hoyle says, in part because the starting materials are cheap and abundant. They include commodity polymers such as polyethylene, widely used in products such as milk jugs and plastic grocery bags, and polystyrene, found in applications as diverse as CD jewel cases and packing peanuts. This easy availability has already prompted numerous groups to begin using click chemistry to tailor their standard polymers. Hoyle's bullet-stopping plastics are one example, and one he says he has improved considerably, although he is not ready to reveal details. To make that material, Hoyle's team first polymerized two pairs of thiol- and ene-containing compounds. One combo gave them the energy-absorbing material, the other the rigid polymer. They then laminated the two polymers together to help the energy-absorbing material shed the energy of the impact without breaking. Down the road, Hoyle says, expect researchers to click new functional groups onto plastic polyethylene films to improve their use as cheap food packaging, to prevent fresh food from spoiling, for example. Although similar plastic films are already on the market, they are typically made using a more expensive process.

Thiol-ene progress promises to open new applications as well. For example, Luis Campos, a postdoctoral associate in Hawker's lab, reported at the meeting that the UCSB group has made thiol-ene polymers that serve as tiny molds for patterning photonic crystals: devices that control the movement of photons much as semiconductors control the motion of electrons. When Campos and his colleagues patterned a titanium-nitride–based photonic crystal atop a semiconductor light-emitting diode, it doubled the light emission from the LEDs, cutting their power consumption in half.

Biology offers another emerging set of applications for click chemistry. Cell biologists Adrian Salic and Timothy Mitchison of Harvard Medical School in Boston, for example, reported in the 19 February issue of the *Proceedings of the National Academy of Sciences* (*PNAS*) that they had created a specialized alkyne-containing DNA building block. They fed it to mice, whose bodies took up the nucleotide base and used it to make DNA in their growing cells. After the mice were sacrificed, the researchers spiked the tissues with a fluorescently labeled azide and a copper catalyst that reacted with the alkyne-containing nucleotide and lit up newly synthesized DNA in fast-growing tissues in the animals.

Such an approach wouldn't work well in live animals, because the copper catalyst is highly toxic. But chemist Carolyn Bertozzi of UC Berkeley and colleagues recently developed a novel version of the azide-alkyne reaction that does away with copper. Last October, they reported in *PNAS* that by tweaking the normally linear alkynes to include eight-membered rings, they produced a strain in the molecules that prompted them to react more readily with an azide. It worked so well that the reaction essentially matched the rate of the copper catalyst. The researchers then used the reaction to click a fluorescent compound to specific sugar groups on live cells, with no apparent toxicity. In the 2 May issue of *Science* (p. 664), Bertozzi and her colleagues took the work a major step forward by showing that they could click a series of such fluorescent reporters to different biomolecules to visualize key steps in the development of zebrafish embryos. Bertozzi's team is now using the technique to try to watch the molecular dance that takes place as stem cells differentiate into various tissues.

Click chemistry may soon be making an impact on medicine as well. Hawker says he and his colleagues are clicking radioactive cobalt-64 to the interior of nanoparticles designed to keep the immune system from clearing the cobalt from the body. Peptides designed to bind to proteins found on damaged vessels of the heart are then clicked to the outside of the nanoparticles to steer them to their target. Ultimately, Hawker says, the system could provide doctors with an extremely sensitive way to spot the warning signs of the blood-vessel damage that accompanies atherosclerosis before any potential heart attack. Bertozzi says she is pursuing a related strategy to image cancer cells.

Clearly, be it in biology, polymers, or materials science, click chemistry is starting to click. **–ROBERT F. SERVICE**

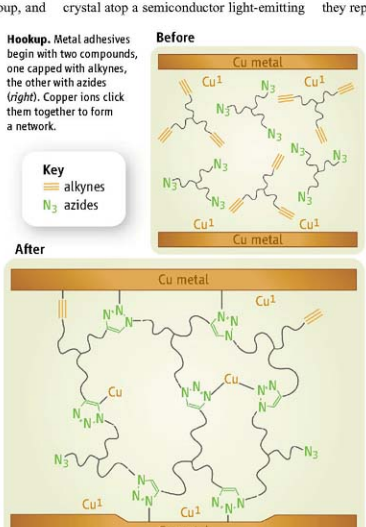

Hookup. Metal adhesives begin with two compounds, one capped with alkynes, the other with azides (*right*). Copper ions click them together to form a network.

CREDIT: ADAPTED FROM K. B. SHARPLESS, SCRIPPS RESEARCH INSTITUTE

PHYSICS

The Hot Question: How New Are The New Superconductors?

Do iron-and-arsenic superconductors work the same way as the older, inscrutable copper-and-oxygen compounds? Early evidence points both ways

Twenty-two years ago, the recondite world of condensed matter physics erupted into a frenzy of headline-grabbing discoveries. In June 1986, German experimenter J. Georg Bednorz and Swiss colleague Karl Alexander Müller reported that a compound called lanthanum barium copper oxide carried electricity without resistance at temperatures as high as 35 kelvin. That was closer to absolute zero than to room temperature (300 kelvin), but it was a whopping 12 degrees above the previous record for such "superconductivity." The discovery sparked a race for other copper-and-oxygen, or cuprate, superconductors with higher "critical temperatures" and bagged a Nobel Prize.

History seems to be repeating itself. In the past 5 months, researchers in Japan and China have cranked out a new family of high-temperature superconductors (*Science*, 25 April, p. 432). In place of copper and oxygen, the new compounds contain iron and arsenic, and the highest critical temperature for them has already reached 55 kelvin. That's far from the current record of 138 kelvin for the cuprates. But even as researchers strive for higher temperatures, they are preoccupied with one question: Do the new materials work the same way as the old ones?

It's a key issue because, after 2 decades of debate, physicists still do not agree on how the electrons in the cuprates perform their magic at such high temperatures. Many researchers regard high-temperature superconductivity as the single deepest mystery in condensed matter physics, and the new compounds might help to solve it. By comparing and contrasting the old and new superconductors, physicists might tease out commonalities that reveal how both of them work—if they work the same way.

That's a tricky if, says Hai-Hu Wen, an experimenter at the Institute of Physics (IOP) at the Chinese Academy of Sciences in Beijing. "The [new family of materials] looks very similar to the cuprates," Wen says. But, he adds, "the mechanism may not be the same." Peter Hirschfeld, a theorist at the University of Florida, Gainesville, notes that given the uncertainties surrounding the older materials, it may not make sense to ask if the new ones employ the same tricks. "Tell me how the cuprates work," he quips.

Still, physicists are pumping out papers on the new superconductors at a prodigious rate, and they have enough data to explain why they might or might not expect the new materials to work the same way as the old ones. Some are already taking sides in the emerging debate.

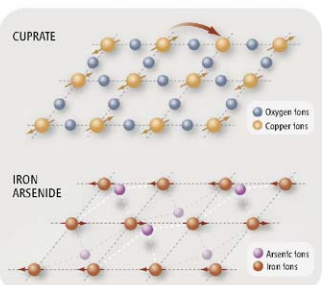

Plainly similar. The old and the new superconductors both contain planes of ions magnetized in opposite directions. In the older ones, electrons hop from copper to copper (arrow).

The mystery of the cuprates

Electricity won't flow through an ordinary wire without power from a battery or another source to push it. That's because the electrons flowing through a metal wire lose energy as they ricochet off the jiggling ions in the crystalline material. In a superconductor, however, the electrons avoid such drag by forming pairs. Deflecting an electron then requires breaking a pair, and at low temperatures there isn't enough energy around to do that. So the pairs glide unperturbed, and current flows without power.

Of course, like-charged electrons repel each other, so something has to hold a pair together. In 1957, American theorists John Bardeen, Leon Cooper, and Robert Schrieffer showed that in conventional superconductors, such as niobium chilled below 9.3 kelvin, vibrations rippling through the material's positively charged ions attract the electrons to one another. When one electron moves, it sets off a vibration that draws the second electron in its wake. But vibrations don't pull hard enough to produce the sky-high critical temperatures in the cuprates.

A cuprate superconductor is like a multitiered dancehall for electrons. The compound contains planes of copper and oxygen atoms along which the electrons glide like paired dancers. Between the planes lie elements such as lanthanum, strontium, barium, and yttrium. By default, a material has one potentially mobile electron per copper ion, and the electrons repel one another so mightily that they get stuck in a massive traffic jam called a Mott insulator state. To produce superconductivity, researchers "dope" the nonsuperconducting "parent material" with extra oxygen, which nestles between the copper-and-oxygen planes and soaks up a few electrons. The impasse then breaks, and the electrons somehow pair and flow freely.

Most physicists believe that the pairing originates not from some external factor such as vibrations but rather solely from the interactions of the electrons among themselves. "It's almost like the electrons are gluing themselves together," says Michael Norman, a theorist at Argonne National Laboratory in Illinois. But physicists still don't agree on how the electrons do that.

For example, electrons act like little magnets, and in a parent compound, those on neighboring copper ions point in opposite directions to form a static pattern known as antiferromagnetism (see figure, left). Some physicists argue that waves rippling through that pattern, which becomes fluid as oxygen is doped in, provide the glue for pairing. Others contend that no glue is needed and that pairing evolves, ironically, out of the repulsion between particles alone. Still others have proposed explanations involving tiny loops of current and other mechanisms. No theory quantitatively accounts for the myriad foibles of the complex materials.

Same tango, different dance floor

The new iron-arsenide superconductors could help sort through the different possibilities. Hideo Hosono, a materials scientist at the Tokyo Institute of Technology, and colleagues found the first compound,

CREDIT: L. CINQUINI/SCIENCE

fluorine-doped lanthanum oxygen iron arsenide ($LaO_{1-x}F_xFeAs$), as they reported online 23 February in the *Journal of the American Chemical Society*. It weighed in with a critical temperature of 26 kelvin.

Four Chinese groups quickly pushed the critical temperatures higher by replacing the lanthanum with other elements. On 25 March, Xianhui Chen of the University of Science and Technology of China in Hefei reported on the arXiv preprint server (www.arXiv.org) that samarium oxygen fluorine iron arsenide ($SmO_{1-x}F_xFeAs$) goes superconducting at 43 kelvin. Four days later, Zhong-Xian Zhao of IOP reported on the server that praseodymium oxygen fluorine iron arsenide ($PrO_{1-x}F_xFeAs$) has a critical temperature of 52 kelvin. On 13 April, Zhao's team reported a critical temperature of 55 kelvin for the samarium compound grown under pressure. The compounds all have the same crystal structure, and higher critical temperatures may be possible if researchers can find structures that pack in the planes more tightly, Zhao says.

The new compounds show striking similarities to the cuprates. Like the cuprates, they are layered materials, with planes of iron and arsenic along which the electrons presumably waltz. As in the older materials, superconductivity sets in only when the "parent material" is doped to change the number of electrons in it. In a cuprate, the extra oxygen absorbs some electrons; in one of the new materials, the fluorine adds electrons to the iron-and-arsenic planes.

Many researchers point to another observation as potentially key. Pengcheng Dai, an experimenter at the University of Tennessee, Knoxville, and Oak Ridge National Laboratory, and colleagues scattered neutrons off lanthanum oxygen iron arsenide doped with different amounts of fluorine. They found that the nonsuperconducting parent compound exhibits antiferromagnetism with alternating rows of iron ions magnetized in opposite directions. That pattern goes away as the material is doped and superconductivity sets in, the researchers reported 4 April on the arXiv.

A similar thing happens in the older high-temperature superconductors, notes Steven Kivelson, a theorist at Stanford University in Palo Alto, California. "Some form of antiferromagnetism turns off as superconductivity turns on," he says. "That's very reminiscent of the cuprates." Given that and the other similarities between the new compounds and the cuprates, Kivelson says, "it's a good working hypothesis that they're parts of the same bigger thing."

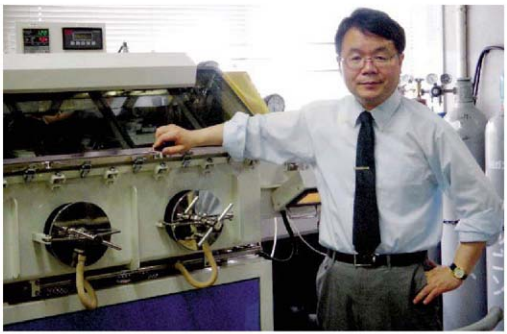

CREDIT: IMAGE COURTESY OF HIDEO HOSONO

Discoverer. Hideo Hosono, a materials scientist at the Tokyo Institute of Technology, cooked the first of the new superconductors that have captivated researchers the world over.

Not quite a chip off the ol' block

The similarities between old and new superconductors may mask more important differences, however. For example, the two families of compounds differ chemically in one obvious way. The new compounds contain iron, and in bulk iron, the individual magnetic ions tend to line up in the same direction to make a "ferromagnet," the sort of thing that will stick to your refrigerator. But ferromagnetism and superconductivity usually mix about as well as vinegar and oil: A superconductor ordinarily expels a magnetic field that's not too strong, but an overwhelming magnetic field will rip apart electron pairs and kill superconductivity. So the very presence of iron hints at new physics, says Hosono, the discoverer of $LaO_{1-x}F_xFeAs$. "This may be the first compound in which ferromagnetic elements and high-temperature superconductivity coexist," he says.

Perhaps more important, the undoped parent compounds for the iron-arsenide materials differ from the undoped parent compounds for the cuprates in one key regard, says Philip Anderson, a theorist at Princeton University. The undoped cuprates are exotic Mott insulators with precisely one electron stuck on each copper ion, he notes. In contrast, the undoped iron-arsenide materials are more conventional metals in which the electrons, numbering two per iron ion, flow relatively freely.

That means superconductivity evolves from very different starting points in the two families of materials, says Anderson, who argues that his "resonating valence bond" theory explains how superconductivity arises in the cuprates, without glue, from the Mott insulator state. "The only way I can make it the same is to invent some improbable chemistry that reduces [the starting point] to one electron" per iron ion, Anderson says. Superconductivity in the iron-and-arsenic materials must be a new beast entirely, he argues.

Revitalizing the field

All agree that physicists will need much more information before they can decipher the new compounds. But such information will surely come in a hurry. Thanks to their decades of work on the cuprates, condensed matter physicists have an arsenal of experimental and theoretical tools that they can now turn to the iron-and-arsenic compounds, says Patrick Lee, a theorist at the Massachusetts Institute of Technology in Cambridge. The fact that in the new materials the superconductivity emerges from a more conventional parent compound may also simplify matters, Lee says. "This may be an easier problem to crack," he says, because "the physics isn't as profound."

Even if the new materials prove as inscrutable as the cuprates, their mere appearance has revitalized the field, as many people have wearied of banging their heads against the same problems, says Dai. "My honest assessment is that this will explode because people are so tired of the cuprates," Dai says. "This will give people a new playground." First one to the top of the jungle gym—or to figure out how closely the new one resembles the old one—is the winner.

–ADRIAN CHO

LETTERS

edited by Jennifer Sills

U.S. Concerns over Bluetongue

M. ENSERINK'S NEWS OF THE WEEK STORY "EXOTIC DISEASE OF FARM animals tests Europe's responses" (8 February, p. 710) describes how bluetongue, a disease caused by a vector-borne orbivirus, has spread widely in ruminant livestock in Europe since 1999. Unlike Europe, which has only experienced bluetongue disease in the past few years, the United States and the Americas in general have been endemic for several bluetongue virus (BTV) serotypes since first reported in the 1950s. The historically prevalent U.S. BTV serotypes, though pathogenic in sheep, have caused little to no disease in U.S. cattle. The vectors of these serotypes have been identified, and their distribution has in the past explained the epidemiology of BTV in the United States (*1*).

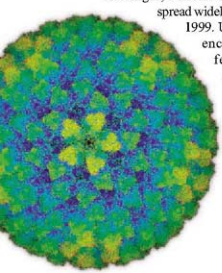

Bluetongue virus particle. A computer model shows the crystalline structure of the core particle of BTV.

Recently, eight new serotypes of BTV and a new serotype of the related orbivirus, epizootic hemorrhagic disease virus (EHDV), have been identified in the United States (*2*, *3*). Some of the virus isolates were from clinically affected sheep and deer, with others being detected through testing of cattle for export. The presence of these new serotypes raises the specter that the epidemiology of these viruses in North America may be changing and could result in more extensive disease in U.S. livestock and wildlife then ever seen previously. This is bad news for the U.S. livestock industries and for our ruminant wildlife.

Our ability to understand the current situation is hindered because there is currently no comprehensive surveillance in the United States for either BTV or EHDV. A comprehensive surveillance system, greater risk assessment, and risk prevention through vaccine development and vector control are all needed. The events in Europe demand that we pay attention before BTV and EHDV have similar repercussions for the United States.

E. PAUL J. GIBBS,[1] WALTER J. TABACHNICK,[2] THOMAS J. HOLT,[3] DAVID E. STALLKNECHT[4]

[1]College of Veterinary Medicine, University of Florida, Gainesville, FL 32608, USA. [2]Florida Medical Entomology Laboratory, University of Florida, Vero Beach, FL 32968, USA. [3]Division of Animal Industry, Florida Department of Agriculture Consumer Services, Tallahassee, FL 32399, USA. [4]SCWDS, College of Veterinary Medicine, University of Georgia, Athens, GA 30602, USA.

References

1. W. J. Tabachnick, *Annu. Rev. Entomol.* **41**, 23 (1996).
2. D. J. Johnson, P. P. C. Mertens, S. Maan, E. N. Ostlund, in *Proceedings of the 50th American Association of Veterinary Laboratory Diagnosticians (AAVLD) Annual Conference*, Reno, NV, 18 to 23 October 2007, p. 138.
3. P. P. C. Mertens *et al.*, *13th International Symposium WAVLD Conference Proceedings* (2007), p. 55; www.wavld2007.com/program.php.

In Defense of Max Planck

THE MAX PLANCK PHDNET, REPRESENTING about 4000 Max Planck graduate students, takes issue with the unfounded claim by Widmar Tanner that a disconnect between German universities and Max Planck Institutes (MPIs) leads to MPI graduates that are "at best average" ("Max Planck accused of hobbling universities," News of the Week, G. Vogel, 25 January, p. 396). As young professionals of this system, we draw a more accurate portrayal of the Max Planck graduates (*1*).

MPIs rely heavily on a competitive, formalized, application process typical of elite universities requiring transcripts, recommendations, and faculty interviews. This results in selectivity on par with, if not more competitive than, elite international programs.

MPIs attract a high number of foreign graduate students; 50% of the student population is international, reflecting MPIs' strong foothold in the global competition for talent. This connection establishes relationships between foreign graduates and German institutes, at a time when Germany is striving to "internationalize" its science ("German science takes an international view," News of the Week, G. Vogel, 29 February, p. 1172).

To ensure a high caliber of graduate research, MPI students are regularly evaluated by national and international committees. The evaluators have been resoundingly impressed by the spirit and scientific quality of the students and their research.

Currently, 49 International Max Planck Research Schools (IMPRSs) represent half of the MPI graduate students. Since their inception (2000), IMPRSs have altered the MPI graduate experience. Their modern approach requires thesis committees, advanced graduate courses, soft-skills training (e.g., presentation, communication, leadership, and time management), and teaching. Their establishment has noticeably raised the bar for education of all MPI graduate students, as the benefits of IMPRSs are increasingly extended to all students.

MELISSA BETH DUHAIME, SÖREN ALSHEIMER, RALITSA ANGELOVA, IAN FITZPATRICK

Max Planck PhDnet, Max Planck Society, Munich, Germany.

Reference

1. Refer to the detailed PhDnet response at www.phdnet.mpg.de/documents/PhDnet_response.pdf.

Molecules in motion
881

Feeding on water
886

Effect of Contraceptive Access on Birth Rate

IN HER PERSPECTIVE "REPRODUCING IN CITIES" (8 February, p. 764), R. Mace assumes that differences in birth rates between rural and urban areas largely represent the wishes of parents. Human beings in all societies have sexual intercourse hundreds or even thousands of times more often than is needed to conceive the number of children they want. Once individuals have access to the means and information to separate sex from childbearing, family size often falls rapidly (*1*). For rural women there are an astonishing number of barriers to access to modern contraception (*2*), while urban women are often better placed to overcome these barriers.

We suggest that birth rates fall in cities primarily because contraception and safe abortion are easier to obtain than in the countryside. For example, in rural Ethiopia only doctors and nurses are permitted to give contraceptive injections, so this popular method is denied to rural women. The total fertility rate (TFR) in Ethiopia as a whole is 5.4, while in Addis Ababa it is now thought to be below 2.0 children. Addis is unusual among African capitals in that safe abortion was available for several years before the recent liberalization of the abortion law. Tens of thousands of operations were performed annually and linked to effective post-abortion contraceptive advice.

We posit that fertility will fall in rural Ethiopia as contraception and safe abortion become more easily available. In Bangladesh, where many women now have access to modern contraception and reasonably safe abortion, two large predominantly rural areas (Khulna and Rajhashi) now have replacement-level fertility (*3*).

MARTHA CAMPBELL AND MALCOLM POTTS
School of Public Health, University of California, Berkeley, CA 94720, USA.

References
1. M. Potts, *Popul. Dev. Rev.* **23**, 1 (1997).
2. M. M. Campbell *et al.*, *Stud. Family Plan.* **37**, 87 (2006).
3. *Bangladesh Demographic and Health Survey 2007* (Macro International, MD, 2007).

Response

IT IS CERTAINLY TRUE THAT CONTRACEPTIVE services can be hard to acquire in rural Ethiopia, as in several other African countries. Sinding *et al.* used data on unmet need for contraception to estimate that the total fertility rate would drop from about 6 to about 4 children in rural areas of Ethiopia if contraceptives were more readily available to all (*1*). Improved reproductive health services would certainly be welcome in much of rural Africa and would further reduce rural poverty and ill health by helping to reduce unwanted births.

But it seems unlikely that rural birth rates would fall to urban levels, given that in Europe (where contraception is available everywhere) rural households do still have larger families than city dwellers.

Access to contraception cannot be considered the original driving force behind fertility decline as, historically, fertility declined in Europe without modern contraceptives; the desire for smaller families created the demand for contraceptives, not vice versa. Furthermore, in Addis Ababa, family size correlates positively with wealth. Poverty is associated with failure to marry, increased rates of divorce, and slower birth rates after marriage (*2*), when the wealthy presumably have as good or better access to medical facilities than the poor.

Demographers have always focused heavily on the proximate determinants of fertility, especially since Bongaarts's classic paper (*3*), but often to the exclusion of any underlying theory of reproductive decision-making. Emphasis on proximate determinants cannot answer questions such as why families of particular sizes are favored, or when fertility is predicted to stop declining (an earlier notion that fertility decline would stop at replacement levels is not supported by the very low fertility now seen in Europe). Demography has been described by its own practitioners as a field without a theory (*4*). Evolutionary demographers are attempting to provide that theory through the related fields of human behavioral ecology, evolutionary life history theory, and cultural evolution. It is possible that demand for contraceptive services will eventually be so high everywhere that much of the variation in fertility will disappear; but even if so, the question of why demand for contraception is so high still needs to be addressed.

RUTH MACE

Department of Anthropology, University College London, London WC1H 0BW, UK.

References

1. S. W. Sinding, J. A. Ross, A. G. Rosenfeld, *Int. Family Plan. Perspect.* **20**, 23 (1994).
2. E. Gumma, R. Mace, *J. Biosoc. Sci.* **40**, 339 (2008).
3. J. Bongaarts, O. Frank, R. Lesthaeghe, *Popul. Dev. Rev.* **10**, 511 (1984).
4. L. Bumpass, *Popul. Stud. Suppl.* **45**, 177 (1991).

Financing Tropical Forest Preservation

IN THEIR REVIEW "CLIMATE CHANGE, DEFORestation, and the fate of the Amazon" (11 January, p. 169), Y. Malhi *et al.* advocate international incentives to reduce tropical deforestation and limit climate change through programs that they admit will require extensive time and effort to develop. But while seeking these kinds of long-term solutions to reduce fossil fuel dependence and global carbon emissions, we need stopgap remedies that require limited technological advances, will not jeopardize developing economies, and have a high chance of success.

Although many promote limitation of tropical deforestation as critical to alleviating climate change (*1*), the relative importance of tropical versus boreal forests as carbon sinks remains uncertain (*2*). Preserving tropical forests may curb net carbon emissions and protect substantial amounts of global biodiversity. However, the capacity of developing nations to manage tropical forests appears limited in terms of current administrative infrastructure, technical knowledge, and political or economic stability. It is essential, therefore, to focus initial attention on the carbon sequestering potential of existing boreal forests (*3*). The financial resources and administrative capacity of the boreal nations (Canada, Russia, the United States, Finland, Sweden, and Norway) make such action possible, even in the face of increasing demands for harvesting. This approach is also fair, given that global warming is a problem that was created primarily by developed nations.

We propose that carbon credit funds be immediately directed toward preserving boreal forests. Boreal countries should then reinvest these carbon funds to build capacity, buy land, swap forests for debt, and provide alternative livelihoods in developing tropical nations. This will result in substantial carbon and biodiversity benefits overall in both boreal and tropical regions.

IAN G. WARKENTIN[1]* AND NAVJOT S. SODHI[2]

[1]Environmental Science, Memorial University of Newfoundland, Corner Brook, NL A2H 6P9, Canada. [2]Department of Biological Sciences, National University of Singapore, 14 Science Drive 4, Singapore 117543, Republic of Singapore.

*To whom correspondence should be addressed. E-mail: iwarkent@swgc.mun.ca

References

1. R. E. Gullison *et al.*, *Science* **316**, 985 (2007).
2. B. B. Stephens *et al.*, *Science* **316**, 1732 (2007).
3. L. Odling-Smee, *Nature* **437**, 614 (2005).

CORRECTIONS AND CLARIFICATIONS

Reports: "Ubistatins inhibit proteasome-dependent degradation by binding the ubiquitin chain" by R. Verma *et al.* (1 October 2004, p. 117). In Fig. 1D, the structure of ubistatin B is incorrect. The correct structure is shown here. The reported results for ubistatin B are correct and reproducible; the only error was in the reporting of the structure.

Ubistatin B: NSC 306455

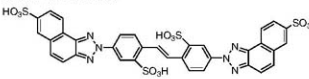

TECHNICAL COMMENT ABSTRACTS

COMMENT ON "Habitat Split and the Global Decline of Amphibians"

David C. Cannatella

Becker *et al.* (Reports, 14 December 2007, p. 1775) reported that forest amphibians with terrestrial development are less susceptible to the effects of habitat degradation than those with aquatic larvae. However, analysis with more appropriate statistical methods suggests there is no evidence for a difference between aquatic-reproducing and terrestrial-reproducing species.

Full text at www.sciencemag.org/cgi/content/full/320/5878/874c

RESPONSE TO COMMENT ON "Habitat Split and the Global Decline of Amphibians"

Carlos Roberto Fonseca, Carlos Guilherme Becker, Célio Fernando Baptista Haddad, Paulo Inácio Prado

Habitat split, defined as human-induced disconnection between habitats used by different life history stages of a species, is a strong factor negatively affecting the richness of Brazilian Atlantic Forest amphibians. Here, the disconnection between streams and forest fragments is shown to reduce the proportion of species with aquatic larvae in local communities.

Full text at www.sciencemag.org/cgi/content/full/320/5878/874d

Letters to the Editor

Letters (~300 words) discuss material published in *Science* in the previous 3 months or issues of general interest. They can be submitted through the Web (www.submit2science.org) or by regular mail (1200 New York Ave., NW, Washington, DC 20005, USA). Letters are not acknowledged upon receipt, nor are authors generally consulted before publication. Whether published in full or in part, letters are subject to editing for clarity and space.

EXHIBITIONS: ART AND MATHEMATICS

Bridging the Cultural Divide

W. Timothy Gowers

I imagine that you are looking at an abstract sculpture and that you learn, after enjoying it for a while, that its shape can be defined by a very simple mathematical formula. Moreover, you find out that the sculptor is actually a technician who was commissioned by a mathematician to give solid realization to the formula. This account of the production of the object in front of you does not seem to leave much room for the creative process, so can the result be art? Should your enjoyment be less than if a similar shape had been produced without the involvement of mathematics? Or are the rigid confines of the mathematical formula entirely compatible with a genuinely aesthetic response?

Beyond Measure, an exhibition about geometry in the arts and sciences, raises several questions of this nature. Perhaps the best attitude to take to the exhibits is one expressed by Ernst Gombrich: "Actually I do not think that there are any wrong reasons for liking a statue or a picture. Someone may like a landscape painting because it reminds him of home, or a portrait because it reminds him of a friend. There is nothing wrong with that" (*1*). Likewise, scientifically trained visitors to *Beyond Measure* will be able to connect many of the exhibits on display with their experience and education, and this is a source of pleasure that does not differ importantly from connecting works of art with other, supposedly more human, forms of experience.

The exhibition aims to foster dialogue among mathematicians, scientists, architects, artists, and designers: anybody, that is, for whom geometry is important. So as well as containing mathematical models, it has working models made by famous scientists, drawings and plans by architects, and mathematically inspired paintings, sculptures, and designs. Taken together, these items form a remarkably coherent whole, and in this sense the exhibition succeeds admirably.

Beyond Measure
Conversations Across Art and Science
Barry Phipps, Curator
Kettle's Yard, Cambridge. Through 1 June 2008. www.kettlesyard.co.uk/exhibitions/beyond.html

Beyond Measure
Conversations Across Art and Science
by Barry Phipps
Kettle's Yard, Cambridge, 2008. Paper, 48 pp. £6.95. ISBN 9781904561262.

My one complaint is that there is not enough information about the exhibits. For instance, one item is a display of crocheted hyperbolic surfaces. As a mathematician, I understood what these were and could appreciate them, but many others would surely have benefited from an account, of a kind that would not have been hard for a mathematician to write, of the difference between positive and negative curvature and of why crochet was a particularly good medium for realizing a negatively curved surface. Without such an account, the surfaces that delighted me must have come across to many people as nothing more than bits of crochet that were oddly twisted.

Similar remarks could be made about a shelf with an extraordinary collection of glass Klein bottles. Or rather, that is what they were topologically speaking, but they did not all look like a typical illustration of the Klein bottle in a book—they included exotic twists and spirals that left one wondering how they could possibly have been made. However, nowhere was there anything to read about one-sided surfaces. Many people will therefore have missed the pleasure of fixing their eyes on a point of the surface and then tracing out a path that ends up on the other side of the glass from the starting point.

I found myself completely stumped by a item titled *Inversions*. It consisted of pairs of interesting three-dimensional curved shapes, of which one saw the top halves directly and the bottom halves in a mirror on which the top halves stood. I very much wanted to know what the inversion was that related one shape in each pair to the other, but there was no attempt to say, even roughly.

The catalog is full of vague pieties about the need for dialogue between artists and scientists. But by not really trying to explain the science behind the exhibits, the exhibition missed the chance for dialogue of the most obvious and potentially fruitful kind. This is missed because the more you know about what you see, the deeper your appreciation, whether or not you wish to call it aesthetic. However, the exhibits themselves cannot be faulted. If you are in Cambridge, you should not miss the chance to see them. And perhaps for some visitors they will spark an interest in mathematics and science that can be followed up on later.

The lack of dialogue goes in the other direction as well. For example, we could have been told how the artist Keith Tyson produced his painting *Quad Start Double Bounded Random Walk*. There were tantalizing clues: a zigzag that had clearly been generated randomly (but how exactly?) was used as the

Glass Klein bottles, Alan Bennett (1995).

Model of a hyperbolic area (crocheted wool), Daina Taimina.

CREDITS: COURTESY KETTLE'S YARD

The reviewer is at the Department of Pure Mathematics and Mathematical Statistics, Centre for Mathematical Sciences, University of Cambridge, Wilberforce Road, Cambridge CB3 0WB, UK. E-mail: wtg10@cam.ac.uk

basis for a curve that approximated it. But how systematic was the derivation of the curve from the zigzag? It would have been good to know, because the curve had a peculiarly satisfying shape. It came across both as a very successful example of abstract expressionism (even if at one level the success was accidental and not necessarily "expressing" anything), and also as a direct and intuitive illustration of large-scale order just beginning to emerge from a succession of random choices.

One item that bucked the trend was a video display of a rotating four-dimensional hypercube. An accompanying audio commentary explained carefully what one was seeing and drew useful analogies between that and the ordinary three-dimensional cube. As a result, one began to feel that one was truly understanding the fourth dimension. This piece showed how much more *Beyond Measure* as a whole could have achieved.

Reference

1. E. H. Gombrich, *The Story of Art* (Phaidon, London, 1950).

10.1126/science.1159559

SCIENCE AND RELIGION

Rethinking History for a New Islamic Science

Jane H. Murphy

In 1727 a Balkan Muslim convert, Ibrahim Muteferrika, procured a license for the first Islamic-run printing press in the Ottoman Empire. Sensitive to the uproar in Christian Europe over the heliocentric model of the universe, he worried that a Turkish translation of the Copernican model would create opposition to his press. However, clerical reaction to the treatise was mild: as long as God's position as creator of the universe was preserved, the movement of Earth caused no theological objection. Still, Muteferrika's press was short lived. It wasn't Islamic opposition but rather the power of the guild of copyists and calligraphers (with tens of thousands of members) that successfully blocked his enterprise.

Muteferrika's story echoes many of the themes of Muzaffar Iqbal's *Science and Islam* and highlights one of the analytic problems of Iqbal's larger project: So-called Islamic opposition to rational study of the natural world has little theological basis or historical evidence. On the contrary, the broad Islamic tradition produced commentaries and new treatises on mathematical, astronomical, astrological, geographic, botanical, and medical sciences from the 8th through 18th centuries. And today scientific education is present in every Islamic nation, although Iqbal (a writer and Islamic scholar who trained as a biochemist) despairs about the quality of such education. If religious opposition did not stop science in the past or now, however, why is Iqbal just as despondent as Islam's harshest critics about the current state of science in Islamic countries? He must embrace a sense of crisis because he is advocating a radical shift in policy and aims.

Iqbal does not merely seek increased funding for science and greater appreciation of scientific inquiry in the Islamic world. Rather, he calls for "a major intellectual revolution in the Muslim world." His goal with the book and his Center for Islam and Science (www.cis-ca.org) is to advocate a new mode of science that is modern in its range and achievement while Islamic in its worldview. This new Islamic science must differ qualitatively from Western science, although he gives little to clarify just what it would look like in scope or practice.

Science and Islam
by Muzaffar Iqbal
Greenwood, Westport, CT, 2007. 269 pp. $65, £37.95. ISBN 9780313335761. Greenwood Guides to Science and Religion.

Ostensibly a history of science and Islam, Iqbal's book is best read as a diagnosis of the current state and a prescription for future reforms. Its most animated analysis comes in the concluding chapters and the author's call for change. Much of the book consists of a selective survey of scientific achievements in the Islamic tradition, with particular focus on mathematics and astronomy. However, his approach to this material is not fundamentally historical. Iqbal rejects the historicization of Islam ("Islam is not a fluid conceptual framework that keeps changing with time"), and he also minimizes the role that astrology and divination, not to mention alchemical beliefs, played in Islamic and European scientific practices well past the Renaissance. To him, the Islamic scientific patrimony is primarily important not for the insight it might offer into earlier historical periods but for the role it should play in creating a new alternative to modern Western science. This is an ambitious intellectual project but one still trying to gain followers.

Iqbal rightly shows that whatever religious antagonism one finds before the 19th century, and particularly the critical writings of al-Ghazali (1058–1111), proved less influential than religious and social encouragement of science loosely termed. However, he is ultimately reluctant to offer social, political, or economic remedies for the current state of affairs and instead returns the debate to the terms of religion. For him, none of the 57 members of the Organization of the Islamic Conference "produce any science worth its name," and this is because the science (and technology) they seek remains ultimately foreign to an Islamic worldview.

The author usefully draws readers' attention to the ways in which modern science and European colonization extended one another's reach and therefore complicated questions of modernization and resistance in 19th- and early-20th-century colonies. In his analysis, reformers like Jamal al-Din al-Afghani (1838–1897) and Sayyid Ahmad Khan (1817–1898) are seen as advocating a kind of scientism that appears just as dated as Herbert Butterfield's faith in science to push out all contenders for social authority.

The problem for Iqbal is that he wants to re-create the European trajectory from various forms of knowledge of the natural world to "science worth its name" while preserving a mode of transformation and ultimate product distinct from that which emerged in Europe. Islamic science must measure up to Western science but must also differ from its yardstick. Iqbal's argument in favor of such a program of Islamic science comes both from a post-1950 critique of science and technology and of the power that this form of knowledge holds in the modern world and from his particular interpretation of the lesson to be drawn from the past two centuries of failed scientific reform movements.

As Iqbal concedes, most Islamic governments and their general publics do not share his goal. Rather, his call comes from "a small minority of Muslim scholars." Indeed, Iqbal ultimately posits "a deep-seated, almost insatiable, hunger for modern science in the Muslim psyche," a hunger explained as a feeling of inferiority emerging from the colonial experience.

Iqbal wants to revive Islamic intellectual society through a reclamation—or more properly the creation—of a modern Islamic science. If his project succeeds, modern Islamic science, rather than bringing Islamic societies further into Euro-American networks of institutions and practices, would be a point of differentiation.

10.1126/science.1157350

The reviewer is at the Department of History, Colorado College, 14 East Cache La Poudre Street, Colorado Springs, CO 80903, USA. E-mail: jane.murphy@coloradocollege.edu

ECONOMICS

The Promise of Prediction Markets

The ability of groups of people to make predictions is a potent research tool that should be freed of unnecessary government restrictions.

Kenneth J. Arrow,[1] Robert Forsythe,[2] Michael Gorham,[3] Robert Hahn,[4]* Robin Hanson,[5] John O. Ledyard,[6] Saul Levmore,[7] Robert Litan,[8] Paul Milgrom,[1] Forrest D. Nelson,[9] George R. Neumann,[3] Marco Ottaviani,[10] Thomas C. Schelling,[11] Robert J. Shiller,[12] Vernon L. Smith,[13] Erik Snowberg,[14] Cass R. Sunstein,[7] Paul C. Tetlock,[15] Philip E. Tetlock,[16] Hal R. Varian,[17] Justin Wolfers,[18] Eric Zitzewitz[19]

Prediction markets are forums for trading contracts that yield payments based on the outcome of uncertain events. There is mounting evidence that such markets can help to produce forecasts of event outcomes with a lower prediction error than conventional forecasting methods. For example, prediction market prices can be used to increase the accuracy of poll-based forecasts of election outcomes (*1*) (see the figure), official corporate experts' forecasts of printer sales, and statistical weather forecasts used by the National Weather Service.

Several researchers emphasize the potential of prediction markets to improve decisions (*2*–*5*). The range of applications is virtually limitless—from helping businesses make better investment decisions to helping governments make better fiscal and monetary policy decisions.

Prediction markets have been used by decision-makers in the U.S. Department of Defense (*6*), the health care industry (*7*), and multibillion-dollar corporations such as Eli Lilly, General Electric, Google, France Telecom, Hewlett-Packard, IBM, Intel, Microsoft, Siemens, and Yahoo (*8*). The prices in these markets reflect employees' expectations about the likelihood of a homeland security threat, the nationwide extent of a flu outbreak, the success of a new drug treatment, the sales revenue from an existing product, the timing of a new product launch, and the quality of a recently introduced software program.

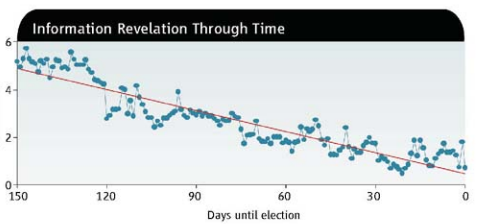

Information revelation through time. Data are from the Iowa Electronic Markets for markets predicting the two-party vote shares from the 1988, 1992, 1996, and 2000 presidential elections (*19*). The vertical axis plots the average absolute difference between the market prediction and the actual vote share. In the week immediately before the election, the market erred by an average of 1.5 percentage points compared with an average error of 2.1 percentage points for the final Gallup poll. The longer-run forecasting performance of the market is also impressive, with an average error of only 5 percentage points 150 days before the election, a time when polls have much larger errors when interpreted as predictions. Calculations are based on data available at www.biz.uiowa.edu/iem.

These markets could assist private firms and public institutions in managing economic risks, such as declines in consumer demand, and social risks, such as flu outbreaks and environmental disasters, more efficiently.

Unfortunately, however, current federal and state laws limiting gambling create significant barriers to the establishment of vibrant, liquid prediction markets in the United States. We believe that regulators should lower these barriers by creating a legal safe harbor for specified types of small-stakes markets, stimulating innovation in both their design and their use (*9*).

How and Why Prediction Markets Work

An example will help to clarify the prediction market concept. Consider a contract that pays $1 if Candidate X wins the presidential election in 2008. If the market price of an X contract is currently 53 cents, an interpretation is that the market "believes" X has a 53% chance of winning. Prediction markets reflect a fundamental principle underlying the value of market-based pricing: Because information is often widely dispersed among economic actors, it is highly desirable to find a mechanism to collect and aggregate that information. Free markets usually manage this process well because almost anyone can participate, and the potential for profit (and loss) creates strong incentives to search for better information. To be sure, a lively debate has arisen about whether prediction market prices are subject to various biases, which might diminish their accuracy as an aggregation mechanism (*10*–*14*). However, prediction markets have been used with success in a variety of contexts.

Legal Impediments

The use of prediction markets has been greatly deterred by state and federal laws restricting Internet gambling because at least some of these laws are plausibly understood to cast serious doubts on prediction

[1]Department of Economics, Stanford University, Stanford, CA 94305, USA. [2]College of Business, University of South Florida, Tampa, FL 33620, USA. [3]Stuart School of Business, Illinois Institute of Technology, Chicago, IL 60661, USA. [4]Reg-Markets Center at American Enterprise Institute, Washington, DC 20036, USA. [5]Department of Economics, George Mason University, Fairfax, VA 22030, USA. [6]Department of Economics, California Institute of Technology, Pasadena, CA 91125, USA. [7]University of Chicago Law School, Chicago, IL 60637, USA. [8]Kauffman Foundation, Kansas City, MO 64110, USA. [9]Department of Economics, University of Iowa, Iowa City, IA 52242, USA. [10]Kellogg Graduate School of Management, Northwestern University, Evanston, IL 60208, USA. [11]School of Public Policy, University of Maryland, College Park, MD 20742, USA. [12]Department of Economics, Yale University, New Haven, CT 06520, USA. [13]Chapman University School of Law, Orange, CA 92866, USA. [14]Graduate School of Business, Stanford University, Stanford, CA 94305, USA. [15]Yale School of Management, New Haven, CT 06520, USA. [16]Haas School of Business, University of California, Berkeley, CA 94720, USA. [17]School of Information, University of California, Berkeley, CA 94720, USA. [18]The Wharton School, University of Pennsylvania, Philadelphia, PA 19104, USA. [19]Department of Economics, Dartmouth College, Hanover, NH 03755, USA.

*Author for correspondence. E-mail: rhahn@aei.org.

markets. Currently, eight states bar Internet gambling outright. In 2006, President Bush signed the Unlawful Internet Gambling Enforcement Act, designed to crack down on such gambling.

The legal questions here are complex, but to create a prediction market in the United States that is unambiguously legal, one must run a regulatory gauntlet (*15*). In principle, these difficulties could be avoided by creating prediction markets outside the United States, but this approach could suppress innovation and reduce opportunities to aggregate information and improve decisions. It would be better for U.S. authorities to clarify the circumstances under which prediction markets are plainly legal.

Breaking the Legal Impasse

We suggest that two steps should be taken to facilitate the use of prediction markets while still meeting the legitimate concerns of lawmakers and regulators.

(i) The Commodity Futures Trading Commission (CFTC), the federal regulatory agency that oversees futures market activity, should establish safe-harbor rules for selected small-stakes markets. One limited safe harbor is the no-action letter, in which the CFTC market oversight staff confirms in writing that it will not recommend enforcement action if the recipient acts in specified ways. The only prediction market to receive a no-action letter (in 1992) is the Iowa Electronic Markets (*16*), which is run by professors at the University of Iowa and which initially focused on presidential elections. Although such no-action letters reduce the chances of legal action under other state and federal laws, they may not be adequate. We would therefore urge the CFTC to explore other approaches to ensuring safe harbors, for example, formal rules or guidance approved by the commission.

We suggest that three types of entities be eligible for safe harbor treatment. The first would be not-for-profit research institutions, including universities, colleges, and think tanks wishing to operate exchanges similar to the Iowa Electronic Markets. The second would be government agencies seeking to do research similar to that of nongovernmental research institutions. The third group would consist of private businesses and not-for-profits that are not primarily engaged in research, which would only be allowed to operate internal prediction markets with their employees or contractors.

In all cases, markets would be limited to small-stakes contracts. Although the definition of small stakes is somewhat arbitrary, we use the term to mean an exchange in which the total amount of capital deposited by any one participant may not exceed some modest sum, perhaps something like $2000 per year.

The exchanges themselves would be not-for-profit but would be allowed to charge modest fees to recoup administrative and regulatory costs. Brokers and paid advisers would be barred, reducing the risks that contracts would be sold to inappropriate or vulnerable customers or that customers would be charged fees above the amounts needed to maintain the markets. Exchanges would be self-regulated, leaving them with the responsibility to make reasonable efforts to keep markets free from fraud and manipulation.

For its part, the CFTC should allow contracts that price any economically meaningful event. This definition could allow for contracts on political events, environmental risks, or economic indicators, such as those offered by the Iowa Electronic Markets, but would presumably not include contracts on the outcomes of sports events.

The contracts qualifying under this safe harbor would also create opportunities for more efficient risk allocation (*17*). Although the small-stakes nature of these markets would necessarily limit their usefulness for hedging risk, they could serve as proofs of concept for larger-scale markets that could be developed under alternative regulatory arrangements.

The CFTC should allow researchers to experiment with several aspects of prediction markets—fee structures, incentives against manipulation, liquidity requirements and the like—with the goal of improving their design. Prediction markets are in an early stage, and if their promise is to be realized, researchers should be given flexibility to learn what kinds of design are most likely to produce accurate predictions. Of course, exchanges would need to inform their customers so that they are aware of the risks and benefits of participating in these markets.

(ii) Congress should support the CFTC's efforts to develop prediction markets (*18*). To the extent that the CFTC incurs costs in promoting innovation, Congress should provide the necessary funding. More fundamentally, Congress should explore alternative ways of securing a legal framework for prediction markets if the CFTC's existing authority proves inadequate. In particular, Congress should specify that a no-action letter, or similar mechanism, preempts overlapping state and federal antigambling laws. Because Congress did not intend the CFTC to regulate gambling, it is important to design new regulations so that socially valuable prediction markets easily qualify for the safe harbor but gambling markets do not.

Conclusion

We have suggested some modest reforms at the federal level that we hope will facilitate the development of prediction markets. These markets have great potential for improving social welfare in many domains. American leadership in this area is likely to encourage parallel efforts in other countries, speeding the development of this tool. The first step in helping prediction markets deliver on their promise is to clear away regulatory barriers that were never intended to inhibit socially productive innovation.

References and Notes

1. J. Berg, F. Nelson, T. Rietz, *Int. J. Forecast.*, in press.
2. R. Hanson, *IEEE Intell. Syst.* **14**, 16 (1999).
3. R. Hahn, P. Tetlock, *Harvard J. Law Pub. Pol.* **28**, 213 (2005).
4. C. Sunstein, *Infotopia: How Many Minds Produce Knowledge* (Oxford Univ. Press, New York, 2006).
5. E. Snowberg, J. Wolfers, E. Zitzewitz, *Q. J. Econ.*, **122**, 807 (2007).
6. R. Hanson, T. Ishikida, J. Ledyard, C. Polk, *Proceedings of the ACM International Conference on Electronic Commerce*, Pittsburgh, PA, 30 September to 3 October 2003 (Association for Computing Machinery (ACM), New York, 2003), p. 272.
7. P. M. Polgreen, F. Nelson, G. Neumann, *Clin. Infect. Dis.* **44**, 272 (2007).
8. B. Cowgill, J. Wolfers, E. Zitzewitz, "Using prediction markets to track information flows: Evidence from Google," Dartmouth College (2008); www.bocowgill.com/GooglePredictionMarketPaper.pdf.
9. K. Arrow *et al.*, "Statement on prediction markets," AEI-Brookings Joint Center Related Publication No. 07-11 (May 2007); available at Social Science Research Network (SSRN), http://ssrn.com/abstract=984584.
10. J. Wolfers, E. Zitzewitz, "Interpreting prediction market prices as probabilities," Stanford Graduate School of Business (2005).
11. C. Manski, *Econ. Lett.* **91**, 425 (2006).
12. C. Sunstein, *Infotopia: How Many Minds Produce Knowledge* (Oxford Univ. Press, New York, 2006).
13. M. Ottaviani, P. N. Sørensen, *J. Eur. Econ. Assoc.* **5**, 554 (2007).
14. P. Tetlock, "Liquidity and prediction market efficiency" (March 2008); available at SSRN: http://ssrn.com/abstract=929916.
15. R. Hahn, P. Tetlock, *J. Regul. Econ.* **29**, 265 (2006).
16. No-action letter from Andrea M. Corcoran, Director, Commodity Futures Trading Commission (CFTC) Division of Trading and Markets, to George R. Neumann, Professor of Economics, University of Iowa (5 February 1992); www.cftc.gov/files/foia/repfoia/foirf0503b002.pdf.
17. R. Shiller, *Macro Markets: Creating Institutions for Managing Society's Largest Economic Risks* (Oxford Univ. Press, Oxford, 1993).
18. On May 1, 2008, the CFTC requested public comment on the appropriate regulatory treatment of prediction markets. "Commodity Futures Trading Commission, Concept release on the appropriate regulatory treatment of event contracts" (May 2008); www.cftc.gov/stellent/groups/public/@lrfederalregister/documents/file/e8-9981a.pdf.
19. J. Wolfers, E. Zitzewitz, *J. Econ. Perspect.* **18**, 107 (2004).

20. The views expressed here represent those of the authors and do not necessarily represent the views of the institutions with which they are affiliated. Support provided by the Reg-Markets Center at AEI (www.reg-markets.org).

10.1126/science.1157679

CIRCADIAN RHYTHMS

Integrating Circadian Timekeeping with Cellular Physiology

Models of circadian timekeeping mechanisms in plants, flies, and mammals are expanding to include intracellular small-molecule signals.

Marie C. Harrisingh and Michael N. Nitabach

Circadian rhythms are daily rhythmic variations in physiology and behavior that are found in organisms as diverse as animals, plants, fungi, and cyanobacteria. The effects of circadian rhythms are ubiquitous, from the opening of flowers in the morning and their closure at night, to the jet lag caused by our inability to rapidly adapt to a change in time zone. Circadian rhythms are generated by interconnecting feedback loops wherein "clock protein" transcription factors negatively regulate the expression of the "clock genes" that encode them. A further level of complexity arises through the post-translational modification of clock proteins, which influences their stability and translocation to the nucleus (*1*). Once in the nucleus, clock proteins control the transcription of not only the genes that encode them, but also of output genes, leading to rhythmic changes in gene expression that ultimately result in rhythmic changes in physiology and behavior. Recent studies suggest that this model of a negative transcriptional feedback oscillatory mechanism is incomplete (*2*–*9*). O'Neill *et al.* on page 949 of this issue (*2*) and other work (*3*, *4*, *6*) suggest that our understanding of the cellular and molecular basis of circadian timekeeping should be expanded to encompass intracellular small molecules that function in cell signaling (see the figure).

O'Neill *et al.* observed circadian oscillations in the concentration of intracellular adenosine 3′, 5′-monophosphate (cAMP) in the mouse suprachiasmatic nuclei, the so-called master circadian pacemaker of the mammalian brain. When the authors generated constitutively low or high concentrations of cAMP by pharmacological means, they eliminated circadian rhythms of clock gene transcription. Furthermore, simultaneously reducing the concentration of cAMP in suprachiasmatic nuclei tissue slices that were previously oscillating with different circadian phases caused the phases to become synchronized. Finally, decreasing the rate of cAMP synthesis slowed the circadian rhythm of gene transcription. Together, these results implicate cAMP as a component of the cellular oscillatory mechanism, and suggest that cAMP signals participate in another feedback loop that integrates with negative transcriptional feedback on clock genes to generate cellular rhythms.

Oscillations in the concentration of the small molecule cyclic adenosine diphosphate ribose (cADPR) have recently been linked to the circadian timekeeping mechanism in plants (*3*). cADPR mobilizes intracellular Ca^{2+} from internal stores. In the flowering plant *Arabidopsis thaliana*, changing the concentration of cADPR alters the period of circadian timekeeping, and oscillations in cADPR concentration are abolished in plants that lack all known circadian rhythms. These results implicate cADPR as another intracellular small-molecular signal that integrates with transcriptional feedback loops in generating circadian rhythms.

Circadian oscillations in the concentration of cADPR drive coordinate oscillations in the concentration of cytoplasmic Ca^{2+} (*3*), raising the possibility that Ca^{2+} oscillations may also participate in rhythm generation. Circadian oscillations in the concentration of cytoplasmic Ca^{2+} have also been observed in the mammalian suprachiasmatic nuclei (*10*, *11*), but until recently have been considered solely a rhythmic output that modulates neuronal excitability in this master pacemaker. However, culturing suprachiasmatic nuclei tissue slices under a range of conditions that interfere with these fluctuations in Ca^{2+} (*4*), including blockade of voltage-gated Ca^{2+} channels, results in a loss of circadian rhythmicity. Thus, cytoplasmic Ca^{2+} signals induced by depolarization-mediated influx through voltage-gated channels appear to play a key role in rhythm generation in the mammalian suprachiasmatic nuclei.

Changes in membrane potential are also essential for maintaining rhythmic oscillations in the expression of clock proteins in the fly *Drosophila melanogaster* (*5*), leading to the hypothesis that voltage-gated conductances influence transcriptional feedback oscillation through cytoplasmic Ca^{2+} signals. Transgenic flies expressing varying amounts

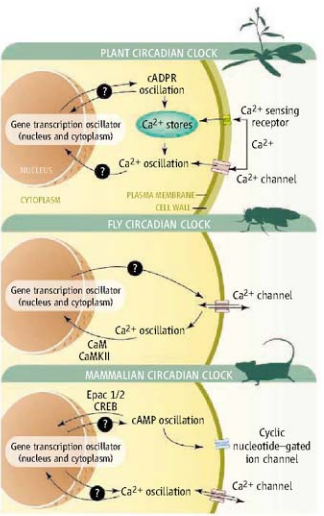

Expanding clocks. Intracellular small molecules couple to circadian clock mechanisms. In *Arabidopsis*, oscillations in cADPR signals are coupled to negative transcriptional feedback loops of the clock, possibly through the release of Ca^{2+} from internal stores. In *Drosophila*, changes in ionic conductances at the cell surface regulate transcriptional feedback oscillations of the clock, possibly by a mechanism involving Ca^{2+}-mediated signaling through CaM and CaMKII. In mammals, oscillations in Ca^{2+} and cAMP signals integrate with transcriptional feedback loops of the clock.

Department of Cellular and Molecular Physiology, Yale School of Medicine, New Haven, CT 06520, USA. E-mail: michael.nitabach@yale.edu

of a Ca^{2+}-buffering protein, parvalbumin, in the pacemaker neurons (cells that determine the periodicity and phase of behavioral rhythms) exhibit a slowing of the transcriptional feedback oscillator, demonstrating that intracellular Ca^{2+} signals control the generation of circadian rhythms in flies as well (*6*).

These studies raise the question of which mechanisms couple oscillations of intracellular signaling molecules to the transcriptional feedback loops of circadian clocks. Of the cAMP effectors studied by O'Neill *et al.*, only inhibition of the hyperpolarization-activated cyclic nucleotide–gated ion channel or the guanine nucleotide–exchange factors Epac 1 and Epac 2 suppressed circadian gene expression. Application of an Epac agonist resulted in the phosphorylation and increased activity of cAMP response element–binding (CREB) protein, a transcription factor. This suggests that changes in cAMP signaling could feed into the circadian transcriptional oscillator by regulating the expression of genes that contain binding sites for CREB. Such genes include the circadian clock genes *Per1* and *Per2*.

Genetic interaction analysis in *Drosophila* (*6*) implicates Ca^{2+}-sensitive calmodulin (CaM) and Ca^{2+}/calmodulin-dependent protein kinase II (CaMKII) proteins in coupling intracellular Ca^{2+} signals to transcriptional feedback loops of the fly clock. CaMKII activity has been linked to CREB phosphorylation in mammals (*12*, *13*), so perhaps changes in intracellular Ca^{2+} concentrations in *Drosophila* lead to changes in circadian gene expression in a manner similar to that of cAMP signals in mammals. Interestingly, *Drosophila* dCREB2 activity cycles in a circadian manner (*14*) and is altered in *per* mutants, and mutations in *dCREB2* in turn affect *per* expression. In *Arabidopsis*, cADPR may regulate the transcriptional oscillator by a mechanism involving Ca^{2+} signaling (*3*). However, Ca^{2+} release from internal stores can also be triggered by the Ca^{2+}-sensing receptor–inositol 1,4,5-trisphosphate pathway (*15*) and may also thereby contribute to regulating Ca^{2+} oscillations.

These recent studies indicate that negative transcriptional feedback is neither sufficient, nor even necessary in some cases, for circadian oscillation (*2*–*9*). Circadian timekeeping should now be thought of as an integrated emergent property of the cell that involves interactions between negative transcriptional feedback loops and key intracellular small-molecule signaling molecules. It is not yet clear how transcriptional feedback oscillations influence oscillations in the concentrations of intracellular small-molecule signaling molecules. Whether other cellular physiological processes and signaling molecules integrate with transcriptional feedback in the generation of cellular rhythms also remains an open question.

References

1. M. Gallego, D. M. Virshup, *Nat. Rev. Mol. Cell Biol.* **8**, 139 (2007).
2. J. S. O'Neill, E. S. Maywood, J. E. Chesham, J. S. Takahashi, M. H. Hastings, *Science* **320**, 949 (2008).
3. A. N. Dodd *et al.*, *Science* **318**, 1789 (2007).
4. G. B. Lundkvist, Y. Kwak, E. K. Davis, H. Tei, G. D. Block, *J. Neurosci.* **25**, 7682 (2005).
5. M. N. Nitabach, J. Blau, T. C. Holmes, *Cell* **109** 485 (2002).
6. M. C. Harrisingh, Y. Wu, G. A. Lnenicka, M. N. Nitabach, *J. Neurosci.* **27**, 12489 (2007).
7. P. L. Lakin-Thomas, *J. Biol. Rhythms* **21**, 83 (2006).
8. M. Nakajima *et al.*, *Science* **308**, 414 (2005).
9. J. Tomita, M. Nakajima, T. Kondo, H. Iwasaki, *Science* **307**, 251 (2005).
10. C. S. Colwell, *Eur. J. Neurosci* **12**, 571 (2000).
11. M. Ikeda *et al.*, *Neuron* **38**, p253 (2003).
12. M. Sheng, M. A. Thompson, M. E. Greenberg, *Science* **252**, 1427 (1991).
13. K. Nomura, Y. Takeuchi, S. Yamaguchi, H. Okamura, K. Fukunaga, *J. Neurosci. Res.* **72**, 384 (2003).
14. M. P. Belvin, H. Zhou, J. C. Yin, *Neuron* **22**, 777 (1999).
15. R. H. Tang *et al.*, *Science* **315**, 1423 (2007).

10.1126/science.1158619

PLANT SCIENCE

Plant Stress Profiles

Laurentius A. C. J. Voesenek and Ronald Pierik

Cell-specific transcript profiles reflecting response to environmental adversity add a new dimension to plant stress biology.

Climate change affects the performance of many crops and wild plants worldwide (*1*), so understanding the interplay between plant development and environmental adversity is key to crop improvement and to predicting changes in species distribution and biodiversity. An important new dimension has been added to this field by Dinneny *et al.* on page 942 of this issue (*2*). With unprecedented detail and developmental resolution, the study reports stress-induced gene expression (transcript profiles) for the flowering plant *Arabidopsis thaliana* and provides a unique entry into understanding the subtleties of plant stress responses.

Dinneny *et al.* generated genome-wide expression maps of *Arabidopsis* roots exposed to either a high-salt medium (osmotic stress) or an iron-deficient medium (nutrient stress) at three organizational levels—intact roots, roots divided into four longitudinal zones as proxies for developmental time, and root cells segregated along the radial axis—yielding six different cell types. Much larger numbers of regulated genes were found in the second and third of these sets relative to the first set, indicating a serious dilution of information when only intact roots are analyzed. A major finding is that cell identity determines the gene pool that is regulated during stress, as reflected by the high degree of cell specificity in functional gene categories. This specificity requires maintenance of cell fate during stress, which is probably ensured by a transcript cohort enriched in cell-identity genes that remains unaffected by environmental stress.

A large portion of the transcript profile per cell type changes dramatically upon stress. However, a comparison of the regulated genes between high-salt treatment and low-iron treatment revealed that only 20% of genes regulated by salt stress are also altered by iron deficiency. Surprisingly, a large proportion of these genes are regulated in a cell-specific manner, which suggests that cell type–specific processes are common targets for stress regulation. It will be interesting to see whether these genes are com-

CREDIT: FRANK MILLENAAR

Multiple stresses at hand. Various environments within a river-dominated system (River Waal, Netherlands) include shallow water bodies that are maintained throughout the year and elevated parts that are better drained. The latter has high plant productivity but suffers from drought stress. The entire region gets flooded occasionally from melting snow in the Alps and strong precipitation.

Plant Ecophysiology, Institute of Environmental Biology, Utrecht University, Sorbonnelaan 16, 3584 CA Utrecht, Netherlands. E-mail: l.a.c.j.voesenek@uu.nl

mon targets for other stresses.

Growth regulation may function in adverse environments to conserve energy for stress resistance. Dinneny *et al.* suggest that genes regulated by both salt stress and iron shortage in the outermost (epidermal) root cell layer suppress root growth for both stresses. Reduced shoot growth in response to high salt involves accumulation of DELLA proteins, transcriptional regulators that inhibit cell growth (*3*). DELLA proteins are targets for the plant hormone gibberellin, and their abundance is controlled by different environmental cues such as salt (*3*) and light (*4*). Integration of different cell signaling routes was also recently described for the protein kinases KIN10 and KIN11 (*5*). These enzymes orchestrate transcriptional networks to globally regulate metabolism during plant development and stress exposure. Further exploration of gene expression profiles may identify yet unknown integrators of environmental stresses and developmental processes in plants.

Comparing the effects of different stresses is an important step toward understanding plant behavior under realistic field conditions where stresses rarely occur alone. The importance of multiple stress exposure was illustrated by a study in which *Arabidopsis* was exposed to heat and drought simultaneously (*6*). Fewer than 10% of the regulated genes in this dual-stress treatment overlapped with the gene cohort regulated by both of the individual stress treatments. This indicates that multiple stresses control largely separate gene networks that cannot be predicted from studying the individual stresses alone (*6*, *7*).

Field observations not only demonstrate that multiple stresses often occur simultaneously, but also that most stresses vary in duration and intensity. These variations can select for different suites of adaptive traits that are cell-specific and set in motion by different signaling and transcriptional networks. One such example is the variation in flooding regimes in river floodplains (*8*) (see the figure). Floods with deep and/or transient high waters select for a so-called "low oxygen quiescence syndrome," characterized by down-regulation of growth (for energy and carbohydrate conservation) and up-regulation of the expression of genes involved in detoxification of reactive oxygen species that accumulate during flooding (*9*, *10*). On the other hand, shallow, long-lasting floods typically select for a "low oxygen escape syndrome," which involves a multitude of traits including elongation of stems and petioles. These traits are regulated in different cell types and help plants to outgrow the water, thus avoiding oxygen depletion and carbohydrate starvation (*8*, *11*–*14*). During submergence, entrapment of the volatile plant hormone ethylene promotes expression of *SUB1A*, a gene encoding an ethylene-responsive transcription factor (*15*). Accumulation of the SUB1A protein induces the low oxygen quiescence syndrome, as it represses the transcription of genes related to cell elongation and carbohydrate catabolism (*9*). This results in energy-conserving, non-elongating rice varieties. In cultivars that lack *SUB1A*, ethylene, by contrast, induces the low oxygen escape syndrome by stimulating cell elongation. Hence, the presence of one particular transcription factor can determine a plant's adaptive strategy for survival. Such insights could help crop breeders deliver cultivars that behave optimally with respect to local environmental conditions.

Genome-wide transcript profiling with high spatial and developmental resolution is a major leap forward in understanding stress tolerance in multicellular organisms. A next step will be detailed functional studies of the signaling networks that coordinately regulate transcripts that determine phenotypic consequences critical to surviving environmental adversities. Another major challenge is to reproduce natural conditions in experimental studies by incorporating multiple stresses that vary in intensity and duration. This will increase our understanding of the diversity of stress adaptation mechanisms and provide opportunities to further improve crops that grow in marginal environments to meet increasing global food demands.

References and Notes

1. F. N. Tubiello *et al.*, *Proc. Natl. Acad. Sci. U.S.A.* **104**, 19686 (2007).
2. J. R. Dinneny *et al.*, *Science* **320**, 942 (2008).
3. P. Achard *et al.*, *Science* **311**, 91 (2006).
4. T. Djakovic-Petrovic *et al.*, *Plant J.* **51**, 117 (2007).
5. E. Baena-Gonzalez *et al.*, *Nature* **448**, 938 (2007).
6. L. Rizhsky *et al.*, *Plant Physiol.* **134**, 1683 (2004).
7. R. Mittler, *Trends Plant Sci.* **11**, 15 (2006).
8. J. Bailey-Serres, L. A. C. J. Voesenek, *Annu. Rev. Plant Biol.* **59**, 313 (2008).
9. T. Fukao *et al.*, *Plant Cell* **18**, 2021 (2006).
10. P. Geigenberger, *Curr. Opin. Plant Biol.* **6**, 247 (2003).
11. L. Mommer *et al.*, *Plant Physiol.* **139**, 497 (2005).
12. R. Lasanthi-Kudahettige *et al.*, *Plant Physiol.* **144**, 218 (2007).
13. T. D. Colmer, O. Pedersen, *New Phytol.* **177**, 918 (2008).
14. M. B. Jackson, *Ann. Bot.* **101**, 229 (2008).
15. K. Xu *et al.*, *Nature* **442**, 705 (2006).

16. We thank L. Mommer, J. Bailey-Serres, and T. Colmer for constructive comments. Supported by Netherlands Organization for Scientific Research VENI grant 86306001 (R.P.).

10.1126/science.1158720

CHEMISTRY

The Changing Shapes of Molecules

A new microwave spectrometer enables the geometries of molecules to be tracked as they interconvert between different shapes.

Dmitry G. Melnik and Terry A. Miller

Precise diagnostics are important for conveying information about an object's properties. In retail stores, bar codes are used to identify goods. Similarly, spectra are widely used in chemistry to identify molecular properties. On page 924 of this issue, Dian *et al.* (*1*) report the use of a new spectroscopic technique that makes it much easier to identify the shapes of molecules as they change.

Laser Spectroscopy Facility, Department of Chemistry, Ohio State University, Columbus, OH 43210, USA. E-mail: tamiller+@osu.edu

Like any good diagnostic, molecular spectroscopy needs to be fast, sensitive, and selective. Several different types of spectroscopy can elucidate molecular properties, but the finest level of molecular detail—the molecule's shape—can best be identified by microwave spectroscopy. Traditionally, this technique provides excellent selectivity and sensitivity but suffers limitations in speed. The new microwave spectroscopic technique used by Dian *et al.* dramatically enhances the speed of acquiring rotational spectra without sacrificing sensitivity or selectivity.

Molecular shape plays an important role in chemical reactivity. Nowhere is this more apparent than in biochemistry. For example, biopolymers are dominated by L-amino acids and D-sugars, whereas their mirror image molecules are nearly absent (*2*). Subtle shape differences also have big effects for fatty acids. Those with hydrogen atoms located on opposite sides of the carbon-carbon double bond are more likely to raise bodily LDL cholesterol levels than are those that have the hydrogens on the same side (*3*).

The complete determination of the three-dimensional molecular geometry by

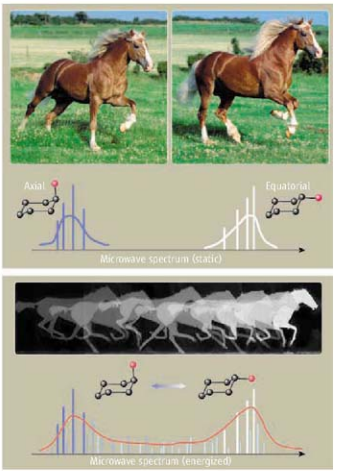

Of horses and molecules. Different poses of horses (**top panel**) correspond to different three-dimensional entities. Similarly, microwave spectra of two differently shaped stereoisomers (axial and equatorial) of a substituted cyclohexane molecule are distinct. However, these entities are not fixed (**bottom panel**). The horse can move between different shapes or forms, with a slow camera capturing elements from them all. Similarly, when the cyclohexane molecule has been energized, it rapidly interconverts between the two stereoisomers, giving rise to a composite spectrum of the nature of that recorded by Dian *et al.* for cyclopropane carboxaldehyde.

microwave spectroscopy alone is feasible only for very simple molecules. Typically, only a few unique shapes (stereoisomers) are stable for a given molecule, and a high-resolution rotational spectrum unambiguously distinguishes among them. Traditionally, microwave spectra were acquired through continuous frequency scanning. In early experiments, the accumulation of a spectrum could require many hours (*4*). Recent advances have reduced acquisition times to minutes or seconds (*5*), albeit with diminished resolution and hence possibly selectivity.

An alternative to continuous frequency scanning was pioneered by Balle and Flygare (*6*), who exposed molecules to a short burst of microwave radiation and then recorded the temporal profile of the emanating radiation. Fourier transformation of this profile yields rotational spectra of superb resolution and sensitivity. This Fourier transform microwave (FTMW) spectroscopy was, however, relatively slow, because the bandwidth covered in a single pulse was limited to less than 1 MHz due to instrumental constraints on pulse duration (*6*). This was a problem because molecular species and shapes often exist transiently, and their rotational spectrum must be acquired in a short time.

The new instrument developed by Dian *et al.*, a chirped-pulse (CP-FTMW) spectrometer, is based on the same principles as the original Balle-Flygare instrument; however, it incorporates recent advances in electronics (*7*). First, the burst of microwaves has been replaced with an extremely fast, chirped pulse containing an ultrarapid frequency scan. The breadth and duration of this pulse are not coupled, because the pulse is produced by digital electronics that can generate phase-reproducible radiation. Typically, an entire 10,000-MHz spectral segment can be scanned in roughly a microsecond. Second, to record the spectrum, radiation emanating from the molecules must be sampled with sufficient temporal resolution to capture all necessary details, which requires gigahertz frequency response in the electronics—a capability that has only recently become available.

Depending on the experiment, the technological breakthroughs increase (*8*) the speed of spectral acquisition by a factor of 100 to 10,000, making possible the experiments described by Dian *et al.* The authors study cyclopropane carboxaldehyde, which exists in two stable shapes, or stereoisomers, called *syn* and *anti*. When such a molecule has low energy, both stereoisomers are typically present and do not interconvert on the time scale of the experiment. The unique rotational spectrum (see the figure) of each stereoisomer can easily be obtained with a conventional spectrometer.

However, a conventional microwave spectrometer would not suffice for the rest of the experiment, which involves energizing a small fraction of the molecules with an infrared laser pulse. This excited ("hot") population decays back to the vibrationless ("cold") level on a time scale of milliseconds (*9*).

During this time interval, the CP-FTMW instrument can acquire, in a single snapshot, a complete rotational spectrum (preserving all the relationships between the spectral elements) of the molecule in its hot state, where the vibrationally excited molecules interconvert on a time scale comparable to their rotational period. This spectrum is fundamentally different from that of either the *syn* or *anti* form in the cold state. The resulting spectrum captures elements from all the differently shaped molecules, resulting in a kind of average. This is analogous to taking a picture of a fast racehorse with a relatively slow camera (see the figure). By examining a number of shots of the racehorse and knowing the speed of the camera, one can deduce how fast the horse is running. Similarly, a more complicated analysis (*10*, *11*) of the positions and intensities of the features in the microwave spectrum yields the interconversion rate between the *syn* and *anti* shapes. The corresponding half-life varies, depending on the vibrationally excited level, but can be as short as ~100 ps (10^{-10} s). The measured rate is 16 times slower than predicted by theory, indicating current theory's limitations for describing processes of this nature.

The experimental approach used by Dian *et al.* has the potential for measuring the rate of change of molecular geometries on very rapid time scales with unprecedented detail and precision. The work may substantially advance understanding of why the products of some chemical reactions depend strongly on the molecular shapes of the reactants.

References

1. B. C. Dian, G. G. Brown, K. O. Douglass, B. H. Pate, *Science* **320**, 924 (2008).
2. M. Quack, in *Modelling Molecular Structure and Reactivity in Biological Systems*, K. J. Naidoo, Ed. (Royal Society of Chemistry, Cambridge, UK, 2006), pp. 3–38.
3. H. J. Edward, in *Fatty Acids in Foods and Their Health Implications*, C. C. Kuang, Ed. (CRC Press, Boca Raton, FL, 2008), pp. 757–790.
4. C. H. Townes, A. L. Schawlow, *Microwave Spectroscopy* (McGraw-Hill, New York, 1955).
5. D. T. Petkie *et al.*, *Rev. Sci. Instrum.* **68**, 1675 (1997).
6. T. J. Balle, W. H. Flygare, *Rev. Sci. Instrum.* **52**, 33 (1981).
7. K. O. Douglass *et al.*, *J. Mol. Spectrosc.* **239**, 29 (2006).
8. G. G. Brown, B. C. Dian, K. O. Douglass, S. M. Geyer, B. H. Pate, *J. Mol. Spectrosc.* **238**, 200 (2006).
9. W. Demtröder, *Laser Spectroscopy. Basic Concepts and Instrumentation* (Springer, Berlin, 2003).
10. B. H. Pate, *J. Chem. Phys.* **109**, 4396 (1998).
11. B. H. Pate, *J. Chem. Phys.* **110**, 1990 (1999).

10.1126/science.1157668

PHOTOS IN TOP PANEL, KIT HOUGHTON/CORBIS; MOVING HORSE IN BOTTOM PANEL, ADAPTED FROM A SERIES OF PHOTOS BY EADWEARD MUYBRIDGE BY KATRINA BAUER/OHIO STATE UNIVERSITY

GEOCHEMISTRY

The Origin of Alkaline Lavas

Alkali-metal-rich lavas on ocean islands are produced from veins that form in oceanic mantle lithosphere as it ages.

Yaoling Niu

Alkaline lavas—mantle-derived magmas rich in alkali metals such as potassium and sodium—are commonly found in the interiors of tectonic plates, both on continents and on islands in ocean basins. Melting of metasomatic materials in the mantle lithosphere has long been conjectured to be the main source of these magmas (*1*, *2*), but this has not been successfully simulated experimentally. On page 916 of this issue, Pilet *et al.* (*3*) report experiments that explain the properties of alkaline magmas in a simple and elegant way.

Oceanic crust forms at mid-ocean ridges, where tectonic plates move apart. As it moves further away from the ridge, the lithosphere thickens, reaching its full thickness after about 70 million years (see the figure, left panel). It has long been widely accepted that the oceanic crust—after recycling into the deep mantle through subduction—becomes the source of alkali-rich melts needed to explain the compositions of ocean island basalts (*4*), but this explanation has been criticized and remains debated (*5*–*7*). One of the problems is that melting of the oceanic crust would lead to silica-rich rather than alkaline melts.

Pilet *et al.* now show that melting not of recycled oceanic crust but of metasomatic veins in the lithosphere produces melts with elemental compositions matching those of extreme alkaline lavas (nephelinites). When these nephelinite melts interact with the host peridotites, they produce modified melts that form a compositional spectrum from less extreme alkaline lavas (basanites) to the more common alkali basalts. The veins consist of amphiboles, a group of minerals that are stable in the lithosphere but not in the seismic low-velocity zone (LVZ). Thus, the results provide convincing evidence for a lithospheric origin of alkaline magmas.

The key question concerns the origin of metasomatic amphibole-rich veins. The volatile- and alkali-rich character of amphibole-rich veins requires that they crystallize in the lithosphere from small-mass-fraction (low-degree) melts that ultimately originated in the LVZ—a process called mantle metasomatism. As Pilet *et al.* explain, these low-degree melts can be produced in regions deeper than and in the vicinity of ocean ridge mantle melting [figure S5 in (*3*)]. Such melts may in fact exist throughout the LVZ (see the figure, left panel) (*5*, *8*, *9*), causing the observed low seismic velocity (*8*). Because of their buoyancy, such low-degree melts tend to concentrate toward the top of the LVZ and are enriched in volatiles (such as water and carbon dioxide) and in "incompatible" elements (such as Ba, Rb, Th, U, Nb, and light rare earth elements) that prefer to enter the melt over solid minerals.

However, metasomatic amphibole-rich veins in the lithosphere do not melt without thermal perturbation. Hot "plume" melts from the deep mantle may cause the veins to melt; mixing of the two melts in different proportions then results in the alkali-rich nature and compositional spectrum of ocean island lavas (see the figure, right panel).

The lithosphere does not reach its full

Department of Earth Sciences, Durham University, Durham DH1 3LE, UK. E-mail: yaoling.niu@durham.ac.uk

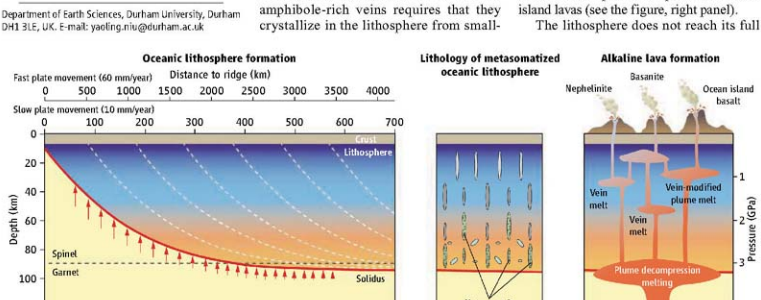

From oceanic lithosphere formation to alkaline lavas. (Left) Oceanic lithosphere grows with time by accreting LVZ material at the base (red arrows), taking ~70 million years to reach its full thickness. The thick red curve is the present-day lithosphere-LVZ interface, which is a natural solidus (the boundary between some melting and no melting). The thin white dashed curves indicate where this interface was in the past, illustrating the continuing lithosphere growth with time as the plate ages. **(Middle)** Close-up of metasomatic veins in the surrounding peridotite. Going upward, the veins are garnet pyroxenite, hornblende pyroxenite and hornblendite. The veinlets at the top are dunite inherited from ridge melting. **(Right)** When the mature oceanic lithosphere is reheated due to a hot plume rising up from deeper in the mantle, the vein melt. The vein melts may be altered through addition of surrounding material and mixing with plume melt. The degree of mixing determines which type of alkaline magma is formed and erupted.

thickness until it is ~70 million years old; mantle metasomatism thus continues during this time. This is equivalent to a distance of 700 km from the ridge if the plate spreads slowly at 10 mm per year and of 4200 km from the ridge if the plate spreads fast at 60 mm per year (see the figure, left panel). Hence, the oceanic lithosphere is a large geochemical reservoir enriched in alkalis, volatiles, and incompatible elements.

Alkaline lavas on ocean islands only sample very small amounts of amphibole-rich veins that may be ubiquitous throughout the oceanic lithosphere (see the figure, middle panel). Recycling of such metasomatized lithosphere into the deep mantle over much of Earth's history will cause mantle compositional heterogeneities on all scales. Involvement of such enriched heterogeneities in mantle source regions can account for the enriched characters of ocean island basalts (*5*).

Amphiboles are important minerals. A type of amphibole called pargasite may be the key mineral that determines the thickness of the mature oceanic lithosphere and the nature of the LVZ. Experimental studies suggested long ago that the lithosphere-to-LVZ transition may be a petrologic transition from solid pargasite-bearing peridotite to peridotite containing a small melt fraction (~1%) (*8*, *9*). This argument suggests that the mature oceanic lithosphere should be less than 95 km thick (*8*)—too thin for models in the 1970s (*10*) but consistent with more recent geophysical observations and models (*11*).

Although melting of amphibole-rich veins can also explain nephelinite lavas on land (*3*), further effort is needed to explain alkaline magmas such as kimberlite, lamproite, carbonatite, some nephelinite and their associations in continental settings with thick lithospheric roots (*12*). Their origin is apparently associated with metasomatized continental lithosphere (*12*). Kimberlite melts may actually originate at great depths, perhaps in the transition zone between the upper and lower mantle (*13*), and may be the agent that metasomatizes the continental lithosphere (*14*). Metasomatic vein amphiboles are potassium-rich (*3*), and potassium-amphiboles can be stable up to 16 GPa in the subducting oceanic lithosphere (*15*) before they undergo dehydration melting in the transition zone. It is possible that such melts, in the presence of carbon dioxide, are of kimberlitic composition, thus offering new perspectives on the origin of continental alkaline magma associations.

References

1. F. E. Lloyd, D. K. Bailey, *Phys. Chem. Earth* **9**, 389 (1975).
2. S.-S. Sun, G. N. Hanson, *Contrib. Mineral. Petrol.* **52**, 77 (1975).
3. S. Pilet, M. B. Baker, E. M. Stolper, *Science* **320**, 916 (2008).
4. A. W. Hofmann, W. M. White, *Earth Planet. Sci. Lett.* **57**, 421 (1982).
5. Y. L. Niu, M. J. O'Hara, *J. Geophys. Res.* **108**, 2209 (2003).
6. A. V. Sobolev *et al.*, *Science* **316**, 412 (2007).
7. Y. L. Niu, M. J. O'Hara, *Geochim. Cosmochim. Acta* **71**, a721 (2007).
8. D. H. Green, R. C. Liebermann, *Tectonophys.* **32**, 61 (1976).
9. D. H. Green, *Philos. Trans. R. Soc. London A* **268**, 707 (1971).
10. B. Parsons, J. Sclater, *J. Geophys. Res.* **82**, 803 (1977).
11. C. A. Stein, S. Stein, *Nature* **359**, 123 (1992).
12. J. G. Fitton, B. G. J. Upton, Eds., *Alkaline Igneous Rocks, Geol. Soc. Spec. Publ.* **30** (Blackwell, London, 1987).
13. A. E. Ringwood, S. E. Kesson, W. Hibberson, N. Ware, *Earth Planet. Sci. Lett.* **113**, 521 (1992).
14. P. J. Wyllie, *Geochem. Soc. Spec. Publ.* **1**, 107 (1987).
15. T. Inoue, T. Irifune, H. Yurimoto, I. Miyagi, *Phys. Earth Planet. Inter.* **107**, 221 (1998).

10.1126/science.1158378

CHEMISTRY

To Be or Not to Be Localized

The hole created by emission of a core electron in a diatomic molecule resides in an entangled state.

Kiyoshi Ueda

Institute of Multidisciplinary Research for Advanced Materials, Tohoku University, Sendai 980-8577, Japan. E-mail: ueda@tagen.tohoku.ac.jp

In molecules, valence electrons form molecular bonds, whereas the underlying core electrons play a supporting role. If a vacancy, or hole, is created in the core orbitals by an excitation process, a rearrangement process called Auger decay can occur: A valence electron drops to fill the core hole, and energy is released by emitting an Auger electron from another valence orbital. It has long remained unclear whether this short-lived core hole in a homonuclear diatomic molecule such as N_2 is localized on one atomic site, or delocalized over both. On page 920 of this issue, Schöffler *et al.* (*1*) show that this question cannot be answered without taking into account how the unstable core hole state relaxes by Auger decay. They show that the photoelectron and the Auger electron that are emitted form an entangled state. Whether one finds the core hole to be localized or delocalized will depend on the experiment used to observe this entangled state.

To answer the question about core hole localization and delocalization experimentally has required the development of sophisticated spectroscopic methods, but this question was first addressed theoretically decades ago. The direct core hole calculation of O_2 within the Hartree-Fock approximation supported a localized core hole picture. The energy of a symmetry-broken ionic state of O_2, in which a core hole is localized and thus the O atoms are inequivalent, is lower and agrees better with the experimental value than does the delocalized state (*2*). However, according to the Green's function approach, which includes more electron correlations, the energy difference between the localized and delocalized core holes calculated within the Hartree-Fock approximation is attributed to the neglect of electron correlations (*3*), and so at this level of theory, it is not possible to decide which description of the core holes better accommodates the experiments.

Core hole localization and delocalization can be built into theoretical calculations, but is it likely that we could see the localization and delocalization experimentally? State-of-the-art ab initio calculations (*4*, *5*) predicted that the two delocalized core hole states of N_2^+, which have different symmetries, are different in energy by ~0.1 eV. This energy gap, which is not seen for the symmetry-broken localized holes, is referred to as gerade-ungerade splitting. When all electron coordinates change sign, a gerade (even) wave function stays the same, but an ungerade (odd) wave function changes sign. Also the equilibrium bond length would differ by ~0.04 pm between gerade and ungerade core hole states (*4*, *5*).

If such energy gap and different bond lengths can be observed, they could be considered as experimental evidence for delocalized core holes. Recent high-resolution photoelectron spectroscopy studies confirmed the gerade-ungerade splitting (*6*) and

the difference in the bond length (*5*) that are the hallmarks of the symmetry-adapted delocalized core hole states. Also, a high-resolution Auger electron spectrum, where the gerade and ungerade core hole states are partially resolved, was best described as an incoherent sum of these two delocalized components (*7*).

The symmetry-adapted delocalized description of the core hole leads to another interesting prediction: Photoelectron emission from the gerade or ungerade core orbital can be described as a superposition of two phase-coherent waves emitted from the two nitrogen atoms (*8*). The resulting interference pattern (*9*) was indeed observed in the gerade-ungerade resolved photoionization cross sections (*10*). This observation also supports the symmetry-adapted delocalized picture of the core hole in N_2^+.

However, the localized or delocalized core hole can be probed more directly if we can establish the direction in which photoelectrons are emitted relative to the molecular frame. The molecular frame can be defined by dissociation; the fragments will be ejected along the molecular axis. The angular distributions of photoelectrons ejected from the core orbitals in C_2H_2 (*11*) and Ne_2 (*12*) were found to be asymmetric when the molecular frame was defined by the asymmetric fragmentation: H^+/C_2H^+ and Ne^+/Ne^{2+}, respectively. Although C_2H_2 is not a homonuclear dimer, the core hole states of C_2H_2 exhibit a gerade-ungerade splitting of 0.1 eV (*13*). The gerade-ungerade splitting for Ne_2 is too small to be observed. The photoelectron angular distribution observed for Ne_2 was well reproduced by a theoretical calculation in which the photoelectron was assumed to be emitted from the Ne^{2+} site leaving the localized core hole there. Thus, the asymmetric photoelectron angular distributions observed for C_2H_2 and Ne_2 seem to provide evidence for a localized core hole, contrary to the conclusion derived from the high-resolution electron spectroscopy on N_2 (*5*–*7*, *10*) and C_2H_2 (*13*).

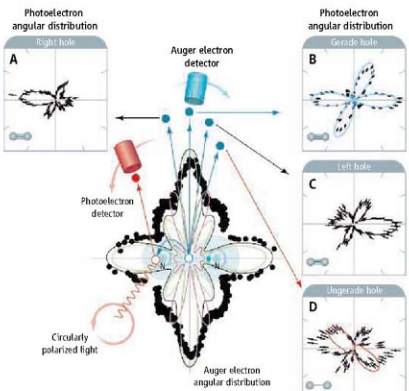

Wave function projector. Molecular nitrogen is fixed in space, and the core-level photoelectron angular distributions are measured in this molecular frame with circularly polarized light (anticlockwise). The observed photoelectron angular distributions of Schöffler *et al.* varied dramatically depending on the direction of the detection for the Auger electron. Each distribution indicates a different location of the core hole. (**A**) A hole in the right nitrogen, (**B**) a hole of gerade symmetry, (**C**) a hole in the left nitrogen, and (**D**) a hole of ungerade symmetry. The Auger electron detector works as a "wave function projector" to make a projection of the quantum-entangled state (consisting of the photoelectron and the Auger electron) and to localize and delocalize the core hole.

As Schöffler *et al.* now show, the differences arise in how the molecules are being studied. The authors have now measured the photoelectron angular distribution of N_2 in the molecular frame, defining it by the N^+/N^+ fragmentation, and furthermore simultaneously determining the direction of the Auger electron emission (see the figure, main panel). The important trick is that their momentum resolution is so high for the N^+ ion fragments that they could extract, by the momentum conservation law, the momentum for the last particle emitted (the Auger electron) without detecting it. Proper selection for the direction of the Auger electron emission then allowed the photoelectron angular distribution to be correlated with each of the theoretical predictions for the delocalized gerade and ungerade core hole states (see the figure, panels B and D), as well as for the localized state on each site (see the figure, panels A and C).

The key finding is that the photoelectron and the Auger electron form a quantum-entangled state. Schöffler *et al.* derived an expression for the differential cross section (the probability of simultaneously detecting a photoelectron and an Auger electron) that is valid if the gerade-ungerade splitting energy is at most comparable to the lifetime broadening of the core hole states. The only term in the equation that can break symmetry and make the core hole localized is an interference term between two amplitudes related to the gerade and ungerade core hole states.

Detection of only a photoelectron or only an Auger electron corresponds to the integration over all angles for the other particle that was not detected. In that case, the interference term disappears, and observable quantities are an incoherent sum of the gerade and ungerade contributions. High-resolution photoelectron and Auger electron spectra (*5*–*7*, *10*, *13*), where gerade and ungerade components are partially resolved, also consist of an incoherent sum of gerade and ungerade contributions and thus are consistent with the expression by Schöffler *et al.*

The physical picture Schöffler *et al.* present is at the heart of quantum mechanics. Whether we see a delocalized or localized core hole depends on how the quantum-entangled state consisting of the photoelectron and the Auger electron is projected to the detector.

References

1. M. Schöffler *et al.*, *Science* **320**, 920 (2008).
2. P. S. Bagus, H. F. Schaefer III, *J. Chem. Phys.* **56**, 224 (1972).
3. L. S. Cederbaum, W. Domcke, *J. Chem. Phys.* **66**, 5084 (1977).
4. A. Thiel, J. Schirmer, H. Köppel, *J. Chem. Phys.* **119**, 2088 (2003).
5. M. Ehara *et al.*, *J. Chem. Phys.* **124**, 124311 (2006).
6. U. Hergenhahn *et al.*, *J. Phys. Chem. A* **105**, 5704 (2001).
7. R. Püttner *et al.*, *Verhandl. DPG (V)* **43**, 141 (2008).
8. D. Rolles *et al.*, *Nature* **437**, 711 (2005).
9. H. D. Cohen, U. Fano, *Phys. Rev.* **150**, 30 (1966).
10. X.-J. Liu *et al.*, *J. Phys. B* **39**, 4801 (2006).
11. J. Adachi *et al.*, *J. Phys. B* **40**, F285 (2007).
12. K. Kreidi *et al.*, http://arxiv.org/pdf/0803.4461.pdf (2008).
13. B. Kempgens *et al.*, *Phys. Rev. Lett.* **79**, 3617 (1997).

10.1126/science.1157968

BIOPHYSICS

The Intrigue of the Interface

Diverse phenomena, ranging from the way shorebirds feed to self-cleaning by leaves, can be explained through surface tension effects.

Mark W. Denny

The surface tension of water has profound effects on life (*1*–*3*). It makes possible the flow of water to the tops of trees, allows some insects to breathe underwater and others to walk on it, and resists the inflation of lungs in premature infants. Collaboration among biologists, engineers, mathematicians, and physicists has produced exciting advances in our understanding of surface tension's effects in both nature and technology. In a new twist on this theme, on page 931 in this issue, Prakash *et al.* (*4*) describe a "capillary ratchet" that explains how some shorebirds feed, highlighting a burgeoning research field that makes practical use of surface tension.

Because water molecules are attracted more to each other than they are to air, water acts to minimize its surface energy by minimizing its area of contact with the atmosphere (*2*, *3*). When a liquid drop contacts a solid surface, additional surface energies come into play (*2*, *5*), defining an equilibrium contact angle θ between liquid and solid (see the figure, panel A). In practice, a finite range of static contact angles ($\theta_r < \theta < \theta_a$) arises due to effects of microscopic irregularities on the solid surface, which explains how raindrops stick to window panes (panels B, C). As a drop attempts to slide earthward, its leading edge may have a contact angle as high as θ_a before it advances, whereas its trailing edge may have an angle as low as θ_r before it retreats. Because $\theta_r < \theta_a$, the upward pull of surface tension at the trailing edge wins and the drop sticks. The net force holding the drop in place is proportional to the length of the contact line between drop and solid, whereas the weight of the drop is proportional to the drop's volume. As a result, drops larger than a maximum size (~2 mm) cannot stick and slide down in streaks.

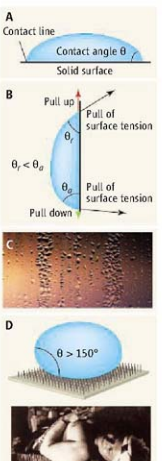

Water contacts: (**A**) Contact angle θ is measured within the liquid, and (**B**) can change as a drop moves, becoming asymmetric. This contact-angle hysteresis explains how raindrops stick to window panes (**C**). (**D**) Micrometer-scale roughness traps air between liquid drop and solid (the Cassie-Baxter or fakir state), producing large contact angles.

Prakash *et al.* build on these basic concepts to explain a novel method of feeding in shorebirds. In water too deep to stand, the bird spins on the surface, creating a vortex that draws up water and food particles (*6*). As it spins, it dips its beak into the water, capturing a drop of fluid and food between the halves of the beak (*7*). The bird then rapidly scissors its beak through a small angle. The beak is never fully closed, but the drop nonetheless moves upward to the mouth. It is here that surface tension comes into play. As the beak opens, the drop is stretched, and its contact lines with the beak's surface retreat. But the contact line nearest the beak's tip retreats more than the contact line nearest the mouth. As a result, the drop moves incrementally toward the mouth. The opposite happens when the beak closes. The drop is squeezed, contact lines advance—but asymmetrically—and the drop again moves toward the mouth. The efficiency of this capillary ratchet depends on the angle through which the beak moves and the surface energy of the beak's material. When the system is well tuned, a drop can move to the mouth in as little as two to three oscillations. Because the ratchet depends on the wetting properties of the beak, it could be stymied by detergents or oily pollutants on the water's surface.

Other research in this fast-paced field reveals how contact angles can be adjusted and how these adjustments have practical consequences (*5*, *8*). Inspired by observations that contact angles can approach 180° on the textured surfaces of plants and water-walking insects (*9*), engineers have determined that micrometer-scale roughness on hydrophobic surfaces can act to retain a microscopic layer of air between water and solid (known as a Cassie-Baxter or fakir state (panel D). Water drops on these superhydrophobic surfaces move with minimal resistance. In nature, the effect allows insects to walk on water (*10*), lotus leaves to clean themselves of dust (*11*), and desert beetles to capture fog droplets (*12*). Engineering analogs of these natural superhydrophobic surfaces are being developed to reduce the drag of fluids flowing through small pipes such as those in microfluidic devices (*13*), to produce self-cleaning and dew-resistant windows (*5*), and to form surfaces that are slippery in one direction and sticky in another (*8*, *14*). Butterflies have already met this last challenge: Scales on their wings have flexible nanotips that allow water drops to flow easily away from the body but inhibit flow toward it (*15*).

Note the interdependence of natural and physical sciences in these advances. If biologists had not reported odd phenomena from nature, physicists, mathematicians, and engineers might not have recognized the surprising potential of surface microtexture. The insights that followed have enabled biologists to explain the natural phenomena they originally observed and have sharpened their eye for further observation. It is not only the interface between water and air that is important here; it is also the productive collaboration at the interface between academic fields that matters.

References

1. S. Vogel, *Life's Devices* (Princeton Univ. Press, Princeton, NJ, 1988).
2. J. W. M. Bush *et al.*, *Adv. Insect Physiol.* **34**, 117 (2008).
3. M. W. Denny, *Air and Water* (Princeton Univ. Press, Princeton, NJ, 1993).
4. M. Prakash, D. Quéré, J. W. M. Bush, *Science* **320**, 931 (2008).
5. D. Quéré, *Rep. Progr. Phys.* **68**, 2495 (2005).
6. B. S. Obst *et al.*, *Nature* **384**, 121 (1996).
7. M. A. Rubega, thesis, University of California, Irvine (1993).
8. D. Quéré, *Ann. Rev. Mater. Res.* **38**, 16.1 (2008).
9. A. B. D. Cassie, S. Baxter, *Nature* **155**, 21 (1945).
10. J. W. M. Bush, D. L. Hu, *Ann. Rev. Fluid Mech.* **38**, 339 (2006).
11. W. Barthlott, C. Neinhuis, *Planta* **202**, 1 (1997).
12. A. R. Parker, C. R. Lawrence, *Nature* **414**, 33 (2001).
13. J. Ou, B. Perot, J. P. Rothstein, *Phys. Fluids* **16**, 4635 (2004).
14. C.-H. Choi *et al.*, *Phys. Rev. Lett.* **18**, 087105 (2006).
15. Y. Zheng *et al.*, *Soft Matter* **3**, 178 (2007).

Hopkins Marine Station of Stanford University, Pacific Grove, CA 93950, USA. E-mail: mwdenny@stanford.edu

10.1126/science.1158189

Transformation of the Nitrogen Cycle: Recent Trends, Questions, and Potential Solutions

James N. Galloway,[1]* Alan R. Townsend,[2] Jan Willem Erisman,[3] Mateete Bekunda,[4] Zucong Cai,[5] John R. Freney,[6] Luiz A. Martinelli,[7] Sybil P. Seitzinger,[8] Mark A. Sutton[9]

Humans continue to transform the global nitrogen cycle at a record pace, reflecting an increased combustion of fossil fuels, growing demand for nitrogen in agriculture and industry, and pervasive inefficiencies in its use. Much anthropogenic nitrogen is lost to air, water, and land to cause a cascade of environmental and human health problems. Simultaneously, food production in some parts of the world is nitrogen-deficient, highlighting inequities in the distribution of nitrogen-containing fertilizers. Optimizing the need for a key human resource while minimizing its negative consequences requires an integrated interdisciplinary approach and the development of strategies to decrease nitrogen-containing waste.

Our understanding of reactive nitrogen (Nr) (*1*) and the N cycle has shifted from how to promote food production to a realization that agricultural intensification damages environmental systems (*2*). Since 1970, world population has increased by 78% and reactive nitrogen creation has increased by 120%. In 1970, Delwiche stated, "The ingenuity that has been used to feed a growing world population will have to be matched quickly by an effort to keep the nitrogen cycle in reasonable balance" (*3*). Thirty-five years later, Dobermann and Cassman pointed out, "Failure to arrest the decrease in cereal crop area and to improve nitrogen use efficiency in the world's most important agricultural systems will likely cause severe damage to environmental services at local, regional, and global scales due to a large increase in reactive N load in the environment (*4*)."

It is clear that an optimum has not been achieved. In some parts of the world, Nr has been used to create an excess of food and a growing prevalence of unhealthy diets, while also contributing to a host of environmental problems (*2*, *5*–*7*). Yet, other world regions lack sufficient Nr to meet even the most basic caloric demands of hundreds of millions of people (*8*).

Major research and management challenges remain and are becoming ever more pressing as the creation and use of Nr continues to accelerate. Although diverse management strategies are necessary, they are also possible, and we believe a more favorable balance between the benefits and unwanted consequences of Nr can be achieved.

Continued Acceleration of Nr Creation

Nr creation continues to increase every year. It is dominated by agricultural activities, but fossil fuel energy plays an important role, and the growing prevalence of biofuels is adding a new and rapidly changing dimension. From 1860 to 1995, energy and food production increased steadily on both an absolute and per capita basis; Nr creation also increased from ~15 Tg N in 1860 to 156 Tg N in 1995. The change was enormous, and it increased further from 156 Tg N yr^{-1} in 1995 to 187 Tg N yr^{-1} in 2005, in large part because cereal production increased from 1897 to 2270 million tons (20%), and meat production increased from 207 to 260 million tons (26%) (*9*). These rising agricultural demands were sustained by a rise in Nr creation by the Haber-Bosch process from 100 Tg N yr^{-1} to 121 Tg N yr^{-1} (20%) (*9*). Cultivation-induced biological nitrogen fixation (C-BNF) occurs in several agricultural systems, with crop, pasture, and fodder legumes being the most important (*10*). The C-BNF estimate for 1995 was 31.5 Tg N (*5*) and, because of the increase in soybean and meat production over the past decade, we estimate that in 2005 C-BNF was 40 Tg N. There is substantial uncertainty in this value, and this is a critical area where more precise data are needed. In parallel, primary commercial energy production by coal, natural gas, and petroleum combustion increased from 8543 million tons of oil equivalents (mtoe) to 10,600 mtoe (24%), much of it in the developing world (*11*). However, decreases in NOx emissions in the developed world, among other reasons, led to a relatively constant global creation rate of Nr–NOx of ~25 Tg N yr^{-1} from 1995 to 2000 (*12*), and we assume for the purpose of discussion that this value also holds for 2005.

Finally, an important but poorly understood aspect of N mobilization is industrial Nr use. NH_3 from the Haber-Bosch process is used as a raw material to create multiple products, including nylon, plastics, resins, glues, melamine, animal/fish/shrimp feed supplements, and explosives. In 2005, ~23 Tg N was used for chemical production (*13*), accounting for 20% of Haber-Bosch Nr, but little is known about the fate of Nr used in these industrial activities.

Nr Distribution Patterns Are Changing

In 2004, ~45 Tg N of the ~187 Tg N of Nr created was traded internationally (Fig. 1), and in the preceding decade, global trade of N commodities increased twice as fast as the rate of Nr creation. Unlike aquatic or atmospheric transport, where Nr is diluted to varying degrees, commerce typically results in injection of Nr to ecosystems in more concentrated doses. Although this has the potential to cause greater damage to a smaller region, it also allows the possibility of greater control over Nr release. However, the rise in international trade is posing new socioeconomic questions, such as who pays for environmental damage associated with Nr losses (*14*). Regions that consume N-containing products, such as meat and milk, may be far removed from regions that produce the commodity and thus do not have to bear the environmental cost of the production. For example, in 1910, The Netherlands used 13 k tonne of fertilizer N yr^{-1} to produce food for its population of 6 million. In 1999, for the same agricultural area, 400 k tonne N yr^{-1} fertilizer N was used, and the yields were enough to feed 32 million people, only half of whom lived in The Netherlands. The rest of the food, and the Nr it contained, was exported, whereas the N lost in the food-production process remained in the Dutch environment, causing increased groundwater pollution, ambient ammonia and particle emissions, and nitrogen deposition (*15*). Similarly, areas of Latin America are bearing the cost of land conversion for soy that is fueling rising meat consumption in Asia (*14*).

On a global basis, atmospheric transport and subsequent deposition has become the dominant Nr distribution process. It is estimated that in 1860, 34 Tg N yr^{-1} of Nr was emitted as NOx and NH_3 and then deposited to the Earth's surface as NOy and NHx; in 1995, it had increased to 100 Tg N yr^{-1}; by 2050, it is projected to be 200 Tg N yr^{-1} (*5*). N deposition to ecosystems in the absence of human influence is generally

[1]Environmental Sciences Department, University of Virginia, Charlottesville, VA 22904, USA. [2]Institute of Arctic and Alpine Research and Department of Ecology and Evolutionary Biology, Campus Box 450, University of Colorado, Boulder, CO 80309, USA. [3]Energy Research Centre of the Netherlands, ECN, Post Office Box 1, 1755 ZG Petten, Netherlands. [4]Faculty of Agriculture, Makerere University, Post Office Box 7062, Kampala, Uganda. [5]Institute of Soil Science, Chinese Academy of Sciences, Nanjing 210008, China. [6]Commonwealth Scientific and Industrial Research Organisation Plant Industry, GPO Box 1600, Canberra, A.C.T., Australia. [7]Centro de Energia Nuclear na Agricultura-Universidade de São Paulo, Avenida Centenario, 303, Piracicaba-SP, Brazil. [8]Rutgers, The State University of New Jersey, Institute of Marine and Coastal Sciences, Rutgers/National Oceanic and Atmospheric Administration Cooperative Marine Education and Research Program, New Brunswick, NJ 08901, USA. [9]Centre for Ecology and Hydrology, Edinburgh Research Station, Bush Estate, Penicuik, Midlothian, EH26 0QB, UK.

*To whom correspondence should be sent. E-mail: jng@virginia.edu

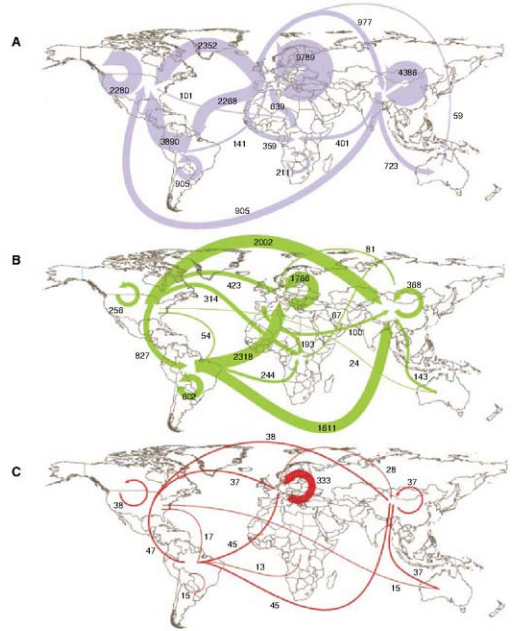

Fig. 1. N contained in internationally traded **(A)** fertilizer (31 Tg N), **(B)** grain (12 Tg N), and **(C)** meat (0.8 Tg N). Data are for 2004 and are in units of thousand of tons. Minimum requirements for drawing a line are 50,000 tons N, 20,000 tons N, and 10,000 tons N for fertilizer, grain, and meat, respectively (*42*).

~0.5 kg N ha^{-1} yr^{-1} or less (*16*). There are now large regions of the world where average N deposition rates exceed 10 kg N ha^{-1} yr^{-1}, greater than an order of magnitude increase compared with natural rates. By 2050, this may double, with some regions reaching 50 kg N ha^{-1} yr^{-1} (*5*), and landscape-level inputs may be much larger, especially for forest ecosystems (*17*). These rates are well in excess of the critical loads that have detrimental impacts on receiving ecosystems (*18*) (Fig. 2). Critical loads for the open ocean have not been calculated, but Duce *et al.* (*19*) conclude that the increasing amounts of atmospheric anthropogenic Nr entering the ocean could increase annual new marine biological production by ~3% and increase the emission of N_2O to the atmosphere by ~1.6 Tg N yr^{-1}.

Given the growing importance of the atmosphere in Nr distribution, it is critical to get a better understanding of emissions rates. There is a relatively good understanding of NOx emissions from fossil fuel combustion, but less so from biomass burning and soil emissions. The largest uncertainties are in the NH_3 emissions rates, from all sources, on all scales (*17*). There are also critical questions about the fate and impact of the N deposited to terrestrial, freshwater, and marine realms.

Vexing Questions

Nr creation is still accelerating, a trend unlikely to change in the near future. The additional anthropogenic Nr affects climate, the chemistry of the atmosphere, and the composition and function of terrestrial and aquatic ecosystems (*2*). Moreover, because a single molecule of reactive N can "cascade" through the environment, it can contribute to more than one of these environmental responses (*20*). Yet, we also know that Nr creation is essential to support a burgeoning human population (*21*) and that hundreds of millions of people still suffer from a "fertilizer deficit" (*8*). Finally, we know that environmental changes wrought by excess Nr can feed back to affect human health and welfare, both directly, for example through increased production of atmospheric particulate matter, and indirectly through impacts on food production (*6*). Thus, the grandest overall challenge posed by a changing N cycle is how to maximize the benefits of anthropogenic Nr while minimizing its unwanted consequences (see www.initrogen.org).

Although the role of Nr in multiple aspects of environmental change is undeniable, important research questions remain unresolved. We have identified five broad categories of questions that are priorities for future research.

What is the ultimate fate of Nr? Although data on the creation of anthropogenic Nr are relatively well constrained, those on its fate are uncertain. For example, in the mid-1990s, the fate of only 35% of Nr inputs to the terrestrial biosphere was relatively well known: 18% was exported to and denitrified in coastal ecosystems, 13% was deposited to the ocean via the marine atmosphere, and 4% was emitted as N_2O (*5*). Thus, the majority (65%) either accumulated in soils, vegetation, and groundwater or was denitrified to dinitrogen (N_2), but the uncertainty of those estimates remains large at every scale.

Even with these uncertainties, it is likely that denitrification is an important Nr sink. The first spatially explicit pattern of denitrification from soils to the coastal ocean suggested that more than 80% of denitrification is occurring in soils and freshwater systems (groundwater, rivers, lakes, and reservoirs). The bulk of the remainder (~15%) appears to occur in continental shelf sediments, thus indicating that rivers, although important sources to coastal systems, are typically small sources of Nr to the open ocean, even in heavily altered regions (*22*).

There is a growing database on Nr riverine fluxes, and several models are available that relate watershed characteristics to Nr flux (*23*, *24*). Even with these advances, some of the largest uncertainties in measuring denitrification rates are in upland terrestrial systems, which seem to account for a considerable, but unknown, Nr "sink." Nr inputs to these systems continue to rise, however, so the question is whether the fraction of N exported to the coasts will remain small or whether upland "sinks" will saturate to allow greater N-fueled coastal change.

Rising levels of atmospheric deposition also lend urgency to multiple questions about the fate of Nr. Ultimately, the fate of Nr that enters terrestrial systems appears to be under strong climatic control (*25*), an interaction that helps explain regional differences in N export and that should be considered in forecasts of future N-cycle dynamics. The fate and impacts of Nr are also often dependent on its chemical form,

further highlighting the need to better resolve changing inputs of oxidized versus reduced forms of Nr.

What are the net climate effects of increasing Nr? Nitrogen is both influenced by and affects climate; the net contributions of anthropogenic Nr to a changing climate remain widely debated (*17*, *26*). Nr can directly increase radiative forcing in the troposphere, principally through the production of N_2O and tropospheric O_3, but atmospheric Nr can also have cooling effects (*26*), largely through tropospheric aerosols and stratospheric O_3 declines. Moreover, Nr has strong interactions with the carbon (C) cycle that can have global-scale effects on atmospheric carbon dioxide (CO_2) and methane (CH_4) (*27*, *28*).

Elevated N deposition may stimulate plant growth in N-limited regions and cause substantial CO_2 uptake in Northern Hemisphere forests, although the size is controversial (see SOM text). N-driven C storage in nonforested or agricultural systems appears modest at best, and N-fueled increases in tropospheric O_3 can reduce C uptake in all systems (*29*). It remains a major research challenge to quantify all relevant N interactions sufficiently to estimate the net effect of Nr on climate forcing (*17*, *26*).

How will tropical regions respond to rising N inputs? Much of our knowledge on N dynamics is from the temperate world, yet tropical regions will receive the most dramatic increases in Nr inputs over the next few decades [see, e.g., (*30*)]. Some tropical regions already experience elevated N deposition, acidic deposition, and aquatic eutrophication (*31*), both from urban development and from a combination of agricultural extensification and intensification. The tropics are also home to the bulk of the planet's terrestrial and freshwater biodiversity. Given that elevated Nr inputs are known to drive biodiversity losses in higher latitude ecosystems (*32*), the projected trends in tropical regions are cause for concern (*33*).

Most biological N fixation in terrestrial systems occurs in tropical regions; this, combined with the widespread existence of phosphorus- and cation-deficient soils causes many tropical ecosystems to exist in a relatively N-rich state (*34*). Thus, at least in theory, the response of these systems to additional N inputs could be very different from those of temperate ecosystems and could result in rapid N losses to air and water, soil cation depletion, and reduced C uptake (*34*). Yet, data on such ecosystem responses and their translation into effects on community structure and biodiversity loss remain notably rare.

How does Nr affect human health? The ability to fix N on large scales is unquestionably a boon to humanity. Perhaps 40% of the world's dietary protein now comes from synthetic fertilizers, and estimates suggest that at least 2 billion people would not be alive today without the modern manifestations of the Haber-Bosch process (*21*). Yet, in many developed nations, the products from N-intensive agricultural practices lead to unhealthy diets, whereas elsewhere a lack of synthetic fertilizers, combined with depleted soil nutrient reserves, directly contributes to widespread malnutrition (*6*).

Once Nr enters the environment, its effects on terrestrial, aquatic, and atmospheric realms can influence human health and welfare in several ways. For example, N-driven increases in tropospheric O_3 pose direct health threats to humans and cause substantial losses in agricultural productivity (*35*). Nitric oxide and ammonia emissions fuel fine-particle and tropospheric O_3 formation, which exacerbate pulmonary disease (*6*). The health consequences of drinking water with elevated nitrate levels, including cancer and reproductive risks, remain poorly known but are important to resolve (*36*). Excess N in the environment may also change the prevalence of important infectious diseases, including malaria, West Nile virus, cholera, and schistosomiasis (*37*). Yet, in some regions with heavy infectious disease burdens, Nr is needed for adequate nutrition to mount effective immune responses to infection. As countries industrialized during the past century, improved nutrition alone reduced the threat from infectious diseases (*6*).

How will biofuel development alter the N cycle? The rapid development of biofuels has created an entirely new link between human activities and the global N cycle, but the full suite of connections is not well resolved. Currently, much of the world's biofuels are produced from corn in the United States or sugar cane in Brazil. U.S. corn covers nearly 29 million ha and is fertilized by an average of 160 kg N ha^{-1} yr^{-1}; Brazilian cane covers ~7 million ha and receives an average of 100 kg N ha^{-1} yr^{-1}. As with many intensive agricultural systems, N fertilizer use efficiency in Brazilian sugar cane is low: Only ~30% ends up in plant tissues (*38*). Thus, most of the applied N reaches the environment, and because the sugar cane area is predicted to double in Brazil by 2016, the biofuel industry will contribute to a rapidly changing tropical N cycle (*38*). Consequently, N-intensive biofuels could cancel out any CO_2 savings by contributing to both N_2O and tropospheric O_3 production (*39*). Second-generation biofuels will use more woody biomass from year-round crops and production forests and tend to have much higher conversion efficiencies. Although the full environmental consequences of these systems are also not well understood, their required N use should be smaller than that of current first-generation crops.

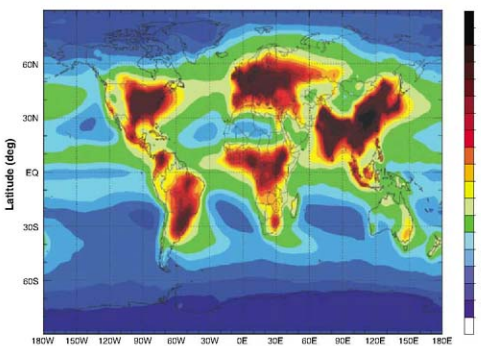

Fig. 2. Estimated N deposition from global total N (NOy and NHx) emissions, totaling 105 Tg N y^{-1}. The unit scale is kg N ha^{-1} y^{-1}, modified from the original units (mg m^{-2} y^{-1}) (*16*).

A Strategy for Now

There is compelling evidence that human alteration of the N cycle is negatively affecting human and ecosystem health. As demands for food and energy continue to increase, both the amount of Nr created and the magnitude of the consequences will also increase. Given the complexities of Nr use, its environmental mobility, and differences among regions, no single strategy will suffice (*40*). However, in keeping with the Nanjing Declaration on Nitrogen Management (*41*), here we highlight the intervention points in the global N cycle where N flows are concentrated and should be easiest to target (Fig. 3). We also give rough estimates of the decreases in Nr use or loss to the environment that are possible to achieve once the suggested strategies are implemented.

Although we realize that the implementation will take time, the estimates are what might

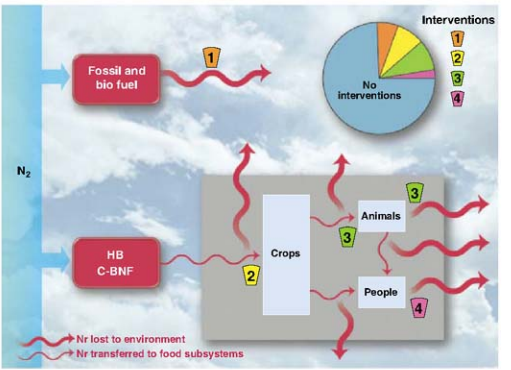

Fig. 3. Conceptual model of where interventions in the N cycle can be used to decrease the amount of Nr created or the amount of Nr lost to the environment. The red boxes represent subsystems where Nr is created. The sky-background space represents the environment. Arrows leaving the red boxes either result in Nr lost to environment (fossil fuel and biofuel combustion) or inputs to the food production system (gray box). The light blue boxes within the gray box represent subsystems within the food production system where Nr is used. Nr can either enter these subsystems (thin red lines), or be lost to the environment (thick red lines). The numbers represent intervention points for N management. The pie chart shows the magnitude of Nr managed by the four interventions relative to the total amount created (187 Tg N) in 2005.

reasonably be expected to occur with current technology (see SOM text). First, controlling NOx emissions from fossil-fuel combustion using maximum feasible reductions would result in a decrease of Nr creation from 25 Tg N yr^{-1} to 7 Tg N yr^{-1}. Second, increasing nitrogen-uptake efficiency of crops would decrease Nr creation by about 15 Tg N yr^{-1}. Third, improved animal-management strategies would decrease Nr creation by about ~15 Tg N yr^{-1}. Fourth, even if only half the 3.2 billion people living in cities had access to sewage treatment, 5 Tg N yr^{-1} could be converted to N_2.

Together, these interventions represent a potential decrease of ~53 Tg N yr^{-1} created per year, or ~28% of the total Nr created in 2005. With this reduction, we would be able to largely offset the increases in Nr losses required for future growth in food, feed, fuel, and fiber production and energy use. Other intervention points are clearly needed if Nr creation rates are to decrease in the future. Although these estimates are necessarily rough, and implementing them would not be trivial, they indicate that a multipronged, integrated approach can decrease the amount of Nr lost to the environment.

Multiple comprehensive analyses of management strategies for some or all of these points have been made in recent years. Common to nearly all such analyses is a clear message that no single strategy will work.

We conclude by stressing two points. First, although reducing Nr creation and its unwanted impacts will be challenging, it is both possible and of critical importance. Second, not all management priorities are about reduction of Nr. Substantial and sustained intervention is also needed in regions that do not have sufficient Nr or other nutrients to sustain the population (δ). In such regions, it will be important to seek ways to increase food production while minimizing nutrient loss and its subsequent environmental damages.

References and Notes

1. The term reactive nitrogen (Nr) as used in this paper includes all biologically active, photochemically reactive, and radiatively active N compounds in the atmosphere and biosphere of Earth. Thus, Nr includes inorganic reduced forms of N (e.g., NH_3 and NH_4^+), inorganic oxidized forms (e.g., NOx, HNO_3, N_2O, and NO_3^-), and organic compounds (e.g., urea, amines, and proteins), by contrast to unreactive N_2 gas.
2. P. M. Vitousek *et al.*, *Ecol. Appl.* **7**, 737 (1997).
3. C. C. Delwiche, *Sci. Am.* **223**, 137 (1970).
4. A. Dobermann, K. G. Cassman, *Sci. China C Life Sci.* **48**, 745 (2005) (Special Issue).
5. J. N. Galloway *et al.*, *Biogeochemistry* **70**, 153 (2004).
6. A. R. Townsend *et al.*, *Front. Ecol. Environ.* **1**, 240 (2003).
7. X. Jin, Q. Xu, C. Huang, *Sci. China C Life Sci.* **48**, 948 (2005).
8. P. A. Sanchez, M. S. Swaminathan, *Lancet* **365**, 442 (2005).
9. Food and Agriculture Organization, FAO statistical databases (2006), Rome, available at http://faostat.fao.org/default.aspx.
10. V. Smil, *Global Biogeochem. Cycles* **13**, 647 (1999).
11. BP Global, Statistical Review of World Energy 2007 (available at www.bp.com/productlanding.do?categoryId=6848&contentId=7033471).
12. J. Cofala *et al.*, *Atmos. Environ.* **41**, 8486 (2007).
13. M. Prud'homme, *Global Fertilizers and Raw Materials Supply and SupplyDemand Balances* (International Fertilizer Industry Association, Istanbul, 2007), pp. 2007–2013.
14. R. Naylor *et al.*, *Science* **310**, 1621 (2005).
15. J. W. Erisman *et al.*, *Sci. China C Life Sci.* **48**, 827 (2005).
16. F. Dentener *et al.*, *Global Biogeochem. Cycles* **20**, GB4003 (2006).
17. M. A. Sutton *et al.*, *Environ. Pollut.* **150**, 125 (2007).
18. B. Achermann, R. Bobbink, Eds., *Empirical Critical Loads for Nitrogen. Environmental Documentation No. 164* (Swiss Agency for the Environment, Forests, and Landscape, Berne, 2003).
19. R. A. Duce *et al.*, *Science* **320**, 893 (2008).
20. J. N. Galloway *et al.*, *Bioscience* **53**, 341 (2003).
21. V. Smil, *Enriching the Earth: Fritz Haber, Carl Bosch and the Transformation of World Food Production* (MIT Press, Cambridge, MA, 2001).
22. S. P. Seitzinger *et al.*, *Ecol. Appl.* **16**, 2064 (2006).
23. E. W. Boyer *et al.*, *Global Biogeochem. Cycles* **20**, GB1S91 (2006).
24. S. P. Seitzinger, J. A. Harrison, E. Dumont, A. H. W. Beusen, A. F. Bouwman, *Global Biogeochem. Cycles* **19**, GB4S01 (2005).
25. R. W. Howarth *et al.*, *Biogeochemistry* **79**, 163 (2006).
26. Intergovernmental Panel on Climate Change, Working Group I Report: The Physical Science Basis (Cambridge Univ. Press, Cambridge, 2007).
27. B. A. Hungate, J. S. Dukes, M. R. Shaw, Y. Q. Luo, C. B. Field, *Science* **302**, 1512 (2003).
28. N. Gruber, J. N. Galloway, *Nature* **451**, 293 (2008).
29. S. P. Long, E. A. Ainsworth, A. D. B. Leakey, J. Nosberger, D. R. Ort, *Science* **312**, 1918 (2006).
30. Z. Zhu, Z. Xiong, G. Xing, *Sci. China C Life Sci.* **48**, 729 (2005).
31. L. B. S. L. Lara *et al.*, *Atmos. Environ.* **35**, 4937 (2001).
32. C. J. Stevens, N. B. Dise, J. O. Mountford, D. J. Gowing, *Science* **303**, 1876 (2004).
33. G. K. Phoenix *et al.*, *Global Change Biol.* **12**, 470 (2006).
34. P. A. Matson, W. H. McDowell, A. R. Townsend, P. M. Vitousek, *Biogeochemistry* **46**, 67 (1999).
35. M. Volk, P. Bungener, F. Contat, M. Montani, J. Fuhrer, *Global Change Biol.* **12**, 74 (2006).
36. M. H. Ward *et al.*, *Environ. Health Perspect.* **113**, 1607 (2005).
37. V. J. McKenzie, A. R. Townsend, *EcoHealth* **4**, 384 (2007).
38. P. C. O. Trivelin, M. W. de Oliveira, A. C. Vitti, G. J. D. Gava, J. A. Bendassolli, *Pesqui. Agropecu. Bras.* **37**, 193 (2002).
39. P. J. Crutzen, A. R. Mosier, K. A. Smith, W. Winiwarter, *Atmos. Chem. Phys.* **8**, 389 (2008).
40. R. W. Howarth *et al.* *Millennium Ecosystem Assessment* (Island Press, Washington, DC, 2005), chap. 9.
41. J. W. Erisman, *Bioscience* **54**, 286 (2004).
42. United Nations Environment Programme and Woods Hole Research Center, Paris, *Reactive Nitrogen in the Environment: Too Much or Too Little of a Good Thing* (2007), Fig. 3.

43. We appreciate the comments and assistance of M. Burke, J. Cofala, K. Cassman, E. Davidson, F. Dentener, D. Kramer, A. Mosier, O. Oenema, P. Wiberg, and the International Fertilizer Industry Association on portions of this paper. We appreciate the editorial assistance of M. J. Gore. This paper is a contribution to the International Nitrogen Initiative (www.initrogen.org) (joint) sponsored by Scientific Committee on Problems of the Environment and International Geosphere-Biosphere Programme), with special reference to the Fourth International Nitrogen Conference held in Brazil in October 2007. This paper is also a contribution to the European projects NitroEurope IP (European Commission), Nitrogen in Europe (NinE, European Science Foundation), and European Cooperation in the field of Scientific and Technical Research (COST) Action 729.

Supporting Online Material

www.sciencemag.org/cgi/content/full/320/5878/889/DC1
SOM Text
References

10.1126/science.1136674

Impacts of Atmospheric Anthropogenic Nitrogen on the Open Ocean

R. A. Duce,[1*] J. LaRoche,[2] K. Altieri,[3] K. R. Arrigo,[4] A. R. Baker,[5] D. G. Capone,[6] S. Cornell,[7] F. Dentener,[8] J. Galloway,[9] R. S. Ganeshram,[10] R. J. Geider,[11] T. Jickells,[5] M. M. Kuypers,[12] R. Langlois,[2] P. S. Liss,[5] S. M. Liu,[13] J. J. Middelburg,[14] C. M. Moore,[11] S. Nickovic,[15] A. Oschlies,[2] T. Pedersen,[16] J. Prospero,[17] R. Schlitzer,[18] S. Seitzinger,[3] L. L. Sorensen,[19] M. Uematsu,[20] O. Ulloa,[21] M. Voss,[22] B. Ward,[23] L. Zamora[17]

Increasing quantities of atmospheric anthropogenic fixed nitrogen entering the open ocean could account for up to about a third of the ocean's external (nonrecycled) nitrogen supply and up to ~3% of the annual new marine biological production, ~0.3 petagram of carbon per year. This input could account for the production of up to ~1.6 teragrams of nitrous oxide (N_2O) per year. Although ~10% of the ocean's drawdown of atmospheric anthropogenic carbon dioxide may result from this atmospheric nitrogen fertilization, leading to a decrease in radiative forcing, up to about two-thirds of this amount may be offset by the increase in N_2O emissions. The effects of increasing atmospheric nitrogen deposition are expected to continue to grow in the future.

Nitrogen is an essential nutrient in terrestrial and marine ecosystems. Most nitrogen in the atmosphere and ocean is present as N_2 and is available only to diazotrophs, a restricted group of microorganisms that can fix N_2. Most organisms can only assimilate forms of reactive nitrogen (fixed nitrogen, N_r), including oxidized and reduced inorganic and organic forms. The availability of N_r limits primary production, the conversion of inorganic carbon to organic carbon (*1*), in much of the ocean. Reactive nitrogen enters the ocean via rivers, N_2 fixation, and atmospheric deposition. It is removed via N_2 formation by denitrification and anaerobic ammonium oxidation (anammox), nitrous oxide (N_2O) and ammonia emissions, and burial of organic matter in sediments. Human activities have severely altered many coastal ecosystems by increasing the input of anthropogenic nitrogen through rivers and groundwater, direct discharges from wastewater treatment, atmospheric deposition, and so forth, resulting in increasing eutrophication. Human activities have also added large quantities of atmospheric N_r to central ocean regions.

Riverine input of N_r to the oceans is estimated as 50 to 80 Tg N $year^{-1}$ (*2*–*4*). However, much is either lost to the atmosphere after N_2 conversion or buried in coastal sediments, never reaching oceanic regions (*5*). We assume that riverine N_r has a negligible impact on the open ocean nitrogen inventory, and we do not consider it further. Estimates of global ocean N_2 fixation range from 60 to 200 Tg N $year^{-1}$ (*2*, *6*–*8*). Although impacts of the amplified nitrogen inputs to terrestrial systems are being continuously evaluated (*3*, *9*), here we show that atmospheric transport and deposition is an increasingly important pathway for N_r entering the open ocean, often poorly represented in analyses of open ocean anthropogenic impacts (*10*–*16*). Atmospheric N_r input is rapidly approaching global oceanic estimates for N_2 fixation and is predicted to increase further due to emissions from combustion of fossil fuels and production and use of fertilizers. Our objective is to highlight the growing importance of anthropogenic atmospheric N_r (AAN) deposition to the oceans and evaluate its impact on oceanic productivity and biogeochemistry.

Atmospheric Emission and Deposition of Nitrogen Species

Atmospheric emissions of N_r are primarily oxidized nitrogen species, NO_x (NO + NO_2) and NH_3. Recent studies suggest that atmospheric water-soluble organic nitrogen is far more abundant than conventionally thought, constituting ~30% of total N_r deposition (*13*, *17*–*20*). Given the uncertain origins and complex composition of this material, the importance of direct emissions and secondary formation of organic nitrogen is unclear. However, measurements suggest that an important fraction is anthropogenic (*13*, *17*). We therefore assume that in 1860, the relationship between organic and inorganic nitrogen deposition was the same as it is today and increase our 1860 estimate so that organic nitrogen represents 30% of total N_r deposition. The uncertainties associated with this assumption emphasize the need for further research on atmospheric organic nitrogen.

Estimated total N_r and AAN emissions in 1860, 2000, and 2030 (Table 1) show that anthropogenic emissions have significantly increased since the mid-1800s and future increases are expected (*21*). Over the next 20 to 25 years, the proportion of NH_3 emissions will likely increase due to enhanced atmospheric emission controls predicted to be more effective for NO_x than NH_3 (Table 1) (*21*). An important fraction of atmospheric N_r emissions is deposited on the ocean (Table 1). In 1860, this amounted to ~20 Tg N $year^{-1}$, of which ~29% was anthropogenic. By 2000, the total N_r deposition to the ocean had more than tripled to ~67 Tg N $year^{-1}$, with ~80% being anthropogenic. This is greater than the 39 Tg N $year^{-1}$ reported by (*14*), in part because our estimate includes water-soluble organic nitrogen. Estimates of anthropogenic emissions for 2030 indicate a ~4-fold increase in total atmospheric N_r deposition to the ocean and an ~11-fold increase in AAN deposition compared with 1860 (*22*).

The spatial distribution of atmospheric deposition has also changed greatly (Fig. 1, A and B). Deposition to most of the ocean was <50 mg N m^{-2} $year^{-1}$ in 1860, with very few areas >200 mg N m^{-2} $year^{-1}$. Most oceanic deposition was from natural sources; anthropogenic sources impacted only a few coastal regions. By 2000, deposition over large ocean areas exceeded 200 mg N m^{-2} $year^{-1}$, reaching >700 mg N m^{-2} $year^{-1}$ in many areas. Intense deposition plumes extend far downwind of major population centers in Asia, India, North and South America, around Europe, and west of Africa (Fig. 1B). A direct comparison of deposition in 1860 and 2000 shows almost all ocean surface areas now being affected by AAN deposition (Fig. 1, A and B). Predictions for 2030 (fig. S1) indicate similar patterns, but with

[1]Departments of Oceanography and Atmospheric Sciences, Texas A&M University, College Station, TX 77843, USA. [2]Leibniz-Institut fuer Meereswissenschaften, 24105 Kiel, Germany. [3]Institute of Marine and Coastal Sciences, Rutgers University, Rutgers/NOAA CMER Program, New Brunswick, NJ 08901, USA. [4]Department of Environmental Earth System Science, Stanford University, Stanford, CA 94305, USA. [5]School of Environmental Sciences, University of East Anglia, Norwich NR4 7TJ, UK. [6]Department of Biological Sciences, University of Southern California, Los Angeles, CA 90089, USA. [7]QUEST–Earth Sciences, University of Bristol, Bristol BS8 1RJ, UK. [8]European Commission, Joint Research Centre, Institute for Environment and Sustainability, TP290, I-21020, Ispra (Va), Italy. [9]Department of Environmental Sciences, University of Virginia, Charlottesville, VA 22904, USA. [10]John Murray Laboratories, The King's Buildings, Edinburgh EH9 3JW, UK. [11]Department of Biological Sciences, University of Essex, Colchester CO4 3SQ, UK, and National Oceanography Centre, University of Southampton, Southampton SO14 3ZH, UK. [12]Max Planck Institute for Marine Microbiology, Celsiusstrasse 1, D-28359 Bremen, Germany. [13]Key Laboratory of Marine Chemistry Theory and Technology Ministry of Education, College of Chemistry and Chemical Engineering, Ocean University of China, Qingdao 266100, Peoples Republic of China. [14]Netherlands Institute of Ecology, Korringaweg 7, 4401 NT Yerseke, Netherlands. [15]Atmospheric Research and Environment Programme, World Meteorological Organization, BP2300, 1211 Geneva 2, Switzerland. [16]University of Victoria, Post Office Box 3055 STN CSC, Victoria, BC V8W 3P6, Canada. [17]Rosenstiel School of Marine and Atmospheric Sciences, University of Miami, Miami, FL 33149, USA. [18]Alfred Wegener Institute for Polar and Marine Research, 27568 Bremerhaven, Germany. [19]National Environmental Research Institute, Aarhus University, Denmark. [20]Ocean Research Institute, University of Tokyo, Tokyo 164-8639, Japan. [21]Departamento de Oceanografía, Centro de Investigación Oceanográfica, COPAS, and Nucleo Milenio EMBA, Universidad de Concepción, Casilla 160-C, Concepción, Chile. [22]Leibnitz Institute for Baltic Sea Research, Warnemünde, 18119 Rostock, Germany. [23]Department of Geosciences, Princeton University, Princeton, NJ 08544, USA.

*To whom correspondence should be addressed. E-mail: rduce@ocean.tamu.edu

increased deposition further into open ocean regions (*21*, *22*). The ratio of 2030-to-2000 deposition rates (Fig. 1C) shows up to a factor of 2 increase in Southeast Asia, the Bay of Bengal, and the Arabian Sea; up to a 50% increase off western Africa; and up to 30% across essentially all the mid-latitude North Atlantic and North Pacific. As Galloway *et al.* (*9*) conclude, controlling NO_x emissions using maximum feasible reductions could substantially decrease future emissions, so the increases we predict on deposition rates (Fig. 1C) may represent upper limits.

Impact on New Primary Production and the Biological Pump

Present global open ocean primary production is estimated at ~50 Pg C $year^{-1}$ (*23*), equivalent to ~8800 Tg N $year^{-1}$, assuming Redfield stoichiometry (Table 2). Because ~78% of this production is driven by regeneration of N_r within surface waters (*24*) (*a* in Fig. 2), it is more relevant to evaluate the impact of AAN deposition on oceanic productivity and biogeochemistry by comparing AAN with global new production, estimated at ~11 Pg C $year^{-1}$ (*24*–*26*). New production (*b* in Fig. 2 and Table 2) is dominated by nitrate regenerated at depth from sinking organic matter and subsequently returned to the euphotic zone via physical transport (*b'* in Fig. 2) (*27*). Over sufficiently large space and time scales

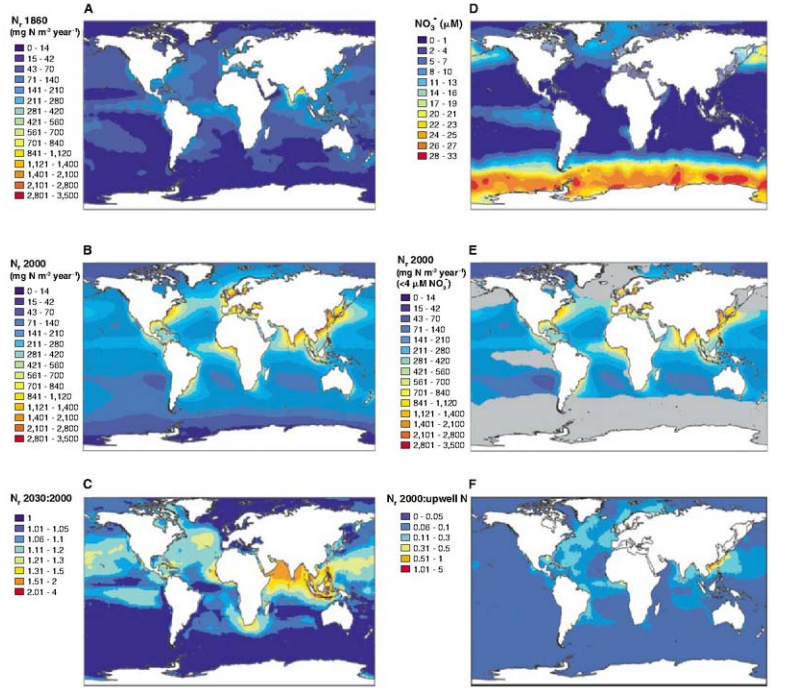

Fig. 1. **(A)** Total atmospheric reactive nitrogen (N_r) deposition in 1860 in mg m^{-2} $year^{-1}$ [NH_x and NO_y are derived from (*3*), with the addition of 30% of the total nitrogen as organic nitrogen]. Total atmospheric N_r deposition in 1860 was ~20 Tg N $year^{-1}$; AAN was ~5.7 Tg N $year^{-1}$. **(B)** Total atmospheric reactive nitrogen (N_r) deposition in 2000 in mg m^{-2} $year^{-1}$ [derived from (*21*) with the addition of 30% of the total nitrogen as organic nitrogen]. Total atmospheric N_r deposition in 2000 was ~67 Tg N $year^{-1}$, AAN was ~54 Tg N $year^{-1}$. **(C)** Ratio of the projected flux of N_r to the ocean in 2030 to that in 2000. **(D)** Nitrate concentrations (μM) in the surface (0 to 1 m) waters of the ocean (*43*). **(E)** Similar to (B), but with regions where surface nitrate >4 μM has been masked out. Total atmospheric N_r deposition in 2000 to the nonmasked areas was ~51 Tg N $year^{-1}$, AAN was ~41 Tg N $year^{-1}$. **(F)** Ratio of total N_r deposition to dissolved inorganic nitrogen (DIN) supply into the upper 130 m as diagnosed from a model fitted to oceanic tracer observations (*44*). To reduce noise, computation of the ratio has been limited to areas with DIN supply exceeding 0.05 mol m^{-2} $year^{-1}$.

(1 to ~1000 years), nitrate-driven new production is balanced by the biologically mediated export of particulate and dissolved organic matter from the surface layer (*b*″ in Fig. 2). On a similar time scale, this component of new production is almost neutral in terms of carbon assimilation (*28*) because degradation processes release N_r and CO_2 in stoichiometric amounts equivalent to the initial elemental composition of the organic matter. In the absence of denitrification and other fixed nitrogen losses in the ocean interior, nitrate-based new production can be considered a closed loop within which the biologically mediated carbon export (*b*″) is balanced by a return flux of dissolved inorganic carbon (*b*′), resulting in near-zero net air-sea CO_2 exchange.

Only external (to the ocean) sources of N_r that reach the surface mixed layer can affect the steady-state balance of the biologically mediated flux of CO_2 across the air-sea interface. The two known open ocean sources of external N_r are biological N_2 fixation (*c* in Fig. 2) and atmospheric deposition (*d*). Together these contribute a net oceanic input of N_r that can support "completely new production" and hence influence global oceanic N_r and the net atmosphere-to-ocean exchange of CO_2, assuming an adequate supply of other nutrients (P, Fe). Although N_2 fixation must have dominated the flux of external new nitrogen in the preindustrial world, atmospheric N_r deposition is now approaching N_2 fixation as a result of the dramatic increase in the anthropogenic component (Table 2).

Can this atmospheric N_r deposition be rapidly assimilated into primary production? It will impact the biogeochemistry of oceanic areas that are either perennially or seasonally depleted in surface nitrate, but will have little effect in high-nutrient, low-chlorophyll (HNLC) regions where the concentration of surface nitrate is always high. Comparing surface nitrate concentrations (Fig. 1D) and total N_r deposition (Fig. 1B) shows the relatively small overlap between high N_r deposition and significant surface nitrate concentrations. In regions where surface nitrate is seasonally depleted (i.e., where productivity is nitrogen limited), atmospheric deposition would likely be assimilated during the year. Although N_r generally is seasonally exhausted in regions where mean annual nitrate is <7 μM, a more conservative value of <4 μM is used to calculate the distribution of the atmospheric N_r deposition in present-day nitrogen-depleted waters (Fig. 1E). The calculated global N_r deposition to regions with mean nitrate <4 μM is ~51 Tg N $year^{-1}$, or ~76% of the total atmospheric N_r deposited in the ocean, compared to ~56 Tg N $year^{-1}$ (~84% of total deposition) if <7 μM is used as a threshold. Corresponding values for AAN are ~41 and ~45 Tg N $year^{-1}$. Using the areas delineated by the <4 μM and <7 μM nitrate concentrations above, we calculate that ~67 to 75% of oceanic surface waters are potentially seasonally nitrogen limited, although some of these areas may not be exclusively nitrogen limited but rather colimited (*1*). It has recently been assumed that only 40% of the ocean is nitrogen limited (*14*), although this estimate did not allow for N/P colimitation such as seen in the North Atlantic and other areas designated P-limited in (*14*). These are likely underestimates because much of the N_r is deposited upstream of N_r-depleted regions (e.g., HNLC Southern Ocean) and will eventually be advected into thermocline waters of nitrogen-limited regions of the Southern Hemisphere and North Atlantic and thus are important to future (decades to centuries) productivity and biogeochemistry (*29*).

The total atmospheric deposition plus N_2-fixation flux to the ocean is ~167 Tg N $year^{-1}$ (Table 2). Assuming complete assimilation, these external N_r sources can support a maximum biologically mediated flux of ~1.0 Pg C $year^{-1}$, of which ~0.4 Pg C $year^{-1}$ is from atmospheric deposition. Deposition of AAN alone could support up to ~0.3 Pg C $year^{-1}$, or ~3% of all new production, including that from nutrients upwelled from deep waters, and ~32% of the productivity derived from external N_r supply (Table 2). In 1860, AAN supported a biologically mediated carbon flux of only ~0.03 Pg C $year^{-1}$, so from 1860 to the present the potential impact of AAN on net primary productivity has increased ~10-fold. An earlier lower estimate (0.16 Pg C $year^{-1}$) of new (export) production generated by AAN deposition (*14*) assumed a different nitrogen-limited area, lower atmospheric fluxes, and the assumption that N enhancement will result in the replacement of diazotrophs by other phytoplankton.

Increased new production due to AAN fertilization coincides with the anthropogenic perturbation of the global carbon cycle and penetration of anthropogenic carbon in the ocean. The current anthropogenic CO_2 uptake by the ocean is ~2.2 ± 0.5 Pg C $year^{-1}$ (*30*), primarily attributed to physical-chemical processes (the "solubility pump"). Assuming that new production draws down atmospheric CO_2 according to Redfieldian stoichiometry, up to ~10% of the present anthropogenic carbon uptake could be attributed to anthropogenic nitrogen fertilization This potentially significant enhancement of the oceanic uptake of anthropogenic carbon indicates the need to incorporate this factor in future Earth system assessments and models, as has already been done for terrestrial ecosystems (*31*). This estimate may be lower if the dissolved organic carbon or particulate organic carbon produced is regenerated at shallow depths (*32*). The efficiency and longevity of this anthropogenic nitrogen fertilization effect depend on temporal uncoupling of the new N_r inputs (N_2 fixation and atmospheric deposition) from N_r removal (e.g., denitrification/anammox and burial). Assuming that all other essential nutrients are in adequate supply, it will be operational as long as the

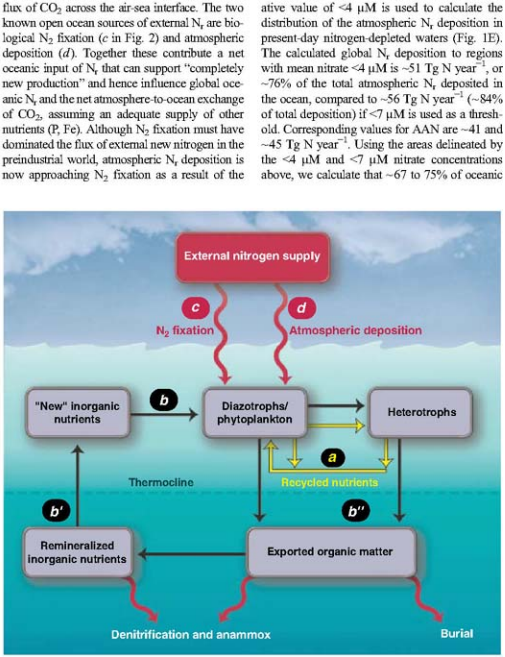

Fig. 2. Schematic of the processes supplying nutrients for surface primary production. See text for detailed description.

increase in new N_r (and associated additional CO_2 uptake) is not balanced by increased regeneration of N_2 and CO_2 and release at the ocean-air interface. Eventually, if AAN deposition levels off, the ocean may reach a new steady state with respect to nitrogen gains and losses that is neutral with respect to CO_2 uptake over time scales similar to the oceanic N residence time (~1000 years).

The future impact of AAN on productivity must be evaluated in the context of predicted changes in productivity caused by other variables. For instance, elevated concentrations of atmospheric CO_2 may have resulted in excess carbon consumption and export because of shifting C:N stoichiometry (*33*), and it is unclear whether projected AAN and high CO_2 concentrations have synergy or compensate. El Niño–Southern Oscillation (ENSO)–induced higher water temperatures and the associated increased stratification in low-latitude oceans may have reduced productivity by 60% in some regions (*34*). Thus, in a warmer climate, decreases in productivity due to restricted injection of nutrient-rich deep water would only accentuate the importance of AAN contributions to new production in low-latitude oligotrophic oceanic areas where AAN already has a strong effect. Assuming that all N_r deposition is assimilated into primary production, this N_r-driven new production could contribute as much as 20% of the total new (or export) production in such regions where upwelling is limited, e.g., the North Atlantic gyre (Fig. 1F). The contribution of N_r deposition to new production is higher in the Atlantic than the Pacific and can reach magnitudes comparable to export production along some continental areas.

Table 1. Atmospheric nitrogen emissions and deposition to the ocean. Assumed uncertainties—emissions: 1860: ±50%; 2000: NO_x ±30%, NH_3 ±50%; 2030: see text and (*20*). Deposition: 1860: ±50%; 2000: NO_y/NH_x ±40%, organic N ±50%; 2030: see text and (*20*).

	1860* (Tg N year^{-1})	2000† (Tg N year^{-1})	2030† (Tg N year^{-1})
	Emission to the atmosphere		
Total NO_x	13 (7–20)	52 (36–68)	54‡
Anthropogenic NO_x	2.6 (1.3–4)	38 (27–49)	43
Total NH_3	21 (11–32)	64 (32–96)	78‡
Anthropogenic NH_3	7.4 (3.7–11)	53 (27–80)	70
Total atmospheric N emissions	34 (18–52)	116 (68–164)	132
Total anthropogenic N_r (AAN)	10 (5–15)	91 (54–129)	113
	Deposition to the ocean		
Total NO_y	6.2 (3.1–9.3)	23 (14–32)	25
Anthropogenic NO_y	1.2 (0.6–1.8)	17 (10–24)	18
Total NH_x	8 (4–12)	24 (14–34)	29
Anthropogenic NH_x	2.4 (1.2–3.6)	21 (13–29)	25
Total organic N_r	6.1 (3.0–9.1)	20 (10–30)	23
Anthropogenic organic N_r	2.1 (1.0–3.1)	16 (8–24)	19
Total N_r deposition	20 (10–30)	67 (38–96)	77
Total anthropogenic N_r (AAN)	5.7 (2.8–8.5)	54 (31–77)	62

*From (*3*). †Derived from (*21*); see text and (*26*). ‡NO_x and NH_3 based on ~80% and ~90% anthropogenic, respectively [from (*3*)].

Table 2. Atmospheric nitrogen deposition to the ocean in 2000 and its impact on productivity. Global-scale estimates of total primary production (*23*); new production (*24–26*); N_2 fixation (*2*, *6–8*). Most letters in italics refer to flux pathways in Fig. 2.

		Global ocean nitrogen (Tg N year^{-1})	Resultant global ocean productivity (Pg C year^{-1})
Total primary production ($a+b+c+d$)		~8800 (7000–10,500)	~50 (40–60)
New production (NP) (b)		~1900 (1400–2600)	~11 (8–15)
Marine N_2 fixation (c)		~100 (60–200)	~0.57 (0.3–1.1)
Total net N_r deposition (d) (NO_y+NH_x+Org. N_r)		~67 (38–96)	~0.38 (0.22–0.55)
Total external nitrogen supply ($c+d$)		~167 (98–296)	~0.95 (0.56–1.7)
Anthropogenic N_r deposition (AAN) (e)		~54 (31–77)	~0.31 (0.18–0.44)
Marine N_2 fixation as % NP N_r	= c/b		~5.3% (2.3–14.3%)
Total N_r deposition as % NP N_r	= d/b		~3.5% (1.5–6.9%)
AAN as % NP N_r	= e/b		~2.8% (1.2–5.5%)
Total N_r deposition as % external N supply	= $d/(c+d)$		~40% (13–98%)
AAN as % external N supply	= $e/(c+d)$		~32% (10–79%)

On the basis of future scenarios for anthropogenic emissions, AAN contribution to primary production could approach current estimates of global N_2 fixation by 2030. Fertilization of the surface layer by atmospheric deposition, primarily AAN, could even lead to a decrease in N_2 fixation due to biological competition (*14*). However, atmospheric N_r deposition has a very small effect on the surface seawater ambient N_r concentrations, too little to inhibit nitrogenase activity directly [e.g., we estimate that an extremely rare and large atmospheric deposition event distributed over a 25-m mixed-layer depth could increase the N_r concentration by only ~ 45 nM (*35*), which is too small to suppress N_2 fixation (*36*)]. Atmospheric N_r deposition more likely represents a long-term low-level fertilization of the ocean that has consequences for the natural biogeochemical cycles of nitrogen and carbon and their ongoing anthropogenic perturbations. Biological evidence suggests that phytoplankton communities in oceanic gyres are presently nitrogen limited (*1*). Atmospheric N_r deposition, in the absence of significant atmospheric deposition of phosphorus, may exacerbate phosphorus limitation of N_2 fixation. The long-term effect of AAN deposition on N_2 fixation depends on whether P or Fe limits N_2 fixation and on the supply ratio of bioavailable N:P:Fe derived from atmospheric deposition (*37*). Atmospheric deposition of phosphorus is much less perturbed by human activity than N_r (*13*, *37*). Hence, the overall impact of atmospheric deposition is likely to be a shift in the N/P balance of surface waters. Some marine diazotrophs can exploit dissolved organic phosphorus pools and may obtain an adequate P supply by degrading compounds such as phosphonates (*38*).

Changes in species composition and productivity can lead to changes in the export of nitrogen and carbon to deep ocean water, resulting in a shift of deep ocean N/P ratios away from Redfield stoichiometry, which could then influence the chemistry of upwelled waters remote from the loci of atmospheric depositions. Remineralization of this extra organic carbon flux in deep waters may reduce the deepwater O_2 concentration, and the resultant microbial N_2 production will act to restore the N/P ratio toward the Redfield value, as suggested to have happened in the past (*39*). (See Supporting Online Material, including fig. S2).

Impact on N_2O Emissions from the Ocean

Another important issue is whether increasing atmospheric N_r inputs to the ocean can alter marine emissions of nitrous oxide (N_2O), a major greenhouse gas. Estimates of global sea-to-air N_2O fluxes vary considerably. Two recent estimates are the Intergovernmental Panel on Climate Change (IPCC) assessment (*30*) (3.8 Tg N year^{-1} as N_2O) and the calculation by Bange of the mean from data in (*40*) (6.2 Tg N year^{-1}). Using the mean (5.0 Tg N year^{-1}) and the range of these two estimates, and assuming that the nitrogen in

this "recent" N_2O flux originally entered the oceans from N_2 fixation (100 Tg N $year^{-1}$) and atmospheric deposition (67 Tg N $year^{-1}$), then the emission of 5.0 Tg N $year^{-1}$ as N_2O results from nitrification and denitrification of part of this 167 Tg N $year^{-1}$ entering the surface ocean. This assumes that N_2O production in the near-surface ocean is at steady state and there are no significant time lags between atmospheric input and N_2O formation. Normalizing the N_2O flux to the atmosphere by the "completely new" nitrogen input (5.0:167) can then be used to estimate that AAN deposition has resulted in the production of up to ~1.6 Tg N_2O-N $year^{-1}$, or about a third of total oceanic N_2O emissions. This approach suggests that in 1860, only ~0.2 Tg N $year^{-1}$ (~5%) of the sea-to-air flux of N_2O was driven by atmospheric anthropogenic inputs, assuming simplistically that N_2O production is linearly related to N supply. [We use linear scaling due to the lack of experimental and modeling studies that address the spatial and nonlinear response of N_2O emissions to N deposition, although important regional variations are likely (*41*).] This suggests that from 1860 to the present, the increase in AAN has led to nearly an order of magnitude increase in anthropogenic N_2O emission from the oceans. Calculations and estimates of increases for 2030 are in table S1.

While oceanic AAN deposition may result in increased N_2O emissions, increasing radiative forcing, AAN also increases primary production (up to ~0.3 Pg C $year^{-1}$ detailed above) and export production to the deep ocean, removing CO_2 from the atmosphere and therefore decreasing radiative forcing. With a Global Warming Potential of 298 for N_2O (*42*), the net balance suggests that about two-thirds of the decrease in radiative forcing from CO_2 uptake could be offset by the increase due to N_2O emissions. The uncertainty in our estimates is considerable; however, the estimates suggest the potential importance of AAN to N_2O emissions and therefore the need for future research in regions such as oceanic Oxygen Minimum Zones (OMZs), which, although small in area, are potentially important for N_2O emissions. The future role of OMZs will be influenced not only by AAN but also by climate and other global changes.

Conclusions

This analysis emphasizes the potential importance of the growing quantity of atmospheric reactive (fixed) nitrogen that enters the open ocean as a result of human activities and its impact on the present marine nitrogen cycle. Considering the increasing demand for energy and fertilizers, the emissions of AAN are expected to grow over the coming decades. Atmospheric deposition of anthropogenic nitrogen to the ocean may account for up to ~3% of the annual new oceanic primary productivity, but about a third of the primary productivity generated as a result of the external input of nitrogen to the ocean. The input of AAN is approaching that of N_2 fixation as a source of marine reactive nitrogen. Although local AAN deposition seems unlikely to alter significantly local phytoplankton species composition, the phytoplankton community could be affected by the slow long-term fertilization of surface waters by AAN. Moreover, AAN inputs to the ocean have potentially important climatic implications. Up to about a tenth of the anthropogenic atmospheric carbon uptake by the ocean (as CO_2) may result from this fertilization. In addition, AAN inputs may stimulate N_2O emissions, with possibly about two-thirds of the decrease in radiative forcing from increased CO_2 uptake by the ocean being offset by the increase in radiative forcing from increased N_2O emissions.

There is clearly much we do not know about the extent and time scale of the impacts of AAN deposition on the oceans and the feedbacks to the climate system. The issues are complex and interactive, and they must be considered in climate scenarios. Areas of particular importance include understanding more fully the sources, chemical speciation, reactivity, and availability of atmospheric organic nitrogen; developing more realistic models of N_r deposition to the ocean, coupled with measuring N_r deposition over extended periods of time in open ocean regions; understanding the relationships between, and impacts of, the atmospheric deposition of bioavailable N, P, and Fe; and understanding the mechanisms and time scales involved in the oceanic response to N_r deposition, coupled with a new generation of Earth system models that take into account long-term low-level nitrogen fertilization of the ocean and evaluate the effect on N_2O emissions and the duration of the enhanced (anthropogenic) CO_2 uptake.

References and Notes

1. M. M. Mills, C. Ridame, M. Davey, J. La Roche, R. J. Geider, *Nature* **429**, 292 (2004).
2. N. Gruber, J. Sarmiento, in *The Sea: Biological-Physical Interactions*, A. R. Robinson, J. F. McCarthy, B. Rothschild, Eds. (Wiley, New York, 2002), vol. 12, pp. 337–399.
3. J. N. Galloway *et al.*, *Biogeochemistry* **35**, 3 (1996).
4. S. P. Seitzinger, J. A. Harrison, E. Dumont, A. H. W. Beusen, A. F. Bouwman, *Global Biogeochem. Cycles* **19**, GB4501 (2005).
5. S. Seitzinger *et al.*, *Ecol. Appl.* **16**, 2064 (2006).
6. C. Mahaffey, A. F. Michaels, D. G. Capone, *Am. J. Sci.* **305**, 546 (2005).
7. J. K. Moore, S. C. Doney, K. Lindsay, N. Mahowald, A. F. Michaels, *Tellus* **58B**, 560 (2006).
8. C. Deutsch, J. L. Sarmiento, D. M. Sigman, N. Gruber, J. P. Dunne, *Nature* **445**, 163 (2007).
9. J. N. Galloway *et al.*, *Science* **320**, 889 (2008).
10. R. A. Duce *et al.*, *Global Biogeochem. Cycles* **5**, 193 (1991).
11. J. M. Prospero *et al.*, *Biogeochemistry* **35**, 27 (1996).
12. C. M. Duarte *et al.*, *J. Geophys. Res.* **111**, G04006 (2006).
13. T. Jickells, *Biogeosciences* **3**, 271 (2006).
14. A. Krishnamurthy, J. K. Moore, C. S. Zender, C. Luo, *J. Geophys. Res.* **112**, G02019 (2007).
15. H. W. Paerl, *Nature* **315**, 747 (1985).
16. S. C. Doney *et al.*, *Proc. Natl. Acad. Sci. U.S.A.* **104**, 14580 (2007).
17. S. E. Cornell, T. D. Jickells, J. N. Cape, A. P. Rowland, R. A. Duce, *Atmos. Environ.* **37**, 2173 (2003).
18. K. A. Mace, R. A. Duce, N. W. Tindale, *J. Geophys. Res.* **108**, 4338 (2003).
19. T. Nakamura, H. Ogawa, D. K. Maripi, M. Uematsu, *Atmos. Environ.* **40**, 7259 (2006).
20. If the assumption that in 1860 the relationship between organic and inorganic N in deposition was the same as today, i.e., that organic nitrogen is ~30% of the total N_r, is in error, then it is likely that both the total and the anthropogenic nitrogen deposition in 1860 would have been less than indicated in Table 1.
21. F. Dentener *et al.*, *Global Biogeochem. Cycles* **20**, GB4003 (2006).
22. The deposition estimates for 2030 are based on the S2 simulation of NO_y and NH_3 emissions to the atmosphere presented in (*21*), which uses an IIASA CLE 2030 current emission regulation scenario, termed "likely" in that paper. We estimate that the atmospheric emission and deposition values shown in Table 1 for 2030 have uncertainties of ~40 to 50%. Dentener *et al.* (*21*) also discuss results using the "optimistic" IIASA Maximum Feasible Reduction (MFR) scenario and the "pessimistic" IPCC SRES A2 scenario. Depending on the regional development path of N, emissions, N_r depositions may be lower by 10 to 70% (MFR) or higher by 30 to 200%.
23. M. E. Carr *et al.*, *Deep-Sea Res. Part II* **53**, 741 (2006).
24. E. A. Laws, P. G. Falkowski, W. O. Smith, H. Ducklow, J. J. McCarthy, *Global Biogeochem. Cycles* **14**, 1231 (2000).
25. A. Oschlies, *Deep-Sea Res. Part II* **48**, 2173 (2001).
26. H. W. Ducklow, *Rev. Geophys.* **33**, 1271 (1995).
27. R. C. Dugdale, J. J. Goering, *Limnol. Oceanogr.* **12**, 196 (1967).
28. W. S. Broecker, *Global Biogeochem. Cycles* **5**, 191 (1991).
29. J. L. Sarmiento, N. Gruber, M. A. Brzezinski, J. P. Dunne, *Nature* **427**, 56 (2004).
30. K. Denman *et al.*, in *Climate Change 2007: The Physical Science Basis*, S. Solomon *et al.*, Eds. (Cambridge Univ. Press, Cambridge, 2007), pp. 544–547.
31. F. Magnani *et al.*, *Nature* **447**, 849 (2007).
32. A. Gnanadesikan, J. L. Sarmiento, R. D. Slater, *Global Biogeochem. Cycles* **17**, 1050 (2003).
33. U. Riebesell *et al.*, *Nature* **450**, 545 (2007).
34. M. J. Behrenfeld *et al.*, *Nature* **444**, 752 (2006).
35. A. F. Michaels, D. A. Siegel, R. J. Johnson, A. H. Knap, J. N. Galloway, *Global Biogeochem. Cycles* **7**, 339 (1993).
36. C. M. Holl, J. P. Montoya, *J. Phycol.* **41**, 1178 (2005).
37. A. R. Baker, S. D. Kelly, K. F. Biswas, M. Witt, T. D. Jickells, *Geophys. Res. Lett.* **30**, 2296 (2003).
38. S. T. Dyhrman *et al.*, *Nature* **439**, 68 (2006).
39. R. S. Ganeshram, T. F. Pedersen, S. E. Calvert, G. W. McNeill, M. R. Fontugne, *Paleoceanography* **15**, 361 (2000).
40. H. W. Bange, *Atmos. Environ.* **40**, 198 (2006).
41. X. Jin, N. Gruber, *Geophys. Res. Lett.* **30**, GL18458 (2003).
42. S. Solomon *et al.*, in *Climate Change 2007: The Physical Science Basis*, S. Solomon *et al.*, Eds. (Cambridge Univ. Press, Cambridge, 2007).
43. M. E. Conkright *et al.*, *World Ocean Atlas 2001*, vol. 4, *Nutrients*, S. Levitus, Ed., NOAA Atlas NESDros. Int. Serv. 52 (U.S. Government Printing Office, Washington, DC, 2002).
44. R. Schlitzer, *J. Phys. Oceanogr.* **37**, 259 (2007).

45. We acknowledge the leadership of the Surface Ocean–Lower Atmosphere Study (SOLAS) project (www.solas-int.org) and the International Nitrogen Initiative (www.initrogen.org) of SCOPE and the International Geosphere-Biosphere Programme (IGBP; www.igbp.kva.se) for conceiving this synthesis. We thank the Scientific Committee on Oceanic Research, IGBP, the U.S. National Oceanic and Atmospheric Administration, and the European Science Foundation for partial support of the work. We thank J. Hare of the SOLAS International Project Office for help in organizing the workshop and E. Breviere of that office for help in making the Nitrogen Workshop in Norwich, UK, a success. We acknowledge two anonymous reviewers for constructive feedback.

Supporting Online Material

www.sciencemag.org/cgi/content/full/320/5878/893/DC1
SOM Text
Figs. S1 and S2
Table S1
References

10.1126/science.1150369

The Energetic Cost of Climbing in Primates

Jandy B. Hanna,[1]*† Daniel Schmitt,[1] Timothy M. Griffin[2]

Intuition tells us that the metabolic costs of climbing should be higher than the costs of walking or running because of the additional work required to lift the center of mass. There are, however, few data available on the absolute and relative metabolic costs of vertical climbing, partly because of the technical difficulties of collecting data on climbing and the lack of a simple animal model for such a study. Additionally, it is difficult to extrapolate the vertical cost of climbing from previous studies because most were performed on inclines, not up vertical supports (*1*, *2*). To date, no study has measured the metabolic cost of climbing up a vertical support across a range of body sizes in mammals. Primates are ideally suited for examining the scaling of the metabolic costs of climbing versus walking because primates are adept climbers and span a large range of body sizes. Furthermore, it is often argued that critical evolutionary transitions in primate and human evolution—including the origin of primates and bipedalism—are associated with adaptations for climbing in a complex arboreal environment.

We measured the rate of oxygen consumption during vertical climbing and level walking for five species of primates across an eightfold range in body mass (0.167 to 1.40 kg). To obtain steady-rate oxygen consumption, animals climbed at their maximum sustainable speed during a 15- to 30-min period on a rope treadmill enclosed in a plexiglass chamber. We then compared the metabolic energy required to transport 1 kg of body mass 1 m (COT_{TOT}) while climbing or walking at the same speed (*4*).

COT_{TOT} for climbing was not significantly different across the range of body sizes tested in this study [119.8 ± 21.4 J kg^{-1} m^{-1} (mean ± SD), $P = 0.368$, analysis of variance] (Fig. 1A), indicating that these different-sized primates used the same amount of energy to lift 1 kg of body mass 1 m while climbing. Additionally, the slope of the logarithmic regression relating COT_{TOT} to body mass (M_b) is not significantly different from zero as indicated by the 95% confidence level ($COT_{TOT} = 107.4M_b \times 10^{0.119\pm0.130}$, $r = 0.858$, $P = 0.063$). Data on human climbing on a vertical climbing ergometer, not included in the regression calculation, fall within the confidence limits of the regression data, further supporting our findings of a consistent COT_{TOT} for climbing across body mass in primates (*3*) (Fig. 1A). COT_{TOT} for walking by the five nonhuman primate species in this study, however, varied significantly with body mass (91.9 ± 78.2 J kg^{-1} m^{-1}, $P = 0.030$) and showed the expected trend of decreasing with increasing size ($COT_{TOT} = 51.5M_b \times 10^{0.750\pm0.882}$, $r = 0.843$, $P = 0.073$) (Fig. 1A) (*4*). A size-dependent decrease in COT_{TOT} for level walking is well documented (*5*) and is associated with increased leg lengths that reduce the rate at which muscles are activated to generate force to support body mass as initially reported for running (*6*). The lack of variation in COT_{TOT} across size for climbing suggests that the underlying mechanism relating body size to COT_{TOT} is different for climbing compared with walking. If the cost of performing work to lift the center of mass is the primary determinant of the metabolic cost of climbing, then the climbing efficiency—the net vertical mechanical work rate divided by the net metabolic rate—should be constant across size. Our data show that climbing efficiency is nearly constant across size (Fig. 1B), suggesting that the metabolic cost of climbing by humans and nonhuman primates can be primarily explained by the cost of performing muscular work against gravity.

These data suggest a possible explanation for how early primates invaded a fine-branch niche (*7*) without engendering new costs associated with climbing. If, as is generally argued [although see (*8*) for a contrary view], the earliest primates weighed less than 0.5 kg, then the uniform costs of climbing and walking demonstrated here may have allowed the earliest primates to exploit a complex arboreal environment without increased metabolic costs.

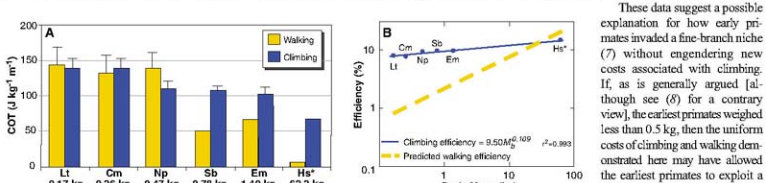

Fig. 1. **(A)** COT_{TOT} () J kg^{-1} m^{-1}) during climbing and speed-matched walking [see (*4*) for description of procedures]: Lt indicates *Loris tardigradus*; Cm, *Cheirogaleus medius*; Np, *Nycticebus pygmaeus*; Sb, *Saimiri boliviensis*; Em, *Eulemur mongoz*; and Hs, *Homo sapiens*. Species are arranged from smallest body mass to largest body mass (left to right). Bars indicate one standard deviation. *Human costs of climbing on a vertical climbing ergometer are calculated from the equation in (*3*), whereas human walking costs are calculated as described in (*4*). **(B)** Efficiency to move the center of mass versus body mass for climbing and walking. Climbing efficiency is nearly constant across body mass, indicating that the metabolic rate during climbing is proportional to the minimum rate of performing mechanical work to lift the center of mass against gravity. *Human metabolic data used to calculate climbing efficiency, included in the regression, are from (*3*). Climbing and walking efficiency calculations are described in (*4*).

References and Notes

1. C. R. Taylor, S. L. Caldwell, V. J. Rowntree, *Science* **178**, 1096 (1972).
2. R. J. Full, A. Tullis, *J. Exp. Biol.* **149**, 307 (1990).
3. J. Booth, F. Marino, C. Hill, T. Gwinn, *Br. J. Sports Med.* **33**, 14 (1999).
4. Materials and methods are available as supporting material on *Science* Online.
5. J. Robinson *et al.*, *J. Exp. Biol.* **210**, 3513 (2007).
6. R. Kram, C. R. Taylor, *Nature* **346**, 265 (1990).
7. M. Cartmill, *Science* **184**, 436 (1974).
8. C. Soligo, R. D. Martin, *J. Hum. Evol.* **50**, 414 (2006).

9. The authors thank T. Roberts, S. Larson, R. Wunderlich, and two anonymous reviewers for helpful comments and the Duke Lemur Center and the Center for Neotropical Primate Research and Resources for access to subjects. Supported by NSF grant DIG-BCS 04-52631 and a graduate research fellowship, NIH grants P40-RR001254 and AR051672), Sigma Xi, the Society for Experimental Biology, and Duke University. This is Duke Lemur Center publication no. 1006.

Supporting Online Material

www.sciencemag.org/cgi/content/full/320/5878/898/DC1
Materials and Methods
Fig. S1

22 January 2008; accepted 18 March 2008
10.1126/science.1155504

[1]Biological Anthropology and Anatomy, Duke University, Durham, NC 27710, USA. [2]Department of Surgery, Orthopaedic Bioengineering Laboratory, Duke University Medical Center, Durham, NC 27710, USA.

*To whom correspondence should be addressed. E-mail: jhanna@wvsom.edu
†Present address: Structural Biology, West Virginia School of Osteopathic Medicine, Lewisburg, WV 24901, USA.

Quasi-Particle Properties from Tunneling in the $\nu = 5/2$ Fractional Quantum Hall State

Iuliana P. Radu,[1] J. B. Miller,[2] C. M. Marcus,[2]* M. A. Kastner,[1] L. N. Pfeiffer,[3] K. W. West[3]

Quasi-particles with fractional charge and statistics, as well as modified Coulomb interactions, exist in a two-dimensional electron system in the fractional quantum Hall (FQH) regime. Theoretical models of the FQH state at filling fraction $\nu = 5/2$ make the further prediction that the wave function can encode the interchange of two quasi-particles, making this state relevant for topological quantum computing. We show that bias-dependent tunneling across a narrow constriction at $\nu = 5/2$ exhibits temperature scaling and, from fits to the theoretical scaling form, extract values for the effective charge and the interaction parameter of the quasi-particles. Ranges of values obtained are consistent with those predicted by certain models of the $5/2$ state.

The fractional quantum Hall (FQH) effect (*1*) results from the formation of novel electronic states of a two-dimensional electron system (2DES) at high magnetic field and low temperature, in which electron-electron interactions lead to gaps in the bulk excitation spectra. Because of these gaps, current can only flow via extended states or conduction channels that propagate around the edges of the 2DES (*2*). At a constriction in the 2DES such as that formed by a quantum point contact (QPC), counter-propagating edge states come close enough together that can tunnel between them. According to theory (*3*), weak quasi-particle tunneling depends strongly on the voltage difference between the edges (or, because of the Hall effect, the current through the QPC) and should scale with temperature in a way that provides a measurement of the effective charge, e^*, of the quasi-particles and the strength of the Coulomb interaction, g. Because both e^* and g are specific to the particular FQH state, such measurements provide a discriminating probe of FQH wave functions.

The FQH state at $\nu = 5/2$ (*4*) is of particular interest because the leading candidates for the wave function for this state have elementary excitations that exhibit nonabelian particle statistics (*5*–*9*). Whereas the interchange of abelian particles such as electrons multiplies the wave function by an overall phase, the interchange of nonabelian quasi-particles can lead to a different wave function altogether. Identifying a physical system with nonabelian statistics would be of fundamental interest but has also been proposed as a basis for a topological quantum information processing scheme (*10*) that is resistant to environmental decoherence (*11*, *12*). The resistance to decoherence arises from the fact that the information is encoded in a many-body state rather than a single-electron state. Although wave functions with nonabelian excitations are the prime candidates (*13*) to describe the state at $\nu = 5/2$, alternatives with abelian properties have also been proposed (*14*–*16*). All candidate wave functions for $\nu = 5/2$ have quasi-particle effective charge $e^* = 1/4$, but they differ in the predicted values of g (*8*, *9*, *17*–*19*).

Weak tunneling theory, developed originally for Laughlin FQH states (*3*), has also been extended to nonabelian states (*17*–*21*). Tunneling measurements on a single constriction can distinguish among candidate wave functions for $\nu = 5/2$; existing proposals to find direct evidence for nonabelian statistics, however, require multiple constrictions to create interference among tunneling paths (*11*, *22*–*26*).

Experimentally, the quasi-particle charge, e^*, has been investigated for FQH states at $\nu < 1$ with use of shot noise (*27*, *28*) and interferometry (*29*), yielding results generally consistent with theory. A recent measurement of quasi-particle charge for the $\nu = 5/2$ state, also using shot noise, obtained values consistent with $e^* = 1/4$ (*30*). Previous experiments of quasi-particle tunneling at a constriction have focused on cases of unequal filling fractions in the bulk and the constriction (*31*–*34*). These experiments identified zero-bias features associated with quasi-particle tunneling at FQH edges and are compared to our present measurements. The interaction parameter, g, has been measured in studies of tunneling of $\nu = 1/3$ FQH edges at a depleted constriction (*35*) through which electrons, rather than quasi-particles, tunnel.

We present experimental measurements of quasi-particle tunneling at a QPC at $\nu = 5/2$, in the regime where the filling fraction (and the carrier density) in the QPC and the bulk 2DES are the same. We found that tunneling conductance across the QPC exhibits a strong zero-bias peak that scales with temperature, in quantitative agreement with the theory for weak tunneling (*3*, *18*, *19*). From these measurements, we extract e^* and g. We observe that among the candidate states for $\nu = 5/2$, the anti-Pfaffian (*8*, *9*) and the $U(1) \times SU_2(2)$ (*7*), both predicted to have nonabelian excitations, are most consistent with the data.

Sample and experimental setup. The sample was a GaAs/AlGaAs heterostructure with the 2DES 200 nm below the surface and two Si δ-doping layers 100 nm above and below the 2DES. Hall bars with a width of 150 μm were patterned

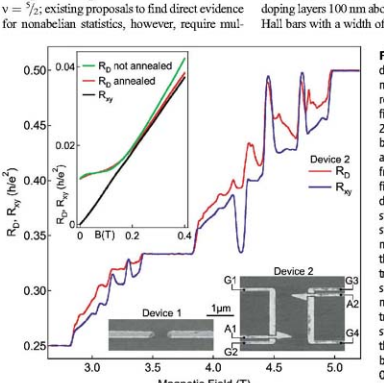

Fig. 1. Magnetic field dependence of the diagonal (R_D) and Hall (R_{xy}) resistance for device 2 at fixed gate voltage from $\nu = 2$ to $\nu = 4$, illustrating that both the QPC and the bulk are at the same filling fraction. (**Top inset**) Low-field data from the same device (device 2), emphasizing that the carrier density in the annealed QPC is nearly the same as that of the bulk (red and black traces with almost-matching slopes), whereas in the nonannealed QPC (green trace) the density shifts significantly. For clarity, the nonannealed data has been offset vertically by $0.003\ h/e^2$. (**Bottom insets**) Scanning electron micrographs of devices with similar gate geometry to those used in these experiments.

[1]Department of Physics, Massachusetts Institute of Technology, Cambridge, MA 02139, USA. [2]Department of Physics, Harvard University, Cambridge, MA 02138, USA. [3]Bell Laboratories, Alcatel-Lucent Technologies, Murray Hill, NJ 07974, USA.

*To whom correspondence should be addressed. E-mail: marcus@harvard.edu

on this heterostructure. The mobility (before the gates are energized) was 2×10^7 cm^2 V^{-1} s^{-1}, the carrier density was 2.6×10^{11} cm^{-2}, and the $\nu = 5/2$ energy gap was ~130 mK in the bulk (*34*). The QPCs were formed by Cr/Au top gates, which were patterned on the Hall bar using e-beam lithography. By applying a negative gate voltage V_g to these gates, the electrons underneath them were depleted, creating a constriction tunable with V_g. We report measurements on devices with two different gate geometries (Fig. 1 bottom insets). Device 1 was a simple QPC with gate separation of 800 nm. Device 2 was a channel ~1200 nm wide, formed by energizing the gates marked G1, G2, G3, and G4 (gates A1 and A2 were held at ground and not used in this experiment). The sample was mounted on the cold finger of a dilution refrigerator with a base temperature of less than 10 mK. In all figures and analysis, we quote electron temperatures. At temperatures $\geq$ 20 mK, the mixing chamber and electron temperatures were measured to be equal with use of resonant electron tunneling in a lateral quantum dot. Temperatures below 20 mK were estimated by using both resonant tunneling and by tracking several strongly temperature-dependent quantum Hall features in the bulk, with consistent results (*36*).

The magnetic field was oriented perpendicular to the plane of the 2DES.

Measurements were performed by using standard four-probe lock-in techniques with an ac current excitation between 100 and 400 pA and in some cases a dc bias of up to 20 nA. To determine the tunneling conductance, g_T, we simultaneously measured the Hall resistance, R_{xy} (voltage probes on opposite sides of the Hall bar away from the QPC), and the diagonal resistance, R_D (voltage probes on opposite sides of the Hall bar and also opposite sides of the QPC) (*34*, *36*, *37*). For a schematic of the sample and measurement setup, see fig. S1. In the weak tunneling regime (*3*) when the bulk of the sample is at a quantum Hall plateau, the tunneling voltage is the same as the Hall voltage, whereas R_D reflects the differential tunneling conductance via

$$g_T = \frac{R_D - R_{xy}}{R_{xy}^2} \quad (1)$$

R_{xy} is independent of dc bias when the bulk is at a FQH plateau. If one assumes that the underlying edge has a filling fraction ν_{under}, then the reflection of the $5/2$ edge state can be calculated as $R = g_T R_{xy}^2/[(1/\nu_{under})h/e^2 - R_{xy}]$.

Same filling fraction in QPC and bulk. A key difference from previous tunneling experiments (*31*–*34*) is that we were able to deplete the electrons under the gates and induce tunneling without substantially changing the filling fraction in the QPC. This was achieved by applying a gate voltage of –3 V while at 4 K and allowing the system to relax for several hours, which we refer to as annealing. We then cooled the sample and limited the voltage to the range –2 to –3 V at dilution refrigerator temperatures. After annealing, R_D and R_{xy} were measured over several integer plateaus, and the fields marking the ends of the plateaus were found to coincide for the QPC and the bulk (Fig. 1), indicating that the filling factors are the same. The extra resistance in R_D at FQH states is consistent with tunneling. Additional evidence that the filling fraction changes little once the QPC is annealed is shown in the Fig. 1 top inset: The slopes of R_{xy} and R_D at low magnetic field, inversely proportional to carrier density, differ by 2% or less. For comparison, we show data from a nonannealed QPC in which the density decreases by ~15%.

Bias and temperature dependence. Focusing on the dependence of g_T on the dc bias, I_{dc}, through the QPC and Hall bar, Fig. 2 shows a color-scale plot of the dependence of g_T on both I_{dc} and magnetic field, B, at four temperatures; a measurement of R_{xy} is shown for comparison. As seen at the highest temperatures, these field sweeps reveal a series of FQH states (*38*) around $\nu = 5/2$, including the $7/3$ and the $8/3$. At the lowest temperatures, strong reentrant integer quantum Hall (RIQH) features are also visible on either side of $5/2$, both in the bulk and in the QPC (Fig. 2). The dc bias behavior at FQH plateaus is quite different from that of the RIQH features: At FQH plateaus, zero-bias peaks in g_T persist up to at least 50 mK (Fig. 2D). By contrast, RIQH states have more-complex dc bias signatures, which decrease rapidly with temperature, disappearing by 30 mK both in the bulk (R_{xy}) and in the QPC (g_T). Qualitatively similar results were observed for device 1. To study the FQH state at $\nu = 5/2$, we set the magnetic field to the center of a bulk FQH plateau ($B = 4.31$ T for device 2, vertical line in Fig. 2C, and $B = 4.3$ T for device 1).

With the field set to the center of the plateau, we investigated the effect of V_g on the zero-bias peak at several temperatures (Fig. 3). At the lowest temperatures (Fig. 3A), the zero-bias peak persists throughout the V_g range. At higher temperatures, a peak in both dc bias and V_g was observed, centered near $V_g = -2.5$ V (Fig. 3C). To study quasi-particle tunneling, we set V_g to the center of this peak, the feature that persists to the highest temperature, because theory predicts that tunneling decreases slowly, as a power law, with temperature.

With the magnetic field and gate voltage set, we measured the dc bias dependence in device 1 at various temperatures (Fig. 4). The traces in Fig. 4A are slices along the dashed lines in Fig. 3.

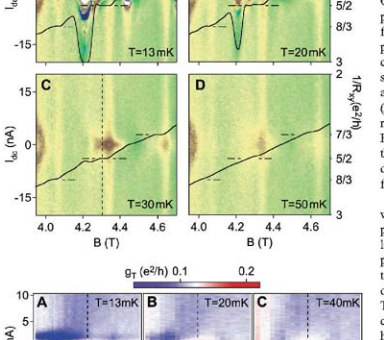

Fig. 2. (**A** to **D**) Differential tunneling conductance g_T (device 2) as a function of magnetic field and dc bias current at several temperatures. On each graph, the zero dc-bias R_{xy} trace from the same temperature is superimposed (right axis). The field range encompasses the FQH states $7/3$, $5/2$, and $8/3$ (marked with horizontal dot-dash lines). At the higher temperatures, dc bias nonlinearities exist only at the fractional plateaus. All other features, such as those from the reentrant quantum Hall effect, disappear at ~30 mK.

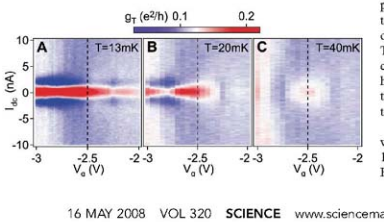

Fig. 3. Differential tunneling conductance g_T (device 1) as a function of V_g and dc bias at several temperatures: (**A**) $T = 13$ mK, (**B**) $T = 20$ mK, and (**C**) $T = 40$ mK. The vertical dashed line marks the gate voltage at which the zero-bias peak persists to highest temperature.

Because the voltage drop between the two counterpropagating edge states in the QPC is the dc current multiplied by the Hall resistance, we have labeled the horizontal axis with both the current and the dc voltage using $R_{xy} = 0.4\ h/e^2$ (*3*). All these traces saturate at the same value, R^{∞}, at high dc bias, higher than the expected value of $0.40\ h/e^2$. The height of the peak, measured from R^{∞}, decreases with increasing temperature, following a power law in temperature with an exponent of −1.3 (Fig. 4B). The full width at half maximum (FWHM) of the peak increases linearly with temperature and extrapolates to zero at zero temperature, consistent with a zero intrinsic line width (Fig. 4C). The data can be collapsed onto a single curve (Fig. 4D) when the horizontal axis is scaled by T and the vertical axis is scaled by $T^{-1.3}$ (after subtracting a common background R^{∞}).

Extracting g and e^*. The observed temperature dependence of the peak height and FWHM is consistent with the theoretical predictions of weak quasi-particle tunneling between fractional edge states (*3*, *18*, *19*). In that picture, the zero-bias peak height is expected to vary with temperature as T^{2g-2}, which gives $g = 0.35$ for the data in Fig. 4B. The weak-tunneling expression, which includes the effects of dc bias (*3*) has the form

$$g_T = AT^{(2g-2)}F\left(g, \frac{e^*I_{dc}R_{xy}}{kT}\right) \quad (2)$$

[see (*36*) for details]. This functional form fits the experimental data well, as seen in Fig. 4E. (Note that R_D and g_T differ only by an offset and scale factor.) All five temperatures are fit simultaneously with four free parameters: a single vertical offset corresponding to R^{∞}, an amplitude A, and the two quantities g and e^*. A least-squares fit over the full data set gives best-fit values $g = 0.35$, the same value found from the power law fit of the peak heights (Fig. 4B), and $e^* = 0.17$. Uncertainties in these values will be discussed below. Similar analysis performed on data from a different device (device 2 but energizing only gates G1 and G4) yields quantitatively similar results.

To characterize the uncertainty of these measured values, we show in Fig. 5 a matrix of fits to the weak-tunneling form, Eq. 2 with g and e^* fixed and A and R^{∞} as fit parameters. The color scale represents the normalized fit error, defined as the residual of the fit per point divided by $0.0005\ h/e^2$, the noise of the measurement. A fit error ≤ 1 indicates that fit is consistent with the data within the noise of the measurement. Higher values indicate worse fits (*36*) (figs. S4 and S5).

This matrix of fits allows various candidate states at $\nu = 5/2$ to be compared with the tunneling data. All of the candidate states predict $e^* = 1/4$, but g can differ. States with abelian quasi-particle statistics include the so-called 331 state (*14*, *15*), which has a predicted $g = 3/8$ (*17*), and the $K = 8$ state with $g = 1/8$ (*16*). States with nonabelian quasi-particle statistics include the Pfaffian (*6*), with $g = 1/4$ (*17*); its particle-hole conjugate, the anti-Pfaffian (*8*, *9*), with $g = 1/2$ (*8*, *9*, *18*); and the $U(1) \times SU_2(2)$ state (*7*), also with $g = 1/2$. Parameter pairs (e^*, g) representing these candidate states are marked in Fig. 5. Evidently the states with $e^* = 1/4$ and $g = 1/2$, both nonabelian, are most consistent with our tunneling data. The abelian state with $e^* = 1/4$ and $g = 3/8$ cannot be excluded; however, we note that weak tunneling of $e^* = 1/2$ quasi-particles appears inconsistent with the data.

Strong tunneling. In contrast to device 1, the dc bias data from device 2 show evidence for strong tunneling. Device 2 has a long, channel-like geometry, which should increase the number of tunneling sites and hence the tunneling strength. Diagonal resistance, R_D, as a function of dc bias at several temperatures is shown in Fig. 6A, which should be compared to those from the short QPC (Fig. 4A). At higher temperatures, the zero-bias peak height can be described by a power law in temperature with an exponent similar to that in the QPC (Fig. 6B and fig. S6B) and a FWHM that is proportional to temperature (Fig. 6C). At lower temperatures, the peak height deviates from a power law and saturates at the lowest temperatures at a value of resistance consistent with the resistance at $\nu = 7/3$ (the resistance is higher than $3/7\ h/e^2$ by the background $R^{\infty} - 0.4$), and the FWHM deviates from the linearity seen at higher temperature. We also observed that the peak develops a flat top and strong side dips (Fig. 6A) at the lowest temperature.

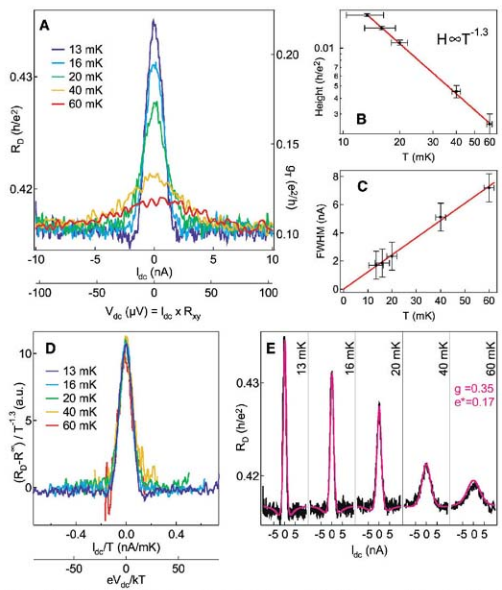

Fig. 4. (A) R_D (device 1) as a function of dc bias at fixed magnetic field ($B = 4.3$ T, middle of $\nu = 5/2$) and fixed gate voltage ($V_g = -2.5$ V) at several temperatures. The bias dependence of R_D is proportional to that of g_T (right axis) up to a constant. **(B)** Zero dc-bias peak height as a function of temperature. The red line is the best fit with a power law in which the exponent is −1.3. **(C)** The peak FWHM as a function of temperature. The red line is the best fit with a line going through zero. **(D)** Data collapsed onto a single curve using an exponent of −1.3. **(E)** Best fit of all the data in (A) with the weak tunneling formula (Eq. 2) returns $e^* = 0.17$ and $g = 0.35$.

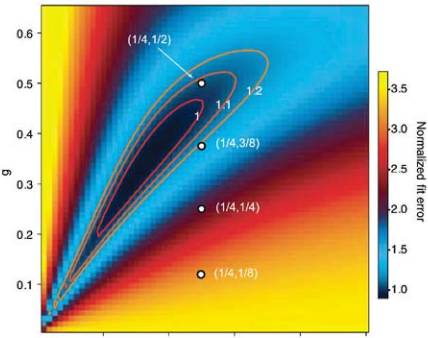

Fig. 5. Map of the fit quality. Normalized fit error is the residual from the least-squares fit, divided by the number of points and by the noise of the measurement. Also marked on the map are proposed theoretical pairs of (e^*, g).

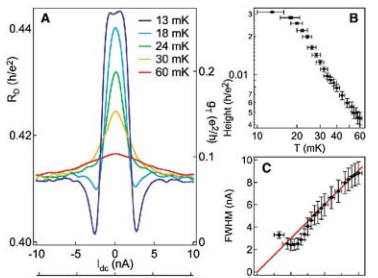

Fig. 6. **(A)** R_D (device 2) as a function of dc bias at fixed magnetic field (B = 4.31 T, middle of $\nu = 5/2$) and fixed gate voltage (V_g = −2.4 V) at several temperatures. At the lowest temperature, the peak develops a flat top at a value of resistance consistent with the resistance at $\nu = 7/3$. **(B)** Zero-bias peak height as a function of temperature. The peak height saturates at the lowest temperatures. **(C)** Peak width as a function of temperature. The red line is the best fit of the high-temperature data with a line going through zero. Below ~30 mK the peak width no longer follows this line.

We are not aware of quantitative predictions for the strong tunneling regime for $\nu = 5/2$. However, qualitative comparisons with strong tunneling theory (*39*) and experiment (*31*–*33*) at other FQH states ($\nu < 1$) can be made. For strong tunneling, the edge states associated with the topmost fractional state ($\nu = 5/2$ in the present case) are backscattered almost entirely so that the quasi-particle tunneling takes place along the QPC rather than across it (*19*, *39*). The flat-top peak shape and strong side dips (Fig. 6A), much stronger than that expected from weak tunneling (Eq. 2), are qualitatively consistent with previous strong-tunneling studies for $\nu < 1$ (*32*, *39*). The value of R_D at the peak is consistent with full backscattering of the $5/2$ edge and a $\nu = 7/3$ underlying edge state.

Outlook. Beyond enabling investigations in the fundamental physics toward a demonstration of nonabelian statistics, these experiments demonstrate a high degree of control of interedge tunneling of the $5/2$ edge state, a prerequisite for quasi-particle braiding operations needed for related schemes of topological quantum computing.

References and Notes

1. D. C. Tsui, H. L. Stormer, A. C. Gossard, *Phys. Rev. Lett.* **48**, 1559 (1982).
2. B. I. Halperin, *Phys. Rev. B* **25**, 2185 (1982).
3. X. G. Wen, *Phys. Rev. B* **44**, 5708 (1991).
4. R. Willett *et al.*, *Phys. Rev. Lett.* **59**, 1776 (1987).
5. F. D. M. Haldane, E. H. Rezayi, *Phys. Rev. Lett.* **60**, 956 (1988).
6. G. Moore, N. Read, *Nucl. Phys. B* **360**, 362 (1991).
7. X. G. Wen, *Phys. Rev. Lett.* **66**, 802 (1991).
8. M. Levin, B. I. Halperin, B. Rosenow, *Phys. Rev. Lett.* **99**, 236806 (2007).
9. S.-S. Lee, S. Ryu, C. Nayak, M. P. A. Fisher, *Phys. Rev. Lett.* **99**, 236807 (2007).
10. A. Y. Kitaev, *Ann. Phys.* **303**, 3 (2003).
11. S. Das Sarma, M. Freedman, C. Nayak, *Phys. Rev. Lett.* **94**, 166802 (2005).
12. C. Nayak, S. H. Simon, A. Stern, M. Freedman, S. Das Sarma, http://arxiv.org/abs/0707.1889 (2007).
13. R. H. Morf, *Phys. Rev. Lett.* **80**, 1505 (1998).
14. B. I. Halperin, *Helv. Phys. Acta* **56**, 75 (1983).
15. B. I. Halperin, P. A. Lee, N. Read, *Phys. Rev. B* **47**, 7312 (1993).
16. X. G. Wen, Q. Niu, *Phys. Rev. B* **41**, 9377 (1990).
17. X.-G. Wen, *Phys. Rev. Lett.* **70**, 355 (1993).
18. W. Bishara, C. Nayak, *Phys. Rev. B* **77**, 165302 (2008).
19. P. Fendley, M. P. A. Fisher, C. Nayak, *Phys. Rev. Lett.* **97**, 036801 (2006).
20. M. Milovanović, N. Read, *Phys. Rev. B* **53**, 13559 (1996).
21. X.-G. Wen, *Adv. Phys.* **44**, 405 (1995).
22. E. Fradkin, C. Nayak, A. Tsvelik, F. Wilczek, *Nucl. Phys. B* **516**, 704 (1998).
23. P. Bonderson, A. Kitaev, K. Shtengel, *Phys. Rev. Lett.* **96**, 016803 (2006).
24. A. Stern, B. I. Halperin, *Phys. Rev. Lett.* **96**, 016802 (2006).
25. C.-Y. Hou, C. Chamon, *Phys. Rev. Lett.* **97**, 146802 (2006).
26. D. E. Feldman, A. Kitaev, *Phys. Rev. Lett.* **97**, 186803 (2006).
27. R. de Picciotto *et al.*, *Nature* **389**, 162 (1997).
28. L. Saminadayar, D. C. Glattli, Y. Jin, B. Etienne, *Phys. Rev. Lett.* **79**, 2526 (1997).
29. V. J. Goldman, B. Su, *Science* **267**, 1010 (1995).
30. M. Dolev, M. Heiblum, V. Umansky, A. Stern, D. Mahalu, *Nature* **452**, 829 (2008).
31. S. Roddaro *et al.*, *Phys. Rev. Lett.* **90**, 046805 (2003).
32. S. Roddaro, V. Pellegrini, F. Beltram, G. Biasiol, L. Sorba, *Phys. Rev. Lett.* **93**, 046801 (2004).
33. S. Roddaro, V. Pellegrini, F. Beltram, L. N. Pfeiffer, K. W. West, *Phys. Rev. Lett.* **95**, 156804 (2005).
34. J. B. Miller *et al.*, *Nat. Phys.* **3**, 561 (2007).
35. C. P. Milliken, C. P. Umbach, R. A. Webb, *Solid State Commun.* **97**, 309 (1996).
36. Materials and methods are available on *Science* Online.
37. C. W. J. Beenakker, H. van Houten, *Solid State Phys.* **44**, 1 (1991).
38. J. S. Xia *et al.*, *Phys. Rev. Lett.* **93**, 176809 (2004).
39. P. Fendley, A. W. W. Ludwig, H. Saleur, *Phys. Rev. B* **52**, 8934 (1995).

40. We acknowledge helpful discussions with W. Bishara, C. Chamon, C. Dillard, P. Fendley, M. Fisher, B. Halperin, E. Levenson-Falk, D. McClure, C. Nayak, B. J. Overbosch, B. Rosenow, A. Stern, X.-G. Wen, and Y. Zhang and experimental help from S. Amasha and A. Klust. This work was supported in part by Army Research Office (W911NF-05-1-0062), the Nanoscale Science and Engineering Center program of NSF (PHY-0117795), NSF (DMR-0701386), the Center for Materials Science and Engineering program of NSF (DMR-0213282) at MIT and by the Microsoft Corporation Project Q and the Center for Nanoscale Systems at Harvard University.

Supporting Online Material

www.sciencemag.org/cgi/content/full/1157560/DC1
Supporting Text
Figs. S1 to S6
References

10 March 2008; accepted 11 April 2008
Published online 17 April 2008;
10.1126/science.1157560
Include this information when citing this paper.

Design Logic of a Cannabinoid Receptor Signaling Network That Triggers Neurite Outgrowth

Kenneth D. Bromberg, Avi Ma'ayan, Susana R. Neves, Ravi Iyengar*

Cannabinoid receptor 1 (CB1R) regulates neuronal differentiation. To understand the logic underlying decision-making in the signaling network controlling CB1R-induced neurite outgrowth, we profiled the activation of several hundred transcription factors after cell stimulation. We assembled an in silico signaling network by connecting CB1R to 23 activated transcription factors. Statistical analyses of this network predicted a role for the breast cancer 1 protein BRCA1 in neuronal differentiation and a new pathway from CB1R through phosphoinositol 3-kinase to the transcription factor paired box 6 (PAX6). Both predictions were experimentally confirmed. Results of transcription factor activation experiments that used pharmacological inhibitors of kinases revealed a network organization of partial OR gates regulating kinases stacked above AND gates that control transcription factors, which together allow for distributed decision-making in CB1R-induced neurite outgrowth.

Signaling through the cannabinoid receptor 1 (CB1R), which couples to the heterotrimeric guanine nucleotide–binding proteins (G proteins) G_i and G_o, regulates many physiological processes. In cultured mouse Neuro2A cells, CB1R stimulation induces neurite outgrowth through a signaling pathway from $G\alpha_o$ that activates the protein kinase c-Src and the transcription factor signal transducer and activator of transcription 3 (Stat3) (*1*, *2*). CB1R signaling also has a key role during central nervous system development and in the adult brain (*3*, *4*). Furthermore, CB1R has been shown to modulate several neurological disorders (*5*). However, the organization of the CB1R signaling network involved in cellular state-change decisions has not been well defined. Delineation of the organization of signaling networks is useful in identifying emergent decision-making capabilities (*6*). To do so, we started with delineating individual pathways (*1*, *2*). However, simply verifying the presence and function of individual pathways will not advance our knowledge of the design of complex cellular regulatory networks and their decision-making capabilities. A key challenge in systems biology is to identify, experimentally verify, and understand the organizations of complex regulatory systems.

To broadly define the cellular network regulating CB1R-induced neurite outgrowth, we integrated transcription factor activity profiling, network biology, and cell biology. First, the CB1R-triggered activation of multiple transcription factors was profiled during neurite outgrowth. We then developed an in silico network in which the activated transcription factors were linked to known interactors and pathways that regulate them to identify new components and pathways involved in neuronal differentiation. Predictions were experimentally tested in cultured and primary neurons. We then used selective pharmacological inhibitors in transcription factor activation experiments to determine the hierarchy between three key kinases and transcription factors. These experiments allowed for construction of a map where partial OR gates at the level of G proteins regulating kinases are stacked on top of AND gates at the level of kinases regulating transcription factors, allowing for a distributed decision-making capability within the network.

CB1R-regulated transcription factors. We assayed transcription factor activation in response to the CB1R agonist HU-210 in Neuro2A cells by using a commercial array (*7*). Spotted on this array are 345 oligonucleotide transcription factor–binding sites (table S1), enabling the activation of a large number of transcription factors to be assayed simultaneously [see (*7*) for array details]. Studies have indicated that CB1R activation of $G\alpha_o$ can stimulate Stat3 (*2*), so we

Department of Pharmacology and Systems Therapeutics, Mount Sinai School of Medicine, New York, NY 10029, USA.

*To whom correspondence should be addressed. E-mail: ravi.iyengar@mssm.edu

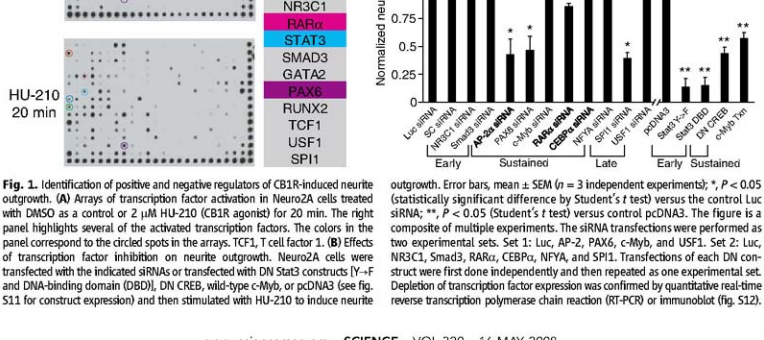

Fig. 1. Identification of positive and negative regulators of CB1R-induced neurite outgrowth. **(A)** Arrays of transcription factor activation in Neuro2A cells treated with DMSO as a control or 2 μM HU-210 (CB1R agonist) for 20 min. The right panel highlights several of the activated transcription factors. The colors in the panel correspond to the circled spots in the arrays. TCF1, T cell factor 1. **(B)** Effects of transcription factor inhibition on neurite outgrowth. Neuro2A cells were transfected with the indicated siRNAs or transfected with DN Stat3 constructs [Y→F and DNA-binding domain (DBD)], DN CREB, wild-type c-Myb, or pcDNA3 (see fig. S11 for construct expression) and then stimulated with HU-210 to induce neurite outgrowth. Error bars, mean ± SEM ($n = 3$ independent experiments); *, $P < 0.05$ (statistically significant difference by Student's t test) versus the control Luc siRNA; **, $P < 0.05$ (Student's t test) versus control pcDNA3. The figure is a composite of multiple experiments. The siRNA transfections were performed as two experimental sets. Set 1: Luc, AP-2, PAX6, c-Myb, and USF1. Set 2: Luc, NR3C1, Smad3, RARα, CEBPα, NFYA, and SPI1. Transfections of each DN construct were first done independently and then repeated as one experimental set. Depletion of transcription factor expression was confirmed by quantitative real-time reverse transcription polymerase chain reaction (RT-PCR) or immunoblot (fig. S12).

expected to observe activation of Stat3 on the array. Mouse Neuro2A cells were treated with HU-210 (2 μM) for 20, 60, 120, and 360 min to assess transcription factor activation. Ongoing transcription was required for at least 360 min to induce neurite outgrowth in response to CB1R signaling (fig. S1). Nuclear extracts were obtained and processed for hybridization to the array. The Entrez Gene names of all the transcription factors activated over the 360-min time course are displayed in table S2. All of the transcription factor–activation arrays described in table S2 are shown in fig. S2A, and several transcription factors that were activated at 20 min are highlighted in Fig. 1A. Activated transcription factors fell into three main categories: those that were activated early and transiently, such as Stat3, Smad3, and Smad4; those that displayed sustained activation, including c-Myb and paired box 6 (PAX6); and those that were activated at later times, such as forkhead box I1 (FOXI1) and upstream transcription factor 1 (USF1). In all, 33 transcription factors were activated over the 6-hour time course of CB1R stimulation. Because the activations of homeobox D8 (HOXD8), HOXD9, and HOXD10 and Smad3 and Smad4 were each represented as single spots on the array, they were grouped together in table S2. For the computational analysis (see below), they were used individually. Stat3 was activated at 20 and 60 min, and this activation was confirmed by gel shift analysis (fig. S3A). cAMP response element–binding protein (CREB), a transcription factor known to be involved in neurite outgrowth (*8*), was also activated, and this result was verified when CREB was phosphorylated on Ser[133] in

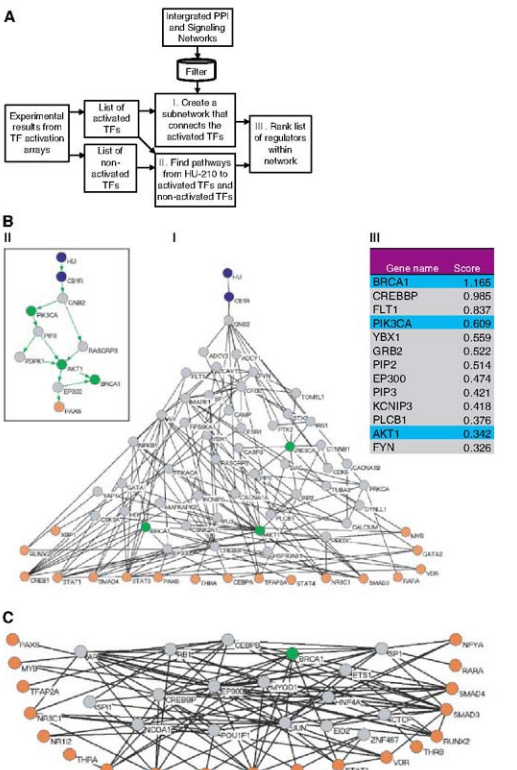

Fig. 2. Construction of networks and identification of BRCA1 and a PI3K-AKT-PAX6 pathway as regulators of CB1R-induced neurite outgrowth. **(A)** Eight mammalian protein-protein interaction databases and one signaling network were consolidated into a single network made of 67,379 human protein-protein and protein-ligand interactions (I). This network was filtered by removing interactions from research articles that reported more than three interactions. The lists of activated and nonactivated transcription factors (TFs) at 20 min were used as input nodes to find direct and neighboring interactions and to identify paths from the CB1R receptor to the transcription factors (II), enabling us to identify and rank regulators within the network (III). **(B)** A subnetwork created by finding the shortest paths of a maximum of seven steps from the HU-210 node (HU) to the 23 activated transcription factors (orange nodes) at 20 min. (I) Paths were found for 17 out of the 23 factors. BRCA1, PI3K, and AKT1 are highlighted (green nodes). HU and CB1R nodes are highlighted in blue. (II) Pathway connecting CB1R to PAX6 through PI3K and AKT1 (edited manually after literature review). (III) Table showing the ranking of components in pathways detected in a control subnetwork (fig. S4 and table S3) versus the activated subnetwork using the ranking method described in the supporting online material (SOM) (*7*). I, II, and III in (B) correspond to I, II, and III in (A), respectively. CREBBP, CREB-binding protein; PIK3CA, PIK3 catalytic, alpha; PIP2, phosphatidylinositol 4,5-bisphosphate; PIP3, phosphatidylinositol 3,4,5-trisphosphate. **(C)** Subnetwork created by finding the shortest paths of a maximum of two steps between the 23 activated transcription factors. Nineteen of the factors were connected using this method (orange nodes). A binomial proportions test was used to prune out most of the less important intermediates. BRCA1 is highlighted in green.

response to HU-210 (fig. S3B). It is likely that CREB is activated through βγ subunit of G_o (Gβγ)–mediated stimulation of p42 and p44 mitogen-activated protein kinase (MAPK) (*9*). MAPK was also activated in response to CB1R stimulation, and the treatment of cells with the upstream MAPK kinase (MEK)–1,2 kinase inhibitor PD 98059 (PD) attenuated phosphorylation of both MAPK and CREB (fig. S3E). Transfection of a dominant-negative (DN) CREB construct inhibited cannabinoid-induced neurite outgrowth, albeit to a lesser extent than did DN Stat3 (Fig. 1B). Retinoic acid receptor (RAR), another well-known regulator of neurite outgrowth (*10*), was also activated on the array, and this finding was confirmed by gel shift analysis (fig. S3C). We also examined several transcription factors, including c-Myb, activating protein 2α (AP-2α), and PAX6, that have not been shown to have a role in neurite outgrowth. Gel shift analysis confirmed the activation c-Myb (fig. S3D). These results validate several of the transcription factors that were activated on the arrays.

To test whether the activated transcription factors might regulate the induction of neurite outgrowth, we assessed 10 of the activated factors, representing all three categories (early, sustained, and late activation) in addition to CREB and Stat3. Depletion of AP-2α, PAX6, and spleen focus forming virus proviral integration oncogene 1 (SPI1) with RNA interference (RNAi) inhibited cannabinoid-induced neurite outgrowth by ~60%, and RNAi of RARα was also slightly inhibitory (Fig. 1B). In contrast, RNAi of Smad3, c-Myb, and nuclear transcription factor–Y α (NFYA) led to an enhancement of HU-210–stimulated neurite outgrowth. Ectopic expression of c-Myb reduced neurite outgrowth by ~30%. Off-target gene-silencing effects of RNAi seemed unlikely because CB1R-induced neurite outgrowth was similar in cells treated with luciferase (Luc) small interfering RNA (siRNA) and a separate scrambled (SC) siRNA. These results suggest that transcription factor profiling is able to detect both positive and negative regulators of neurite outgrowth.

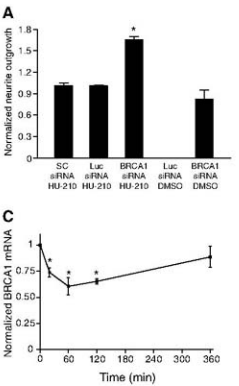

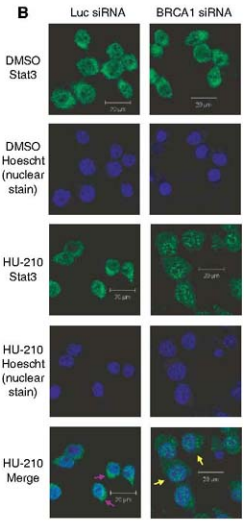

Fig. 3. Regulation of CB1R-induced neurite outgrowth by BRCA1. **(A)** Effect of BRCA1 siRNA on cannabinoid-induced neurite outgrowth. Neuro2A cells were transfected with Luc siRNA or BRCA1 siRNA and stimulated with 2 μM HU-210 to induce neurite outgrowth or with DMSO as a control. Amounts of neurite outgrowth in cells exposed to Luc siRNA and HU-210 were normalized to 1, and baseline amounts of neurite outgrowth were normalized to 0 (*7*). Treatment of cells with an SC siRNA (SC siRNA HU) resulted in similar amounts of cannabinoid-induced neurite outgrowth as Luc siRNA (Luc siRNA HU). Error bars, mean ± SEM (n = 3 independent experiments), *, $P < 0.01$ (student's t test) versus Luc siRNA HU-210 control. **(B)** Regulation of Stat3 localization. Neuro2A cells were transfected with Luc siRNA or BRCA1 siRNA and treated with DMSO or HU-210 for 20 min. Cells were fixed, permeabilized, and stained with Stat3 antibodies. Purple and yellow arrows indicate cytosolic and nuclear Stat3 localization, respectively. Scale bars indicate distance in micrometers. Nuclei were visualized with Hoescht stain. **(C)** Decreased BRCA1 expression in response to CB1R stimulation. Neuro2A cells were stimulated with HU-210 and RNA was isolated at the indicated times. Quantitative real-time RT-PCR was performed as described in the SOM (*7*). Error bars, mean ± SEM (n = 4 independent experiments); *, $P < 0.01$ (Student's t test) versus 0 min control.

In silico network construction and predicting new components and pathways. Although the transcription factor arrays indicate that many transcription factors are activated during neurite outgrowth, they do not provide information about the cell signaling pathways and components that lead to their activation. We identified the upstream signaling pathways and components regulating the activated transcription factors by constructing a network in silico. For this we used available protein-protein interaction databases, graph-theory analysis, and statistical tests. We consolidated eight existing mammalian protein-protein interactions networks, the Biomolecular Interaction Network Database (BIND) (*11*), the Human Protein Reference Database (HPRD) (*12*), the Molecular Interaction database (MINT) (*13*), the Database of Interacting Proteins (DIP) (*14*), IntAct (*15*), BioGRID (*16*), Reactome (*17*), and the Protein-Protein Interaction Database (PPID) (*18*), with a neuronal signaling network we developed (*19*). To remove potentially low-confidence interactions, such as interactions reported from yeast two-hybrid screens, we filtered the nine consolidated data sets by removing all articles reporting more than three interactions. This method reduced the number of interactions in the consolidated database from 67,379 to 15,494 (Fig. 2A). Applying a shortest-path analysis, we first automatically found undirected paths of a limited path length (two steps, all direct- and second-neighbor interactions) between all the transcription factors, knowing the consensus-binding sequences on the transcription factor–activation array. Combining all the paths from this search resulted in a subnetwork made of 444 nodes and 1873 interactions from 1843 unique references. We merged this subnetwork with a large-scale curated signaling network we developed from the neuroscience literature (*19*). Again applying shortest-path analysis, we searched for directed paths with a limited threshold path length (seven steps) from the CB1R agonist HU-210 to the transcription factors associated with the consensus sequences on the array. We found paths from HU-210 to 104 transcription factors, including 17 of the 23 transcription factors that were activated within 20 min in table S2 (Fig. 2B) and 87 transcription factors that were not activated (fig. S4). Counting and comparing the number of times that components appeared in pathways to activated factors or nonactivated factors enabled us to identify intermediate components in pathways predicted to participate in the regulation of the activated transcription factors (Fig. 2B and algorithm S1). BRCA1, the breast cancer susceptibility protein (*20*), was ranked highest as the most specific regulator of the

activated transcription factors (Fisher exact test, $P = 0.05$; table S3, using equation S1; and Fig. 2B). One of the unanticipated pathways that emerged from using this method connected CB1R stimulation to PAX6 through phosphoinositol 3-kinase (PI3K) and the protein kinase Akt (table S3 and Fig. 2B). We applied a similar analysis by building a subnetwork that attempted to connect only the activated transcription factors (algorithm S2). Starting with a list of the 23 activated factors, we searched for paths of three links in length using the consolidated mammalian protein-protein interactions networks. This subnetwork contained 79 nodes and 328 links, significantly more links than those in subnetworks created from 20 randomly generated seed lists of the same size, created from factors that were not activated on the transcription factor–activation arrays (table S4; z test, $P < 0.001$). The clustering coefficients and characteristic path lengths (*21*) were similar (0.18 versus 0.21 ± 0.09 and 2.37 versus 2.46 ± 0.39) in the subnetwork of activated factors and the control subnetworks. We used a binomial proportions test to remove components that were found in the activated factors subnetwork but not specifically interacting with the activated factors,

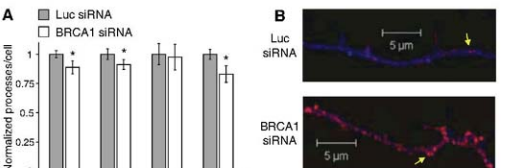

Fig. 4. Regulation of neuronal differentiation by BRCA1. **(A)** BRCA1 regulates neurite outgrowth in rat primary hippocampal neuron cultures. Hippocampal cultures were transfected with Luc siRNA or BRCA1 siRNA after plating and adhesion. Cells were fixed 30 hours after transfection. The mean number of processes per cell in each field was analyzed morphometrically. The mean number of processes for neurons treated with Luc siRNA was normalized to 1. Error bars, mean ± SEM ($n = 10$ wells of four fields per well for each experiment set); *, $P < 0.05$ (Student's t test) versus Luc siRNA control. **(B)** BRCA1 regulates synaptic density in hippocampal neuron cultures. Neurons were transfected with Luc siRNA or BRCA1 siRNA using NeuroPORTER after 3 days in cultures. Four days later, cells were fixed and stained with synaptophysin (red) and β-tubulin (blue) antibodies. Yellow arrows denote synaptophysin puncta. Quantification is shown in fig. S7B.

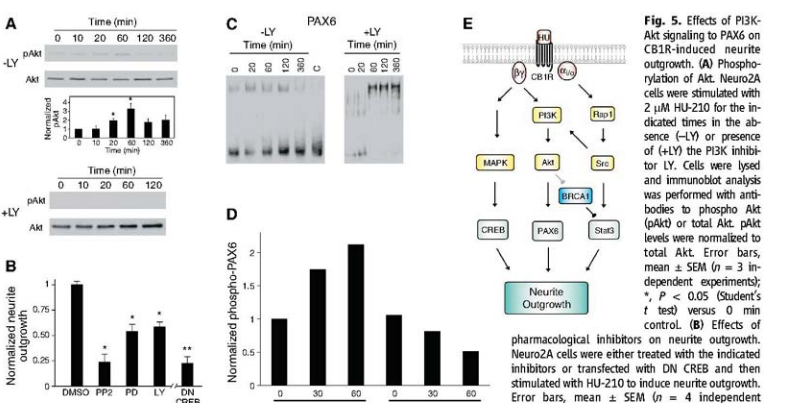

Fig. 5. Effects of PI3K-Akt signaling to PAX6 on CB1R-induced neurite outgrowth. **(A)** Phosphorylation of Akt. Neuro2A cells were stimulated with 2 μM HU-210 for the indicated times in the absence (–LY) or presence of (+LY) the PI3K inhibitor LY. Cells were lysed and immunoblot analysis was performed with antibodies to phospho Akt (pAkt) or total Akt. pAkt levels were normalized to total Akt. Error bars, mean ± SEM ($n = 3$ independent experiments); *, $P < 0.05$ (Student's t test) versus 0 min control. **(B)** Effects of pharmacological inhibitors on neurite outgrowth. Neuro2A cells were either treated with the indicated inhibitors or transfected with DN CREB and then stimulated with HU-210 to induce neurite outgrowth. Error bars, mean ± SEM ($n = 4$ independent experiments for PD, $n = 3$ for all others); *, $P < 0.02$ (Student's t test) versus DMSO control; **, $P < 0.01$ (Student's t test) versus pcDNA3 control. The figure is a composite of multiple experiments. DN CREB + LY was performed with the other DNA transfections in Fig. 1B. **(C)** Gel shift assay of PAX6 binding. Neuro2A cells were stimulated with 2 μM HU-210 for the indicated times in the absence (–LY) or presence (+LY) of LY. Nuclear extracts were prepared and gel shift assays were performed with oligonucleotides containing consensus-binding sites for PAX6. **(D)** PAX6 phosphorylation in rat primary hippocampal neuron cultures. Hippocampal cultures were stimulated with 1 μM HU-210 for the indicated times in the absence (–LY) or presence (+LY) of 10 μM LY 294002. Cells were lysed, and immunoprecipitations were performed with rabbit antibodies to PAX6 or rabbit immunoglobin G as a control. Immunoblot analysis was performed with mouse antibodies directed against phospho-Thr. Phospho-Thr levels were normalized to PAX6 after stripping and re-probing the blots with PAX6 antibodies. Values were averaged from two independent experiments. **(E)** Simple schematic of signal flow through Src, MAPK, and PI3K during neurite outgrowth. CB1R stimulation by HU-210 (HU) activates the alpha subunits of G_i and G_o ($\alpha_{i/o}$) and leads to activation of Stat3 through the kinase Src. BRCA1 is depicted in blue. The putative interaction between BRCA1 and Akt is shaded gray (*38*).

because these components interact with many proteins. Thus, their presence in the activated factors subnetwork might be by chance (*22*). Again, BRCA1 was identified as a specific interactor with the activated transcription factors (binomial test, z score 58.9; table S5 and Fig. 2C). We experimentally tested whether BRCA1 regulated neuronal differentiation and for the existence of a CB1R-to-PAX6 pathway.

Regulation of neuronal differentiation by BRCA1. Although the molecular mechanisms by which BRCA1 functions have remained enigmatic, BRCA1 is thought to participate in the response to DNA damage, centrosome amplification regulation, and mitotic spindle assembly (*20*, *23*, *24*). BRCA1 may also function in neural development, because mice with homozygous deletion of BRCA1 die as embryos because of neural defects (*25*). However, no cell-biological function for BRCA1 during neurogenesis has been reported. Several clinical case studies have linked BRCA1 mutant alleles found in breast cancer to epilepsy (*26*, *27*). Thus, BRCA1 may influence the pathology of neurological conditions.

To examine whether BRCA1 regulates neurite outgrowth, we inhibited BRCA1 expression by use of RNAi in Neuro2A cells (fig. S12D). Ablation of BRCA1 expression enhanced cannabinoid-induced neurite outgrowth by 70% (Fig. 3A). In addition, 80% of the neurite outgrowth normally observed in response to cannabinoid signaling was seen upon loss of BRCA1 expression in the absence of HU-210. This result raises the possibility that BRCA1 may also affect neuronal differentiation in the absence of cannabinoid signaling. Indeed, several of the transcription factors that interact with BRCA1 (*28*–*30*) and were activated through CB1R stimulation participate in neuronal differentiation in multiple contexts (*8*, *10*, *31*).

Network analysis indicated that BRCA1 interacts with several of the transcription factors, including Stat1, Stat3, and Smad3, within 20 min of cannabinoid treatment. We tested whether BRCA1 regulated Stat3 and Smad3 during CB1R stimulation. BRCA1 siRNA treatment resulted in an increase in the nuclear localization of Stat3 in response to HU-210 at 20, 60, and 120 min (Fig. 3B and fig. S5B) and in nuclear localization of Smad3 at 60 and 120 min (fig. S6). Stat3 also accumulated in the nucleus within 60 to 120 min after HU-210 treatment of Luc siRNA–treated cells (fig. S5A), but to a lesser extent than in cells treated with BRCA1 siRNA (fig. S5B). These results indicate that BRCA1 influences cannabinoid-regulated nuclear localization of Stat3 and Smad3. Consistent with these findings, stimulation of Neuro2A cells with HU-210 caused an ~40% decrease in amounts of BRCA1 mRNA by 60 min that was sustained until 120 min (Fig. 3C), which correlates with the time that Stat3 accumulates in the nucleus after HU-210 stimulation (fig. S5A). By 6 hours after treatment of cells with HU-210, amounts of BRCA1 mRNA were similar to those in unstimulated cells.

Because the loss of BRCA1 expression induced neurite outgrowth in the absence of CB1R stimulation, we investigated whether BRCA1 played a general role in neuronal differentiation. In primary cultures of rat hippocampal neurons, the neurons initially form neurites that further develop into a single axon and multiple dendrites (*32*). To assess the role of BRCA1 in differentiation, primary hippocampal cultures were transfected with BRCA1 siRNA after the cells had adhered to the culture plates (fig. S12E). After 30 hours, cells were fixed and stained with β-tubulin to mark neurites, and neurite outgrowth was analyzed morphometrically. In three of four experiments, RNAi of BRCA1 appeared to decrease the number of processes per cell by 10 to 15% (Fig. 4A and fig. S7A), suggesting BRCA1 is a positive general regulator of neuronal dif-

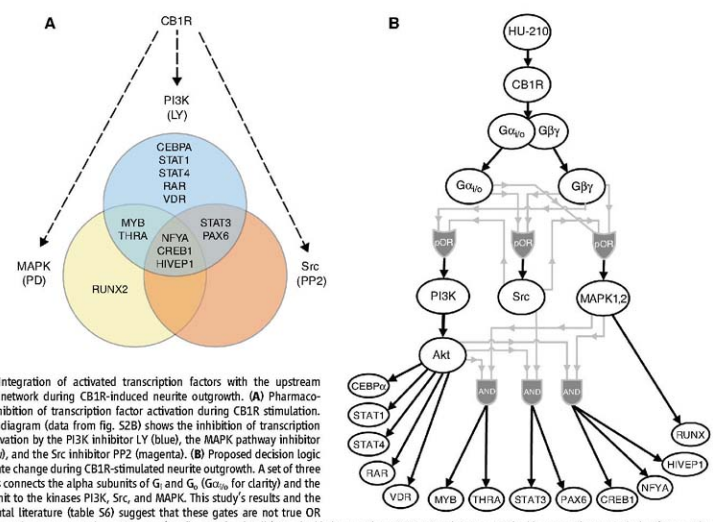

Fig. 6. Integration of activated transcription factors with the upstream signaling network during CB1R-induced neurite outgrowth. **(A)** Pharmacological inhibition of transcription factor activation during CB1R stimulation. The Venn diagram (data from fig. S2B) shows the inhibition of transcription factor activation by the PI3K inhibitor LY (blue), the MAPK pathway inhibitor PD (yellow), and the Src inhibitor PP2 (magenta). **(B)** Proposed decision logic for cell-state change during CB1R-stimulated neurite outgrowth. A set of three pOR gates connects the alpha subunits of G_i and G_o ($G\alpha_{i/o}$ for clarity) and the Gβγ subunit to the kinases PI3K, Src, and MAPK. This study's results and the experimental literature (table S6) suggest that these gates are not true OR gates and are thus represented as pOR gates (see fig. S13 for details). Stacked below are three AND gates that connect the kinases to the transcription factors. The components and connections are in black. The gray arrows and gate symbols are in gray to denote information flow and the abstract nature of the pOR and AND gates.

ferentiation. Because several case studies have linked BRCA1 mutations to epileptic seizures (*26*, *27*), we also examined whether BRCA1 regulated synapse formation in primary hippocampal cultures. Synapses are proposed to form between neurons through protrusions by dendritic filopodia, which extend toward axon terminals and form stable contacts during differentiation (*33*). Rat primary hippocampal cultures were transfected with Luc siRNA or rat BRCA1 siRNA on the third day that cells were cultured (fig. S12F). On day 7, cultures were fixed and stained with antibodies to the synaptic vesicle marker synaptophysin and β-tubulin to mark dendrites (Fig. 4B and fig. S7B). The loss of BRCA1 expression in primary cultures resulted in an increase in the punctuate synaptophysin staining in hippocampal cultures, indicating that BRCA1 may function in regulating locations where synapses may be forming during differentiation of hippocampal neurons. This was not due to an effect of BRCA1 on cell viability, as the number of live and dead cells was similar in neurons treated with Luc or BRCA1 siRNA (fig. S8). Overall, these findings indicate that BRCA1 is a regulator of cannabinoid-mediated and general neuronal differentiation and raise the possibility that loss or dysregulation of BRCA1 may also contribute to abnormal neuronal morphology and neurological disorders.

PI3K signaling to PAX6 during CB1R-stimulated neuronal differentiation. Network analysis also predicted that a CB1R-PI3K-Akt pathway regulates neurite outgrowth and linked this pathway to PAX6. To assess this possibility, we first examined whether the PI3K pathway was activated during neurite outgrowth in Neuro2A cells. Stimulation of CB1R resulted in Akt activation, as demonstrated by phosphorylation of Ser^{473}, which is required for activation of Akt (Fig. 5A) (*34*). This activation was blocked by the selective PI3K inhibitor LY 294002 (LY), suggesting that Akt activation was occurring through PI3K. Treatment of Neuro2A cells with LY also inhibited neurite outgrowth by ~50%, similar to the effects of the MAPK pathway inhibitor PD and DN CREB (Fig. 1B and Fig. 5B). Blockade of both MAPK and PI3K pathways led to further inhibition of neurite outgrowth (Fig. 5B). This inhibition is similar to that observed with DN Stat3 (Fig. 1B) or the upstream kinase Src inhibitor 4-amino-5-(4-chlorophenyl)-7-(t-butyl)pyrazolo[3,4-d]pyrimidine (PP2) (Fig. 5B). These results suggest that PI3K regulates cannabinoid-induced neurite outgrowth and that PI3K and MAPK may act independently to induce neurite outgrowth.

We assessed with gel shift analysis whether PI3K signaling activated PAX6 in Neuro2A cells. Treatment of Neuro2A cells with LY before HU-210 blocked the shift of a PAX6 consensus site after 20 min of stimulation but not at later time points (Fig. 5C), suggesting that PI3K acts in the early activation of PAX6 during cannabinoid-induced neurite outgrowth. The role of PAX6 in cannabinoid signaling in primary hippocampal neurons was also examined. PAX6 is activated by phosphorylation on Ser and Thr residues (*35*, *36*). To assess whether PI3K is involved in PAX6 activation in primary hippocampal cultures, we cultured neurons for 3 days, treated them with LY or dimethyl sulfoxide (DMSO), and then stimulated them with HU-210 (1 μM) for 30 or 60 min. PAX6 was immunoprecipitated and then immunoblotted with a phosphothreonine antibody to examine PAX6 phosphorylation. Stimulation of CB1R with HU-210 led to the phosphorylation of PAX6, and blockade of PI3K inhibited this effect (Fig. 5D and fig. S9), indicating that PI3K may influence PAX6 activation in response to CB1R signaling.

Signal processing for neuronal differentiation. Many of the transcription factors that we identified by the profiling approaches are involved in neurite outgrowth. This, taken together with the validation of the network predictions that BRCA1 is an important regulator and that PI3K-to-PAX6 is a signaling pathway regulating neuronal differentiation, suggests the validity of the network that we are identifying by using this combination of experiments and bioinformatics. However, these experiments do not shed light on the design logic of this network. We sought to determine the relationship between the upstream kinases and downstream transcription factors as an approach to understand how the different logic gates might be organized within the network. We used the transcription factor activation arrays to assess how Src, MAPK, and PI3K signals influence the 23 transcription factors that are activated after 20 min of stimulation of CB1R (table S2) in the presence of their pharmacological inhibitors LY, PD, and PP2, respectively (fig. S2). Each inhibitor affected the activation of a group of transcription factors and activation of some transcription factors was inhibited by several inhibitors (Fig. 6A). As expected, PD inhibited CREB activation and PP2 inhibited Stat3. Both LY and PP2 inhibited PAX6 activation (Fig. 6A), suggesting that in addition to PI3K, Src signaling may also influence PAX6 activation. Blockade of either PI3K or Src inhibited Akt activation (fig. S10). However, other molecules in addition to Src may signal to Akt because the inhibition of Src did not completely abrogate the activation of Akt. The inhibition of MAPK enhanced Akt activation, suggesting that the PI3K pathway may compensate for the loss of MAPK signaling during neurite outgrowth. A simplified schematic of the signal flow during cannabinoid-induced neurite outgrowth is shown in Fig. 5E.

Network organization and cell state–change decisions. This study provides the framework to explore the mechanistic details of individual interactions during neuronal differentiation. These relationships are likely to be cell type–specific as highlighted by BRCA1 inhibition of neurite outgrowth in Neuro2A cells and stimulation of outgrowth in hippocampal neurons. This study has enabled us to develop a systems-level logic diagram for cell state–change decisions in Neuro2A cells (Fig. 6B). For this we used the results of this study and the experimental literature on the G_i and G_o signaling pathways (fig. S13 and table S6). The picture that emerges has a set of partial OR (pOR) gates that connect the $G\alpha_i$, $G\alpha_o$, and Gβγ subunits to the kinases PI3K, Src, and MAPK. Src itself may stimulate both PI3K and MAPK. This redundancy of pathways indicates that the upstream region of the network is abundant in positive feed-forward motifs that function as pOR gates, a topology reminiscent of what we have observed in our literature-based signaling network of the hippocampal neuron (*19*). The three pOR gates are stacked on top of three AND gates that connect the kinases to many transcription factors. Akt also appears to participate in a single-input module–type motif (*37*) connecting to a number of transcription factors, but the role of most of these transcription factors, except RAR_γ in neurite outgrowth in Neuro2A cells is not clear. In contrast, AND gates connect kinases to c-Myb, Stat3, PAX6, NFYA, and CREB, all of which function in CB1R neurite outgrowth as shown by functional ablation experiments. This organization of pOR gates stacked on top of AND gates suggests a distributed decision-making process. This provides a balance between redundancy of response pathways at the upper level and a balanced funneling of signals at the lower level, in which the AND gates can serve as filters. Such filtering would ensure that only signals of sufficient intensity and duration turn on the transcription factors to trigger state change. Thus, this overall organization allows for reliable state-change responses to appropriate signals.

References and Notes

1. J. D. Jordan *et al.*, *J. Biol. Chem.* **280**, 11413 (2005).
2. J. C. He *et al.*, *J. Biol. Chem.* **280**, 33426 (2005).
3. T. Harkany *et al.*, *Trends Pharmacol. Sci.* **28**, 83 (2007).
4. V. Chevaleyre, K. A. Takahashi, P. E. Castillo, *Annu. Rev. Neurosci.* **29**, 37 (2006).
5. D. Centonze, A. Finazzi-Agro, G. Bernardi, M. Maccarrone, *Trends Pharmacol. Sci.* **28**, 180 (2007).
6. U. S. Bhalla, P. T. Ram, R. Iyengar, *Science* **297**, 1018 (2002).
7. Materials and methods are available as supporting material on *Science* Online.
8. R. A. Segal, *Annu. Rev. Neurosci.* **26**, 299 (2003).
9. J. S. Gutkind, *Sci. STKE* **2000**, re1 (2000).
10. M. Clagett-Dame, E. M. McNeill, P. D. Mulley, *J. Neurobiol.* **66**, 739 (2006).
11. G. D. Bader, D. Betel, C. W. V. Hogue, *Nucleic Acids Res.* **31**, 248 (2003).
12. G. R. Mishra *et al.*, *Nucleic Acids Res.* **34**, D411 (2006).
13. A. Chatr-aryamontri *et al.*, *Nucleic Acids Res.* **35**, D572 (2007).
14. I. Xenarios *et al.*, *Nucleic Acids Res.* **29**, 239 (2001).
15. S. Kerrien *et al.*, *Nucleic Acids Res.* **35**, D561 (2007).
16. C. Stark *et al.*, *Nucleic Acids Res.* **34**, D535 (2006).
17. G. Joshi-Tope *et al.*, *Nucleic Acids Res.* **33**, D428 (2005).
18. H. Hwei, M. A. Ward, J. S. Choudhary, W. P. Blackstock, S. G. Grant, *Nat. Neurosci.* **3**, 661 (2000).
19. A. Ma'ayan *et al.*, *Science* **309**, 1078 (2005).
20. A. R. Venkitaraman, *Cell* **108**, 171 (2002).
21. D. J. Watts, S. H. Strogatz, *Nature* **393**, 440 (1998).
22. S. I. Berger, J. M. Posner, A. Ma'ayan, *BMC Bioinform.* **8**, 372 (2007).

23. K. Gudmundsdottir, A. Ashworth, *Oncogene* **25**, 5864 (2006).
24. V. Joukov *et al.*, *Cell* **127**, 539 (2006).
25. L. C. Gowen, B. L. Johnson, A. M. Latour, K. K. Sulik, B. H. Koller, *Nat. Genet.* **12**, 191 (1996).
26. D. M. Eccles, S. Barker, D. T. Pitz, C. Kennedy, *J. Med. Genet.* **40**, 24e (2003).
27. D. Eccles, D. Bunyan, S. Barker, B. Castle, *J. Med. Genet.* **42**, e42 (2005).
28. Y. Houvras *et al.*, *J. Biol. Chem.* **275**, 36230 (2000).
29. B. Gao *et al.*, *FEBS Lett.* **488**, 179 (2001).
30. A. Dubrovska *et al.*, *Oncogene* **24**, 2289 (2005).
31. L. García-Campmany, E. Martí, *Development* **134**, 65 (2007).
32. E. E. Govek, S. E. Newey, L. Van Aelst, *Genes Dev.* **19**, 1 (2005).
33. N. E. Ziv, S. J. Smith, *Neuron* **17**, 91 (1996).
34. D. R. Alessi *et al.*, *EMBO J.* **15**, 6541 (1996).
35. D. Lang, S. K. Powell, R. S. Plummer, K. P. Young, B. A. Ruggeri, *Biochem. Pharmacol.* **73**, 1 (2007).
36. Q. Yan *et al.*, *J. Biol. Chem.* **282**, 13954 (2007).
37. S. S. Shen-Orr, R. Milo, S. Mangan, U. Alon, *Nat. Genet.* **31**, 64 (2002).
38. T. Nitzan, H. K. Avraham, *Mol. Cell. Biol.* **23**, 579 (2003).
39. This research is supported by the NIH grants GM54508 and GM072853 and Systems Biology Center grant P50-071558. Confocal laser scanning microscopy was performed at the Mount Sinai School of Medicine–Microscopy Shared Resource Facility, supported with funding from NIH–National Cancer Institute shared resources grant 5R24 CA095823-04, NSF-Major Research Instrumentation grant DBI-9724504, and NIH shared instrumentation grant 1 S10 RR0 9145-01. We thank C. Karan and R. Realubit and the Rockefeller High Throughput Screening Resource Center for expert technical assistance in hippocampal neuron imaging and neurite outgrowth analysis. We thank E. Reddy for the c-Myb expression construct and members of the Iyengar laboratory for helpful discussions. K.D.B is supported by an individual American Cancer Society Spirit of Birmingham and Johnson Memorial Postdoctoral Fellowship Award and was supported by NIH grant T32 CA88796. Author contributions are described in the supporting online material.

Supporting Online Material

www.sciencemag.org/cgi/content/full/320/5878/903/DC1
Materials and Methods
Figs. S1 to S13
Tables S1 to S6
References

6 November 2007; accepted 5 March 2008
10.1126/science.1152662

REPORTS

Turbulence and Magnetic Fields in the Large-Scale Structure of the Universe

Dongsu Ryu,[1]* Hyesung Kang,[2] Jungyeon Cho,[1] Santabrata Das[3]

The nature and origin of turbulence and magnetic fields in the intergalactic space are important problems that are yet to be understood. We propose a scenario in which turbulent-flow motions are induced via the cascade of the vorticity generated at cosmological shocks during the formation of the large-scale structure. The turbulence in turn amplifies weak seed magnetic fields of any origin. Supercomputer simulations show that the turbulence is subsonic inside clusters and groups of galaxies, whereas it is transonic or mildly supersonic in filaments. Based on a turbulence dynamo model, we then estimated that the average magnetic field strength would be a few microgauss (μG) inside clusters and groups, approximately 0.1 μG around clusters and groups, and approximately 10 nanogauss in filaments. Our model presents a physical mechanism that transfers the gravitational energy to the turbulence and magnetic field energies in the large-scale structure of the universe.

There is growing evidence that the intergalactic medium (IGM) is permeated with magnetic fields and is in a state of turbulence, similar to the interstellar medium within galaxies. Magnetic fields in the intracluster medium (ICM) have been measured with a variety of techniques, including observations of diffuse synchrotron emission from radio halos, inverse-Compton scattered cosmic background radiation in extreme ultraviolet and hard x-ray radiation, and Faraday rotation measure (RM). The inferred strength of the magnetic field is on the order of 1 μG (*1*–*3*). In the IGM outside of clusters, an upper limit of ~0.1 μG has been placed on the magnetic field strength of filaments, based on the observed limit of the RMs of background quasars (*4*, *5*).

So far, signatures of turbulence have been observed only in the ICM. The analysis of the gas pressure maps of the Coma cluster revealed that pressure fluctuations are consistent with Kolmogoroff turbulence, and turbulence is likely to be subsonic with $\varepsilon_{\rm turb} \geq 0.1\ \varepsilon_{\rm th}$, where $\varepsilon_{\rm turb}$ and $\varepsilon_{\rm th}$ are the turbulence and thermal energy densities, respectively (*6*). These results agree with predictions of numerical simulations of large-scale structure (LSS) formation (*7*, *8*). Turbulence in the ICM also has been studied in RM maps of a few clusters (*9*, *10*).

It has been suggested that cosmological shocks with Mach numbers up to ~10^4 and speeds up to a few thousand kilometers per second exist in the IGM (*11*–*13*). Such shocks result from the supersonic flow motions that are induced by the hierarchical formation of LSS in the universe. They are collisionless shocks, which form in a tenuous plasma via collective electromagnetic interactions between particles and electromagnetic fields (*14*). The gravitational energy released during the structure formation is transferred by these shocks to the IGM plasma in several different forms: in addition to the gas entropy, cosmic rays are produced via diffusive shock acceleration (*15*, *16*), magnetic fields are generated via the Biermann battery mechanism (*7*, *17*) and Weibel instability (*18*, *19*), and vorticity is generated at curved shocks (*20*, *21*).

In astrophysical plasmas in which charged particles are coupled to magnetic fields, turbulent-flow motions and magnetic fields are closely related. We suggest that the turbulence in the IGM is induced by the cascade of the vorticity generated at cosmological shocks. The turbulence then amplifies the intergalactic magnetic fields (IGMFs) through the stretching of field lines, a process known as the turbulence dynamo. This scenario provides a theoretically motivated model for the evolution of the IGMFs in LSS, independent of the origin of seed fields.

There are other sources that can also provide turbulence and magnetic fields to the IGM. For instance, galactic winds can drag out the galactic magnetic fields on the order of 1 μG strength into the surrounding IGM (*22*). The magnetic fields in the lobes of the jets from galactic black holes can also contaminate the IGM (*23*). Mergers of smaller objects are expected to produce turbulent motions in the ICM, which in turn amplify the existing magnetic fields (*24*). Those processes, although possibly important, are not topics of this study.

We first calculated the vorticity $\vec{\omega} = \vec{\nabla} \times \vec{v}$ (curl of flow velocity) in the IGM, from a numerical simulation using particle-mesh/Eulerian hydrodynamic code (*25*) for the formation of LSS in a cold dark matter–dominated universe with a cosmological constant [supporting online

[1]Department of Astronomy and Space Science, Chungnam National University, Daejeon 305-764, Korea. [2]Department of Earth Sciences, Pusan National University, Pusan 609-735, Korea. [3]Astrophysical Research Center for the Structure and Evolution of the Cosmos, Sejong University, Seoul 143-747, Korea.

*To whom correspondence should be addressed. E-mail: ryu@canopus.cnu.ac.kr

material (SOM) text S1]. As shown in Fig. 1, numerous shocks exist in the LSS that are bounded by accretion shocks (*11*). The distribution of vorticity closely matches that of shocks, suggesting that a substantial portion of the vorticity, if not all, must have been generated at the shocks.

There is a clear trend that the vorticity is larger in hotter (Fig. 2) and denser (fig. S1) regions. As shown in the top right panel of Fig. 2, at the present epoch $\omega_{rms} t_{age} \sim 10$ to 30 (ω_{rms}, the root mean square of the velocity; t_{age}, the present age of the universe) in clusters and groups [temperature (T) > 10^7 K] and filaments ($10^5 < T < 10^7$ K), whereas it is on the order of unity in sheetlike structures ($10^4 < T < 10^5$ K) and even smaller in voids ($T < 10^4$ K) (see SOM text S2 for the temperature phases of the IGM). It increases a little with time and asymptotes after red shift $z \lesssim 1$. Because the local eddy turnover time, t_{eddy}, can be defined with the vorticity as $t_{eddy} = 1/\omega$, $\omega t_{age}(z)$ represents the number of eddy turnovers in the age of the universe at a given z. Roughly, if ωt_{age} is greater than a few, we expect there has been enough time for the vorticity to cascade down to smaller scales and for turbulence to develop in the IGM. So it is likely that turbulence is well developed in clusters, groups, and filaments, but the flow is mostly nonturbulent in sheets and voids.

In our simulation, the vorticity was generated either directly at curved cosmological shocks or by the baroclinity of flows. The baroclinity resulted from the entropy variation induced at shocks. Therefore, the baroclinic vorticity generation also can be attributed to the presence of cosmological shocks. Our estimates of vorticity generation by the two processes (SOM text S3) are shown with open symbols in the top right panel of Fig. 2. They agree reasonably well with the vorticity present in the simulation, although the estimates are intended to be rough. The plot indicates that the contributions from the two processes are comparable.

To estimate the energy associated with turbulence, the curl component of flow motions $\vec{v}_{curl}$, which satisfies the relation $\vec{\nabla} \times \vec{v}_{curl} = \vec{\nabla} \times \vec{v}$, is extracted from the velocity field (SOM text S4). As vorticity cascades to develop into turbulence, the energy $(1/2)\rho v_{curl}^2$ (ρ, gas density) is transferred to turbulent motions, so we regard it as the turbulence energy, ϵ_{turb}. As shown in Fig. 3, $\epsilon_{turb} < \epsilon_{th}$ in clusters and groups. In particular, the mass-averaged value is $\langle \epsilon_{turb}/\epsilon_{th} \rangle_{mass} = 0.1$ to 0.3 for $T > 10^7$ K, which is in good agreement with the observationally inferred value in cluster cores (*6*). The turbulence Mach number (M_{turb}) = $v_{turb}/c_s = \sqrt{1.8(\epsilon_{turb} / \epsilon_{th})^{1/2}}$, where c_s is the sound speed. Therefore, overall turbulence is subsonic in clusters and groups, whereas it is transsonic or mildly supersonic in filaments.

The general consensus regarding the origin of the IGMFs is that no mechanism can produce strong coherent magnetic fields in the IGM before the formation of LSS and galaxies (*26*).

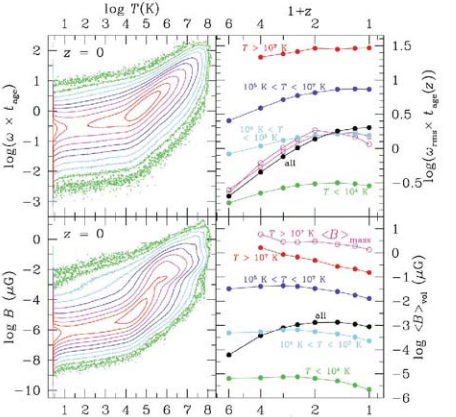

Fig. 2. (Left) Volume fraction with given temperature and vorticity magnitude (top left) and temperature and magnetic field strength (bottom left) at present. **(Right)** Time evolution of the root mean square of the vorticity (top right) and volume-averaged magnetic field strength (bottom right) for four temperature phases of the IGM and for all the gas as a function of red shift z. Magenta symbols in the top right panel are our estimates of the vorticity generated directly at curved shocks (open circles) and by the baroclinity of flows (open squares). Magenta open circles in the bottom right panel show the mass-averaged magnetic field strength for $T > 10^7$ K.

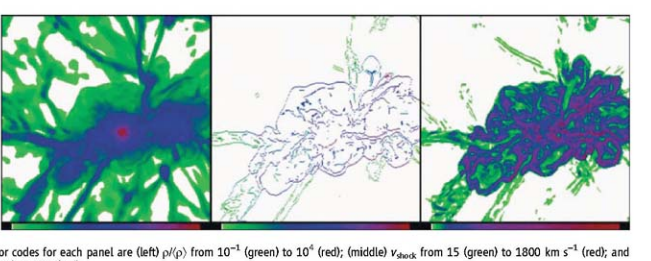

Fig. 1. Two-dimensional images showing gas density ρ in a logarithmic scale **(left)**, locations of shocks with color-coded shock speed v_{shock} **(middle)**, and magnitude of vorticity, ωt_{age} **(right)**, around a cluster complex of (25 h^{-1}Mpc)^2 area at present ($z = 0$). Here, h is the Hubble constant in units of 100 km s^{-1} Mpc^{-1}. The complex includes a cluster of x-ray emission–weighted temperature $T_x \approx 3.3$ keV. Color codes for each panel are (left) $\rho/\langle\rho\rangle$ from 10^{-1} (green) to 10^4 (red); (middle) v_{shock} from 15 (green) to 1800 km s^{-1} (red); and (right) ωt_{age} from 0.5 (green) to 100 (red).

However, it is reasonable to assume that weak seed fields were created in the early universe (SOM text S5). The seed fields can be amplified by the intergalactic turbulence discussed above. In principle, if we were to perform magneto-hydrodynamic (MHD) simulations of structure formation, the amplification of the IGMFs could be followed. In practice, however, the currently available computational resources do not allow a numerical resolution high enough to reproduce the full development of MHD turbulence in LSS (*7*).

In order to follow the growth of the IGMFs by the dynamo action of turbulence, we turned to a separate simulation in a controlled box. Starting with a very weak regular field, a three-dimensional incompressible simulation of driven MHD turbulence was performed (SOM text S6). In the simulation, the evolution of magnetic fields goes through three stages: (i) the initial exponential growth stage, when the back-reaction of magnetic fields is negligible; (ii) the linear growth stage, when the back-reaction starts to operate; and (iii) the final saturation stage (*27*). Adopting the simulation result, we modeled the growth and saturation of magnetic energy as

$$\phi(t/t_{\rm eddy}) = \frac{\varepsilon_B}{\varepsilon_{\rm turb}} = \begin{cases} 0.04 \times \exp[(t/t_{\rm eddy} - 4)/0.36] & \text{for } t/t_{\rm eddy} < 4 \\ (0.36/41) \times (t/t_{\rm eddy} - 4) + 0.04 & \text{for } 4 < t/t_{\rm eddy} < 45 \end{cases} \quad (1)$$

(fig. S2). Assuming that the fraction of turbulence energy governed by Eq. 1, ϕ, is converted into the magnetic energy, we estimate the strength of the IGMFs as $B = [8\pi\varepsilon_{\rm turb} \cdot \phi(\omega t_{\rm age})]^{1/2}$. Here, the values of ω and $\varepsilon_{\rm turb}$ are calculated locally from the structure formation simulation.

The resulting IGMFs follow the cosmic web of matter distribution as shown in Fig. 4 (and in fig. S3). On average, the IGMFs are stronger in hotter (Fig. 2) and denser (fig. S1) regions in our model. The strength of the IGMFs is $B \geq 1$ μG inside clusters and groups (the mass-averaged value for $T > 10^7$ K), ~0.1 μG around clusters and groups (the volume-averaged value for $T > 10^7$ K), and ~10 nG in filaments at present (bottom right panel of Fig. 2) (see SOM text S7 for the numerical convergence of the estimation). These values agree with the observed field strengths discussed earlier. They also agree with the previous study (*7*), in which the magnetic field strength in clusters was estimated to be a few microGauss, based on a kinetic theory. The IGMFs should be much weaker in sheetlike structures and voids. But as noted above, turbulence is not fully developed in such low-density regions, so our model is not adequate to predict the field strength there. For each temperature phase, the IGMFs are stronger in the past, because the gas density is higher. However, the IGMFs averaged over the entire computational volume are weaker in the past because the fraction of strong-field regions is smaller.

While being amplified, magnetic fields become coherent through the inverse cascade (*27*). The coherence scale of magnetic fields in fully developed turbulence is expected to be several times smaller than the driving scale; that is, the scale of dominant eddies (SOM text S8). In the IGM outside of clusters, the curvature radius of typical cosmological shocks is approximately a couple of megaparsecs (*11*) (fig. S4), which should represent a characteristic scale of dominant eddies. The coherence length of the IGMFs there is then expected to be several hundred kiloparsecs. On the other hand, the scale height of the ICM is several 100 kpc. The coherence length in the ICM is expected to be ~100 kpc or so, if it corresponds to the scale of the dominant eddies.

Our model can predict the RMs owing to the IGMFs, which may be tested in future observations with Low Frequency Array and Square Kilometer Array (*28*). Also, our model IGMFs can be employed in the study of the propagation of ultra–high-energy cosmic rays, which is crucial to search for astrophysical accelerators of such high-energy particles (*29*).

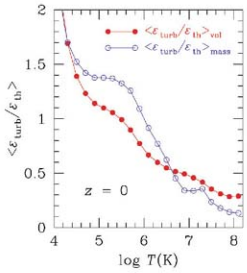

Fig. 3. Ratio of turbulence to thermal energies as a function of temperature at present. The values shown are volume-averaged and mass-averaged over temperature bins.

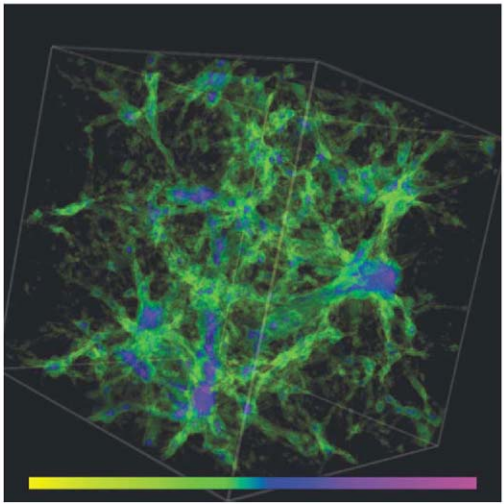

Fig. 4. Volume-rendering image showing the logarithmically scaled magnetic field strength at $z = 0$ in the whole computational box of (100 h^{-1} Mpc)^3 volume. Color codes the magnetic field strength from 0.1 nG (yellow) to 10 μG (magenta). The colors were chosen so that clusters and groups show as magenta and blue and filaments as green.

References and Notes

1. C. L. Carilli, G. B. Taylor, *Annu. Rev. Astron. Astrophys.* **40**, 319 (2002).
2. F. Govoni, L. Feretti, *Int. J. Mod. Phys. D* **13**, 1549 (2004).
3. T. E. Clarke, P. P. Kronberg, H. Böhringer, *Astrophys. J.* **547**, L111 (2001).
4. D. Ryu, H. Kang, P. L. Biermann, *Astron. Astrophys.* **335**, 19 (1998).
5. Y. Xu, P. P. Kronberg, S. Habib, Q. W. Dufton, *Astrophys. J.* **637**, 19 (2006).
6. P. Schuecker, A. Finoguenov, F. Miniati, H. Böhringer, U. G. Briel, *Astron. Astrophys.* **426**, 387 (2004).
7. R. M. Kulsrud, R. Cen, J. P. Ostriker, D. Ryu, *Astrophys. J.* **480**, 481 (1997).
8. D. Nagai, A. Vikhlinin, A. V. Kravtsov, *Astrophys. J.* **655**, 98 (2007).
9. M. Murgia *et al.*, *Astron. Astrophys.* **424**, 429 (2004).
10. C. Vogt, T. Enßlin, *Astron. Astrophys.* **434**, 67 (2005).
11. D. Ryu, H. Kang, E. Hallman, T. W. Jones, *Astrophys. J.* **593**, 599 (2003).
12. C. Pfrommer, V. Springel, T. A. Enßlin, M. Jubelgas, *Mon. Not. R. Astron. Soc.* **367**, 113 (2006).
13. H. Kang, D. Ryu, R. Cen, J. P. Ostriker, *Astrophys. J.* **669**, 729 (2007).
14. K. B. Quest, *J. Geophys. Res.* **93**, 9649 (1988).
15. A. R. Bell, *Mon. Not. R. Astron. Soc.* **182**, 147 (1978).
16. R. D. Blandford, J. P. Ostriker, *Astrophys. J.* **221**, L29 (1978).
17. L. Biermann, *Z. Naturforsch. Sa.* 65 (1950).
18. E. S. Weibel, *Phys. Rev. Lett.* **2**, 83 (1959).
19. M. V. Medvedev, L. O. Silva, M. Kamionkowski, *Astrophys. J.* **642**, L1 (2006).
20. J. Binney, *Mon. Not. R. Astron. Soc.* **168**, 73 (1974).
21. G. Davies, L. M. Widrow, *Astrophys. J.* **540**, 755 (2000).
22. H. J. Völk, A. M. Atoyan, *Astropart. Phys.* **11**, 73 (1999).
23. P. P. Kronberg, Q. W. Dufton, H. Li, S. A. Colgate, *Astrophys. J.* **560**, 178 (2001).
24. K. Subramanian, K. A. Shukurov, N. E. L. Haugen, *Mon. Not. R. Astron. Soc.* **366**, 1437 (2006).
25. D. Ryu, J. P. Ostriker, H. Kang, R. Cen, *Astrophys. J.* **414**, 1 (1993).
26. R. M. Kulsrud, E. G. Zweibel, *Rep. Prog. Phys.* **71**, 046901 (2008).
27. J. Cho, E. T. Vishniac, *Astrophys. J.* **538**, 217 (2000).
28. B. M. Gaensler, R. Beck, L. Feretti, *N. Astron. Rev.* **48**, 1003 (2004).
29. S. Das, H. Kang, D. Ryu, J. Cho, *Astrophys. J.* **681**, in press (2008).

30. This work was supported by the Korea Foundation for International Cooperation of Science and Technology through grant K20702020016-07E0200-01610 provided by the Ministry of Education, Science and Technology. The work of D.R. was also supported by the Korea Science and Engineering Foundation (KOSEF) through the grant of basic research program R01-2007-000-20196-0. The work of H.K. and S.D. was also supported by KOSEF through the Astrophysical Research Center for the Structure and Evolution of the Cosmos. The work of J.C. was also supported by the Korea Research Foundation, grant KRF-2006-331-C00136, funded by the Korean Government.

Supporting Online Material

www.sciencemag.org/cgi/content/full/320/5878/909/DC1
Materials and Methods
SOM Text
Figs. S1 to S6
References

7 January 2008; accepted 10 April 2008
10.1126/science.1154923

Stress and Fold Localization in Thin Elastic Membranes

Luka Pocivavsek,[1] Robert Dellsy,[2] Andrew Kern,[1] Sebastián Johnson,[3] Binhua Lin,[2] Ka Yee C. Lee,[1] Enrique Cerda[3]*

Thin elastic membranes supported on a much softer elastic solid or a fluid deviate from their flat geometries upon compression. We demonstrate that periodic wrinkling is only one possible solution for such strained membranes. Folds, which involve highly localized curvature, appear whenever the membrane is compressed beyond a third of its initial wrinkle wavelength. Eventually the surface transforms into a symmetry-broken state with flat regions of membrane coexisting with locally folded points, reminiscent of a crumpled, unsupported membrane. We provide general scaling laws for the wrinkled and folded states and proved the transition with numerical and experimental supported membranes. Our work provides insight into the interfacial stability of such diverse systems as biological membranes such as lung surfactant and nanoparticle thin films.

Crumple a piece of paper and a meshwork of highly deformed ridges and perfectly straight planes appear. This focusing behavior is universal for any strongly confined membrane (*1*, *2*). Compress a similar membrane now resting on some substrate like water or a gel, and it responds differently. Its initial response is wrinkling, producing beautiful sinusoidal undulations across the entire surface (*3*–*7*). Yet if the wrinkled surface is laterally compressed even further, a different geometry emerges. The wrinkles disappear everywhere except for a few select locations on the surface that exhibit folds, a geometry similar to the crumpled piece of paper.

A variety of real systems can be thought of as elastic membranes resting on softer substrates. Our lungs are lined by a thin membrane, composed of lipids and proteins, that stabilizes them and is often modeled as an elastic sheet on a fluid subphase (*8*–*10*). The membrane's mechanical response via reversible folding is believed to play a key role in normal lung function (*9*). Likewise, thin layers of nanoparticles—which show promise as unique electronic, optical, and magnetic materials (*11*)—have recently been spread at air/water interfaces as a method of controlling their packing structure and to allow ease of deposition onto solid substrates for potential technological use (*12*, *13*). Wrinkling and folding of such layers during deposition could be exploited to create nanopatterned structures.

Several theoretical approaches have been developed to treat particular cases of either wrinkling (*3*, *6*, *7*, *14*–*16*) or folding (*8*, *17*, *18*) in given systems. However, the generality of these instabilities has not been developed, and existing theories treat one state or the other without connecting the two. Here, we explore the evolution of a general elastic interface under lateral compression. We show that wrinkles appear as a first-order linear response of the membrane and can be suppressed by nonlinear effects that give rise to the fold at greater confinement.

A thin (10-μm) sheet of polyester resting on the surface of water is initially flat. Clamping one set of free edges between two movable barriers and compressing by some small amount Δ, the sheet instantaneously forms wrinkles with a wavelength λ (a in Fig. 1A). If the sheet is continually compressed, the wrinkle amplitude grows uniformly across the surface (*19*). Eventually one wrinkle will grow in amplitude, whereas the others decay as seen in b in Fig. 1A. Further confinement leads to the eventual formation of a fold where all of the distortion is focused within a narrow region of the surface (c in Fig. 1A).

Although the wrinkle-to-fold transition in Fig. 1A takes place when the polyester sheet is lying on top of water, a fluid substrate is not necessary for the transition. Figure 1B shows a similar evolution of the surface with the polyester adhered to a soft gel. Smooth wrinkling (a in Fig. 1B) becomes unstable (b in Fig. 1B) and eventually localizes into several folds relaxing the rest of the surface (c in Fig. 1B).

A phenomenologically similar transition can be observed in films three orders of magnitude thinner. At an air/water interface, gold nanoparticles 5 nm in diameter are compressed to form a self-assembled trilayered film that is 15 nm thick. With the use of light microscopy, one can observe the initial periodic wrinkles with $\lambda \sim 10$ μm (a in Fig. 1C). If the compression is stopped, the surface remains wrinkled. However, further confinement leads to the focusing behavior observed in the macroscopic polyester film. Panel b in Fig. 1C shows the beginning of fold formation: The brightness of one wrinkle increases as its amplitude grows, scattering more light. Eventually the two leaflets of the sheet make self-contact, and the fold

[1]Department of Chemistry and James Franck Institute (JFI), University of Chicago, Chicago, IL 60637, USA. [2]Center for Advanced Radiation Sources and JFI, University of Chicago, Chicago, IL 60637, USA. [3]Departamento de Física and Centro para Investigación Interdisciplinaria Avanzada en Ciencias de los Materiales, Universidad de Santiago, Av. Ecuador 3493, Santiago, Chile.

*To whom correspondence should be addressed. E-mail: ecerda@lauca.usach.cl

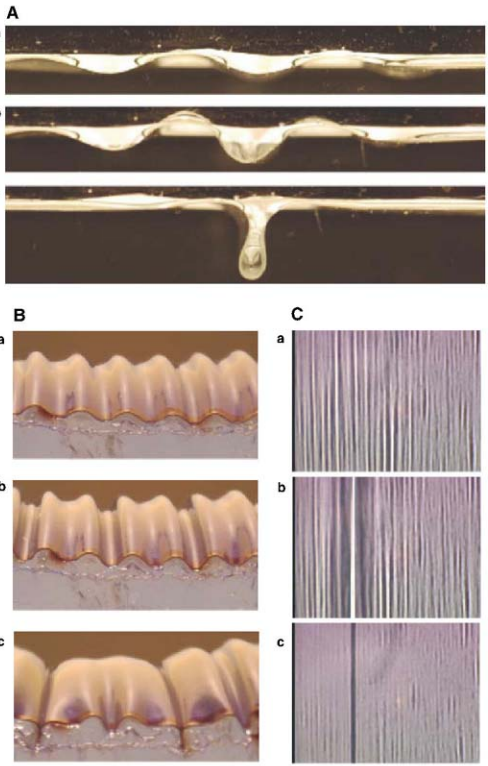

Fig. 1. (**A**) Polyester film on water, (**B**) polyester film on gel substrate [where K is much higher than in (A)], and (**C**) trilayer of colloidal gold nanoparticles on water [where B is much lower than in (A)] transitioning from an extended wrinkled state, a, to a localized folded state upon further compression, c. Polyester films are 10 μm thick. The nanoparticle layer is 15 nm thick. The macroscopic systems are imaged from the side. The nanoparticles, compressed in a Langmuir trough, are microscopically imaged from above. Panel a in (C) shows a uniform wrinkled surface, with the wrinkle troughs and peaks providing the contrast in brightness. As one wrinkle grows in amplitude, it becomes brighter still [b in (C)]. Upon fold completion [c in (C)], the fold extending underneath the surface is several microns long and far below the focal plane of the surface so scattering is not seen. It appears dark because of its thickness suppressing transmission. As a length scale for each set, one can use the initial wrinkle wavelength: (A), $\lambda \sim 1.6$ cm; (B), $\lambda \sim 3.3$ mm; and (C), $\lambda \sim 10$ μm. The membranes here span three orders of magnitude in thickness and initial wrinkle wavelength. Furthermore, the intermolecular forces holding them together are very different: The polyesters are cross-linked polymers, whereas the gold nanoparticles are simply held together by van der Waals forces (*12*).

(appearing dark) is formed, relaxing the wrinkles to either side. A movie of the process is available as supporting online material (SOM; movie S1) (*20*); also available is a movie showing folding in a model lung surfactant layer (movie S2).

A thin membrane can be bent far more easily than stretched (*1*). As such, thin membranes are often described as inextensible so that their length is preserved upon deformation. In the above experiments, a membrane of length L is compressed by a horizontal distance Δ, so that the total projected length along the horizontal direction is $L - \Delta$. The lack of compression along the plane of the membrane leads to the constraint $L - \Delta = \int_0^L dl \cos\phi$, where the integration and differentiation are in terms of distance along the curve l (arc length). Figure 2A defines ϕ as the angle between the tangent to the curve and the horizontal; the derivative of the angle with respect to arc length ($\dot{\phi}$) gives the curvature.

To understand the observed nonlinear folds, we studied the energy, U, for a thin inextensible elastic sheet. The energy per unit of width is made up of two parts: the elastic bending energy, $U_B = (B/2)\int_0^L dl\dot{\phi}^2$, of the film and the potential energy due to the displacement of the substrate underneath, $U_K = (K/2)\int_0^L dl \cos\phi y^2$, where y is the vertical displacement of the surface from the flat state, B is the bending stiffness of the surface, and K is the stiffness of the substrate. In the case of a fluid substrate, Hertz was the first to realize that its weight could act as an effective stiffness; thus, for a fluid $K = \rho g$, where ρ is the fluid density and g is the acceleration due to gravity (*21*).

The shape of the film is obtained by minimization of the total energy $U = U_B + U_K$ with a Lagrangian multiplier to satisfy the inextensibility. To study the weakly confined wrinkled state, we make the linear approximation $\phi \approx \dot{y}$, where $\dot{y}$ is the derivative of the vertical displacement with respect to the arc length. Given a smooth sinusoidal undulation of the surface as seen in the experiments, the bending energy scales as $U_B \approx (B/2)\int_0^L d\ddot{y}^2 \sim BL(A/\lambda^2)^2$ (where $\ddot{y}$ is the second derivative of the vertical displacement with respect to the arc length), and the potential energy as $U_K \approx (K/2)\int_0^L dy^2 \sim KLA^2$, where A is the wrinkle amplitude. A balance of these two energies gives the wavelength of the wrinkles as $\lambda \sim (B/K)^{1/4}$ (see fig. S1 and SOM for exact calculation and experimental fitting). Furthermore, the inextensibility in the linear approximation is $\Delta \approx \int_0^L d\dot{y}^2 \sim L(A/\lambda)^2$. This gives the amplitude as $A \sim \lambda\sqrt{(\Delta/L)}$. The wrinkles are

predicted to grow continuously in amplitude as $\sqrt{\Delta}$, which is in agreement with our observations.

The total energy for a wrinkled state scales as $U \sim (BK)^{1/2}\Delta$ and is distributed across the entire undulating surface. The specific energy U/L has a finite value for a given applied external strain Δ/L independent of the system size. Furthermore, a constant pressure is necessary to confine a film in a wrinkled state $p = \partial_\Delta U \sim (BK)^{1/2}$ (where $\partial_\Delta U$ is the derivative of the energy with respect to the horizontal displacement), independent of the amount of lateral displacement so long as the system size is large (*20*). Thus, the conclusions from the linear analysis are that once a wrinkled surface appears, it is the stationary solution. Further confinement leads to a simple increase in amplitude that gives rise to an increase in energy for the system.

Whereas the above linear analysis explains the wrinkled state, it does not provide insight into the wrinkle-to-fold transition. To examine the transition into the strongly confined state where fold localization begins, we experimentally studied a thin polyester film on water and numerically analyzed the lowest energy solutions to the energy functional defined earlier. The insets in Fig. 3, A and C, show profiles of the physical and numerical sheets as compression is increased. $N = L/\lambda$ and $d = \Delta/\lambda$ are the only dimensionless parameters in the problem (here, N is the number of wrinkles, and d is the dimensionless lateral displacement). A_1 is chosen as the amplitude of the wrinkle that decays and A_0 as the amplitude of the one that grows (Fig. 2A). Both the physical and numerical systems show divergence of the amplitudes from the square root dependence on displacement seen in uniform wrinkles beyond a certain confinement (Fig. 2B). Notably, around $d = \Delta/\lambda \approx 0.3$ (i.e., $\Delta \approx \lambda/3$), A_0 begins to increase linearly, and the buttressing wrinkle amplitude A_1 begins to decay. This is the hallmark of the wrinkle-to-fold transition.

The amplitude data also bring forth an emergent size independence within the folding regime. The wrinkle amplitude derived above depends on strain (Δ/L); however, the fold amplitude depends only on Δ. The fact that the wrinkle-to-fold transition occurs at $d \approx 0.3$ thus gives rise to the increased scatter in the data for $d < 0.3$ and a collapse of the data onto linear curves beyond this critical point (Fig. 2B).

To avoid the finite size effect at low compression, one can look at the ratio of the two amplitudes, A_0/A_1, that acts as an effective order parameter for the transition. For a uniformly wrinkled state, the order parameter should fluctuate around one. However, as confinement increases above a critical point, the order parameter must diverge. Figure 3A shows the overlay of physical (circles) and numerical (solid blue line) data for the order parameter. When $d < 0.3$, both sets lie on the line $A_0/A_1 \approx 1$. As compression is increased beyond this point, there is a seemingly asymptotic divergence.

The theoretical data in Fig. 3A represent an upper bound to the data for the order parameter, which can be explained by considering the final fold shape. In the numerical analysis, up/down as well as S and anti-S folds are seen as final states (Fig. 3B). However, in the polyester experiments, S and anti-S folds eventually relax toward an up/down geometry upon further compression (*22*). In Figs. 2B and 3A, the data are divided between membranes that formed intermediate S and anti-S folds (gray symbols) and those that did not (black symbols). The untwisting is driven by line tension at the polyester/water/air interface, not accounted for in the numerical analysis, and occurs at higher values of d; thus, some physical data are slightly shifted to the right as shown in Fig. 3A (gray circles).

The correspondence between the numerical and physical data attests that the essential physics of the phenomenon is captured in the simulation. Both experiments show that a wrinkled surface should be stable against further confinement by a third of its wavelength ($\lambda/3$), beyond which the surface geometry becomes unstable toward the new localized folded state. The fold eventually collapses as two nonadjacent parts of the surface make self-contact, and confinement approaches the initial wrinkle wavelength.

We now provide a physical interpretation of the transition in the original unscaled variables. For a fold with a maximum curvature at its tip $\dot{\phi}_{max}$, the energy is localized inside a perimeter of $l \sim 1/\dot{\phi}_{max}$ so that the bending energy of the fold scales as $U_B \sim B/l$. The height of the fold is proportional to the applied displacement Δ; hence, the potential energy must scale as $U_K \sim K l\Delta^2$. We have not considered the nonlinear effect due to the factor $\cos\phi$ in the potential energy. This term represents the projection of the fold shape along the horizontal direction. Writing the inextensibility constraint as the sum of linear and nonlinear terms, we obtain $\int_0^L dl(1 - \cos\phi) = \Delta$. The potential energy can similarly be divided, $U_K = (K/2)\int_0^L dly^2 - (K/2)\int_0^L dl(1 - \cos\phi)y^2$. This yields the scaling $U_K \sim Kl\Delta^2 - K\Delta^2\int_0^L dl(1-\cos\phi) \sim Kl\Delta^2 - K\Delta^3$.

The size of the fold l is obtained by minimizing the total energy $\partial_l (U_B + U_K) = 0$, giving $l \sim (B/K)^{1/2}(1/\Delta)$, which is confirmed by

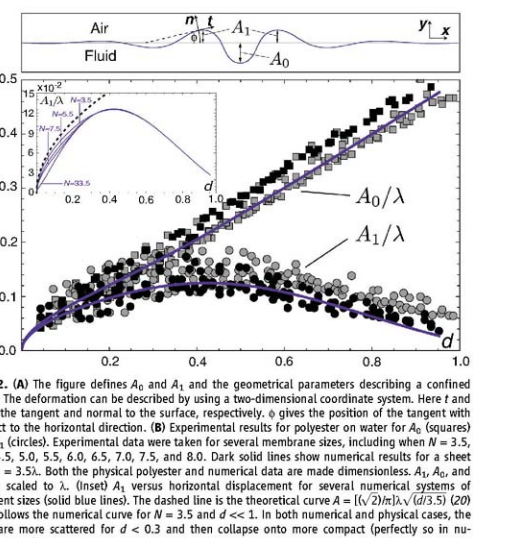

Fig. 2. (A) The figure defines A_0 and A_1 and the geometrical parameters describing a confined sheet. The deformation can be described by using a two-dimensional coordinate system. Here t and n are the tangent and normal to the surface, respectively. ϕ gives the position of the tangent with respect to the horizontal direction. **(B)** Experimental results for polyester on water for A_0 (squares) and A_1 (circles). Experimental data were taken for several membrane sizes, including when N = 3.5, 4.0, 4.5, 5.0, 5.5, 6.0, 6.5, 7.0, 7.5, and 8.0. Dark solid lines show numerical results for a sheet with $L = 3.5\lambda$. Both the physical polyester and numerical data are made dimensionless. A_1, A_0, and Δ are scaled to λ. (Inset) A_1 versus horizontal displacement for several numerical systems of different sizes (solid blue lines). The dashed line is the theoretical curve $A = [(\sqrt{2})\pi]\lambda\sqrt{(d/3.5)}$ (*20*) that follows the numerical curve for $N = 3.5$ and $d << 1$. In both numerical and physical cases, the data are more scattered for $d < 0.3$ and then collapse onto more compact (perfectly so in numerical case) curves past this point. This behavior is indicative of the size-dependent behavior in the wrinkling ($d < 0.3$) regime and size-independent behavior in the folding ($d > 0.3$) regime.

our numerical analysis. Thus, the total energy for the folded state in terms of only material constants and displacement is $U \sim (BK)^{1/2}\Delta - K\Delta^3$.

One way to check this energy is to calculate the pressure needed to confine a sheet. From our scaling law, $p = \partial_\Delta U \sim (BK)^{1/2} - K\Delta^2$. In dimensionless form, the pressure can be written as $p/(BK)^{1/2} = a - bd^2$, where a is obtained from the linear analysis [$a \approx 2$, see derivation in (*20*)] and b from fitting the numerics ($b \approx 2.47$) (solid curve in Fig. 3C).

The energies of the wrinkled state and folded state differ only in a term of higher order that is related to the geometry of the localized fold. This term lowers the total energy, which explains why a localized fold is observed for high values of confinement instead of a stationary wrinkled state that extends throughout the surface. Rewriting the scaling in terms of d, the wrinkle and fold energies are within 10% of each other around $d \approx 0.3$. As such, the energy-scaling arguments are in quantitative agreement with the experiments. The fold energy becomes more stable when the sheet is compressed beyond a third of the initial wrinkle wavelength, at which point energy begins to be localized within a narrow part of the surface proportional to l (*23*).

This focusing effect and the wrinkle-to-fold transition should generally occur when the thin membrane and substrate foundation are considerably mismatched in their elastic properties. In the case of a fluid substrate where the fluid has no static elasticity, the transition occurs as described. In the case of soft gels (such as the system in Fig. 1B) where the ratio of the Young's moduli of the membrane (E_m) and substrate (E_s) is ~1000, localization still occurs (c in Fig. 1B) yet is distributed into several folds. Work on very stiff substrates ($E_m/E_s < 100$) has shown the persistence of wrinkles at large confinement with no stress focusing (*24*). We believe the relaxation of wrinkles into multiple folds is linked to the underlying ability of the substrate to stretch and shear. We predict that in the range $1000 > E_m/E_s > 100$, the number of wrinkles relaxing into one fold should decrease, giving rise to a larger number of folds with smaller amplitudes. As the lower limit is reached, surface focusing is suppressed, and the excess membrane length due to compression is accommodated in wrinkles of longer wavelengths and larger amplitudes (*24*).

Many physical examples exist where the mismatch in membrane and substrate elasticity is large. A long-standing problem in supported membranes has been understanding the focused and large-amplitude folds seen in lipid monolayers. More than 50 years ago, Ries and Kimball showed that such monolayers at air/water interfaces develop large-amplitude folds at localized sites on the surface (*25*). Since then, folding has been reported in several other lipid (*10*, *26*) and nanoparticle films (*12*), yet existing theories relying on defects (*8*, *15*, *17*, *18*) fail to account for the universality of how these ultrathin membranes transition from flat structures only nanometers in thickness to folds orders of magnitude larger. We conjecture that the large-amplitude folds in self-assembled layers like lipids and gold nanoparticles initiate via the mechanism explored here. Generally, self-assembled films at air/liquid interfaces should become unstable to wrinkling and folding when they become solidlike and capable of supporting lateral compression (*27*).

Our model also provides an elegant mechanism that accounts for fold size and directionality by simply invoking the film's elastic character and confinement to the interface. The bending stiffness of a lipid monolayer is $O(10\ \mathrm{kT})$ (*4*), which would give it a wrinkle wavelength of $O(1\ \mu\mathrm{m})$ using $K = \rho g$. Wrinkles have been difficult to detect in lipids because of their poor scattering of light; however, diffuse x-ray scattering has shown wrinkle signatures with wavelengths of $O(1\ \mu\mathrm{m})$ (*4*, *26*). If the monolayer transforms as an elastic sheet, then we expect folds of the same order as the wavelength appearing perpendicular to the direction of compression; in particular, our scaling shows $l \sim \lambda^2/\Delta$, yet as the fold makes self-contact $\Delta \sim \lambda$, so $l \sim \lambda$. The most detailed study of monolayer folding where thousands of folding events were analyzed showed that the most probable folds in a model lung surfactant system were 2 μm in size and oriented

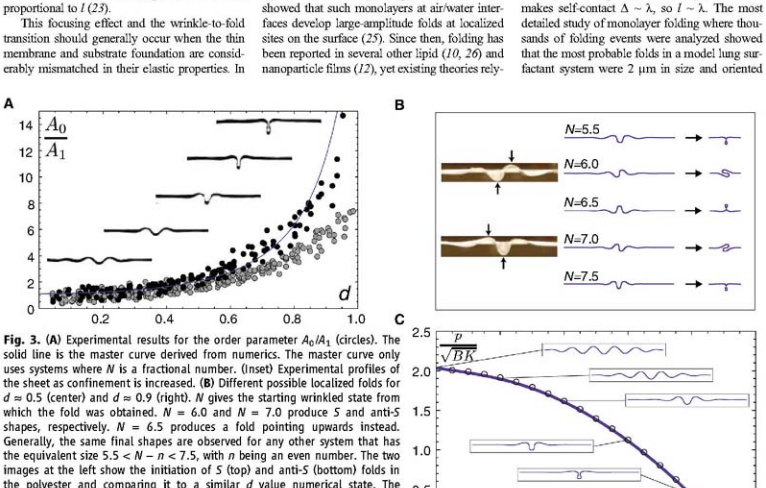

Fig. 3. **(A)** Experimental results for the order parameter A_0/A_1 (circles). The solid line is the master curve derived from numerics. The master curve only uses systems where N is a fractional number. (Inset) Experimental profiles of the sheet as confinement is increased. **(B)** Different possible localized folds for $d \approx 0.5$ (center) and $d \approx 0.9$ (right). N gives the starting wrinkled state from which the fold was obtained. $N = 6.0$ and $N = 7.0$ produce S and anti-S shapes, respectively. $N = 6.5$ produces a fold pointing upwards instead. Generally, the same final shapes are observed for any other system that has the equivalent size $5.5 < N - n < 7.5$, with n being an even number. The two images at the left show the initiation of S (top) and anti-S (bottom) folds in the polyester and comparing it to a similar d value numerical state. The numerical membrane in each case will continue to form the S and anti-S folds reaching the state seen at the right. However, the physical membrane will eventually untwist to a down fold in both cases (*22*). **(C)** Dimensionless cross-sectional pressure versus horizontal displacement for $N = 5.5$. Here, the dimensionless pressure was obtained from the numerical analysis (solid line) and compared to our theoretical prediction (empty circles). (Insets) Profiles of the sheet for each value of the horizontal displacement with the maximum amplitude normalized to 1.

directly perpendicular to the axis of compression (*28*). This is in agreement with our prediction. In the gold nanoparticle layers shown in Fig. 1C, wrinkles are more easily seen because of the strong scattering of the metal cores. As the image shows, the length scale over which the fold forms (l) is set by the initial wrinkle wavelength (λ).

Understanding compaction of nanometer-thin membranes through controllable and reversible modes like wrinkling and folding opens the door to technological use of these systems (*29*). In medicine, developing synthetic lung surfactant formulations depends on our capability to reproduce the incredible ability of native lung surfactant to compact by folding (*9*). Likewise, nanoparticle thin film applications rely on understanding the mechanical properties and responses of such layers (*12*, *13*, *29*). From wrinkle wavelengths, constants like the bending modulus can be found (*5*, *6*, *30*), whereas controlling the wrinkle-to-fold transition can help the development of adaptive functions in new technologies like flexible electronics (*29*, *31*).

References and Notes

1. T. A. Witten, *Rev. Mod. Phys.* **79**, 643 (2007).
2. A. Lobkovsky, S. Gentges, H. Li, D. Morse, T. A. Witten, *Science* **270**, 1482 (1995).
3. D. Vella, P. Aussillous, L. Mahadevan, *Europhys. Lett.* **68**, 212 (2004).
4. L. Bourdieu, J. Daillant, D. Chatenay, A. Braslau, D. Colson, *Phys. Rev. Lett.* **72**, 1502 (1994).
5. J. Huang *et al.*, *Science* **317**, 650 (2007).
6. N. Bowden, S. Brittain, A. G. Evans, J. W. Hutchinson, G. M. Whitesides, *Nature* **393**, 146 (1998).
7. R. Huang, Z. Suo, *J. Appl. Phys.* **91**, 1135 (2002).
8. H. Diamant, T. A. Witten, C. Ege, A. Gopal, K. Y. C. Lee, *Phys. Rev. E* **63**, 061602 (2001).
9. J. A. Zasadzinski, J. Ding, H. E. Warriner, F. Bringezu, A. J. Waring, *Curr. Opin. Colloid Interface Sci.* **6**, 506 (2001).
10. A. Gopal, K. Y. C. Lee, *J. Phys. Chem. B* **105**, 10348 (2001).
11. C. P. Collier, T. Vossmeyer, J. R. Heath, *Annu. Rev. Phys. Chem.* **49**, 371 (1998).
12. D. G. Schultz *et al.*, *J. Phys. Chem. B* **110**, 24522 (2006).
13. K. E. Mueggenburg, X. M. Lin, R. H. Goldsmith, H. M. Jaeger, *Nat. Mater.* **6**, 656 (2007).
14. S. T. Milner, J. F. Joanny, P. Pincus, *Europhys. Lett.* **9**, 495 (1989).
15. A. Saint-Jalmes, F. Graner, F. Gallet, B. Houchmandzadeh, *Europhys. Lett.* **28**, 565 (1994).
16. Q. Zhang, T. A. Witten, *Phys. Rev. E* **76**, 041608 (2007).
17. E. S. Nikomarov, *Langmuir* **6**, 410 (1990).
18. W. Lu *et al.*, *Phys. Rev. Lett.* **89**, 146107 (2002).
19. E. Cerda, L. Mahadevan, *Phys. Rev. Lett.* **90**, 074302 (2003).
20. Supporting material is available on *Science* Online.
21. H. Hertz, *Wiedemann's Ann. Phys. Chem. (Kyoto)* **22**, 449 (1884).
22. Although both up and down folds are observed, we note that the down fold is favored over the up fold. This asymmetry is not present in the numerics and can be accounted for by considering the meniscus geometry at the polyester/water/air contact line. Given that the wetting angle at the contact line is constant, the meniscus on the up fold will be slightly larger than the down fold. This geometric difference generates a slight asymmetry in the gravitational energy for the two states and favors the down fold. However, our current work has been done in a "deep" water regime. The up fold is more likely to be observed when the subphase is very shallow because the down fold cannot develop.
23. In certain conditions, a stretched state could play the role of a wrinkled state. The specific energy (U/L) for both has a finite value independent of system size. On the other hand, the specific energy of a folded state for a given applied strain Δ/L diverges to negative values for large systems. This predicts that a direct transition from a stretched to a folded state could be possible for large systems. The internal compression necessary to observe a transition from a stretched flat surface to a wrinkled state is $\Delta_2 = L \times 2(Bt)^{1/2}/ED$, where t is film thickness. The critical compression for the wrinkle to fold transition is $\Delta_1 = \lambda/3$. So a wrinkled state should be observed before folding if the inequality $\Delta_0 < \Delta_1$ or $L/\lambda < [3/(8\pi^2)](Et/B)^{1/2}$ is satisfied.
24. K. Efimenko *et al.*, *Nat. Mater.* **4**, 293 (2005).
25. H. E. Ries, W. A. Kimball, *J. Phys. Chem.* **59**, 94 (1955).
26. C. Ybert, W. Lu, G. Moller, C. M. Knobler, *J. Phys. Condens. Matter* **14**, 4753 (2002).
27. Solid monolayers continue to have positive surface tensions measured by Wilhelmy plates when they fold (*8*, *10*). Whereas the Wilhelmy plate accurately measures all interfacial forces at liquid interfaces, the measurement breaks down when the interface becomes solidlike (*32*). For a solid monolayer capable of supporting a deviatoric shear stress, a small increase in pressure at the periphery should lead to a smaller increase at the plate, with the weakening being governed by the ratio of shear to bulk moduli of the monolayer. Thus, parts of the monolayer close to the barriers may be under a compressive stress even if a finite surface tension is measured at the plate.
28. A. Gopal, V. A. Belyi, H. Diamant, T. A. Witten, K. Y. C. Lee, *J. Phys. Chem. B* **110**, 10220 (2006).
29. R. Vaia, J. Baur, *Science* **319**, 420 (2008).
30. The wrinkle wavelength observed in our experiments gives $B \sim 15$ kT for the gold layer. Using $B = Eh^3/12(1 - \nu^2)$, where t is the film thickness and ν is its Poisson ratio, we estimate the Young's modulus (E) of the 15-nm gold trilayer with $\nu = 0.3$ on the order of 100 kPa.
31. D.-H. Kim *et al.*, *Science* **320**, 507 (2008); published online 25 March 2008, 10.1126/science.1154367.
32. A. Saint-Jalmes, M. Assenheimer, F. Gallet, *J. Phys. Chem. B* **102**, 5810 (1998).

33. We thank T. Witten for many fruitful discussions as well as his leadership of the NSF Inter-American Materials Collaboration: Chicago-Chile (DMR-0303072) under whose support this collaboration began; M. Meron for many rich discussions; S. Rice, F. Melo, J. Pavez, A. Pocivavsek, and K. Lam for experimental help; and E. Sultan and A. Boudaoud for sharing their unpublished/in press manuscript "The Buckling of a Swollen Thin Gel Layer Bound to a Compliant Substrate" with us for guidance. This work was supported in part by the University of Chicago Materials Research Science and Engineering Center program of the NSF (DMR-0213745) and the U.S.-Israel Binational Foundation (2006076). L.P. thanks the University of Chicago Medical Scientist Training Program for support; A.K. was supported by the Dreyfus Summer Research Program at the University of Chicago (SG-06-039); K.Y.C.L. is grateful for support from March of Dimes (No. 6-FY07-357); R.D. and B.L. acknowledge the support of NSF/U.S. Department of Energy grant no. CHE-0535644 for ChemMatCARS; and E.C. acknowledges the support of Anillo Act 15, Fondap grant no. 11980002 and Fondecyt Project no. 1050083.

Supporting Online Material

www.sciencemag.org/cgi/content/full/320/5878/912/DC1
Materials and Methods
SOM Text
Fig. S1
Movies S1 and S2

12 December 2007; accepted 14 April 2008
10.1126/science.1154069

Metasomatized Lithosphere and the Origin of Alkaline Lavas

Sébastien Pilet,* Michael B. Baker, Edward M. Stolper

Recycled oceanic crust, with or without sediment, is often invoked as a source component of continental and oceanic alkaline magmas to account for their trace-element and isotopic characteristics. Alternatively, these features have been attributed to sources containing veined, metasomatized lithosphere. In melting experiments on natural amphibole-rich veins at 1.5 gigapascals, we found that partial melts of metasomatic veins can reproduce key major- and trace-element features of oceanic and continental alkaline magmas. Moreover, experiments with hornblendite plus lherzolite showed that reaction of melts of amphibole-rich veins with surrounding lherzolite can explain observed compositional trends from nephelinites to alkali olivine basalts. We conclude that melting of metasomatized lithosphere is a viable alternative to models of alkaline basalt formation by melting of recycled oceanic crust with or without sediment.

Trace-element and isotopic characteristics of alkaline [i.e., nepheline (ne)–normative] basalts from ocean islands and continents suggest the presence of enriched components in their mantle sources (*1*). These components are often interpreted as derived from recycled oceanic crust with or without sediment (*1*). An alternative is that the enriched components are recycled, metasomatized lithospheric mantle (*2*–*6*). Although both hypotheses are compatible with trace-element and isotopic characteristics of oceanic and continental alkaline magmas, they must also be capable of accounting for the distinctive major- and minor-element characteristics of alkaline basalts (Fig. 1).

Although basic to ultrabasic ne-normative liquids can be produced by low-degree melting of garnet lherzolite, no high-pressure melting experiments on "dry" peridotite have produced melt compositions that are plausible parents of alkaline ocean-island basalts (OIBs) (*7*–*10*). Addition of CO_2 to peridotite substantially modifies liquid compositions: Near-solidus melts are carbonatitic (*11*, *12*), but with increasing temperature, low-degree melts are silica-poor and CaO- and CO_2-rich (*11*). Such findings suggest that ne-normative magmas similar to natural alkaline basalts could be produced by low-degree melting (2 to 5%) of primitive mantle sources

Division of Geological and Planetary Sciences, California Institute of Technology, Pasadena, CA 91125, USA.

*To whom correspondence should be addressed. E-mail: sebastien.pilet@unil.ch

containing 0.1 to 0.25 weight percent (wt %) CO_2 (*11*). However, primitive mantle is too poor in TiO_2 to produce in this way melts with the high TiO_2 contents of alkaline basalts (*13*); this is consistent with the premise of both of the above hypotheses that components in addition to normal mantle peridotite are required in the sources of these magmas.

The melting of recycled oceanic crust has been investigated experimentally, and high-pressure partial melts of quartz and coesite eclogites (approximating average oceanic crust at high pressures) are hypersthene (hy)–normative, not ne-normative (i.e., they are silica-oversaturated rather than alkaline) (*14*, *15*) and thus cannot produce alkaline magmas directly. A possible resolution is that silica-oversaturated oceanic crust transforms to silica-deficient garnet pyroxenite by the extraction of silica-rich fluids or melts during subduction (*16*, *17*). High-pressure melting experiments on silica-deficient garnet-clinopyroxenite compositions, either dry (*16*, *17*) or with CO_2 (*18*), have indeed produced ne-normative liquids close in some respects to the compositions of alkaline basalts (Fig. 1). However, liquids from such experiments do not reproduce the K_2O contents of alkaline basalts (Fig. 1G), and the expected trace-element compositions of these liquids, although not addressed in these experimental studies, are dependent on the processes assumed for the origin of the silica-deficient pyroxenite sources and are consequently poorly constrained.

Hydrous minerals and enrichments in incompatible elements in mantle xenoliths demonstrate that metasomatism occurs in lithospheric mantle (*19*). Here, we present results of melting experiments on natural hornblendite and clinopyroxene (cpx) hornblendite to investigate whether melting of metasomatic hydrous veins could produce liquids consistent with the major- and trace-element compositions of alkaline magmas.

We selected hornblendite (AG4) and cpx hornblendite (AG7) starting materials from the French Pyrenees because they contain amphiboles (amph) typical of those in hydrous veins from the oceanic and continental lithosphere (Fig. 2). We conducted piston-cylinder experiments on these compositions at 1.5 GPa (corresponding to a depth of ~45 km, i.e., within the lithospheric mantle) and 1150° to 1400°C for 24 to 64 hours (*20*).

Glass compositions from experiments on both vein compositions were strongly alkaline (normative ne + leucite > 18 wt % for AG4 and > 11 wt % for AG7), and all had ≤44.1 wt % SiO_2 (Fig. 1A). Glasses from experiments at 1250° to 1300°C for both compositions overlapped the compositional fields of nephelinites and basanites from ocean islands and continental settings for most elements (Fig. 1 and fig. S1). Compositional similarities between initial partial melts of AG4 and AG7 reflected incongruent melting of amphibole in both lithologies [amph → ~0.6 melt + 0.3 cpx + minor olivine (ol) + spinel (sp)] at ~1150°C, the solidus for both compositions; that is, the composition of the subsolidus amph rather than the abundance

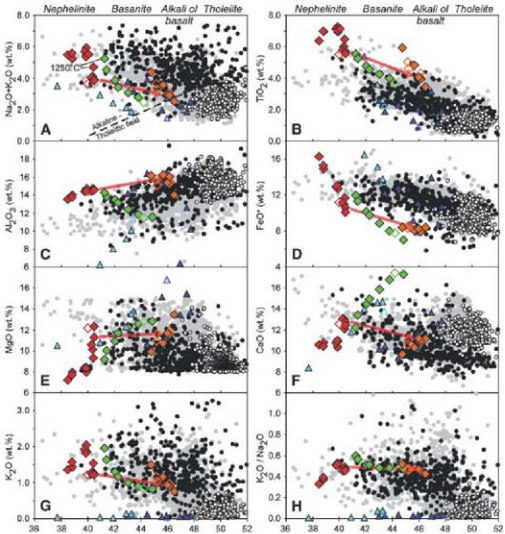

Fig. 1. Major oxides (**A** to **G**) and K_2O/Na_2O (**H**) versus SiO_2 (volatile-free) for hornblendite, clinopyroxene-hornblendite, sandwich experiments (hornblendite + peridotite), and silica-deficient garnet-pyroxenite melts (±CO_2) compared to continental and oceanic intraplate basalts and mid-ocean ridge basalt (MORB) compositions. The Macdonald-Katsura line [dashed line in (A)] separates alkaline from tholeiitic basalts. Positions of the terms nephelinite, basanite, alkali olivine (ol.) basalt, and tholeiite along the top of (A) and (B) denote the approximate silica values of each rock type. Solid gray circles, OIBs; solid black circles, continental intraplate basalts; open black circles, MORBs [all rock compositions are from GEOROC and PetDB databases (*36*) and have 8 to 15 wt % MgO]. Solid red and green diamonds, glass compositions from 1.5-GPa experiments on AG4 and AG7, respectively (the open diamonds are the starting compositions). Solid and open orange diamonds, glass compositions from 1.5-GPa sandwich experiments where orthopyroxene is present or absent, respectively, in the peridotitic layers. Solid dark and light blue triangles, glass compositions from 2- to 5-GPa experiments on silica-deficient garnet pyroxenites, dry (*16*, *17*) and in the presence of 5 wt % CO_2 (*18*), respectively (the open triangles are the starting compositions). The orange arrow in each panel connects the AG4 melt compositions to the compositions of glasses produced at same temperature (1300°C) in the sandwich experiments (AG4 + peridotite) and illustrates how melt compositions change with the assimilation of orthopyroxene (+ spinel) from the peridotite layers.

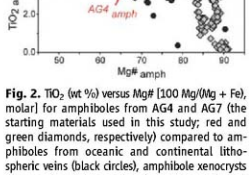

Fig. 2. TiO_2 (wt %) versus Mg# [100 Mg/(Mg + Fe), molar] for amphiboles from AG4 and AG7 (the starting materials used in this study; red and green diamonds, respectively) compared to amphiboles from oceanic and continental lithospheric veins (black circles), amphibole xenocrysts from continental basanites (open triangles), and amphiboles from metasomatized peridotite (gray diamonds) (*20*).

of cpx in the starting material was the major control on the solidus temperature and the composition of the initial melt. However, the liquidus temperatures of the two compositions were different: AG7 (with 45 wt % cpx) had a higher liquidus temperature than AG4 (with no observed cpx), ~1385°C versus ~1315°C.

The trace-element patterns of AG4 and AG7 experimental glasses were similar to those of the starting materials (Fig. 3A) but were progressively enriched relative to them with decreasing melt fraction and were somewhat enriched in more-incompatible relative to less-incompatible elements. The patterns of the starting materials and their partial melts were also generally similar to those of alkaline lavas, including features such as positive Nb and negative Pb anomalies (*1*) and elevated La/Yb ratios. In summary, the melts of amphibole-bearing metasomatic veins at 1.5 GPa were similar in major-, minor-, and trace-element compositions to those of oceanic and continental nephelinites and basanites.

The compositional continuum from nephelinites to alkali olivine basalts shown in Fig. 1 is observed in many alkaline suites (*21*, *22*). The trace-element patterns are generally similar for the various basic magmas from a single province, but with overall trace-element concentrations decreasing with decreasing alkalinity (i.e., as magmas become less ne-normative) (Fig. 3, C and D). This decrease in trace-element concentrations has been used to suggest that the continuum from nephelinite to alkali olivine basalt reflects an increase in the degree of partial melting of a common source (*21*, *22*); however, this continuum could also be explained by mixing of alkaline and tholeiitic liquids or reaction between nephelinitic or basanitic liquid and surrounding peridotite (*23*).

To test this latter hypothesis, we performed sandwich experiments in which a layer of AG4 hornblendite was packed between layers of moderately depleted peridotite (DMM1) (*24*) at 1.5 GPa and 1225° to 1325°C. The sandwich experiments yielded reactions between partial melts of the hornblendite (i.e., nephelinitic melts) and peridotite, even though temperatures were below the estimated anhydrous DMM1 solidus [~1330°C (*24*, *25*)]. Glasses from these experiments (Fig. 1) had SiO_2 contents 5 to 6 wt % higher than glasses from AG4 experiments at similar conditions (and therefore had lower normative nepheline; i.e., from ~4.5 wt % ne to ~2.0 wt % hy); somewhat lower TiO_2, FeO*, CaO, Na_2O, K_2O, and H_2O contents; and higher Al_2O_3 and MgO contents. Glasses from the sandwich experiments were generally similar to oceanic and continental alkaline basalts with 44 to 47 wt % silica (Fig. 1), and trends extending from the glasses from the hornblendite-only experiments to those from the sandwich experiments (red arrows in Fig. 1) paralleled the well-defined natural trends from nephelinites and basanites to alkali olivine basalts. The trace-element patterns of the sandwich experiments were parallel to, but ~25% lower than, those in glasses from AG4 experiments at the same temperature (Fig. 3B). These results suggest that major- and trace-element trends from nephelinites and basanites to alkali olivine basalts and tholeiites could be explained by interaction between hydrous nephelinitic melt and spinel peridotite dominated by reaction between the low-silica melt and orthopyroxene, generating a higher-silica melt plus olivine.

Two scenarios have been proposed for the production of alkaline magmas by melting of metasomatized lithosphere: (i) Shortly after or coincident with metasomatism, the lithosphere experiences a thermal perturbation or decompression and thereby melts in situ without recycling through the deeper mantle (*3*, *5*, *19*, *26*); or (ii) the metasomatized lithosphere is recycled into the convecting mantle by subduction or delamination and melts during later upwelling (e.g., in a plume) (*2*–*6*). The presence in continental alkaline magmas (*27*) of amphibole xenocrysts compositionally similar to amphiboles in metasomatic veins (Fig. 2 and fig. S2) and in metasomatized peridotite xenoliths (*19*) is consistent with the in situ hypothesis; that is, these xenocrysts and xenoliths could come from veins and associated cryptically metasomatized lithosphere formed during an earlier stage of volcanic activity that subsequently melted to produce the host alkaline magmas (*19*, *26*). The time between metasomatism of the lithosphere and the formation of the alkaline magmas cannot exceed the age of the lithosphere; however, long times are required to explain the range of isotopic ratios observed in some OIBs (e.g., from Tahaa, Raratonga, Tubuai, etc., in Polynesia) (*3*, *6*). The recycling scenario (*2*–*6*) could account for these long time scales: Such recycling could isolate metasomatic veins for times sufficient (1 billion to 2 billion years) for ingrowth of extreme isotopic ratios such as those observed in the OIBs from Polynesia (*6*).

Note that the details of melting of recycled metasomatic veins are likely to differ from those of our experiments; because amphiboles in lithospheric veins are not stable above 2.5 to 3 GPa (~100 km depth), deep recycling of these veins would result in amphibole breakdown, and thus subsequent melting of the veins during upwelling would involve dehydrated equivalents of the hydrous compositions we have studied. Experiments on dehydrated AG4 at 1.5 GPa (*20*) (table S1) show that glass compositions are still strongly ne-normative [consistent with experiments on

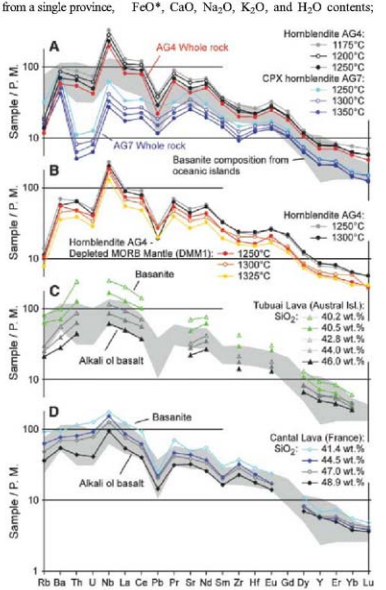

Fig. 3. Primitive mantle (*2*)–normalized trace-element abundances for **(A)** hornblendite and clinopyroxene-hornblendite melts, **(B)** melts produced in the hornblendite (AG4) + peridotite sandwich experiments (results from the 1250° and 1300°C AG4 melting experiments are shown for comparison), and **(C** and **D)** basanites (SiO_2 < 45 wt %) to alkali olivine basalts (SiO_2 > 45 wt %) from the island of Tubuai (Polynesia islands) (*22*) and the Cantal massif (France) (*6*). The gray band in (A), (C), and (D) shows the range (defined as ±1σ of the average of 195 analyses) of trace-element contents in low-silica OIB lavas (40 to 44 wt % SiO_2) with 8 to 15 wt % MgO [compiled from the GEOROC database (*36*)].

silica-poor garnet pyroxenites (*16*, *17*)] and similar to those produced in the experiments on the hydrated AG4 composition, which suggests that even deeply recycled metasomatized lithosphere could produce nephelinitic and basanitic magmas.

Although our data are consistent with the hypothesis that alkaline magmas are produced by melting of metasomatic veins, they do not provide constraints on vein formation mechanisms. The most widely cited mechanism is that these veins crystallize from low-degree melts of H_2O- and CO_2-bearing garnet peridotite (*4*, *5*, *28*, *29*), but individual veins are not thought to be representative of these low-degree melts (fig. S3). Instead, veins are explained as concentrations of phases crystallized from such melts as they cooled on ascent through the lithosphere, generating a continuum from anhydrous to hydrous assemblages (plus cryptically metasomatized adjacent peridotite) (*28*, *29*), and it is these fractionated cumulate assemblages that are the hypothesized sources of nephelinitic and basanitic magmas. Partial melts of amphibole-bearing veins formed as cumulates from low-degree mantle melts would have features characteristic of the trace-element patterns of alkaline lavas (*20*). For example, the positive Nb/La and Ce/Pb ratios observed in metasomatic veins (Fig. 3A and fig. S4) and in basic alkaline magmas (*1*) would not be interpreted as a characteristic of the mantle sources of the metasomatic liquid but would instead reflect amphibole-liquid distribution coefficients [$D_{Nb}^{amph/liq} > D_{La}^{amph/liq}$ and $D_{Ce}^{amph/liq} > D_{Pb}^{amph/liq}$ (*30*, *31*)]. On the other hand, some compositional characteristics of the metasomatic veins would be inherited directly from the low-degree melts of garnet peridotite from which they crystallize—for example, the high La/Yb ratios observed in whole-vein compositions (Fig. 3A) and in amphibole separates (fig. S4).

An important element of any model for the petrogenesis of alkaline basalts that invokes the melting of lithospheric lithologies (e.g., oceanic crust, with or without sediment or metasomatic veins) during upwelling is that the solidi of these lithologies must be lower than that of the enclosing peridotite. This point is satisfied by amphibole-bearing veins (or their dehydrated equivalents) and by oceanic crust [as eclogite (*15*) or after transformation into silica-deficient garnet pyroxenite (*16*, *17*)]. However, an aspect of decompression melting of a multilithologic mantle is that the various lithologies each influence the other's melting behavior, such that knowledge of the melting behaviors of the individual lithologies is not necessarily a guide to their behavior when they ascend together in a parcel of upwelling mantle (*32*, *33*). For example, suppose low-solidus vein material embedded in high-solidus peridotite begins to melt during adiabatic decompression but maintains thermal equilibrium with the adjacent, unmelted peridotite. In such a case, the degree of melting of the veins will be enhanced relative to the amount of melting that the same vein material would undergo if it were not embedded in the peridotite; meanwhile, the required latent heat essentially refrigerates the enclosing peridotite, and thus it will melt at lower pressure and to lower degrees than if the veins were not present (*33*). Thus, it can be anticipated that low-solidus vein material in upwelling mantle would melt more, relative to expectations based on its initial potential temperature, and that the peridotite would melt less (*32*, *33*). Therefore, recycled lithologies characterized by low solidus temperatures that are embedded in peridotite will likely melt to moderate to high degrees (especially if the enclosing peridotite also exceeds its solidus at some point during the ascent). However, subducted oceanic crust would have to melt to a low extent (≤1%) in order to explain the high trace-element contents of alkaline OIBs (*34*); such low degrees of melting seem inconsistent with the analysis above, and thus it is difficult to envision oceanic crust [or silica-deficient pyroxenite residual to extraction of fluids or melts from subducted oceanic crust (*16*, *17*)] as major trace element–bearing components of the sources of alkaline basalts. In sum, the consequences of multilithologic decompression melting are consistent with our experimental results, which suggest that high degrees of melting of metasomatic veins best explain the major- and trace-element contents of alkaline basalts.

Our results imply that the enriched component in alkaline basalts should not necessarily be equated with recycled oceanic crust and suggest that recycled components in the sources of islands characterized by tholeiitic magmas (i.e., Hawaii or Iceland) interpreted as recycled oceanic crust (*35*) are distinct from those in the sources of islands where ne-normative compositions are dominant (i.e., Polynesia, islands in the Atlantic Ocean, etc.). They also suggest that alkaline magmas are produced by high degrees of melting of a volumetrically minor mantle component rather than low degrees of melting of the dominant peridotite component. If so, these alkaline rocks do not carry as much information about the major components of the convecting mantle as is often presumed. Finally, the ranges in isotopic ratios observed in alkaline lavas from a single oceanic island do not necessarily imply the interaction between distinct mantle components such as high μ (μ = $^{238}U/^{204}Pb$), enriched mantle, and depleted MORB mantle (*1*). Instead, they could reflect in part the time-integrated history of a suite of veins with variable trace-element ratios (e.g., Nb/Th, Ba/Nb, and Ce/Pb; including ratios that control the evolution of critical isotopic systems such as U/Pb, Rb/Sr, and Sm/Nd) (*6*) resulting from percolative fractional crystallization of metasomatic agents in the lithosphere (*6*, *28*).

References and Notes

1. A. W. Hofmann, *Nature* **385**, 219 (1997).
2. S. S. Sun, W. F. McDonough, in *Magmatism in the Ocean Basins*, A. D. Saunders, M. J. Norry, Eds., Geological Society Special Publication 42 (Blackwell Scientific, Oxford, 1989), pp. 313–345.
3. A. N. Halliday *et al.*, *Earth Planet. Sci. Lett.* **133**, 379 (1995).
4. Y. L. Niu, M. J. O'Hara, *J. Geophys. Res.* **108**, 10.1029/2002JB002048 (2003).
5. D. McKenzie, R. K. O'Nions, *J. Petrol.* **36**, 133 (1995).
6. S. Pilet, J. Hernandez, P. Sylvester, M. Poujol, *Earth Planet. Sci. Lett.* **236**, 148 (2005).
7. E. Takahashi, I. Kushiro, *Am. Mineral.* **68**, 859 (1983).
8. K. Hirose, I. Kushiro, *Earth Planet. Sci. Lett.* **114**, 477 (1993).
9. I. Kushiro, in *Earth Processes: Reading the Isotopic Code*, A. Basu, S. Hart, Eds. (American Geophysical Union, Washington, DC, 1996), pp. 109–122.
10. M. J. Walter, *J. Petrol.* **39**, 29 (1998).
11. R. Dasgupta, M. M. Hirschmann, *J. Petrol.* **48**, 2093 (2007).
12. K. Hirose, *Geophys. Res. Lett.* **24**, 2837 (1997).
13. J. Prytulak, T. Elliott, *Earth Planet. Sci. Lett.* **263**, 388 (2007).
14. T. H. Green, D. H. Green, A. E. Ringwood, *Earth Planet. Sci. Lett.* **2**, 41 (1967).
15. M. Pertermann, M. M. Hirschmann, *J. Petrol.* **44**, 2173 (2003).
16. M. M. Hirschmann, T. Kogiso, M. B. Baker, E. M. Stolper, *Geology* **31**, 481 (2003).
17. T. Kogiso, M. M. Hirschmann, D. J. Frost, *Earth Planet. Sci. Lett.* **216**, 603 (2003).
18. R. Dasgupta, M. M. Hirschmann, K. Stalker, *J. Petrol.* **47**, 647 (2006).
19. F. E. Lloyd, D. K. Bailey, *Phys. Chem. Earth* **9**, 389 (1975).
20. See supporting material on *Science* Online.
21. F. A. Frey, D. H. Green, S. D. Roy, *J. Petrol.* **19**, 463 (1978).
22. M. Caroff, R. C. Maury, G. Guille, J. Cotten, *Contrib. Mineral. Petrol.* **127**, 369 (1997).
23. C. C. Lundstrom, J. Gill, Q. Williams, *Chem. Geol.* **162**, 105 (2000).
24. L. E. Wasylenki, M. B. Baker, A. J. R. Kent, E. M. Stolper, *J. Petrol.* **44**, 1163 (2003).
25. M. M. Hirschmann, *Geochem. Geophys. Geosyst.* **1**, 10.1029/2000GC000070 (2000).
26. S. Pilet, J. Hernandez, F. Bussy, P. J. Sylvester, *Geology* **32**, 113 (2004).
27. J. B. Dawson, J. V. Smith, *Mineral. Mag.* **45**, 35 (1982).
28. B. Harte, R. H. Hunter, P. D. Kinny, *Philos. Trans. R. Soc. London Ser. A* **342**, 1 (1993).
29. E. M. Morris, J. D. Pasteris, *Mantle Metasomatism and Alkaline Magmatism*, Special Paper 215 (Geological Society of America, Boulder, CO, 1987).
30. M. Tiepolo *et al.*, *Geochem. Geophys. Geosyst.* **1**, 10.1029/2000GC000064 (2000).
31. M. Tiepolo *et al.*, *Earth Planet. Sci. Lett.* **176**, 185 (2000).
32. M. M. Hirschmann, E. M. Stolper, *Contrib. Mineral. Petrol.* **124**, 185 (1996).
33. E. M. Stolper, P. D. Asimow, *Am. J. Sci.* **307**, 1051 (2007).
34. A. Stracke, M. Bizimis, V. J. M. Salters, *Geochem. Geophys. Geosyst.* **3**, 10.1029/2001GC000223 (2003).
35. A. V. Sobolev *et al.*, *Science* **316**, 412 (2007); published online 28 March 2007 (10.1126/science.1138113).
36. GEOROC database (http://georoc.mpch-mainz.gwdg.de/georoc); PetDB database (www.petdb.org/petdbWeb/index.jsp).
37. We thank S. Newman and A. Ulianov for their help during data acquisition by Fourier transform infrared spectroscopy and laser ablation inductively coupled plasma mass spectrometry, respectively, and B. Asambre and J. Hernandez for their help during sample collection. Supported by the Swiss National Science Foundation, the Société Académique Vaudoise, and NSF grant EAR-9528594.

Supporting Online Material

www.sciencemag.org/cgi/content/full/320/5878/916/DC1
Materials and Methods
Figs. S1 to S4
Tables S1 to S3
References

15 February 2008; accepted 2 April 2008
10.1126/science.1156563

Ultrafast Probing of Core Hole Localization in N_2

M. S. Schöffler,[1]* J. Titze,[1] N. Petridis,[1] T. Jahnke,[1] K. Cole,[1] L. Ph. H. Schmidt,[1] A. Czasch,[1] D. Akoury,[1,2] O. Jagutzki,[1] J. B. Williams,[3] N. A. Cherepkov,[4] S. K. Semenov,[4] C. W. McCurdy,[2,5] T. N. Rescigno,[2] C. L. Cocke,[5] T. Osipov,[2] S. Lee,[2] M. H. Prior,[2] A. Belkacem,[2] A. L. Landers,[3] H. Schmidt-Böcking,[1] Th. Weber,[2] R. Dörner[1]

Although valence electrons are clearly delocalized in molecular bonding frameworks, chemists and physicists have long debated the question of whether the core vacancy created in a homonuclear diatomic molecule by absorption of a single x-ray photon is localized on one atom or delocalized over both. We have been able to clarify this question with an experiment that uses Auger electron angular emission patterns from molecular nitrogen after inner-shell ionization as an ultrafast probe of hole localization. The experiment, along with the accompanying theory, shows that observation of symmetry breaking (localization) or preservation (delocalization) depends on how the quantum entangled Bell state created by Auger decay is detected by the measurement.

Valence electrons in molecules owe their binding force to their delocalization over two or more sites. By contrast, the orbital density of inner-shell electrons is confined near individual nuclei. The overlap of these wave functions from neighboring atoms is almost negligible (*1*). Still, the electronic structure of molecules with equivalent sites is generally calculated using symmetry-adapted delocalized wave functions for inner- as well as outer-shell electrons. In N_2, for example, the spatial distributions of the innermost electrons are usually described by $1\sigma_g$ and $1\sigma_u$ molecular orbitals, which are both delocalized over the two nuclei. For full shells, the quantum mechanical indistinguishability of the electrons renders the question of localization or delocalization meaningless. For a single hole created in an inner shell, however, the question is relevant.

Bagus and Schäfer (*2*), following a proposal of Snyder (*3*), found that allowing for a localization of the hole in a Hartree-Fock–type calculation lowers the total energy of the $O_2^+(1s^{-1})$ ion, yielding better agreement with experiment. However, it is now known that with more accurate approaches than Hartree-Fock, it is always possible to obtain accurate energies without the assumption of localized orbitals (*4*). Thus, the question of whether a localized hole is formed by photoionization of the K shell is left unanswered by quantum chemistry (*5*–*7*). Experimentally, the question is similarly controversial (*8*).

For K-shell ionization, the latest studies using high-resolution electron spectroscopy seem to support the picture of a delocalized hole. These experiments resolved the energy splitting between the gerade (g) and ungerade (u) states of the hole (*9*–*11*), which was found to be 100 meV for N_2. Ehara *et al.* (*11*) were able to track the photon energy dependence and even the photoelectron angular dependence for the g and u hole states separately, yielding very good agreement with a theory built on symmetry-adapted wave functions (i.e., a delocalized hole). In contrast, recent core hole photoelectron-photoion coincidence experiments on acetylene (HCCH) support the opposite view (*12*). The photoelectron angular distributions associated with nonsymmetric fragmentation show evidence of a localized core hole.

A puzzling question throughout this discussion is what physical process could possibly be responsible for the apparent break in the inversion symmetry of the system, leading to localization of the electron in the molecule. For molecules such as HCCH with equivalent sites, asymmetric vibrational modes are excited. The vibrational excitation breaks the original symmetry of the molecule and allows a localization of the hole [see, e.g., (*13*–*15*)]. For homonuclear diatomics, however, no such asymmetric modes exist and the only remaining means of labeling left

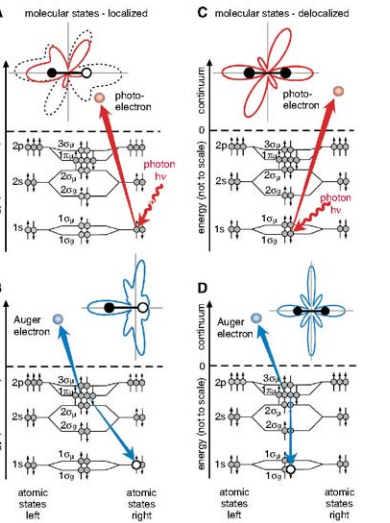

Fig. 1. Ultrafast probing of core hole localization by coincident detection of a photoelectron and an Auger electron. (**A** and **B**) Scenario for the case of a K hole localized at one atom. (**A**) Photoelectron is emitted from the right atom. The red line in the diagram shows the calculated angular distribution for this photoelectron at 9 eV; the light is circularly polarized, propagating into the plane of the figure. The orientation of the molecule is indicated by the barbell. In a standard experiment, where the Auger electron is not detected, one would measure the dotted black angular distribution, which is the sum of the electron emission pattern from the left and right atoms. (**B**) With a time delay of ~7 fs, the core hole decays by emission of an Auger electron (blue). The blue line in the diagram shows the calculated angular distribution of the Auger electron for assumed localization of the hole at the right atom. (**C** and **D**) Scenario for the case of a delocalized core hole in the $1\sigma_g$ molecular orbital. (**C**) The red line shows a RPA calculation of the photoelectron angular distribution, with electron energy of 9 eV, ejected from the $1\sigma_g$ shell by circularly polarized light. (**D**) Calculated angular distribution of Auger electron from decay of delocalized $1\sigma_g$ hole state. Detecting photoelectrons and Auger electrons in coincidence in the localized scenario reveals broken symmetry, whereas inversion symmetry is preserved in a coincidence experiment for the delocalized scenario.

[1]Institut für Kernphysik, Johann Wolfgang Goethe-Universität Frankfurt am Main, Max-von-Laue-Str. 1, 60438 Frankfurt, Germany. [2]Lawrence Berkeley National Laboratory, Berkeley, CA 94720, USA. [3]Department of Physics, Auburn University, Auburn, AL 36849, USA. [4]State University of Aerospace Instrumentation, 190000 St. Petersburg, Russia. [5]Department of Physics, Kansas State University, Cardwell Hall, Manhattan, KS 66506, USA.

*To whom correspondence should be addressed. E-mail: schoeffler@atom.uni-frankfurt.de

and right sides is by the charge states of the ions created by fragmentation. For H_2 ionization followed by asymmetric dissociation to a neutral H atom and a proton, we have recently shown that the symmetry of the photoelectron can be broken if intermediate doubly excited states are involved (*16*). The case discussed here is much more fundamental because even the ion charge states are symmetric. The N_2 ultimately fragments into two indistinguishable N^+ ions, both in their electronic ground state. Does this mean that the symmetry must be conserved?

We used a distinct approach to address this question. A core-ionized molecule is not stable. The core hole decays, in many cases by emission of an Auger electron. In the Auger decay, an electron from an outer shell fills the core hole while a second outer-shell electron is emitted, carrying the excess energy. This decay can be thought of as a measurement: The photoabsorption is a pump step, and the Auger decay acts as an ultrafast probe step delayed by the lifetime of the hole (~7 fs). The Auger electron carries information about the hole that was filled. In our coincidence experiment we read out this information.

The experimental idea is sketched in Fig. 1 together with our calculated distributions (see below), assuming either a localized hole (Fig. 1, A and B) or one of the two possible delocalized core holes (Fig. 1, C and D). Clearly, the Auger and photoelectron angular distributions in the body-fixed frame of the molecule are different in the two cases. However, if (as in all previous experiments) the two electrons are not detected in coincidence, then, even with the localized assumption, emission from the left and right atoms would be equally probable, and the experiment would yield a distribution characterized by the inversion symmetry shown by the black dashed line in Fig. 1A (the sum of the red curve and its inverse image). An identical result would be obtained by summing the delocalized $1\sigma_g$ (Fig. 1, C and D) and $1\sigma_u$ core hole contributions. By tracking both electrons, however, the localized case might be expected to show an asymmetric pattern for the photoelectron, if the Auger electron is detected (for example) on the left. In contrast, with the delocalized assumption (Fig. 1, C and D), all coincident electron distributions will always show inversion symmetry. In reality, both situations are realized, depending on the angles of the photoelectron and Auger electron emissions. This is possible because of the quantum nature of the two entangled electrons, which form a Bell state.

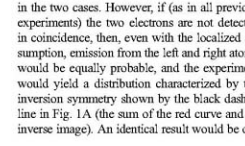

Scheme 1.

The photoinduced process can be described more completely as a three-step model (Scheme 1). First, the absorption of a photon ejects a photoelectron from the K shell of N_2, creating a hole in the 1s shell $N_2^+(1s^{-1})$. We directly measure the trajectory of this electron with respect to the molecular axis in our experiment. The energy of the photoelectron (9 eV in this case) is determined by the excess photon energy. Second, the $N_2^+(1s^{-1})$ decays to N_2^{2+} by emission of a fast Auger electron (around 370 eV), which is also measured in coincidence. Finally, the N_2^{2+} dissociates into two N^+ ions with a kinetic energy release (KER) in the region of 4 to 20 eV. The question of core hole localization concerns the character of a short-lived transient state of $N_2^+(1s^{-1})$.

Parity describes the behavior of a system's wave function under inversion through the center of the molecule. If the system is in a quantum state of well-defined gerade or ungerade parity, all observables are fully symmetric under inversion, because they are obtained from the squared modulus of the wave function. A hole localized on one of the N_2 atoms implies that the wave function is not a pure symmetry eigenstate but rather a coherent superposition of gerade and ungerade states.

The process we measure begins with the N_2 molecule in its ground state, which has $^1\Sigma_g$ symmetry. After absorption of the photon, simple selection rules dictate that the system consisting of N_2^+ and the photoelectron must have (Σ or Π) ungerade symmetry. After the Auger decay, the new system consisting of N_2^{2+}, the photoelectron, and the Auger electron must also have ungerade symmetry, because Auger decay cannot change the overall parity of the system. Auger decay can, however, populate states of N_2^{2+} of any symmetry or parity. In our data reduction, we select the decay to the $^1\Sigma_g^+(1\pi_u^{-2})$, $^1\Delta_g(1\pi_u^{-2})$, and $^3\Pi_g(1\pi_u^{-1}2\sigma_g^{-1})$ states of N_2^{2+} for further analysis [see (*17*) for the assignment of states]. All these states have gerade parity, but the total system must have ungerade parity, as explained above. Consequently, the photoelectron and Auger electron must have opposite parity to each other, one gerade and the other ungerade.

To analyze our findings theoretically, we exploit a two-step model in which we describe the steps of photoionization and subsequent Auger decay by the product of a dipole amplitude $\langle\Psi^+_{f,\sigma_{u/g}}\psi_{\mathbf{k}_p}|d|\Psi_0\rangle$ describing the former, and of a Coulomb matrix element $\langle\Psi^{2+}_f\psi_{\mathbf{k}_e}|V|\Psi^+_{f,\sigma_{u/g}}\rangle$ describing the latter. The subscript f refers to the final state of N_2^{2+}. We choose gerade and ungerade molecular states $\Psi^+_{f,\sigma_{u/g}}$ for the intermediate, core-ionized singly charged ion, and coherently sum the amplitudes corresponding to these intermediate core hole states before computing the probabilities for producing the various N_2^{2+} final states.

Using a completely coherent superposition of two pathways to the final state via the $1\sigma_u^{-1}$ and $1\sigma_g^{-1}$ intermediate states would be correct only if the two states were energetically degenerate or if the pathways could not be distinguished by the energy of the photoelectron. The core g/u energy splitting of 100 meV in N_2 (*9*, *11*) is comparable to the natural widths of the $^2\Sigma_g^+(1\sigma_g^{-1})$ and $^2\Sigma_u^+(1\sigma_u^{-1})$ states, which are lifetime-limited. Therefore, the states cannot be fully resolved in principle and their amplitudes must be added coherently. With this assumption, the cross section for coincident detection of a photoelectron into the solid-angle element $d\Omega_{\mathbf{k}_p}$ and an Auger electron into $d\Omega_{\mathbf{k}_e}$ is given by

$$\frac{d\sigma}{d\Omega_{\mathbf{k}_e}d\Omega_{\mathbf{k}_p}} = \sum_f \left|\langle\Psi^{2+}_f\psi_{\mathbf{k}_e}|V|\Psi^+_{\sigma_g}\rangle\langle\Psi^+_{\sigma_g}\psi_{\mathbf{k}_p}|d|\Psi_0\rangle + \langle\Psi^{2+}_f\psi_{\mathbf{k}_e}|V|\Psi^+_{\sigma_u}\rangle\langle\Psi^+_{\sigma_u}\psi_{\mathbf{k}_p}|d|\Psi_0\rangle\right|^2 \quad (1)$$

It is only the interference term between the $1\sigma_g$ and $1\sigma_u$ amplitudes in Eq. 1 (the product of the terms being added in the coherent sum) that can break the symmetry of the system, as the individual cross sections are symmetric under inversion.

To simulate the photoionization process and the photoelectron wave function $\psi_{\mathbf{k}_p}$, we applied the random phase approximation (RPA) with relaxation effects included (*18*, *19*). The equations derived by Zähringer *et al.* (*20*) were used for the calculation of the Auger decay amplitudes (*21*) into three final N_2^{2+} states, $^1\Sigma_g^+(1\pi_u^{-2})$, $^1\Delta_g(1\pi_u^{-2})$, and $^3\Pi_g(1\pi_u^{-1}2\sigma_u^{-1})$, which correspond to the experimental KER values. For every final state, the Auger electron wave function $\psi_{\mathbf{k}_e}$ was calculated using the Hartree-Fock (HF) approximation in the frozen field of the corresponding doubly charged ion. We note that the contribution from the $^3\Pi_g(1\pi_u^{-1}2\sigma_u^{-1})$ state is very small.

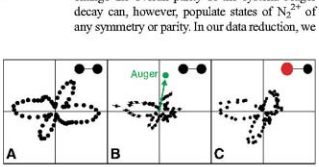

Fig. 2. Photoelectron angular distribution in the molecular frame for circularly polarized light. The photon propagation direction is into the plane of the figure. The orientation of the molecular axis is indicated by the barbells. The photoelectron energy is 9 eV. **(A)** N_2 K-shell ionization integrated over all Auger electron angles. **(B)** Subset of data in (A), where the Auger electron is emitted at 80° to the molecular axis, as indicated by the arrow. **(C)** Distribution of photoelectrons emitted from the carbon K shell of CO (black end of the barbell).

The results shown in Fig. 1, C and D, for an assumed delocalized core hole were calculated from the square of the $1\sigma_g$ amplitudes in Eq. 1. The case of the localized core hole was calculated by a coherent sum of the gerade and ungerade amplitudes with equal weight for the g and u states. In general, although the calculations provide two different types of distributions (localized and delocalized) for the Auger electron and the photoelectron, the experiment shows that the emission pattern depends on the observation angle of either the Auger electron or the photoelectron.

The experiment was performed at the Advanced Light Source of Lawrence Berkeley National Laboratory via the cold target recoil ion momentum spectroscopy (COLTRIMS) technique (*22*, *23*). Circularly polarized photons (419 eV) from beamline 11 were intersected with a precooled supersonic beam of N_2 in the vibrational ground state. The photoelectron was guided by parallel electric (12 V/cm) and magnetic (6.5 G) fields toward a multichannel plate detector (diameter 80 mm) with delay-line position readout (*24*). Those N_2^{2+} ions that fragmented within 15° parallel to the electric field axis of our spectrometer were guided toward a second position-sensitive detector, 72 cm from the interaction point. From the position of impact and the time of flight of the photoelectron and ions, we could determine their vector momenta. To improve the ion momentum resolution, we used a three-dimensional time and space–focusing ion optics setup [see figure 12 in (*22*)]. Momentum vectors of the photoelectron and the two ions from the four-body final state (ϵ_{photo}, ϵ_{Auger}, N^+, and N^+) were measured directly, whereas the momentum of the fourth particle, the Auger electron, was obtained through momentum conservation.

The experiment yielded the full 4π solid angle distribution for the Auger electron and photoelectron and ~1% solid angle for the ion momentum. We obtained an overall resolution of better than 50 meV for the KER and 0.5 atomic unit momentum resolution on the center of mass motion (the calculated Auger electron). The breakup is known to be much faster than the rotation, so the direction of the N^+ fragments coincides with the direction of the molecule upon photoabsorption (*25*) [axial recoil approximation (*26*)]. By coincident measurement of electron and fragmentation direction, we determined the electron angular distributions in the body-fixed frame of the molecule without aligning the gas-phase molecule in advance (*27*). The data were recorded in list mode, so any combination of angles and energies of the particles could be sorted in the off-line analysis without repeating the experiment. All spectra reported were taken simultaneously with the same apparatus to reduce possible systematic errors.

The coincident detection measurements directly show the localized character of the emission site for certain emission angles of the Auger electron. Figure 2A displays the photoelectron angular distribution for a 9-eV photoelectron ejected by circularly polarized light in the molecular frame. No specific Auger electron direction is selected in this spectrum (noncoincident detection). The data agree very well with similarly measured published data (*28*). The distribution has inversion symmetry because the N^+ fragments are indistinguishable. However, if we examine a subset of these data in which the Auger electron is emitted at an angle of 80° with respect to the molecular axis, the inversion symmetry of the photoelectron angular distribution is strongly broken (Fig. 2B). These coincident data closely resemble the pattern found for carbon K-shell ionization in CO, shown in Fig. 2C for comparison. CO is isoelectronic with N_2, and the carbon K shell is selected by the energy. The comparison suggests that in Fig. 2B the K hole in N_2 is localized to the right.

We now show that the results presented in Fig. 2 strongly depend on the choice of direction of the Auger electron. The angular distributions of the Auger electron and photoelectron are shown in Fig. 3, A and F, respectively. In both cases, the corresponding other electron is not detected (integrated over all angles in our case): The experiment thus measures the incoherent sum of the theoretical amplitudes for the gerade and ungerade contributions. Although theoret-

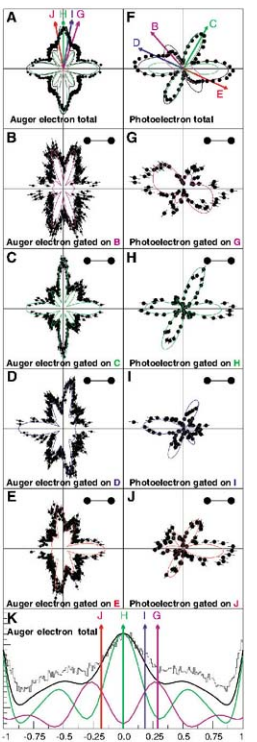

Fig. 3. Auger electron and photoelectron angular distributions in the molecular frame for circularly polarized light with an incident energy of E_γ = 419 eV. Dots are experimental data; lines represent theory according to Eq. 1. The molecular axis (N_2) is shown by the barbell, and the photon propagation direction is into the plane of the figure. (**A** to **E**) Auger electron angular distribution; (**F** to **J**) photoelectron angular distribution. (**A**) and (**F**), noncoincident detection (integrated over the second electron); (**B**) to (**E**), Auger electron distributions when photoelectrons are emitted at selected angles as indicated in (**F**); (**G**) to (**J**), photoelectron distributions when Auger electrons are emitted at selected angles as indicated in (**A**). (**K**) The same data as in (**A**), but not in polar form. The pink and green lines represent the g and u contributions; the black line is the sum.

ically we can perform the full calculation with either localized or delocalized hole states, only the experiment tells unambiguously which description is appropriate. The experimental data allow selection of the theoretical model that adequately describes the observed phenomena. From such noncoincident angular distributions, no information about the character of the core hole can be obtained. The calculated Auger electron angular distribution shows very narrow structures.

The photoelectron angular distributions for four different fixed directions of the Auger electron are shown in Fig. 3, G to J. We find a striking change in these distributions upon small changes in the angle of the coincident Auger electron. If the Auger electron is detected in a direction where, according to the calculations, only the components associated with filling a $1\sigma_u$ vacancy contribute (72.5°, Fig. 3A), then the photoelectron shows an angular distribution that coincides with that calculated for the gerade photoelectron. Correspondingly, if the Auger electron is detected around 90° to the molecular axis, where the $1\sigma_u$ contribution has a node, the photoelectron angular distribution appears dominated by ungerade symmetry. Note that for this particular geometry at 90° to the molecule, our analysis of the symmetry of the Auger electron does not even require a calculation. If we ignore the small contribution from the $^3\Pi_g(1\pi_u^{-1},2\sigma_u^{-1})$ final state, then the node at 90° follows from the properties of an ungerade Auger electron wave of σ or δ symmetry. Two waves emerging from a double slit with π phase shift destructively interfere at the center between the slits.

Our results show that if the Auger electron is selected in a direction where only gerade waves contribute, the corresponding photoelectron wave has ungerade parity, and vice versa. Because the photoelectron and the hole states must have opposite parities, knowledge of the photoelectron parity reveals the parity of the hole state, which must be delocalized in this case.

The other extreme is shown in Fig. 3, I and J. Here the Auger electron is selected in directions slightly to the left or the right of 90° to the molecular axis, where, according to the calculations, the g and u components contribute equally. In this case, the photoelectron angular distribution shows the strongly broken symmetry already discussed in connection with Fig. 2. The hole appears localized on the right or left atom, respectively. A change of the Auger angle from 80° to 100° is sufficient to apparently switch the site of the core hole from left to right (Fig. 3, I and J). On the other hand, these angular distributions are correctly reproduced by our calculation using a coherent superposition of the gerade and ungerade hole states in Eq. 1.

In our calculations, we used gerade and ungerade orbitals, but we would obtain equivalent results with left- and right-localized functions. Wave functions in one basis are easily expressed through the wave functions in the other basis. It is the coherent combination of amplitudes, expressed in either basis, that leads to the observed results. Photoelectron ejection and the subsequent decay create a fully entangled electron pair, which by our measurement we project onto either of these basis states. This is by analogy to an entangled two-photon state, for which measurement of one photon by a horizontal linear polarizer projects the other photon onto a state of vertical polarization; similarly, circular polarizers project onto left and right circular bases.

If we select from all Auger electrons depicted in Fig. 3A only those associated with a photoelectron in a certain direction (indicated by the arrows in Fig. 3F), then measuring the photoelectron in a direction where only gerade photoelectrons contribute projects the Auger electrons onto the ungerade continuum states (Fig. 3B). Correspondingly, selecting a photoelectron direction where only the u state contributes results in a g-type angular distribution of the Auger electron (Fig. 3C). Selecting photoelectron angles where g and u contribute equally projects the Auger electron onto a left (Fig. 3D) or right (Fig. 3E) state.

What conclusion can be drawn with respect to the question of core hole localization? To discuss this question in a quantum mechanically meaningful way, it is first necessary to include the decay, which is an inherent property of the excited molecule. Whether the core hole is better thought of as being localized or delocalized depends on the direction in which the photoelectron or Auger electron is emitted. Detecting the direction of the photoelectron in the experiment selects between cases in which the transient core hole is best described by a delocalized state of g or u symmetry, and other cases for which it is more appropriate to think of a localized hole. This situation can be described by a coherent superposition of gerade and ungerade states, or alternatively by a superposition of states corresponding to a hole on the left and one on the right.

In using a coherent superposition of g/u hole states to analyze our results, we have ignored any physical processes that might destroy this localization. The g/u hole states have a small energy splitting (*9*, *11*), which can be expressed in the time domain as a hopping of a 1s vacancy between the two atoms (*3*). The 100-meV splitting corresponds to a hopping time from one side to the other of ~20 fs. This time is long relative to the ~7-fs lifetime of the hole states, so in most cases the Auger decay takes place before the hole changes sites. Cases where the hopping time and Auger lifetime are comparable would require a time-dependent treatment and invite time-resolved experiments. An example of a time-resolved experiment for a different process was recently reported (*29*). To date, only the coupling of vacancies to the nuclear degrees of freedom (such as vibrational modes) has been considered in the literature. Our experiment shows that this topic should be revisited while carefully addressing the electronic decay of the states (*30*).

More generally, we have shown that detecting the signals (electrons in our case) from the creation and time-delayed decay of vacancies gives insight into the transient structure of extremely short-lived species. This methodology is not limited by the time resolution of the pump and probe pulses. Therefore, it allows us to exploit high-resolution radiation sources such as synchrotrons and future free-electron lasers. The ultrafast time correlation is provided by the short-lived transient species and its decay dynamics. Recent progress in coincidence techniques for electrons from surfaces (*31*–*33*) shows that application of this scheme in solid-state physics is within reach.

References and Notes

1. N. Kosugi, *Chem. Phys.* **289**, 117 (2003).
2. P. S. Bagus, H. F. Schäfer, *J. Chem. Phys.* **56**, 224 (1972).
3. L. C. Snyder, *J. Chem. Phys.* **55**, 95 (1971).
4. J. F. Stanton, J. Gauss, R. J. Bartlett, *J. Chem. Phys.* **97**, 5554 (1992).
5. J. A. Kintop, W. V. M. Machando, L. G. Ferreira, *Phys. Rev. A* **43**, 3348 (1991).
6. D. Dill, S. Wallace, *Phys. Rev. Lett.* **41**, 1230 (1978).
7. L. S. Cederbaum, W. Domcke, *J. Chem. Phys.* **66**, 5084 (1977).
8. O. Björneholm *et al.*, *Phys. Rev. Lett.* **84**, 2826 (2000).
9. U. Hergenhahn, O. Kugeler, A. Rüdel, E. E. Rennie, A. Bradshaw, *J. Phys. Chem. A* **105**, 5704 (2001).
10. D. Rolles *et al.*, *Nature* **437**, 711 (2005).
11. M. Ehara *et al.*, *J. Chem. Phys.* **124**, 124311 (2006).
12. J. Adachi *et al.*, *J. Phys. B* **40**, F285 (2007).
13. A. Kivimäki *et al.*, *Phys. Rev. Lett.* **79**, 998 (1997).
14. W. Domcke, L. S. Cederbaum, *Chem. Phys.* **25**, 189 (1977).
15. F. X. Gadea, H. Köppel, J. Schirmer, L. S. Cederbaum, *Phys. Rev. Lett.* **66**, 883 (1991).
16. F. Martín *et al.*, *Science* **315**, 629 (2007).
17. M. Lundqvist, D. Edvardsson, P. Baltzer, B. Wannberg, *J. Phys. B* **29**, 1489 (1996).
18. S. K. Semenov, N. A. Cherepkov, T. Jahnke, R. Dörner, *J. Phys. B* **37**, 1331 (2004).
19. S. K. Semenov *et al.*, *J. Phys. B* **39**, 375 (2006).
20. K. Zilberinger, H.-D. Meyer, L. S. Cederbaum, *Phys. Rev. A* **45**, 318 (1992).
21. S. K. Semenov *et al.*, *Phys. Rev. A* **75**, 032707 (2007).
22. R. Dörner *et al.*, *Phys. Rep.* **330**, 95 (2000).
23. J. Ullrich *et al.*, *Rep. Prog. Phys.* **66**, 1463 (2003).
24. O. Jagutzki *et al.*, *Nucl. Instr. Methods A* **477**, 244 (2002).
25. T. Weber *et al.*, *J. Phys. B* **34**, 3669 (2001).
26. R. N. Zare, *Mol. Photochem.* **4**, 1 (1972).
27. E. Shigemasa, J. Adachi, M. Oura, A. Yagishita, *Phys. Rev. Lett.* **74**, 359 (1995).
28. T. Jahnke *et al.*, *Phys. Rev. Lett.* **88**, 073002 (2002).
29. E. Gagnon *et al.*, *Science* **317**, 1374 (2007).
30. S. A. Malinovskaya, L. S. Cederbaum, *Int. J. Quantum Chem.* **80**, 950 (2000).
31. M. Hattass *et al.*, *Rev. Sci. Instrum.* **75**, 2373 (2004).
32. W. S. M. Werner *et al.*, *Phys. Rev. Lett.* **94**, 038302 (2005).
33. F. O. Schumann, C. Winkler, J. Kirschner, *Phys. Rev. Lett.* **98**, 257604 (2007).

34. We thank K. Ueda, L. Cederbaum, U. Becker, and U. Hergenhahn for enlightening discussions; the staff of the Advanced Light Source for outstanding support, in particular by H. Bluhm and T. Tyliszczak; and the J. W. Goethe-Universität for hospitality and financial support during S.K.S.'s stay in Frankfurt. Supported by INTAS grant 03-51-4706 (N.A.C. and S.K.S.), the Deutsche Forschungsgemeinschaft, and the Office of Basic Energy Sciences, Division of Chemical Sciences, U.S. Department of Energy, under contracts DE-AC03-76SF00098 and DE-FG02-07ER46357.

8 January 2008; accepted 2 April 2008
10.1126/science.1154989

Measuring Picosecond Isomerization Kinetics via Broadband Microwave Spectroscopy

Brian C. Dian,* Gordon G. Brown, Kevin O. Douglass, Brooks H. Pate†

The rotational spectrum of a highly excited molecule is qualitatively different from its pure rotational spectrum and contains information about the intramolecular dynamics. We have developed a broadband Fourier transform microwave spectrometer that uses chirped-pulse excitation to measure a rotational spectrum in the 7.5- to 18.5-gigahertz range in a single shot and thereby reduces acquisition time sufficiently to couple molecular rotational spectroscopy with tunable laser excitation. After vibrationally exciting a single molecular conformation of cyclopropane carboxaldehyde above the barrier to C–C single-bond isomerization, we applied line-shape analysis of the dynamic rotational spectrum to reveal a product yield and picosecond reaction rate that were significantly different from statistical predictions. The technique should be widely applicable to dynamical studies of radical intermediates, molecular complexes, and conformationally flexible molecules with biological interest.

Pure rotational spectroscopy has played an important role in molecular structure determination for many decades. Much of the current work in molecular rotational spectroscopy uses pulsed molecular-beam sources to produce cold, gas-phase samples. The high resolution and sensitivity of current cavity-based Fourier transform microwave (FTMW) molecular-beam spectrometers, a design pioneered by Balle and Flygare almost 30 years ago (*1*), allow structure determination for a wide range of biologically relevant molecules (*2*), weakly bound van der Waals clusters (*3*), environmentally important radicals (*4*), and molecules of potential importance in astronomy such as the first molecular anion detected in the interstellar medium, which was identified by its laboratory rotational spectroscopic signature (*5*).

Beyond structure determination, we have applied rotational spectroscopy to probe intramolecular dynamics (*6*–*8*). The rotational spectrum of a highly excited molecule displays qualitatively new features that come from the nuclear motion associated with intramolecular vibrational energy redistribution (IVR) and isomerization. Whereas the moments of inertia are constant in pure rotational spectroscopy, they become time-dependent quantities in a highly excited molecule. The modulation of the molecular rotational frequency by the fluctuating nuclear geometry causes changes to the overall line shape of the spectrum in a way that is analogous to motional effects in dynamic nuclear magnetic resonance spectroscopy (*9*, *10*). In particular, isomerization kinetics can be determined through coalescence of the spectrum at a frequency between the characteristic pure rotational frequencies of the reactant and product. The frequency separation between characteristic rotational frequencies can be several gigahertz for dynamic rotational spectroscopy (DRS), making it possible to study picosecond–time scale isomerization reactions.

The experimental demands for DRS are challenging. For example, coalescence caused by isomerization can produce a rotational spectrum that spans a range of several gigahertz. Because the molecule remains bound at all times during isomerization, the spectrum will consist of a series of quantum state–resolved transitions whose intensity profile reflects the smooth coalescence line shape. Accurate spectral intensity information across the entire measurement bandwidth is therefore essential to the kinetic analysis. Furthermore, the total rotational spectral intensity is conserved during coalescence, meaning that the signal strength of any individual transition will be diluted by the isomerization kinetics. Finally, the experiments are limited by the properties of the laser source used to generate the excited-state population. A high-resolution laser is used to prepare one (or a small number) of highly excited quantum states. The laser frequency must be stabilized and power fluctuations minimized during the course of the rotational spectrum acquisition to ensure constant population transfer to the excited state. A rotational spectroscopy technique capable of fast spectrum acquisition is favored to minimize the effects of power variation and laser frequency drift.

We have developed a broadband FTMW spectrometer for applications in DRS that offers orders of magnitude improvement in spectrum acquisition times (*11*). This spectrometer exploits recent advances in digital electronics to measure the molecular rotational spectrum in the 7.5- to 18.5-GHz frequency range in a single data acquisition event. By comparison, a cavity-FTMW spectrometer has a measurement bandwidth of about 500 kHz and would require 22,000 measurement steps to cover the same spectral region. The technique introduces three major changes to previous FTMW measurements. First, a chirped pulse with a linear frequency sweep from 7.5 to 18.5 GHz is used to polarize the sample through fast passage excitation. McGurk, Schmalz, and Flygare first recognized that rapid passage produces strong sample polarization in rotational spectroscopy, in experiments where the molecular transition frequency was swept through a fixed microwave frequency using the Stark effect (*12*). Second, the chirped pulse is generated by a high-speed arbitrary waveform generator (AWG) that is phase-locked

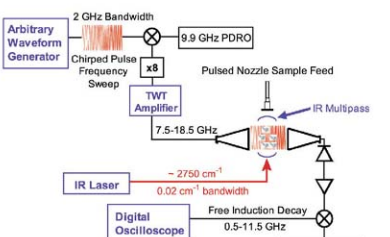

Fig. 1. A schematic diagram of the CP-FTMW spectrometer. The chirped pulses are generated via an AWG (AWG710B, Tektronix Inc., Beaverton, Oregon) and a microwave circuit for frequency up-conversion and bandwidth extension (fig. S1). The chirped pulse (linear frequency sweep of 7.5 to 18.5 GHz with a 1-μs pulse duration) is amplified by a pulsed traveling wave-tube (TWT) amplifier (1000TP8G18, Amplifier Research, Souderton, Pennsylvania). The amplified pulse is broadcast into the sample interaction region of a molecular-beam spectrometer with a WRD750 standard gain horn. The molecular beam is created by a pulsed-jet expansion of 0.5% CPCA in an 80:20 neon-to-helium gas mixture. The backing pressure behind the nozzle (Series 9, Parker Hannifin, Pine Brook, New Jersey) is 1 atm, the nozzle diameter is 1 mm, and the pulse duration is 500 μs. The infrared laser pulse is coupled into the interaction region with a plane-parallel multipass cell. After the rotational FID is collected by the second WRD750 horn, amplified, and down-converted to the 0.5- to 11.5-GHz band, it is digitized at 40 Gs/s via a digital oscilloscope (TDS6124C, Tektronix Inc., Beaverton, Oregon).

Department of Chemistry, University of Virginia, McCormick Road, Charlottesville, VA 22904–4319, USA.

*Present address: Department of Chemistry, Purdue University, 560 Oval Drive, West Lafayette, IN 47907–2084, USA. †To whom correspondence should be addressed. E-mail: brookspate@virginia.edu

to a rubidium-disciplined crystal oscillator. The phase-reproducible chirped pulses created by the AWG allow time-domain signal averaging of the coherent molecular emission. Third, the rotational free induction decay (FID) is recorded with a high-speed digital oscilloscope to capture signals over the full spectrometer bandwidth on each data acquisition event. The frequency-domain spectrum is recovered through fast Fourier transform of the rotational FID. We term the technique chirped-pulse Fourier transform microwave (CP-FTMW) spectroscopy to emphasize these essential features of the design.

For broadband FTMW spectroscopy, the chirped pulse offers two more crucial advantages. First, frequency bandwidth and pulse duration are decoupled in the chirped pulse. This behavior is different from the transform-limited, or "hard," pulses usually used in Fourier transform spectroscopy, where bandwidth increases must be achieved by shortening the pulse. Using "stretched" pulses, we can deliver more energy to the sample from a microwave amplifier with fixed peak power. Second, there is a simple method to extend the bandwidth of a chirped microwave pulse. When a chirped pulse passes through a microwave frequency multiplier, the bandwidth increases by the multiplication factor of the device while the pulse duration is preserved. This effect enables high-bandwidth pulse synthesis via current AWG technology.

A schematic of the CP-FTMW spectrometer is shown in Fig. 1. The three major components are the pulse generation system, the sample interaction region, and the broadband FID detector. The most important design choices are related to the pulse generation system, where a chirped excitation pulse with a linear frequency sweep is created and amplified. The first step

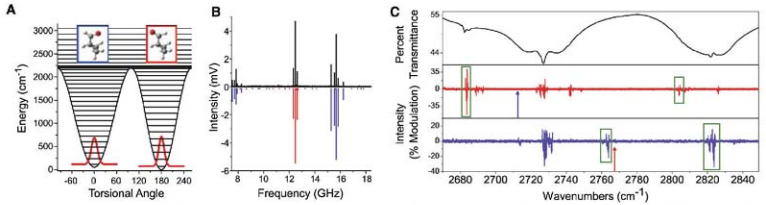

Fig. 2. The key physical quantities for the DRS experiments. **(A)** The potential energy surface for conformational isomerization of CPCA calculated at the B3LYP/6-31+G** level of theory is shown. Superimposed on the surface are the torsional energy levels calculated from the 1D torsional Hamiltonian. Molecular structures of the syn (blue) and anti (red) conformers are shown as insets. This conformer color code is also used in Figs. 3 and 4. The probability distributions for the lowest torsional energy levels of each conformer are displayed. **(B)** The CP-FTMW spectrum of CPCA recorded with a single valve pulse (positive, black) is compared with the calculated spectrum for the syn (negative, blue) and anti (negative, red) conformers. The strongest pure rotational transition for each conformer is the 2_{02}–1_{01} (standard asymmetric top notation, $J_{K_aK_c}$) *a*-type transition at 12471 MHz (anti) and 15686 MHz (syn). A larger version of this figure is shown in the SOM (fig. S2). **(C)** The conformer-selective infrared spectra of CPCA in the aldehyde C–H stretch region extracted from the CP-FTMW spectra are shown. The red trace shows the laser-induced changes to the 2_{02}–1_{01} rotational frequency of the anti conformer (12471 MHz) as a function of the laser frequency. The laser-induced signal changes for the 2_{02}–1_{01} rotational transition of the syn conformer (15686 MHz) are shown in blue. Arrows indicate the ab initio predictions for the aldehyde C–H–stretching fundamental (table S2). Boxes highlight the vibrational bands examined in this study. The room-temperature gas-phase Fourier transform infrared spectrum of CPCA is shown in the upper panel for comparison.

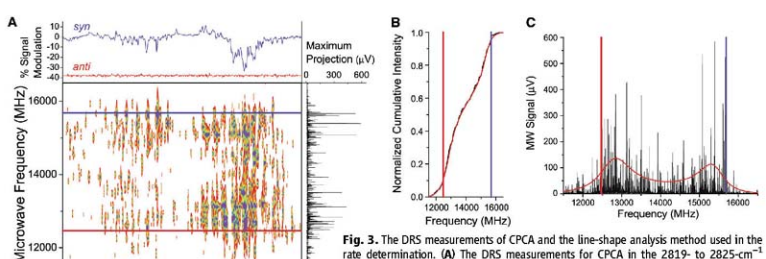

Fig. 3. The DRS measurements of CPCA and the line-shape analysis method used in the rate determination. **(A)** The DRS measurements for CPCA in the 2819- to 2825-cm^{-1} region are presented in a 2D format. The strong pure rotational transitions of CPCA (Fig. 2B) are cut from the spectrum to isolate the laser-induced rotational transitions. The red and blue lines indicate the pure rotational frequencies for the anti and syn 2_{02}–1_{01} transitions, respectively. The top panel shows an expanded region of the spectrum shown in Fig. 2C and demonstrates that the laser selectively excites the syn conformer. The anti conformer spectrum trace is offset by –40% for clarity. The right panel shows the maximum signal level at each microwave frequency over the laser scan region. **(B)** The isomerization rate determination is performed by fitting the cumulative intensity distribution of the microwave spectrum to the integrated line shape of the rotational Bloch model modified for chemical exchange (see section "B" in the materials and methods of the SOM). The best fit (red trace) to the experimental cumulative intensity distribution (black trace) is shown in (B). **(C)** The best-fit overall line shape is compared with the experimental dynamic rotational spectrum measured in the microwave (MW) frequency region. The smooth line-shape profile from the rotational Bloch model is displayed in red.

in pulse generation uses an AWG with a 3.96–gigasamples (Gs)/s sample rate to generate a chirped pulse with a linear frequency sweep from 162.5 to 1537.5 MHz. After up-conversion into the microwave frequency range with a 9.90-GHz phase-locked dielectric resonator oscillator (PDRO), a microwave circuit is used to expand the pulse bandwidth by a factor of eight in two stages. The components used in the microwave circuit are shown in fig. S1. The final pulse output of this circuit provides a linear frequency sweep from 7.5 to 18.5 GHz. This pulse is amplified by a broadband-pulsed traveling wave-tube amplifier with 2-kW peak power.

We coupled the chirped pulse into the interaction region using a double-ridge (WRD750) standard gain horn with 20-dB gain. A second horn is used to receive the molecular FID. By using broadband standard gain horns to broadcast the microwave polarizing pulse and receive the weak molecular emission, we achieve a flat spectral response that produces accurate relative intensities over the spectrometer bandwidth. Molecules are introduced through a pulsed, free-jet expansion. A tunable, pulsed infrared laser (10-Hz repetition rate, 8-ns pulse duration, 0.02-cm^{-1} bandwidth, 8 mJ per pulse near 2750 cm^{-1}) is used to vibrationally excite the molecules in the collision-free region of the free-jet expansion. The laser pulse interacts with the sample before the microwave excitation. When the laser is resonant with a vibrational transition, it transfers the population to excited vibrational states. In DRS, we are interested in the rotational spectrum of the quantum states populated by laser excitation. However, the population transfer also changes the signal level of the rotational transitions in the ground vibrational state. Therefore, by monitoring the signal level of the pure rotational transitions, we obtain the conformer-selective vibrational spectrum in a multiplexed version of infrared (IR)–FTMW double-resonance spectroscopy (*13*).

The microwave chirped pulse with 1-μs pulse duration is coupled into the spectrometer immediately after the infrared laser pulse. After a delay time of 2 μs to permit dissipation of the high-power excitation pulse, the molecular emission is switched out to a low-noise, broadband amplifier and subsequently mixed with a PDRO operating at 18.99 GHz to bring the 7.5- to 18.5-GHz molecular emission into the operating range of the digital oscilloscope (dc to 12-GHz hardware bandwidth). In the DRS measurements reported here, the FID was acquired for 2 μs. The lifetime of the excited molecular quantum states must exceed the 5-μs time interval required to complete the rotational spectrum acquisition. In the collision-free region of the expansion, the only lifetime contribution comes from radiative decay, and this process occurs on the millisecond time scale for infrared fluorescence.

Reduced measurement time is the major advance of the CP-FTMW spectrometer that facilitates DRS measurements. Because the excited-state rotational signals are about one-tenth as strong as the pure rotational signals, we perform 85 time-domain signal averages for each spectrum. With the system operating at the 10-Hz repetition rate of the laser, we can measure and archive the broadband spectrum (7.5 to 18.5 GHz) in 11 s. In the experiment presented in this report, we acquire 17,000 rotational spectra as the laser frequency is scanned continuously from 2670 to 2850 cm^{-1} in a total measurement time of 52 hours. By comparison, the computer-controlled cavity-FTMW spectrometer in our laboratory takes 14 hours to complete a broadband scan from 8 to 18 GHz and would require about 27 years of continuous operation to complete the measurements. The short acquisition times also minimize the effects of laser frequency drift, because only short-term frequency stability is required. Further, by the acquisition of the full rotational spectrum on each laser pulse, shot-to-shot variation in the laser pulse energy affects only the overall signal level and does not skew the line-shape profile that contains the reaction rate information.

We applied this broadband FTMW spectrometer to rotational spectroscopy of cyclopropane carboxaldehyde (CPCA). CPCA has two stable molecular conformations—syn and anti—as shown in Fig. 2A. These two geometries interconvert by internal rotation about a C–C single bond. The one-dimensional (1D) potential curve, calculated by ab initio methods (*14*), is shown in Fig. 2A. The anti conformer is calculated to be 46-cm^{-1} (zero-point–corrected) more stable than

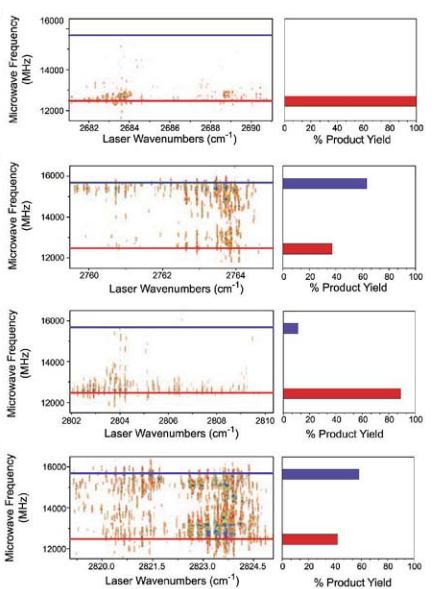

Fig. 4. The dynamic rotational spectra are shown for four infrared bands at: **(A)** 2686 cm^{-1}, originating from the anti conformer; **(B)** 2762 cm^{-1}, originating from the syn conformer; **(C)** 2806 cm^{-1}, originating from the anti conformer; and **(D)** 2822 cm^{-1}, originating from the syn conformer. The horizontal axis gives the laser frequency, and the vertical axis is the microwave frequency. The red and blue reference lines mark the position of the pure rotational 2_{02}–1_{01} transition of the anti and syn conformers, respectively. Horizontal bars to the right of the spectra represent the present product yield for syn/anti isomerization determined from the total spectra intensity in either the anti or syn region of the dynamic rotational spectrum.

the syn conformer. The calculated barrier to conformational isomerization is about 2200 cm^{-1}. The highest level calculations in the literature use the CBS-4 method and have the anti conformer more stable by 85 cm^{-1}, with a barrier of 1910 cm^{-1} for isomerization to the syn geometry (*15*). These computational results are in good agreement with previous gas-phase microwave (*16*) and infrared (*17*) studies of CPCA, which have determined a small difference in the conformational energies (10 to 30 cm^{-1}) and conformational isomerization barriers of ~1600 cm^{-1}. We acquired the pure rotational spectrum of CPCA measured via CP-FTMW spectroscopy (Fig. 2B) using a single molecular-beam pulse. The signal-to-noise ratio on the strongest transitions is about 100:1.

The fast acquisition of the CP-FTMW spectrometer allows "on-the-fly" kinetics measurements by recording the dynamic rotational spectrum of the excited state as the laser frequency is scanned. Here, we focus on the region of the infrared spectrum in the vicinity of the aldehyde C–H stretch (Fig. 2C). Electronic structure calculations predict no additional normal-mode fundamental vibrations for either conformer in this 180-cm^{-1} spectral range (table S2). However, several absorption features appear for each conformer in this frequency region. The extra spectral features indicate the presence of IVR caused by the anharmonic coupling of different normal-mode vibrational states (*18*). In addition to the strong vibrational coupling that produces the few discrete vibrational bands in the 2670- to 2850-cm^{-1} region, there also exist weaker interactions with near-resonant vibrational states that cause further local fragmentation of the infrared oscillator strength. Although the vibrational spectrum shows that IVR occurs, the existence of extensive vibrational coupling does not guarantee that isomerization occurs.

We detect whether isomerization occurs through the properties of the dynamical rotational spectrum. If CPCA isomerizes at the excitation energy, then the wave functions prepared by laser excitation acquire characteristics of both stable conformations. The conformational composition of the wave functions is probed by rotational spectroscopy and provides the product yield for the reaction. Furthermore, the overall intensity profile of the dynamic rotational spectrum contains rate information that can be extracted through line-shape analysis via a rotational spectroscopy Bloch model modified for chemical exchange. The rotational Bloch model for a reversible first-order isomerization reaction is presented in the supporting online material (SOM) text. The extraction of the reaction rate and product yield from the spectra are illustrated in Figs. 3 and 4.

The conformer-selective vibrational spectrum in Fig. 2C shows that the vibrational bands at 2822 cm^{-1} originate from the ground vibrational state of the syn conformer. However, the dynamic rotational spectrum of these laser-prepared quantum states is peaked around the characteristic frequencies of both stable conformational geometries, as shown in Fig. 3A. The spectrum as a function of laser frequency is displayed by a contour plot, with the conformer-selective vibrational spectrum shown at the top for reference. The resolution of the rotational spectrum is deliberately degraded in the figure so that this 2D plot can convey the general appearance of the spectrum at each laser frequency. To the right of the contour plot, we show the total projection of the dynamic rotational spectrum for all measurements in this spectral region at the resolution of the CP-FTMW measurement. A video representation of the experiment (movie S1), showing each acquired rotational spectrum, is included in the SOM.

The determination of the isomerization rate of CPCA in the energy region around 2822 cm^{-1} by line-shape analysis is illustrated in Fig. 3, B and C. The rate analysis is based on the overall intensity pattern of the spectrum. Because the intensities of each individual rotational transition must fluctuate around the smooth line-shape profile, we analyze the cumulative spectral intensity (Fig. 3B) (*19*). The cumulative intensity for the contour of a coalescence line shape characterized by a reaction rate of $k_{ex} = 5.60 \times 10^9\ s^{-1}$ ($\pm 0.35 \times 10^9\ s^{-1}$ at the 95% confidence level) is found to best represent the data, corresponding to an isomerization time scale of 180 ps. This total reaction rate is the sum of the forward and reverse reactions of the reversible conformational isomerization process. The best-fit individual rates are $k_{anti \rightarrow syn} = 3.08 \times 10^9\ s^{-1}$ ($\pm 0.16 \times 10^9\ s^{-1}$) and $k_{syn \rightarrow anti} = 2.52 \times 10^9\ s^{-1}$ ($\pm 0.19 \times 10^9\ s^{-1}$). The SOM includes a more detailed description of the rate-constant analysis procedures.

The DRS experiments directly measure the microcanonical rate [$k(E)$] for the conformational isomerization reaction. The experimental result can be compared with a statistical prediction via Rice-Ramsperger-Kassel-Marcus (RRKM) theory (Eq. 1) (*20*)

$$k(E) = \frac{\sigma W(E)}{h\rho(E)} \quad (1)$$

where σ is the symmetry number of the reaction coordinate, $W(E)$ is the number of energy levels of the transition state, h is Planck's constant, and ρ is the density of states of the reactant. We have evaluated Eq. 1 using the scaled normal-mode frequencies and the reaction barrier obtained from the best-reported electronic structure calculations (1910 cm^{-1}). The RRKM theory calculation yields a total reaction rate that is 16 times faster than the experimental determination: $k_{RRKM} = 9.09 \times 10^{10}\ s^{-1}$. The RRKM calculation is described more fully in the SOM.

We have examined the dynamic rotational spectra for the other vibrational features in Fig. 2C that can be specifically assigned to selective excitation of either the syn or anti conformer. The reaction product yields observed in these spectra demonstrate conformation-specific isomerization reaction dynamics. We obtained an estimate of the reaction yield using the total spectral intensity in each of the characteristic rotational frequency regions, which is shown for four vibrational features in Fig. 4. We observe similar product distributions for selective excitation of the syn conformer near 2764 and 2822 cm^{-1}: 63%/37% syn/anti and 58%/42% syn/anti, respectively. These yields are near the equal distribution expected for a reaction where the reactant and product have about the same zero-point energy. In contrast, we do not observe efficient production of the syn conformer after excitation of the anti conformer, as shown by the dynamic rotational spectra recorded near 2686 and 2806 cm^{-1}. Although the analysis is not shown, the reaction rates in regions where isomerization occurs are nearly constant: $k_{tot} = 5.78 \times 10^9\ s^{-1}$ ($\pm 0.40 \times 10^9\ s^{-1}$) (2764 cm^{-1}), $k_{tot} = 5.60 \times 10^9\ s^{-1}$ ($\pm 0.35 \times 10^9\ s^{-1}$) [2822 cm^{-1} (Fig. 3)], and $k_{tot} = 4.84 \times 10^9\ s^{-1}$ ($\pm 0.60 \times 10^9\ s^{-1}$) (for the small region around 2804 cm^{-1} where anti excitation leads to product formation).

This application of CP-FTMW spectroscopy to isomerization kinetics has revealed rich dynamical behavior for a simple, two-geometry reversible reaction. The unimolecular isomerization rates of the isolated molecule are 16 times slower than those predicted by RRKM theory. Low-barrier isomerization reactions have been the subject of much experimental (*21*–*24*) and theoretical (*25*–*27*) investigation and are believed to be a general class of reactions that are poorly predicted by statistical reaction rate theory. We also observe strongly conformer-specific reaction yields. This observation suggests that special doorway resonances that are sparse at this level of excitation facilitate the isomerization reaction. These DRS measurements on isolated molecules in a molecular-beam environment directly probe the intrinsic intramolecular reaction dynamics and complement recent 2D ultrafast infrared spectroscopy techniques that have been used to measure C–C single-bond isomerization kinetics in room-temperature solution (*28*). The combination of techniques applicable to isolated molecules and dilute solutions will make it possible to understand the interplay of purely intramolecular dynamics and intermolecular interactions in thermal conformational isomerization reactions in solution (*29*–*31*).

References and Notes

1. T. J. Balle, W. H. Flygare, *Rev. Sci. Instrum.* **52**, 33 (1981).
2. E. J. Cocinero *et al.*, *Chem. Phys. Lett.* **435**, 336 (2007).
3. J. Tang, Y. Xu, A. R. W. McKellar, W. Jäger, *Science* **297**, 2030 (2002).
4. K. Suma, Y. Sumiyoshi, Y. Endo, *Science* **308**, 1885 (2005).
5. M. C. McCarthy, C. A. Gottlieb, H. Gupta, P. Thaddeus, *Astrophys. J.* **652**, L141 (2006).
6. B. H. Pate, *J. Chem. Phys.* **109**, 4396 (1998).
7. B. H. Pate, *J. Chem. Phys.* **110**, 1990 (1999).

8. J. Keske, D. A. McWhorter, B. H. Pate, *Int. Rev. Phys. Chem.* **19**, 363 (2000).
9. P. W. Anderson, *J. Phys. Soc. Jpn.* **9**, 316 (1954).
10. R. Kubo, K. Tomita, *J. Phys. Soc. Jpn.* **9**, 888 (1954).
11. G. G. Brown, B. C. Dian, K. O. Douglass, S. M. Geyer, B. H. Pate, *J. Mol. Spectrosc.* **238**, 200 (2006).
12. J. C. McGurk, T. G. Schmalz, W. H. Flygare, *J. Chem. Phys.* **60**, 4181 (1974).
13. K. O. Douglass *et al.*, *J. Mol. Spectrosc.* **239**, 29 (2006).
14. M. J. Frisch *et al.*, Gaussian 03, revision C.02 (Gaussian, Inc., Wallingford, CT, 2004).
15. K. B. Wiberg, H. Castejon, *J. Org. Chem.* **60**, 6327 (1995).
16. H. N. Volltrauer, R. H. Schwendeman, *J. Chem. Phys.* **54**, 260 (1971).
17. J. R. Durig, F. Feng, T. S. Little, A. Wang, *Struct. Chem.* **3**, 417 (1992).
18. D. J. Nesbitt, R. W. Field, *J. Phys. Chem.* **100**, 12735 (1996).
19. S. Mukamel, J. Sue, A. Pandey, *Chem. Phys. Lett.* **105**, 134 (1984).
20. T. Baer, W. L. Hase, *Unimolecular Reaction Dynamics: Theory and Experiments* (Oxford Univ. Press, New York, 1996).
21. D. B. Borchardt, S. H. Bauer, *J. Chem. Phys.* **85**, 4980 (1986).
22. T. Baer, A. R. Potts, *J. Phys. Chem. A* **104**, 9397 (2000).
23. B. C. Dian, A. Longarte, T. S. Zwier, *Science* **296**, 2369 (2002).
24. R. Schanz, V. Botan, P. Hamm, *J. Chem. Phys.* **122**, 044509 (2005).
25. M. J. Davis, S. K. Gray, *J. Chem. Phys.* **84**, 5389 (1986).
26. S. K. Gray, S. A. Rice, *J. Chem. Phys.* **86**, 2020 (1987).
27. D. M. Leitner, P. G. Wolynes, *Chem. Phys. Lett.* **280**, 411 (1997).
28. J. Zheng, K. Kwak, J. Xie, M. D. Fayer, *Science* **313**, 1951 (2006).
29. H. S. Yoo, M. DeWitt, B. H. Pate, *J. Phys. Chem. A* **108**, 1348 (2004).
30. C. G. Elles, M. J. Cox, F. F. Crim, *J. Chem. Phys.* **120**, 6973 (2004).
31. R. von Benten, O. Link, B. Abel, D. Schwarzer, *J. Phys. Chem. A* **108**, 363 (2004).
32. This work was supported through the Major Research Instrumentation program of the NSF (grant no. 0215957) and the chemistry division of the NSF (grant nos. CHE-0315961 and CHE-0616660).

Supporting Online Material

www.sciencemag.org/cgi/content/full/320/5878/924/DC1
Materials and Methods
SOM Text
Figs. S1 to S5
Tables S1 to S3
References
Movie S1
Data Set S1

28 January 2008; accepted 3 April 2008
10.1126/science.1155736

Hidden Neotropical Diversity: Greater Than the Sum of Its Parts

Marty A. Condon,[1,2]* Sonja J. Scheffer,[2,3,4] Matthew L. Lewis,[3] Susan M. Swensen[5]

The diversity of tropical herbivorous insects has been explained as a direct function of plant species diversity. Testing that explanation, we reared 2857 flies from flowers and seeds of 24 species of plants from 34 neotropical sites. Samples yielded 52 morphologically similar species of flies and documented highly conserved patterns of specificity to host taxa and host parts. Widespread species of plants can support 13 species of flies. Within single populations of plants, we typically found one or more fly species specific to female flowers and multiple specialists on male flowers. We suggest that neotropical herbivorous insect diversity is not simply a function of plant taxonomic and architectural diversity, but also reflects the geographic distribution of hosts and the age and area of the neotropics.

The diversity of neotropical herbivorous insects, ranging in number from 3 million to 30 million species (*1*), has been hypothesized to be a function of plant diversity (*2*, *3*), but the degree to which specialization shapes that function is contentious. Plant architecture (*4*, *5*) and distribution also affect patterns of insect diversity (*6*, *7*). Diversity estimates have traditionally been generated from counts of morphologically distinguishable insect species (morphospecies) collected on plant surfaces (*2*, *3*). However, molecular evidence suggests that tallies of morphospecies underestimate both diversity and host specificity (*8*, *9*). Temperate zone research has revealed diverse assemblages of host-specific cryptic species as well as recently diverged host races (*10*), including groups that diversified to different parts (e.g., leaves, flowers, stems) of the same host plant (*11*). Although different plant tissues represent numerous niches in the tropics, few studies have assessed the diversity of concealed larvae feeding inside those parts (*12*, *13*), and even fewer have used molecular markers to reveal cryptic species (*14*).

To address the relationship between host and insect diversity, we focused on *Blepharoneura* (*15*), a neotropical genus of tephritid fruit flies that, as larvae, feed within the flowers or fruits of plants in the cucumber family (Cucurbitaceae). *Blepharoneura* larvae rarely cause external signs of damage, and few host records existed prior to this study. More than half of the known host species of this group of *Blepharoneura* belong to the Guraniinae, a cucurbit subtribe characterized by architectural complexity. The two largest genera within the Guraniinae (*Gurania* and *Psiguria*) have brightly colored flowers with succulent outer floral organs (calyces), typical of many hummingbird-pollinated plants (fig. S1). Most species have male and female flowers borne on sexually dimorphic branches, which are temporally and spatially isolated on individual plants (*16*). Because only large plants produce female branches, which produce fewer flowers for a shorter period of time than male inflorescences, female flowers are rarer than male flowers. Thus, a population of a single host species represents a mosaic of morphologically distinctive targets differing in abundance at any point in time (fig. S2).

To investigate patterns of host use and diversity in *Blepharoneura*, we reared 2857 flies from 24 different cucurbit host species in nine genera and three tribes. Our sample encompassed 10 distinct biogeographic neotropical regions (table S1) spanning the geographic distribution of the subtribe Guraniinae, from Mexico to southern Bolivia (~5500 km) and from the Pacific to the Atlantic coasts of South America (~3000 km). We analyzed 419 specimens from 34 sites in 10 countries. With a conservative 4% sequence divergence cutoff for species limits (*15*), a phylogenetic analysis of mitochondrial cytochrome c oxidase subunit I (mtCOI) sequence revealed 52 species of flies (figs. S3 to S8). Most of these species were morphologically indistinguishable (*15*) but had sequence differences ranging from 6 to 18% (Fig. 1). Because divergent groups revealed by mtCOI can incorrectly identify species (*17*), we examined two nuclear genes from 58 specimens from the Napo region of Ecuador. Analysis of nuclear elongation factor 1-α (EF1-α) and CAD (*15*) recovered the same 10 lineages (fig. S9) and corroborated the mtDNA results (Fig. 1), which suggests that these lineages indeed represent distinct species. Subsequent morphological analyses of a subset of these genetically defined species revealed slight but statistically significant differences in morphology (*18*).

Cryptic species of *Blepharoneura* showed specificity both to host part and to host taxon: Of 45 species reared from reproductive tissues, only a single species (sp. 39) fed on both flowers and seeds, whereas all other species appeared to be restricted to either flowers or seeds. Among flower-feeders, most specialized on flowers of a single gender. This is surprising because most flower-feeders feed primarily on calyx tissue, which is similar in flowers of both sexes. Furthermore, many species specialized on female flowers, which are rare relative to male flowers (fig. S2) (*15*, *16*), in contrast to predictions that insects are less likely to specialize on rare hosts (*19*). Both seed- and flower-feeders tended to

[1]Department of Biology, Cornell College, Mount Vernon, IA 52314, USA. [2]Department of Entomology, National Museum of Natural History, Smithsonian Institution, Washington, DC 20560, USA. [3]Systematic Entomology Laboratory, ARS-USDA, Beltsville, MD 20705, USA. [4]Department of Entomology, University of Maryland, College Park, MD 20742, USA. [5]Department of Biology, Ithaca College, Ithaca, NY 14850, USA.

*To whom correspondence should be addressed. E-mail: mcondon@cornellcollege.edu

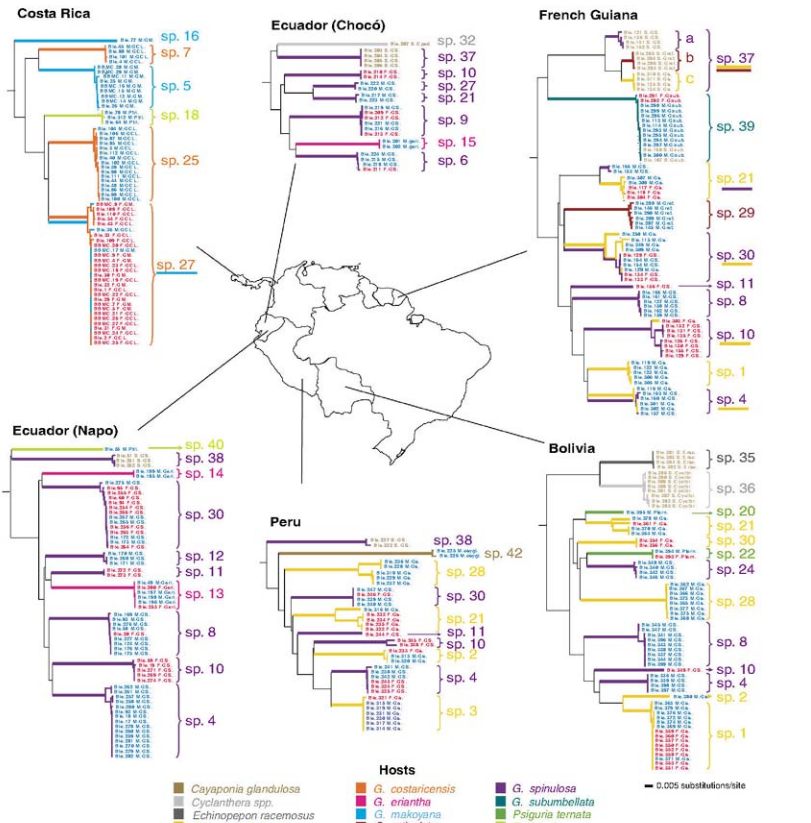

Fig. 1. Multiple sympatric species, often specific to flower gender, infest single species of hosts in diverse geographic areas. Neighbor-joining trees were constructed from mtCOI sequence data from specimens collected in 6 of the 10 biogeographic regions we sampled (*15*). Branch colors indicate host species (see key). Terminal labels indicate host part infested: red, female flowers; blue, male flowers; tan, seeds. Species are identified with numbers as in figs. S3 to S8; underlined identification numbers indicate species reared from more than one host species; letters (a, b, c) highlight lineages within species 37 that would be recognized as distinct species if less conservative criteria were used to delineate species (*15*). See table S1 for locality data for transects (identified by italic letters and numbers): Trees denoted Costa Rica (*C14*), the Chocó region of northwestern Ecuador (*E20*), the Napo of eastern Ecuador (*E19*), and Peru (*P31*) were constructed from samples collected along single transects (each <20 km long with elevation variation of <400 m); trees denoted French Guiana (*F22* to *F25*) and Bolivia (*B1* to *B7*) were from samples collected along more than one transect.

specialize on a single species; 80% were reared from a single host plant species (*15*). The proportion of host taxon specialists did not significantly change when we used less conservative criteria for species delimitation (*15*). We also found, contrary to predictions (*19*), that the rarer host plants in this study supported only host-taxon specialists and were not hosts to generalist species (Fig. 1).

Maximum likelihood analysis of the genetic data revealed distinct groups of seed- and flower-feeding species restricted to specific plant parts and plant taxa (Fig. 2). Two clades of flower-feeders associated with groups characterized by relatively large flowers and succulent tissues. Species 1 to 30 were flower-feeders found on plants within the subtribe Guraniinae (98% bootstrap support). Alternatively, species 41 to 43 were restricted to the tribe Cucurbiteae (100% bootstrap support). Within the seed-feeding clade (spp. 31 to 39), two strongly supported lineages appeared to be restricted to the subtribe Sicyeae (100% bootstrap support) and the Guraniinae (100% bootstrap support), respectively (Fig. 2). Thus, the number of *Blepharoneura* species reflects the diversity of different plant parts and host taxa but exceeds the sum of plant part types for some plant taxa, because multiple species of flies infest a single type of plant part. We observed that some host species were infested by at least 13 species of *Blepharoneura*. We typically found four to six species infesting flowers in a population of a single species of host (Fig. 1 and table S1).

Our data show that geographically widespread host plants supported more species, both locally and regionally, than did hosts with more limited distributions (Fig. 3), reflecting patterns observed in the temperate zone (*6*, *7*). The most abundant and widespread species of *Gurania* (*G. spinulosa*) was infested by 13 species of *Blepharoneura* (Figs. 1 to 3, table S1, and appendix S1). *Gurania acuminata*, another widespread but locally rare species, hosted nine species of *Blepharoneura*, four of which were reared from flowers collected on a single day from the same tangle of vines in Peru (spp. 2, 3, 21, and 28; Fig. 1). The close ecological associations of sympatric species feeding on the same host taxon and tissue were not unusual; even on less common hosts (e.g., *G. eriantha*), we reared multiple species from single inflorescences (spp. 13 and 14; see Napo, Fig. 1).

More than half of the *Blepharoneura* species we discovered were found at only one site and may have very limited ranges (Figs. 1 and 2, figs. S3 to S8, and table S1). Species endemic to particular regions were not restricted to rare hosts or to hosts with limited geographic distributions. Three of the 13 species infesting the widespread *G. spinulosa* appeared to be local endemics: One species appeared to be restricted to the Napo region of eastern Ecuador (sp. 12; Fig. 2 and fig. S5), one to northwest Ecuador (sp. 9; Fig. 2 and fig. S5), and one to the southernmost limit of *G. spinulosa*'s distribution in Bolivia (sp. 24; Fig. 2 and fig. S3). Most widespread species of *Blepharoneura* showed a high degree of fidelity to host species and tissue, but we detected some geographic variation in host use patterns (e.g., spp. 27 and 30; Fig. 1 and figs. S6 and S7). For example, species 10 was distributed

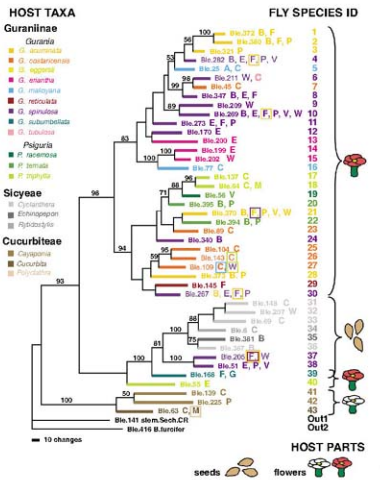

Fig. 2. Maximum likelihood tree of 45 species of *Blepharoneura*. Maximum likelihood analysis used a combined data set of the nuclear CAD and EF1-α genes and the mitochondrial COI gene. Fly species, each represented by a single individual, are identified by numbers (figs. S3 to S8; spp. 44 and 45 lack nuclear sequences and are not included here). Collection localities for each species are indicated by letters: A, Panama; B, Bolivia; C, Costa Rica; E, eastern Ecuador; F, French Guiana; G, Guyana; M, Mexico; P, Peru; V, Venezuela; W, western Ecuador (table S1). Colors of branches and letters indicate most commonly used hosts in an area; colors of rectangles around letters indicate additional hosts at some sites. Flower color indicates host taxon: red, Guraniinae; white, Cucurbiteae. Host nomenclature is as in appendix S1.

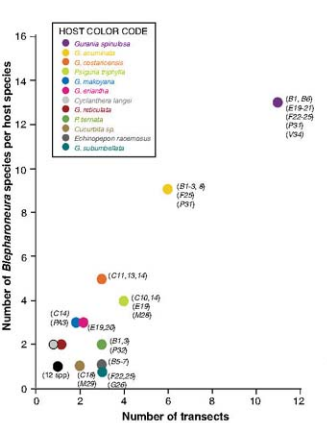

Fig. 3. Diversity of *Blepharoneura* species per host species increases with number of transects. Host plants found in multiple transects host more species of *Blepharoneura* than do rarer species and species with more limited distribution ($r^2 = 0.9337$). Colors (see key) identify hosts; transect identification numbers are listed by country (table S1). All transects are <20 km long with elevation variation of <400 m.

throughout tropical South America, fed exclusively on female flowers, and, in all but one locality, fed on a single species of host (Fig. 1 and fig. S4). Other species (e.g., sp. 27) fed almost exclusively on female flowers (30 of 32 specimens) of at least two host species in Central America, but commonly fed on male ($N = 4$) and female ($N = 4$) flowers in areas west of the Andes in Ecuador (Fig. 1 and fig. S6). These variable patterns of host use form a mosaic that varies from community to community across large geographic areas (*20*) and complicates attempts to extrapolate local samples to global estimates of tropical diversity (*21*).

Although we report diversity exceeding the original morphological estimates by an order of magnitude (*15*), this must underrepresent the actual diversity of this group because our criterion for species delimitation is highly conservative (*15*). This is because we used a 4% mtCOI divergence, whereas other studies recognize species differing by less than 1% (*8*). As a result of this conservative criterion, we may be lumping biologically distinct species together, and single generalist species may actually represent multiple host-specific species (e.g., sympatric monophyletic lineages feeding on separate hosts; see sp. 37 in French Guiana, Fig. 1 and fig. S8). Also, our samples are limited; most of our collections were made during single trips, and our samples were restricted to species in fruit or flower at that time (table S1). Finally, the number of fly species recorded for a particular host plant species was most likely limited because the number of insect species detected rose as the number of collection localities increased (Fig. 3).

We also found that the distribution of hosts may also predict herbivore diversity at both local and regional scales (*6*, *7*). The neotropics include a mosaic of biogeographic zones reflecting a long history of repeated habitat fragmentation (*22*). During periods of habitat fragmentation, insect populations may be more likely than these plant populations to diverge, as insects have shorter generation times and can evolve more quickly than plants with long generation times (*15*). Furthermore, sexual selection accelerates rates of evolution in insects, particularly in groups with complex courtship displays such as *Blepharoneura* (*9*, *18*, *23*). When these new species come together, as habitats expand and host populations rejoin, assemblages of highly host-specific cryptic species result. In local assemblages of *Blepharoneura* (Fig. 1), the minimum pairwise divergence among sympatric species is ~6%, which suggests that they diverged at least 2.6 million years ago (*24*). During the past 2.6 million years, even seemingly uniform habitats experienced multiple cycles of fragmentation and expansion (*22*). If host plants represent "hard boundaries" (*25*) for ranges of host-specific insects, simple neutral models incorporating changes in habitat area (*25*) as well as time (*26*, *27*) could help account for patterns of diversity. Conflicting assessments of host specificity and diversity in the tropics (*2*, *3*, *28*) may reflect differences in geographic scale rather than differences in evolutionary or ecological processes.

References and Notes

1. R. M. May, *Philos. Trans. R. Soc. London Ser. B* **330**, 293 (1990).
2. V. Novotny *et al.*, *Science* **313**, 1115 (2006); published online 13 July 2006 (10.1126/science.1129237).
3. L. A. Dyer *et al.*, *Nature* **448**, 696 (2007).
4. I. S. Winkler, C. Mitter, in *Specialization, Speciation, and Radiation: The Evolutionary Biology of Herbivorous Insects*, K. J. Tilmon, Ed. (Univ. of California Press, Berkeley, CA, 2008), pp. 240–263.
5. T. Hunt *et al.*, *Science* **318**, 1913 (2007).
6. T. R. E. Southwood, *J. Anim. Ecol.* **30**, 1 (1961).
7. H. V. Cornell, *Ecology* **66**, 1247 (1985).
8. P. D. Hebert, E. H. Penton, J. H. Burns, D. H. Janzen, W. Hallwachs, *Proc. Natl. Acad. Sci. U.S.A.* **101**, 14812 (2004).
9. D. Bickford *et al.*, *Trends Ecol. Evol.* **22**, 148 (2006).
10. J. O. Stireman, J. D. Nason, S. B. Heard, *Evolution* **59**, 2573 (2005).
11. J. B. Joy, B. J. Crespi, *Evolution* **61**, 784 (2007).
12. H. C. T. Godfray, O. T. Lewis, J. Memmott, *Philos. Trans. R. Soc. London Ser. B* **354**, 1811 (1999).
13. V. Novotny, A. R. Clarke, R. A. I. Drew, S. Balagawi, B. Clifford, *J. Trop. Ecol.* **21**, 67 (2005).
14. M. A. Condon, G. J. Steck, *Biol. J. Linn. Soc.* **60**, 443 (1997).
15. See supporting material on *Science* Online.
16. M. A. Condon, L. E. Gilbert, *Am. J. Bot.* **75**, 875 (1988).
17. D. J. Funk, K. E. Omland, *Annu. Rev. Ecol. Evol. Syst.* **34**, 397 (2003).
18. M. A. Condon *et al.*, *Biol. J. Linn. Soc.* **93**, 779 (2008).
19. D. A. Norton, R. K. Didham, *Science* **315**, 1666b (2007).
20. J. N. Thompson, *The Geographic Mosaic of Coevolution* (Univ. of Chicago Press, Chicago, 2005).
21. C. D. Thomas, *Nature* **347**, 237 (1990).
22. J. Cracraft, R. O. Prum, *Evolution* **42**, 603 (1988).
23. T. C. Mendelson, K. L. Shaw, *Nature* **433**, 375 (2005).
24. We used Brower's (*29*) calibration of 2.3% (pairwise divergence) MY-1, which is used as the standard mitochondrial molecular clock estimate (*27*).
25. R. K. Colwell, D. C. Lees, *Trends Ecol. Evol.* **15**, 70 (2000).
26. S. P. Hubbell, *The Unified Neutral Theory of Biodiversity and Biogeography* (Princeton Univ. Press, Princeton, NJ, 2001).
27. M. A. McPeek, J. M. Brown, *Am. Nat.* **169**, E97 (2007).
28. V. Novotny *et al.*, *Nature* **448**, 692 (2007).
29. A. V. Z. Brower, *Proc. Natl. Acad. Sci. U.S.A.* **91**, 6491 (1994).

30. We thank many colleagues and students for assistance; museums and governmental agencies in Bolivia, Costa Rica, Ecuador, French Guiana, Peru, the United States, and Venezuela for assistance and permission to carry out the study; and D. C. Adams, D. J. Futuyma, D. H. Feener, L. E. Gilbert, S. H. McKamey, C. Mitter, A. L. Nordbom, M. C. Singer, and I. S. Winkler for helpful comments on the manuscript. Supported by the Smithsonian Institution, NSF, Hofstra University, Ithaca College, and Cornell College. Sequences of *Blepharoneura* specimens have been deposited in GenBank (accession numbers EF531751 to EF531769, EF531789 to EF531828, EF531890, EF531891, EU601764 to EU60230, and EU623470).

Supporting Online Material

www.sciencemag.org/cgi/content/full/320/5878/928/DC1
Materials and Methods
Figs. S1 to S10
Tables S1 and S2
Appendices S1 and S2

29 January 2008; accepted 9 April 2008
10.1126/science.1155832

Surface Tension Transport of Prey by Feeding Shorebirds: The Capillary Ratchet

Manu Prakash,[1] David Quéré,[2] John W. M. Bush[3]

The variability of bird beak morphology reflects diverse foraging strategies. One such feeding mechanism in shorebirds involves surface tension–induced transport of prey in millimetric droplets: By repeatedly opening and closing its beak in a tweezering motion, the bird moves the drop from the tip of its beak to its mouth in a stepwise ratcheting fashion. We have analyzed the subtle physical mechanism responsible for drop transport and demonstrated experimentally that the beak geometry and the dynamics of tweezering may be tuned to optimize transport efficiency. We also highlight the critical dependence of the capillary ratchet on the beak's wetting properties, thus making clear the vulnerability of capillary feeders to surface pollutants.

Phalaropes (Fig. 1A) and several other shorebirds with long thin beaks feed primarily on small crustaceans and other invertebrates (*1*). By swimming in a tight circle on the water surface, they generate a vortex that draws underlying fluid and suspended prey toward the surface (*2*). By pecking on the water surface at a rate of ~1.5 Hz (*1*, *3*–*6*), the birds capture water droplets with a characteristic scale of ~2 mm between their upper and lower mandibles (movie S1). Suction cannot be used to raise the drops mouthward because of the geometry of the open beak; gravity acts to oppose the drop motion. Nevertheless, the birds succeed in raising the drops mouthward by opening and closing their beaks successively (*1*, *5*, *7*, *8*). Although the importance of surface tension in this process was inferred (*1*), the physical mechanism responsible for the droplet transport, specifically

[1]Center for Bits and Atoms, Massachusetts Institute of Technology (MIT), 20 Ames Street, Cambridge, MA 02139, USA. [2]Physique et Mécanique des Milieux Hétérogènes, UMR 7636 du CNRS, Ecole Supérieure de Physique et de Chimie Industrielles, 10 rue Vauquelin, 75005 Paris, France. [3]Department of Mathematics, MIT, 77 Massachusetts Avenue, Cambridge, MA 02139, USA.

the critical role of the beak's characteristic tweezering action, has yet to be rationalized.

When a fluid drop is placed on a flat solid, the equilibrium contact angle θ between the wetted solid surface and the interface is defined by the well-known Young's equation. If $\theta \to 0$, the drop completely wets the solid, whereas for any finite θ, the drop is said to partially wet the solid. In practice, static contact angles observed in the case of partial wetting may lie anywhere in a finite range bounded above and below by the values at which contact line motion is initiated; specifically, the advancing and receding contact angles, respectively θ_a and θ_r (*9–11*). An important consequence of this so-called contact-angle hysteresis is a contact force that causes drops to adhere to surfaces; for example, rain drops stick to window panes because of the difference in the contact angles on their upper and lower edges (*12*). Although contact-angle hysteresis typically acts to resist the sliding of droplets on solids (*10*, *11*), it may be overcome by vibration (*13*, *14*). We demonstrate that, in capillary feeding, contact-angle hysteresis couples to the time-dependent beak geometry corresponding to the mandibular spreading cycles (*1*, *5–8*), thereby driving drop motion via a ratcheting mechanism.

Surface tension transport relies explicitly on the bird opening and closing its beak and so varying the beak opening angle α (*1*, *5*) (Fig. 1B). This angle has an upper bound because a drop pinned between two plates will break at an opening angle α_{break} if its height-to-radius ratio exceeds 2π (*15–17*). Denoting the beak length by L_b and the drop size by the capillary length $l_c \sim (\gamma/\rho g)^{1/2} \sim 2$ mm (where γ is surface tension, ρ is density, and g is the gravitational acceleration), the maximum opening angle is thus on the order of $\alpha_{break} \sim l_c/L_b \sim 11°$ for capillary feeders (Fig. 1B and fig. S1). The characteristic time to transport a drop along the beak length $L_b \sim 2$ cm is 20 ms, corresponding to mean drop speeds as high as 100 cm/s (*1*, *4*). In Fig. 1B, we present the mean beak length and width of 18 shorebird species with straight bills and emphasize that surface tension transport is used only by birds with the smallest beaks. Rubega (*3*) demonstrated that beak dimensions do not scale with body size in adult red-necked phalaropes, *Phalaropus lobatus*, suggesting the critical role of beak morphology in capillary feeding. Recently, Estrella *et al.* (*5*) substantially expanded the list of capillary feeders (Fig. 1B), underscoring the prevalence of surface tension transport. Though morphometric analysis of bird bills commonly yields insight into foraging mechanisms (*18*) and has led to new understanding of feeding modes (*19*), analytical and experimental studies of these mechanisms are exceedingly rare (*20*). We here present one such study.

In our experimental study, we constructed mechanical wedgelike geometries modeled after the bird beak. Mechanical beaks with a stainless steel surface were polished with a Buehler Metadi diamond slurry (average particle size ~ 3 μm). The surface was ultrasonically cleaned for an hour, plasma-treated in oxygen for 1 min to remove any residue, then left in air for an hour before experiments were performed. The mechanical beaks were mounted and actuated by a motorized micrometer stage so that the beak opening and closing angle could be precisely controlled by a computer. Drops of known volume (ranging from 0.5 to 2 μl) were inserted via a micropipette at the tip of the beak. A high-speed video camera (Phantom v5.0) recorded the resulting drop dynamics.

We first deposited a completely wetting fluid (silicone oil, $\gamma = 0.02$ N/m) in the form of a droplet that spanned the wedge (Fig. 2A). The drops propagated toward the narrower region, advancing first at a constant speed then accelerating as they approached the apex of the wedge (Fig. 2, B and C). The behavior in this fully wetting regime may be rationalized by simple scaling arguments (supporting online material). The jump in pressure across a surface is proportional to γ and the local curvature; such curvature pressures are capable of driving fluid motion. In 1712, Hauksbee (*21*) reported that "oil of orange" droplets trapped between two nonparallel glass plates moved spontaneously in the direction of decreasing gap thickness. Similarly, a completely wetting fluid drop confined in a conical capillary is known to self-propel toward the narrower end because of the axial force arising from differing curvature pressures across its end caps (*22*). In our wedge geometry, the opening angle is denoted by α, the width of the drop by W, the distance of the drop from the apex by x, and the length of the drop by L (Fig. 2B). The drop height is necessarily αx. For $x > L$, the pressure difference between the two caps scales

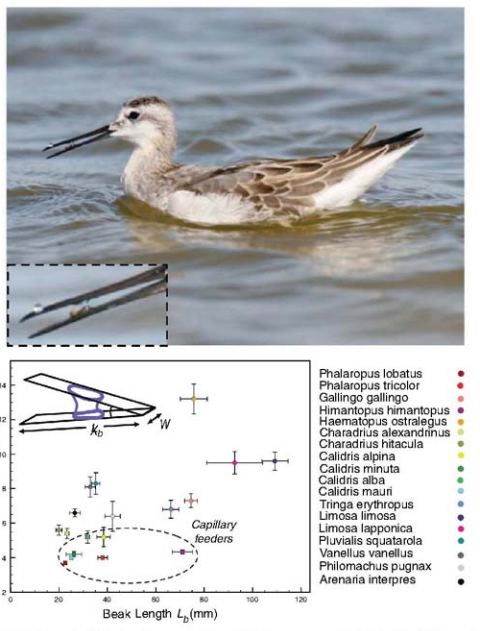

Fig. 1. (A) A juvenile Wilson's phalarope feeding. Note the prey suspended in the droplet trapped in its beak (inset). [Photo courtesy of Robert Lewis] **(B)** Shorebirds use a variety of foraging strategies (*28*) and so exhibit large variations in beak size and shape. Here we plot the bill length and base width of common shorebirds with straight bills [data compiled from (*4*, *18*, *29*)]. Scale bars represent the standard deviation in the reported data.

as $\gamma L/\alpha x^2$ and the drop volume as $\Omega \sim \alpha x L W$; hence a driving force $F \sim \gamma W L/x$ arises. For a fluid drop with dynamic viscosity η advancing at a speed v, the viscous force resisting its motion is given by $F_\eta \sim \eta W L v/(\alpha x)$; the force balance thus yields a steady speed $v_0 \sim \gamma\alpha/\eta$ that is independent of drop position x and drop length L. As the drop approaches the apex, $x < L$, the pressure difference between the caps scales as $\gamma/(\alpha x)$ and the volume as $\alpha L^2 W$. The resulting driving force now varies as $\gamma L W x$, and the viscous resistance as $\eta W v \alpha$. The resulting drop speed $v_0 L/x$ diverges as the drop approaches the apex despite the progressively increasing confinement. After a brief transient period, these two distinct regions of constant speed and acceleration are apparent in Fig. 2C.

When water is used in place of oil, the behavior is strikingly different: No droplet motion arises (Fig. 3A, top row). Unlike the silicone oil, the water only partially wets the solid; consequently, the droplet motion is resisted by contact-angle hysteresis. Specifically, there is an adhesive force whose magnitude scales as $\gamma W \Delta\cos\theta = \gamma W(\cos\theta_r - \cos\theta_a)$ (*10*, *23*), where W is the length of the advancing contact line. In our system, water droplets on stainless steel beaks have an advancing angle $\theta_a \sim 65°$ and receding angle $\theta_r \sim 20°$ that are comparable to those of water droplets on keratin (*24*). Drop motion is possible only if the capillary driving force $F \sim \gamma\cos\theta\ (WL/x)$ exceeds this sticking force; that is, if $\alpha > [(\Delta\cos\theta)/\cos\theta]\ [\Omega/(WL^2)]$. This condition cannot be satisfied, because both $\Delta\cos\theta/\cos\theta$ and $\Omega/(WL^2)$ are order-one quantities, whereas α must be less than $\alpha_{break} \sim 0.2$ radians for drop stability. The relatively minor influence of the fully three-dimensional geometry was examined numerically (fig. S1). The influences of beak taper and orientation were examined both experimentally and numerically. Realistic beak tapers (*3*, *5*) were found to have only a weak quantitative effect on the drop propulsion, whereas beak orientation had a negligible effect in the ratcheting regime.

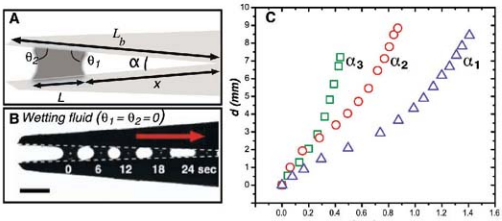

Fig. 2. Fluid drop in a horizontal beak. **(A)** Schematic of a bird beak with a fluid drop trapped between upper and lower mandibles. **(B)** A completely wetting drop of silicone oil ($\theta_1 = \theta_2 = 0$, dynamic viscosity $\eta = 0.05$ kg m^{-1} s^{-2}) self-propels toward the apex of a mechanical bird beak with a constant opening angle $\alpha = 3.4°$ and uniform width of 1 mm. Scale bar, 2 mm. **(C)** Plot of drop front position versus time for silicone oil ($\eta = 0.01$ kg m^{-1} s^{-2}) for three opening angles $\alpha_1 = 1.9°$ (blue triangles), $\alpha_2 = 2.8°$ (red circles), and $\alpha_3 = 4.2°$ (green squares), where d (in millimeters) represents the distance from the beak tip to the drop's trailing edge.

Phalaropes induce drop motion by cyclically opening and closing their beaks (*1*). We followed their lead in actuating the mechanical beak by opening and closing the wedge geometry at a constant angular velocity ω, with α_{close} and α_{open} being the minimum and maximum opening angles, respectively. We recorded the location of both front and rear contact lines of the drop with a high-speed camera mounted on a microscope (Fig. 3A). For a given drop volume, varying α_{close} and α_{open} reveals three distinct regimes.

If $\alpha_{open} - \alpha_{close}$ is sufficiently small that the leading and trailing contact angles, θ_1 and θ_2 respectively, satisfy $\theta_r < \theta_2 < \theta_1 < \theta_a$, then the drop remains pinned (Fig. 4A). The dynamics for larger values of $\alpha_{open} - \alpha_{close}$ are best understood by considering in turn the closing and opening phases. During the closing phase, both contact lines have the tendency to progress outward, but the leading edge (A) always does so first. During the opening phase, both contact lines tend to retreat inward, but the trailing edge (B) does so first. The drop thus advances through a slipping ratcheting motion: In each cycle, both leading and trailing edges of the contact lines advance and retreat. Nevertheless, due to the asymmetry in the wedge geometry, net mouthward drop motion is still achieved, albeit inefficiently. When α_{close} and α_{open} are optimally tuned, the droplet advances through a pure ratcheting motion with no slippage. The two contact lines move asynchronously but progressively toward the apex: During the opening phase, the leading edge (B) remains pinned while the trailing edge (A) retreats; during closing, the leading edge (B) advances while the trailing edge (A) remains pinned (Fig. 4A). The time dependence of the contact line positions and opening angle for nearly pure capillary ratcheting is plotted in Fig. 3B. The ratcheting motion is quasi-static, with the instantaneous position of the drop being determined by the history of the beak motion; therefore, the

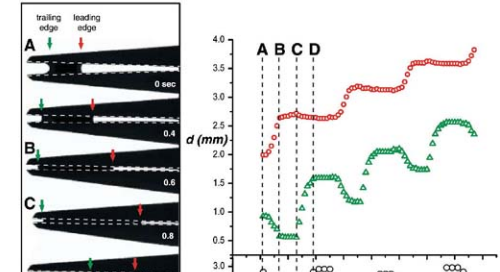

Fig. 3. The capillary ratchet. **(A)** Time sequence illustrating the water droplet transport generated by an opening and closing cycle of the mechanical beak. In the closing cycle, the leading contact line proceeds toward the mouth; in the opening cycle, the trailing contact line recedes toward the mouth. The result is net drop transport toward the mouth. Scale bar, 2 mm. **(B)** Plot of the associated motion of the leading (red) and trailing (green) contact lines generated by varying the opening angle α over three cycles. d (in millimeters) represents the distance from the beak tip to the contact line. [See also movie S2]

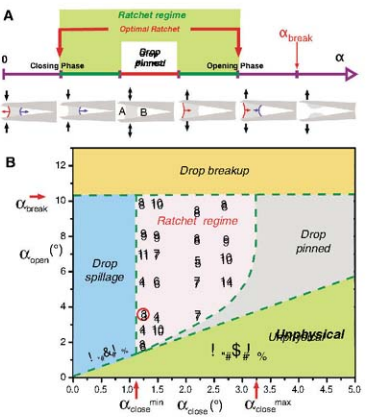

Fig. 4. **(A)** A schematic illustration of droplet dynamics in an oscillating bird beak. The drop is pinned for region $\theta_2 > \theta_1 > \theta_2 > \theta_0$, marked by the red line. As the beak is closed progressively, first the leading (A) then the leading and trailing (B) contact lines advance. As the beak is opened, first the trailing (B) then the trailing and leading (A) contact lines retreat. Ultimately, the drop breaks when $\alpha > \alpha_{break}$. The ratcheting regime is indicated in green and the optimal ratchet by the red arrows. **(B)** Regime diagram for droplet transport in an oscillating mechanical bird beak illustrates the dependence of the system's behavior on the minimum and maximum opening angles α_{close} and $\alpha_{open} > \alpha_{close}$, respectively. The drop volume was fixed at 1.5 μL. For $\alpha_{open} > \alpha_{break}$, the drop breaks, whereas for $\alpha_{close} < \alpha_{close}^{min}$, the drop spills from the beak. The numbers denote the number of cycles required to transport the drop from the beak tip to the mouth in the ratcheting regime. The optimal capillary ratchet transports the drop in three cycles.

drop speed increases linearly with the ratcheting frequency ω.

Figure 4B illustrates the various regimes of droplet transport observed in our mechanical bird beak when the minimum and maximum opening angles, α_{close} and α_{open}, respectively, were varied. In addition to regimes characterized by drop pinning and drop breakup, we report the number of cycles required for drop transport from the mechanical beak tip to the apex of the wedge in the ratchet regime. For our specific combination of droplet volume (1.5 μl) and mechanical beak geometry, the minimum number of cycles, three, corresponds to the most efficient capillary ratchet. It is interesting to speculate as to the degree of optimization of capillary feeding in the wild. On average, a single drop is transported from the beak tip to the buccal cavity of the red-necked phalarope in two to three mandibular spreading cycles (*1*, *4*). Wilson's phalaropes are evidently less optimized for capillary feeding, and require seven to eight cycles (*7*). Our observations provide a quantitative measure of the efficiency of shorebird beaks in capillary feeding, and so may yield insight into their degree of adaptation. Moreover, they yield new insight into recent observations of rynchokinesis, in which capillary feeding may be enhanced by beak flexure (*6*).

The beaks of shorebirds may be largely vertical during capillary feeding; thus, the influence of gravity needs to be considered. Although gravity acts to resist the climbing drop, it is overcome by contact-angle hysteresis provided that the pinning force, $F_p = \gamma W \Delta \cos\theta$, exceeds the drop and prey weight, Mg. Characteristic values for the phalarope [$W \sim 2$ mm, $\Omega \sim 5$ to 10 μl (*1*)] indicate that $F_p/(Mg) > 1$: Contact-angle hysteresis can safely support the drop's weight. In our experimental study, changing the orientation of the mechanical beaks from horizontal to vertical indeed had a negligible effect on the dynamics of the water drops. Conversely, wetting silicone droplets were observed to slip downward under the influence of gravity, owing to the absence of contact-line pinning. Wetting droplets would slip if the propulsive capillary force $\gamma WL/x$ were exceeded by the drop's weight. Because the relative magnitudes of these forces are given by $L^2/(aL_b^2) \sim 0.1$, with $\alpha \sim 5° = 0.1$ rad and beak length $L_b \sim 2$ cm, we conclude that gravity would preclude capillary feeding if the beaks were wetting. We thus see that, although the partially wetting nature of the bird beaks disables static capillary propulsion through the introduction of an adhesive force, it enables droplet transport via capillary ratcheting, a mechanism that naturally overcomes gravity. We thus highlight the precarious nature of capillary feeding: Any surface contamination that alters the wetting properties of the beaks represents a serious threat, particularly to shorebirds such as the red-necked phalarope that rely exclusively on this mode of feeding (*1*). Given the drastic changes in wetting behavior that accompany contamination with pollutants such as petroleum or detergents (*23*), our study makes clear the critical danger posed to this class of shorebirds by chemical or oil spills (*25*, *26*).

Contact-angle hysteresis typically resists the motion of drops on solid substrates; conversely, in capillary feeding, it couples with the time-dependent beak geometry to drive the drops. As such, surface tension transport represents a peculiarity for which contact-angle hysteresis enables rather than impedes drop motion. By elucidating the dependence of the efficiency of the capillary ratchet on dynamic beak morphology, we have enabled quantitative comparative studies of capillary feeding across species. The efficiency of capillary feeding may be enhanced by tuning the beak geometry, dynamics, and wetting properties. Analogous mechanisms for small-scale drop transport in microfluidic systems (*27*) are currently being explored.

References and Notes

1. M. A. Rubega, B. S. Obst, *Auk* **110**, 169 (1993).
2. B. S. Obst *et al.*, *Nature* **384**, 121 (1996).
3. M. A. Rubega, *J. Morphol.* **228**, 45 (1996).
4. M. A. Rubega, thesis, University of California, Irvine, CA (1993).
5. S. M. Estrella, J. A. Masero, A. Perez-Hurtado, *Auk* **124**, 1244 (2007).
6. S. M. Estrella, J. A. Masero, *J. Exp. Biol.* **210**, 3757 (2007).
7. M. A. Rubega, *Ibis* **139**, 488 (1997).
8. G. Zweers, *Acta Biotheor.* **39**, 15 (1991).
9. F. Brochard, *Langmuir* **5**, 432 (1989).
10. P. G. de Gennes, *Rev. Mod. Phys.* **57**, 827 (1985).
11. R. H. Dettre, R. E. Johnson, *Contact Angle, Wettability, and Adhesion*, vol. 43 of *Advances in Chemistry Series* (American Chemical Society, Washington, DC, 1964).
12. E. Dussan, R. T. P. Chow, *J. Fluid Mech.* **137**, 1 (1983).
13. S. Daniel, M. K. Chaudhury, *Langmuir* **18**, 3404 (2002).
14. S. Daniel, M. K. Chaudhury, P.-G. de Gennes, *Langmuir* **21**, 4240 (2005).
15. T. Y. Chen, J. Tsamopoulos, R. J. Good, *J. Colloid Int. Sci.* **151**, 49 (1992).
16. B. J. Lowry, P. H. Steen, *Proc. R. Soc. London Ser. A* **449**, 411 (1995).
17. P. Concus, R. Finn, *Phys. Fluids* **10**, 39 (1998).
18. S. Nebel, D. Jackson, R. Elner, *Anim. Biol.* **55**, 235 (2005).
19. R. W. Elner, P. G. Beninger, D. L. Jackson, T. M. Potter, *Mar. Biol.* **146**, 1223 (2005).
20. S. Humphries, R. H. C. Bonser, M. P. Witton, D. M. Martill, *PLoS Biol.* **5**, 1647 (2007).
21. F. Hauksbee, *Philos. Trans.* **27**, 395 (1712).
22. H. Bouasse, *Capillarité et Phénomènes Superficiels* (Librairie Delagrave, Paris, 1924).
23. P. G. de Gennes, F. Brochard-Wyart, D. Quéré, *Capillarity and Wetting Phenomena: Drops, Bubbles, Pearls and Waves* (Springer-Verlag, Berlin, 2003).
24. Y. K. Kamath, C. J. Dansizer, H. Weigmann, *J. Appl. Polym. Sci.* **22**, 2295 (1978).
25. Z. A. Eppley, M. A. Rubega, *Nature* **340**, 513 (1989).
26. R. Stephenson, *Environ. Conserv.* **24**, 121 (1997).
27. M. Prakash, N. Gershenfeld, *Science* **315**, 832 (2007).
28. A. Barbosa, E. Moreno, *Auk* **116**, 712 (1999).
29. T. Szekely, R. P. Freckleton, J. D. Reynolds, *Proc. Natl. Acad. Sci. U.S.A.* **101**, 12224 (2004).

30. J.B. acknowledges support from NSF. M.P. acknowledges support from the MIT Center for Bits and Atoms (NSF grant CCR-0122419). A patent on the use of contact-angle hysteresis for the directed transport of fluid droplets, relevant to microfluidic technologies, has been filed by MIT.

Supporting Online Material

www.sciencemag.org/cgi/content/full/320/5878/931/DC1
SOM Text
Figs. S1 and S2
Movies S1 and S2

4 February 2008; accepted 24 March 2008
10.1126/science.1156023

Termination Factor Rho and Its Cofactors NusA and NusG Silence Foreign DNA in *E. coli*

Christopher J. Cardinale,[1]* Robert S. Washburn,[2]* Vasisht R. Tadigotla,[3]† Lewis M. Brown,[4] Max E. Gottesman,[2,5]‡ Evgeny Nudler[1]‡

Transcription of the bacterial genome by the RNA polymerase must terminate at specific points. Transcription can be terminated by Rho factor, an essential protein in enterobacteria. We used the antibiotic bicyclomycin, which inhibits Rho, to assess its role on a genome-wide scale. Rho is revealed as a global regulator of gene expression that matches *Escherichia coli* transcription to translational needs. We also found that genes in *E. coli* that are most repressed by Rho are prophages and other horizontally acquired portions of the genome. Elimination of these foreign DNA elements increases resistance to bicyclomycin. Although *rho* remains essential, such reduced-genome bacteria no longer require Rho cofactors NusA and NusG. Deletion of the cryptic *rac* prophage in wild-type *E. coli* increases bicyclomycin resistance and permits deletion of *nusG*. Thus, Rho termination, supported by NusA and NusG, is required to suppress the toxic activity of foreign genes.

The complete genome sequence of *Escherichia coli* revealed that 90% of its nucleotide sequence could encode protein (*1*). The remaining noncoding genome is densely packed with regulatory signals for transcription initiation and termination. This high information density requires that transcription terminate precisely at operon ends to avoid interference with neighboring transcription units. Based on sequence, approximately half of the transcription units, or operons, in *E. coli* are predicted to end with a specific structure, an intrinsic terminator, consisting of a hairpin followed by several U residues at the 3′ terminus of the RNA. This structure alone is sufficient to dissociate the polymerase elongation complex in vitro (*2*, *3*). In contrast, transcription termination of the remaining half of operons could not be predicted from DNA sequence and has been generally assumed to rely on an adenosine triphosphate–dependent RNA-DNA helicase known as Rho factor. In the decades since its discovery (*4*), Rho has been well studied biochemically and structurally (*2*, *5*–*8*), but its role as a biological regulator is still unclear. Rho factor recognizes no specific consensus but rather binds to naked, untranslated RNA, favoring C-rich sites that contain little secondary structure (*9*–*11*). Rho-dependent termination sites occur frequently in operons. For example, Rho can stop transcription when the end of the coding information is reached (*12*) and attenuate transcription conditionally at the beginning of operons (*13*), and even within open reading frames (ORFs) when mRNA is uncovered by a

[1]Department of Biochemistry, New York University School of Medicine, New York, NY 10016, USA. [2]Department of Microbiology, Columbia University Medical Center, New York, NY 10032, USA. [3]BioMaPS Institute for Quantitative Biology, Rutgers, The State University of New Jersey, Piscataway, NJ 08854, USA. [4]Comparative Proteomics Center, Department of Biological Sciences, Columbia University, New York, NY 10027, USA. [5]Department of Biochemistry and Molecular Biophysics, Columbia University Medical Center, New York, NY 10032, USA.

*These authors contributed equally to this work.
†Present address: Department of Physics, Boston University, Boston, MA 02215, USA.
‡To whom correspondence should be addressed. E-mail: evgeny.nudler@med.nyu.edu (E.N.); meg8@columbia.edu (M.E.G.)

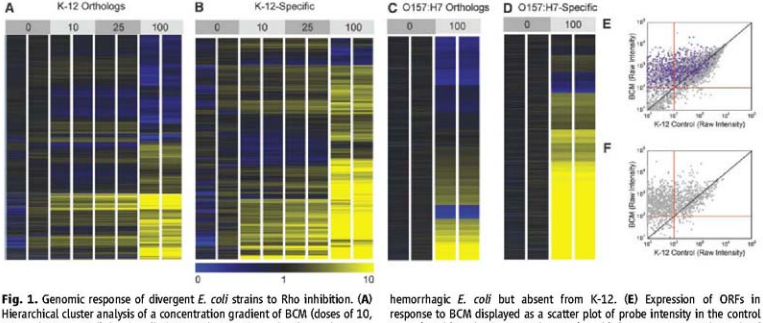

Fig. 1. Genomic response of divergent *E. coli* strains to Rho inhibition. **(A)** Hierarchical cluster analysis of a concentration gradient of BCM (doses of 10, 25, and 100 μg/ml) in *E. coli* K-12 strain MG1655, showing only genes orthologous between K-12 and enterohemorrhagic *E. coli*. Arrays (columns) are shown in biological duplicates, normalized so that the average of each gene on the untreated control arrays is equal to 1 and expression in treated cultures is displayed as a ratio of treated to untreated. Yellow blocks represent up-regulation by BCM, and blue represents down-regulation. **(B)** Response to BCM of genes present in K-12 *E. coli* but absent from enterohemorrhagic *E. coli*, displayed as in (**A**). **(C)** Hierarchical cluster analysis of the response of orthologous genes in enterohemorrhagic *E. coli* O157:H7 strain EDL933. **(D)** Response to BCM treatment of genes present in enterohemorrhagic *E. coli* but absent from K-12. **(E)** Expression of ORFs in response to BCM displayed as a scatter plot of probe intensity in the control array (*x* axis) and BCM-treated array (*y* axis) from a representative pair of arrays. The diagonal line represents equal probe hybridization intensity between both arrays; points above the diagonal are genes up-regulated by treatment with BCM, and points below the diagonal are down-regulated. The red lines located at 100 intensity units represent the threshold below which probe-level analysis is 90% likely to call the probe absent. Therefore, probes in the upper left quadrant are ORFs whose expression was induced de novo. Gray points are orthologous genes and violet points are K-12–specific genes. **(F)** Scatter plot of probe intensity for intergenic (IG) regions of MG1655 after treatment by BCM.

nonsense mutation (*14*). In each case, the hypothesized roles of Rho are to prevent transcription from impinging on neighboring operons, to prevent the wasteful production of unusable transcripts, and to recycle polymerases promptly to locations where they are needed. However, because only a handful of Rho terminators (<10) have been actually located and characterized (*15*), there is still much to be learned about the role of Rho-dependent termination in vivo.

To investigate the biological role of Rho, we assayed gene expression using the Affymetrix *E. coli* Genome 2.0 array, an in situ synthesized oligonucleotide array covering the entire genome of four evolutionarily divergent *E. coli* strains: the laboratory strain K-12 MG1655, the enterohemorrhagic strains O157:H7 (EDL933 and Sakai), and uropathogenic CFT073. Specific and potent inhibition of Rho can be achieved rapidly by treatment with the antibiotic bicyclomycin (BCM) (*16*). An advantage of chemical over genetic intervention is that the transcriptome content of control and experimental cultures remains identical until the moment the inhibitor is added. Indeed, total inhibition of Rho termination activity cannot be achieved by genetic manipulation because *rho* is an essential gene (*17*). BCM is highly specific to Rho; it rapidly permeates cells and has no other known in vivo targets (*16*, *18*). Changes in gene expression in response to BCM reflect, therefore, a snapshot of Rho activity. Treatment of MG1655 with a series of concentrations of BCM for short time intervals revealed a pervasive change in gene expression (Fig. 1). One theme that emerges from the array data is a widespread increase in the expression of genes derived from recent horizontal transfer into the genome of K-12 from other species or from defective bacteriophage (Fig. 1, B and D, and fig. S2B). Based on whole-genome alignment, ~14 to 18% of the K-12 genome differs from other families of *E. coli*, tending to occur in contiguous blocks known as K islands (*19*, *20*). K islands are characterized by an altered guanine-cytosine/adenine-thymine (GC/AT) content, distinct codon preference, and reduced evolutionary conservation. The genomic islands are enriched in defective prophages, transposons, and insertion sequences (*21*). Comparing MG1655 with the enterohemorrhagic strain O157:H7 (EDL933) shows that the two strains possess 3658 genes that are nearly identical in sequence, as well as 648 and 1769 unique genes, respectively (*22*). As shown in Fig. 1, B and D, the genes unique to each strain and prophage genes tended to be up-regulated, with half of these genes increasing expression by a factor of more than 3. By contrast, a quarter of orthologous genes, common between the two strains, were up-regulated by a factor of more than 3 (compare orthologous and K-12–specific genes in Fig. 1E).

We find that expression of the noncoding intergenic (IG) regions is in general increased by Rho inhibition (Fig. 1F). Of the IG probes that were reproducibly measured, as selected by significance analysis of microarrays at the 1% false discovery rate (*23*), 72% were increased by a factor of at least 3 and only 1% were decreased by a factor of at least 3. The general up-regulation of IG regions confirms that Rho has a global role in preventing synthesis of untranslated transcripts. Taken together, the array data from BCM treatment of *E. coli* indicate that Rho is intimately involved in operon regulation throughout the genome and is not only acting on a rare subset of genes or when translation terminates abnormally.

We next sought to determine whether this extensive perturbation in the transcriptome was reflected in the proteome. We used difference gel electrophoresis (DIGE) to analyze the protein complement of MG1655 cells treated under the same conditions used in the microarray experiments (*24*). The workflow for this analysis is shown in fig. S6A. Two-dimensional gels of fluorescently labeled proteins show that of 3341 unique spots analyzed, 101 were increased by a factor of more than 2 and 8 were decreased by a factor of more than 2 by BCM treatment. Altered spots were robotically excised from gels, and the proteins were identified by mass spectrometry (Fig. 2). As shown in Fig. 2 and tables S1 and S2, among the most affected unique proteins is Rho itself and the RecE protein of the Rac prophage. For reasons not understood, most of the other proteins identified are involved in anaerobic metabolism and the response to acidic pH. Based on the microarray result, that many de novo transcripts of unique

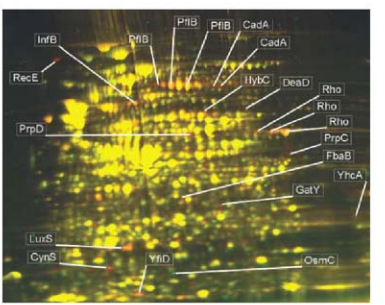

Fig. 2. Proteomic response to Rho inhibition as detected by DIGE. Two-dimensional electrophoresis gel of protein extracted from BCM-treated and control cultures. Control protein is pseudocolored green, and BCM-treated protein is red. Differentially expressed proteins (indicated by name) were identified by mass spectrometry.

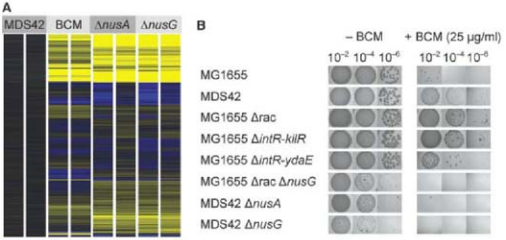

Fig. 3. Reduced-genome *E. coli* is resistant to Rho inhibition and deletion of elongation factors NusA and NusG. **(A)** Hierarchical cluster analysis of ORF gene expression in strain MDS42, BCM-treated MDS42, MDS42 Δ*nusA*, and MDS42 Δ*nusG*. Probe intensity is normalized to the untreated MDS42 strain. **(B)** Efficiency of colony formation assay of the indicated strains. Cultures at dilutions of 10^{-2}, 10^{-4}, and 10^{-6} were spotted onto a control plate or a plate containing BCM at 25 μg/mL. *int-kilR* and *int-ydaE* are fragments of the *rac* prophage that were deleted.

genes were being produced, we expected to see many new spots appearing on the gel from the BCM-treated sample. However, this did not occur. The proteomic results corroborate the role of Rho as a general inhibitor of transcription under normal growth conditions. There is a profound excess of transcriptional output over translational needs when Rho activity is reduced. The lack of perturbation of the proteome also suggests that protein expression is frequently controlled post-transcriptionally.

Because Rho strongly represses transcription of horizontally transferred genes, we investigated a synthetic *E. coli* strain, MDS42, that lacks these genes. Fourteen percent of the MDS42 genome has been removed by targeted deletion of prophages, IS elements, and K-island clusters (*25*, *26*). Figure 3B shows that MDS42 was ~10^4 times as resistant to BCM (25 μg/ml) as the parent strain, MG1655. MG1655 contains the remnants of a lambdoid bacteriophage known as *rac*. This defective prophage carries a *kil* gene encoding an inhibitor of cell division. Deletion of *rac* alone produced levels of BCM resistance comparable to the MDS42 strain. The resistance was conferred by deletion of *kil* and the remaining downstream operon but not DNA downstream of *kil* (Fig. 3B).

Studies of λ phage revealed that endogenous host proteins NusA, NusB, NusE (ribosomal protein S10), and NusG were required for the λ N protein to suppress transcription termination on the phage chromosome (*27*, *28*). NusA and NusG have been implicated in both Rho-dependent and intrinsic termination and are essential for *E. coli* to survive (*29*, *30*). It was possible to delete both *nusA* and *nusG* in strain MDS42, although stationary phase survival was poor, and the strains were highly sensitive to BCM (Fig. 3B). Deleting *nusA* or *nusG* also adversely affected growth rate, increasing the doubling time in rich media from 32 min to 57 min and 68 min, respectively. Unexpectedly, it was possible to transfer the *nusG* knockout allele to a wild-type MG1655 strain lacking the *rac* prophage alone, which indicates that suppression of *rac* gene expression is the critical function of NusG.

Strains lacking NusA or NusG are highly similar in their overall pattern of gene expression, as shown by the hierarchical cluster analysis in Fig. 3A and the scatter plot of intergenic region expression in supplemental fig. S2, C and D. We therefore conclude that these proteins normally act in concert, recognizing the same elongation and termination signals.

To understand the basis of how Rho inhibition could affect gene expression on such a pervasive scale, we examined two specific operons, one in the *rac* prophage and one in λ. The maps in Fig. 4, A and B, show that the leftward operons of *rac* and λ are homologous, which implies that there should be a Rho-dependent terminator (t_{tmn}) in *rac* after the *racR* gene, as there is in λ. Addition of BCM enables the RNA polymerase to continue through this terminator and express downstream genes, including the toxic *kil* gene. Reverse transcription polymerase chain reaction (RT-PCR) analysis reveals the elongated transcript (Fig. 4C). Similarly, the leftward operon of λ (Fig. 4B) exhibits read-through of the t_{tmn} terminator into the downstream *N::lacZ* reporter fusion in the presence of BCM (Fig. 4D). The HK022 Nun termination protein, which blocks transcription elongation at the λ *nutL* site, prevents reporter gene expression, consistent with a transcript originating from the P_{RM} promoter (*31*).

As shown by the maps of prophages in fig. S4, genes that are up-regulated by treatment with BCM tend to occur in consecutive series in the same strand orientation, suggesting that preventing readthrough into neighboring operons is an important function of Rho. Rho's bias toward suppressing foreign DNA could be related to the lower density of the Rho-independent intrinsic terminators in the K-island regions. Using the terminator-prediction model of Lesnik *et al.* (*32*), there is an intrinsic terminator on average every 4.0 kb in the conserved regions of the genome, but only every 8.5 kb in the K islands (table S7) (*32*). Moreover, the genes up-regulated by treatment with BCM tend to be more AT rich than the genome as a whole (fig. S1) and have a lower codon adaptation index (fig. S5B). The lower secondary structure of AU-rich RNA could make it a favored target of Rho-dependent termination despite Rho's in vitro binding affinity for C-rich RNA, whereas the suboptimality of translation in genes with poor codon preference leaves them open to Rho.

Our results reveal Rho factor as a global regulator of bacterial gene expression under normal growth conditions. Rho serves the crucial role of maintaining transcriptional boundaries throughout the genome. In particular, Rho is responsible for silencing horizontally transferred DNA elements, some of which are detrimental to the host. Recently, H-NS protein has been implicated in selective silencing of foreign DNA in *Salmonella* by acting at the level of promoter initiation (*33*). Rho-dependent termination may represent a separate "immunity" system that protects bacterial cells from the harmful activity of certain foreign genes. The existence of such different defensive tools against new acquisitions to the genome underscores the importance of this phenomenon for bacterial evolution.

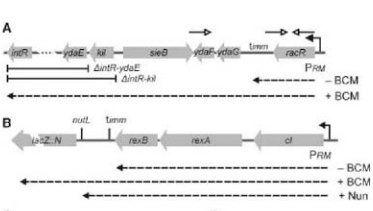

Fig. 4. Effect of BCM on the leftward operons of *rac* and λ phages. **(A)** Map of the leftward operon of the *rac* prophage. Gray arrows, genes; open-headed arrows, PCR primers; brackets, deletions of *intR-ydaE* and *intR-kil*; bent arrow, the operon's promoter (P_{RM}). **(B)** Map of the homologous operon of λ phage. Dashed lines show proposed transcripts produced. **(C)** RT-PCR using primer pairs indicated on the map in panel A shows that BCM treatment yields an elongated transcript. RT, reverse transcriptase. **(D)** Average β-galactosidase activity (*lacZ* expression) from the phage strain shown in (B). The standard error is <5%.

References and Notes

1. F. R. Blattner *et al.*, *Science* **277**, 1453 (1997).
2. E. Nudler, M. E. Gottesman, *Genes Cells* **7**, 755 (2002).
3. T. Platt, *Annu. Rev. Biochem.* **55**, 339 (1986).
4. J. W. Roberts, *Nature* **224**, 1168 (1969).
5. R. J. Browne, E. W. Barr, B. L. Stitt, *J. Biol. Chem.* **280**, 13292 (2005).
6. J. Geiselmann, Y. Wang, S. E. Seifried, P. H. von Hippel, *Proc. Natl. Acad. Sci. U.S.A.* **90**, 7754 (1993).
7. J. P. Richardson, *Cell* **114**, 157 (2003).
8. E. Skordalakes, J. M. Berger, *Cell* **127**, 553 (2006).
9. C. M. Hart, J. W. Roberts, *J. Biol. Chem.* **266**, 24140 (1991).
10. T. Platt, *Mol. Microbiol.* **11**, 983 (1994).
11. L. V. Richardson, J. P. Richardson, *J. Biol. Chem.* **271**, 21597 (1996).
12. D. Court *et al.*, *J. Mol. Biol.* **138**, 231 (1980).
13. V. Stewart, R. Landick, C. Yanofsky, *J. Bacteriol.* **166**, 217 (1986).
14. S. Adhya, M. Gottesman, *Annu. Rev. Biochem.* **47**, 967 (1978).
15. M. S. Ciampi, *Microbiology* **152**, 2515 (2006).
16. A. Zwiefka, H. Kohn, W. R. Widger, *Biochemistry* **32**, 3564 (1993).
17. A. Das, D. Court, S. Adhya, *Proc. Natl. Acad. Sci. U.S.A.* **73**, 1959 (1976).
18. F. Vincent *et al.*, *Biochemistry* **39**, 9077 (2000).
19. H. Ochman, J. G. Lawrence, E. A. Groisman, *Nature* **405**, 299 (2000).

20. N. T. Perna *et al.*, *Nature* **409**, 529 (2001).
21. M. McClelland *et al.*, *Nature* **413**, 852 (2001).
22. J. D. Glasner *et al.*, *Nucleic Acids Res.* **36**, D519 (2008).
23. V. G. Tusher, R. Tibshirani, G. Chu, *Proc. Natl. Acad. Sci. U.S.A.* **98**, 5116 (2001).
24. C. J. Rivard *et al.*, *J. Biol. Chem.* **282**, 6644 (2007).
25. V. Kolesnychenko *et al.*, *Genome Res.* **12**, 640 (2002).
26. G. Posfai *et al.*, *Science* **312**, 1044 (2006).
27. T. F. Mah, J. Li, A. R. Davidson, J. Greenblatt, *Mol. Microbiol.* **34**, 523 (1999).
28. Y. Zhou, J. J. Filter, D. L. Court, M. E. Gottesman, D. I. Friedman, *J. Bacteriol.* **184**, 3416 (2002).
29. M. C. Schmidt, M. J. Chamberlin, *J. Biol. Chem.* **259**, 15000 (1984).
30. S. L. Sullivan, M. E. Gottesman, *Cell* **68**, 989 (1992).
31. R. S. Washburn, Y. Wang, M. E. Gottesman, *J. Mol. Biol.* **329**, 655 (2003).
32. E. A. Lesnik *et al.*, *Nucleic Acids Res.* **29**, 3583 (2001).
33. W. W. Navarre *et al.*, *Science* **313**, 236 (2006).
34. This work was supported by NIH grants R01 GM58750 and GM72814 (E.N.) and R01 GM37219 (W.G.), and by the Office of the Vice President for Arts and Sciences, Columbia University (L.B.). The authors thank Jiri Zavadil and the NYU Cancer Institute Genomics Facility for processing of arrays and help with data analysis. Microarray data discussed in this paper are available from the National Center for Biotechnology Information Gene Expression Omnibus accession number GSE10345.

Supporting Online Material

www.sciencemag.org/cgi/content/full/320/5878/935/DC1
Materials and Methods
SOM Text
Figs. S1 to S7
Tables S1 to S6
References

8 November 2007; accepted 2 April 2008
10.1126/science.1157263

Genome-Scale Proteomics Reveals *Arabidopsis thaliana* Gene Models and Proteome Dynamics

Katja Baerenfaller,[1,2]* Jonas Grossmann,[1,2,3] Monica A. Grobei,[2,4] Roger Hull,[5] Matthias Hirsch-Hoffmann,[1] Shaul Yalovsky,[6] Philip Zimmermann,[1] Ueli Grossniklaus,[2,4] Wilhelm Gruissem,[1,2,3]* Sacha Baginsky[1,2]*

We have assembled a proteome map for *Arabidopsis thaliana* from high-density, organ-specific proteome catalogs that we generated for different organs, developmental stages, and undifferentiated cultured cells. We matched 86,456 unique peptides to 13,029 proteins and provide expression evidence for 57 gene models that are not represented in the TAIR7 protein database. Analysis of the proteome identified organ-specific biomarkers and allowed us to compile an organ-specific set of proteotypic peptides for 4105 proteins to facilitate targeted quantitative proteomics surveys. Quantitative information for the identified proteins was used to establish correlations between transcript and protein accumulation in different plant organs. The *Arabidopsis* proteome map provides information about genome activity and proteome assembly and is available as a resource for plant systems biology.

Sequencing of complete genomes has advanced our understanding of biological systems, mostly by enabling a broad range of technologies for the analysis of gene functions and by providing information about the theoretical protein-coding capacity of organisms (*1*). Because proteins are usually the effectors of biological function, knowledge about their expression levels provides relevant information for the characterization of a biological system. Mass spectrometry instruments with increased detection sensitivity, together with protein and peptide fractionation technologies and data analysis tools, have facilitated cataloguing of proteomes to acquire information about functional properties and activities of the genome (*2*–*4*).

To assemble a high-density *Arabidopsis* proteome map, we performed 1354 LTQ (linear trap quadrupole) ion-trap mass spectrometry runs with protein extracts from six different organs [fig. S1, table S1, and (*5*)]. The resulting data files were analyzed with two search algorithms, PeptideProphet (*6*) and PepSplice (*7*) (fig. S2). We identified 13,029 proteins with 86,456 unique peptides originating from 790,181 tandem mass spectrometry (MS/MS) spectrum assignments at a false-discovery rate below 1%. The data set of 13,029 proteins is formed by merging the set of 10,902 distinct proteins identified from plant organs, including roots, cotyledons, juvenile leaves, flower buds, open flowers, carpels, siliques, and seeds, with the set of 8698 proteins identified from undifferentiated cultured cells (Table 1). Together, these proteins represent assignments for nearly 50% of all predicted *Arabidopsis* gene models. Our data set is publicly available in the PRIDE database (*8*, *9*), together with information about protein and peptide identification, as well as the corresponding original MS/MS spectra to ensure compliance with the current standards for proteome data deposition (MIAPE) (*10*). The data can be queried in the PRIDE BioMart at www.ebi.ac.uk/pride/prideMart.do, and an enhanced view of the data set is available from our server at www.AtProteome.ethz.ch.

Table 1. Number of assigned spectra, distinct peptides, and proteins in different samples and organs. MoI. mass, average molecular mass in kD.

Plant tissue	Spectra	Distinct peptides	Proteins	MoI. mass
Differentiated organs	465,836	64,219	10,902	54.6
Roots	71,516	27,546	6,125	55.0
Roots 10 days	38,476	20,301	5,159	55.7
Roots 23 days	33,040	16,984	4,466	54.3
Leaves	80,186	20,417	4,853	57.5
Cotyledons	39,419	13,628	3,665	58.2
Juvenile leaves	40,767	14,437	3,892	57.8
Flowers	147,650	33,192	7,040	57.4
Flower buds	54,588	19,467	5,104	58.5
Open flowers	57,861	20,205	5,215	59.0
Carpels	35,201	13,393	3,946	56.7
Siliques	79,589	23,054	5,779	54.6
Seeds	86,895	13,901	3,789	54.7
Cell culture	324,345	49,842	8,698	57.3
Dark	149,051	34,551	6,547	59.7
Light; small	143,583	32,656	6,474	59.8
Light; small	31,711	15,318	4,472	43.2
Total	790,181	86,456	13,029	54.7
TAIR7			27,029	45.9

[1]Institute of Plant Sciences, ETH (Swiss Federal Institute of Technology) Zurich, Universitätstrasse 2, 8092 Zurich, Switzerland. [2]Center for Model Organism Proteomes, University of Zurich, Winterthurerstrasse 190, 8057 Zurich, Switzerland. [3]Functional Genomics Center Zurich, Winterthurerstrasse 190, 8057 Zurich, Switzerland. [4]Institute of Plant Biology, University of Zurich, Zollikerstrasse 107, 8008 Zurich, Switzerland. [5]Faculty of Life Sciences, University of Manchester, Brunswick Street, Manchester M13 9PL, UK. [6]Department of Plant Sciences, Tel Aviv University, Tel Aviv 69978, Israel.

*To whom correspondence should be addressed. E-mail: kbaerenfaller@ethz.ch (K.B.); wgruissem@ethz.ch (W.G.); sbaginsky@ethz.ch (S.B.)

We evaluated the distribution of the identified proteins into different biological processes on the basis of the TAIR7 Gene Ontology (GO) annotation (*11*), using the *elim* method provided with topGO (*12*), and performed Fisher's exact test to assess the significance of over- or underrepresentation of GO categories compared with all proteins in the *Arabidopsis* database. Our analysis revealed an underrepresentation of known low-abundance proteins, such as those involved in transcriptional regulation and signaling, and an overrepresentation of proteins involved in basic metabolic processes, including glycolysis, photosynthesis, cellulose synthesis, and translation (fig. S3). We furthermore observed a preferential detection of large proteins (Table 1). This known bias is particularly pronounced for very complex protein mixtures in high-throughput proteomics (*3*, *13*). In order to mitigate this detection bias, we enriched for low-molecular-mass proteins from cultured cells by alternative gel electrophoresis on 10% Tricine gels. This approach added 714 (~9%) protein identifications with an average molecular mass of 41.2 kD to the cell culture protein set (Table 1).

PepSplice was specifically designed for operating in large search spaces (*7*), which allowed us to identify peptides containing post-translational modifications (*5*) and peptides with nontryptic ends in extended database searches, including protein N termini with N-terminal acetylation or with their initiator methionine removed (tables S2 and S3). Most of the detected modified peptides were either oxidized at methionine (10,089) or tryptophan (347) or carbamidomethylated at cysteine (11,373). Amino acid carbamidomethylation and oxidation usually occur during sample preparation in vitro, but a function for methionine and tryptophan oxidation in signal transduction in vivo is currently being discussed (*14*). We also identified 195 N-terminal acetylated peptides. Because acetylation can be catalyzed by acetyltransferases in vivo, the identified peptides provide information about the substrate spectrum and activity of acetyltransferases (table S3).

We used the PepSplice extended search functionality to match all MS/MS spectra against the TAIR7 genome database and identified peptides from genome regions that have no annotated protein-coding capacity. We required at least two distinct peptides to support a gene model different from those in the *Arabidopsis* protein database. We found 57 new or alternative gene models based on 261 unambiguously identified unique peptides from 2671 spectrum assignments. The revised gene models (Fig. 1 and table S4) fall into several different categories. For 22 annotated gene models, we found different 5′ or 3′ ends. In seven gene models, peptides were identified in predicted intron sequences. We also identified peptides from seven intergenic regions and 15 pseudogenes, which suggests that these genome regions are expressed. Six of the detected pseudogenes are related to open reading frames in transposable elements, which are often listed as pseudogenes, although some are known to be transcribed and translated. Expression of the pseudogenes was further validated by analysis of recent TILING arrays, in which 12 of the 15 pseudogenes were found to be transcribed (*15*). For two annotated gene models, we were able to establish a different open reading frame, whereas four new gene models represent a mixture of the different categories detailed above. Altogether, EST evidence was found for 185 out of the 261 peptides in GenBank (table S4). Genscan, a de novo gene prediction algorithm (*16*), calculated 226 of the 261 peptides, which encompassed 51 of the 57 new or alternative gene models (table S4).

We used topGO to compare the GO category distribution of the cataloged proteins in each *Arabidopsis* organ with the distribution of proteins in the entire map of identified *Arabidopsis* proteins (*11*, *12*). Proteins in GO categories *translation* and *glycolysis* were overrepresented in all organs, whereas proteins were overrepresented for *photosynthesis* and *chloroplast organization* in leaves; for *intracellular protein transport*, *response to oxidative stress*, and *toxin catabolic process* in roots; and for *response to heat stress* and *embryo development* in seeds (Fig. 2A and table S5). Thus, each plant organ can be assigned a specific and functionally significant proteome map. Proteins in the GO category *RNA metabolism* were overrepresented in the proteome of cultured cells, which may reflect their high cell-division rate and their unique metabolism in the presence of sucrose.

For a more detailed comparison of the different organ proteomes on a genome-wide scale, we modified the APEX-indexing method to calculate approximate abundance values for all identified proteins (*17*). From the values obtained for each protein in the different organs, we calculated a correlation matrix to assess the degree of similarity between the different organs (Fig. 2B).

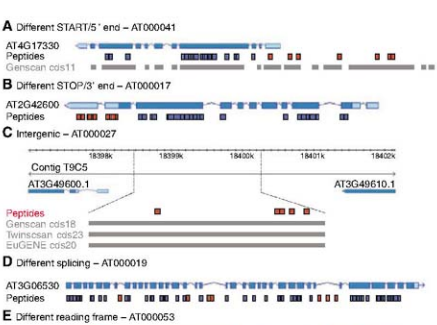

Fig. 1. New or alternative gene models identified by expression evidence from identified peptides. (**A** to **E**) Five examples of newly identified gene models. The upper blue line depicts the gene model in the TAIR 7 protein database, the red boxes indicate the localization of the peptides identified in the whole-genome search, the blue boxes are the peptides of the corresponding gene model identified in the standard protein database search, and the gray line represents gene prediction by alternative gene prediction tools [Genscan (*16*), Twinscan (*27*), EuGENE (*28*)]. The different categories of gene model revisions include (**A**) evidence for a different START/5′ end for gene model AT4G17330, (**B**) evidence for a different STOP/3′ end for gene model AT2G42600, (**C**) evidence for gene expression in the intergenic region between the two gene models AT3G49600 and AT3G49610, (**D**) evidence for different splicing of AT3G06530, and (**E**) evidence for a different reading frame within gene model AT5G39570.

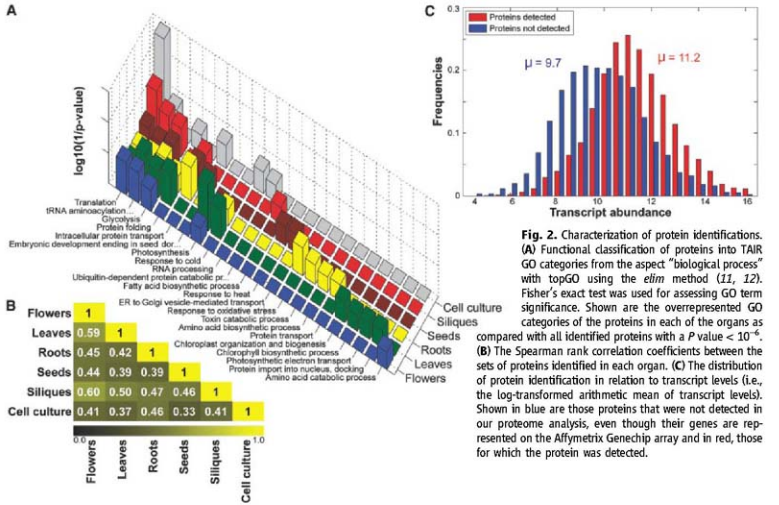

Fig. 2. Characterization of protein identifications. **(A)** Functional classification of proteins into TAIR GO categories from the aspect "biological process" with topGO using the *elim* method (*11*, *12*). Fisher's exact test was used for assessing GO term significance. Shown are the overrepresented GO categories of the proteins in each of the organs as compared with all identified proteins with a P value $< 10^{-6}$. **(B)** The Spearman rank correlation coefficients between the sets of proteins identified in each organ. **(C)** The distribution of protein identification in relation to transcript levels (i.e., the log-transformed arithmetic mean of transcript levels). Shown in blue are those proteins that were not detected in our proteome analysis, even though their genes are represented on the Affymetrix Genechip array and in red, those for which the protein was detected.

The pairwise comparison of undifferentiated cultured cells as a reference with cells from differentiated organs resulted in Spearman rank correlation values ranging from 0.33 for the seed proteome up to 0.46 for the root proteome. Among the proteomes of differentiated organs, the correlation values range from a minimum of 0.39 between the root and leaf and the seed proteome to a maximum of 0.60 between the flower and silique proteome. These correlation coefficients support the results in Fig. 2A and indicate that specialization between different plant organs is reflected in the differential accumulation of proteins.

We next identified proteins from our data set that were found in only one organ, no others, with at least three different spectra. These proteins we called "organ-specific biomarkers." The biomarkers are enriched for specific functional categories (fig. S4 and table S6) and support the GO term assignments of organ-enriched functional proteome maps (Fig. 2A). Our list of 571 organ-specific proteins (table S7) may help identify cis-regulatory elements that control the organ-specific expression of the corresponding gene models. We compared the distribution of the 571 organ-specific biomarkers (table S7) with the distribution of biomarkers identified with transcriptional profiling, by using the Genevestigator anatomy profiles (*18*). We found that the two biomarker data sets cluster similarly in the different organs, which validates the specificity of biomarker detection using proteomics and transcriptomics (fig. S5).

After quantifying proteins using the modified APEX-indexing method described above, we integrated transcriptional profiling data from Genevestigator with our proteomics data to assess the correlation between transcript levels and protein accumulation in different organs (*18*). Our proteome analysis preferentially detected proteins that are expressed at higher transcript frequencies (Fig. 2C). To quantify this effect, we calculated the correlation coefficients from the transcript and protein levels in the different organs. The highest correlation coefficient of 0.68 was found for leaves, and the lowest, 0.52, was found for seeds (fig. S6). Seeds contain a high percentage of stable storage proteins that are deposited in protein bodies, which could explain the low correlation between transcript and protein accumulation compared with other organs. Although transcript and proteomics data were obtained from similar, but distinct, samples and from different experiments, the positive correlation in the different organs suggests that this approach is robust. Overall, the correlation analysis between transcript and protein accumulation at a genome-wide scale suggests that the accumulation of proteins in *Arabidopsis* is primarily regulated at the transcript level. More detailed information will be required to establish the level of posttranscriptional control for individual genes.

Targeted quantitative proteomics requires comprehensive information about detectable peptides that unambiguously identify a protein. Prediction efforts depend on peptide properties and are useful but limited in reliability, because ion suppression effects from coeluting analyte molecules influence which peptides are detectable (*19*). With the constraint that a peptide must be detected with at least three different spectra in a fraction (table S1) in order to be considered proteotypic, we found that the majority of proteotypic peptides were only detected in one fraction or organ, and only a few peptides were detected multiple times (Fig. 3, A and B). One possibility to establish a selection of reliably detectable peptides is to consider only those peptides as proteotypic that are observed in more than 50% of all identifications of the corresponding protein (*20*). Such a strict definition, however, does not allow for a systematic assessment of peptide traceability, because it does not distinguish between peptide samples that were generated with different extraction methods or from different plant samples. An illustrative example for this issue is acetyl-CoA C-acetyltransferase (AT5G48230), for which different peptides were detected in different organs and different fractions (Fig. 3C).

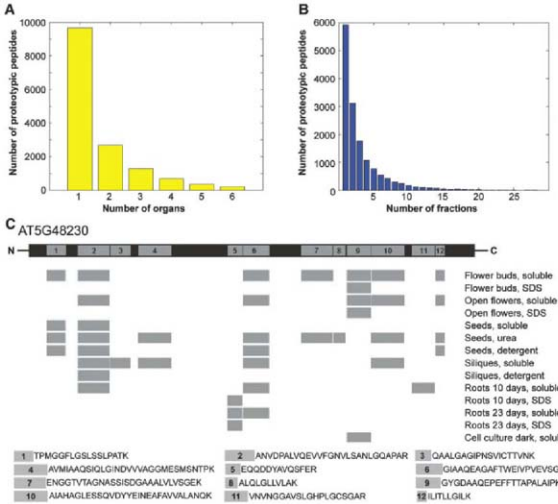

Fig. 3. Organ- and fraction-specific detection of proteotypic peptides. **(A)** Distribution of proteotypic peptides in different organs. The majority (65%) of all proteotypic peptides reported here were detected in only one organ (see number of organs, 1), with a pronounced drop in the number of proteotypic peptides identified in more than one organ, and only 1.3% identified an all organs. **(B)** Distribution of proteotypic peptides in different fractions. The same trend as in (A) applies to the detection of proteotypic peptides in different fractions. **(C)** Example for the fraction- and organ-specific detection of proteotypic peptides (gray boxes) from acetyl-CoA C-acetyltransferase (AT5G48230).

The *Arabidopsis* proteome map provides a detailed map of 14,867 organ-specific proteotypic peptides, which accounts for the diverse composition of protein samples and confers higher sensitivity to proteotypic peptide selection for targeted and quantitative proteomics. Similar proteome maps are available for *Drosophila*, human, and yeast, and the *Drosophila* and human proteome maps have pointed to gene structures not identified by other means (*3*, *21*–*23*). Collectively, these proteomics data complement other strategies for genome annotation and gene prediction. The quantitative proteome map we have assembled for *Arabidopsis* will also facilitate genome-scale transcript and protein abundance correlation analyses to increase our understanding of gene expression control in specific tissues or organs (*24*, *25*). The library of *Arabidopsis* organ-specific proteotypic peptides now allows expanding quantitative correlation analyses to high-resolution surveys of metabolic or regulatory pathways, or even individual enzymes, by sensitive detection and quantification of minute amounts of protein (*26*). Organ-specific proteotypic peptide maps are key to the successful design of such targeted proteomics surveys (supporting online material) and allow proteomics to be used as a routine scoring method in plant systems biology.

References and Notes

1. *Arabidopsis* Genome Initiative, *Nature* **408**, 796 (2000).
2. J. Cox, M. Mann, *Cell* **130**, 395 (2007).
3. E. Brunner *et al.*, *Nat. Biotechnol.* **25**, 576 (2007).
4. J. Eriksson, D. Fenyo, *Nat. Biotechnol.* **25**, 651 (2007).
5. Materials and methods are available as supporting material on *Science* Online.
6. A. I. Nesvizhskii, *Methods Mol. Biol.* **367**, 87 (2007).
7. F. F. Roos *et al.*, *Bioinformatics* **23**, 3016 (2007).
8. P. Jones *et al.*, *Nucleic Acids Res.* **34**, D659 (2006).
9. P. Jones *et al.*, *Nucleic Acids Res.* **36**, D878 (2008).
10. C. F. Taylor *et al.*, *Nat. Biotechnol.* **25**, 887 (2007).
11. T. Z. Berardini *et al.*, *Plant Physiol.* **135**, 745 (2004).
12. A. Alexa, J. Rahnenführer, T. Lengauer, *Bioinformatics* **22**, 1600 (2006).
13. S. Baginsky, T. Kleffmann, A. von Zychlinski, W. Gruissem, *J. Proteome Res.* **4**, 637 (2005).
14. E. R. Stadtman, *Free Radic. Res.* **40**, 1250 (2006).
15. K. Yamada *et al.*, *Science* **302**, 842 (2003).
16. C. B. Burge, S. Karlin, *Curr. Opin. Struct. Biol.* **8**, 346 (1998).
17. P. Lu, C. Vogel, R. Wang, X. Yao, E. M. Marcotte, *Nat. Biotechnol.* **25**, 117 (2007).
18. P. Zimmermann, M. Hirsch-Hoffmann, L. Hennig, W. Gruissem, *Plant Physiol.* **136**, 2621 (2004).
19. T. M. Annesley, *Clin. Chem.* **49**, 1041 (2003).
20. P. Mallick *et al.*, *Nat. Biotechnol.* **25**, 125 (2007).
21. N. L. Kong *et al.*, *Genome Biol.* **7**, R106 (2006).
22. F. Desiere *et al.*, *Nucleic Acids Res.* **34**, D655 (2006).
23. S. Tanner *et al.*, *Genome Res.* **17**, 231 (2007).
24. K. Gallardo *et al.*, *Mol. Cell. Proteomics* **6**, 2165 (2007).
25. T. Kleffmann *et al.*, *Curr. Biol.* **14**, 354 (2004).
26. B. Kuster, M. Schirle, P. Mallick, R. Aebersold, *Nat. Rev. Mol. Cell Biol.* **6**, 577 (2005).
27. I. Korf, P. Flicek, D. Duan, M. R. Brent, *Bioinformatics* **17** (suppl. 1), S140 (2001).
28. S. Foissac, T. Schiex, *BMC Bioinformat.* **6**, 25 (2005).

29. We thank the Functional Genomics Center Zurich, especially B. Roschitzki, C. Panse, and M. Schmidt, for providing infrastructure and technical support; E. Brunner from the Center for Model Organism Proteomes (C-MOP) for project coordination; and J. Fütterer from the Institute of Plant Sciences for critical reading of the manuscript. We also thank our colleagues at the European Bioinformatics Institute for their help in building the PRIDE *Arabidopsis* peptide database. This work was supported by the SystemsX initiative of ETH Zurich (K.B., W.G., S.B.) and the University Research Priority Program in Systems Biology/Functional Genomics (U.G. and M.A.G.) in the framework of the C-MOP project, and by the European Framework Programme 6 AGRON-OMICS project (LSHG-CT-2006-037704, W.G.). S.Y. was supported by a sabbatical fellowship provided by ETH Zurich.

Supporting Online Material

www.sciencemag.org/cgi/content/full/1157956/DC1
Materials and Methods
SOM Text
Figs. S1 to S7
Tables S1 to S7
References

18 March 2008; accepted 15 April 2008
Published online 24 April 2008;
10.1126/science.1157956
Include this information when citing this paper.

Cell Identity Mediates the Response of *Arabidopsis* Roots to Abiotic Stress

José R. Dinneny,[1*†] Terri A. Long,[1*] Jean Y. Wang,[1] Jee W. Jung,[1] Daniel Mace,[2] Solomon Pointer,[1] Christa Barron,[3] Siobhan M. Brady,[1] John Schiefelbein,[3] Philip N. Benfey[1,2‡]

Little is known about the way developmental cues affect how cells interpret their environment. We characterized the transcriptional response to high salinity of different cell layers and developmental stages of the *Arabidopsis* root and found that transcriptional responses are highly constrained by developmental parameters. These transcriptional changes lead to the differential regulation of specific biological functions in subsets of cell layers, several of which correspond to observable physiological changes. We showed that known stress pathways primarily control semiubiquitous responses and used mutants that disrupt epidermal patterning to reveal cell-layer–specific and inter–cell-layer effects. By performing a similar analysis using iron deprivation, we identified common cell-type–specific stress responses and revealed the crucial role the environment plays in defining the transcriptional outcome of cell-fate decisions.

High salinity is an important agricultural contaminant (*1*) and has complex effects on root physiology. Although a small set of studies has begun to explore salt responses at the cell-type–specific level (*2*, *3*), it remains unclear to what extent cell identity influences stress responses and what mechanisms enable this regulation. To directly address these issues, we generated a genome-scale, high-resolution expression map for roots grown under standard and high-salinity conditions (*4*). We first performed a phenotypic analysis using different concentrations of salt and a time-course analysis [TC data set in the supporting online material (SOM) text, Fig. 1, A and F, fig. S1, and tables S1 and S2)] of the response of whole roots to salt to select the specific parameters (1 hour of exposure to 140 mM NaCl) for our spatial microarray analysis.

The root of *Arabidopsis* grows from stem cells at the tip. We dissected roots into four longitudinal zones (LZ data set in Fig. 1A and table S1) for analysis, using the position of cells along the longitudinal axis as a proxy for developmental time (fig. S2) (*5*). Cell identity varies along the radial axis; epidermal cells constitute the outermost tissue, followed by the cortex, endodermis, and the central stele (fig. S2). Cell-type–specific transcriptional profiles were generated by fluorescence-activated cell sorting (FACS) of roots that express green fluorescent protein (GFP) reporters in specific cell types (*6*, *7*) (RZ data set in Fig. 1A and table S1). Six different GFP reporters were used to profile all radial zones, including the columella root cap and phloem vasculature (fig. S3 and table S3). Intact roots rather than protoplasted or isolated populations of cells were exposed to salt to ensure that the observed transcriptional response occurred in the context of the whole organ. We performed control experiments to test the effects of sorting on salt-responsive genes (SOM text and tables S4 and S5) and used GFP reporters (*8*) along with image analysis software (*9*) to validate the accuracy of the RZ microarray data (Fig. 1, B to D, and figs. S4 and S5).

With stringent statistical significance criteria, we identified increasing numbers of differentially expressed genes at higher spatial resolution: 238 (at 1 hour), 1173, and 3862 genes were identified in our TC, LZ, and RZ experiments, respectively (Fig. 1A and table S2). Genes regulated in our TC experiment tended to respond to salt stress in multiple radial or longitudinal zones, whereas the majority of genes regulated in the spatial data sets changed in only one zone (Fig. 1, E, G, and H, and fig. S6).

One explanation for the prevalence of cell-type–specific responses may be that salt might not have fully penetrated all root tissues, which led to localized responses. We found, however, that internal tissues tend to be highly responsive; 48% of salt-responsive genes were regulated in

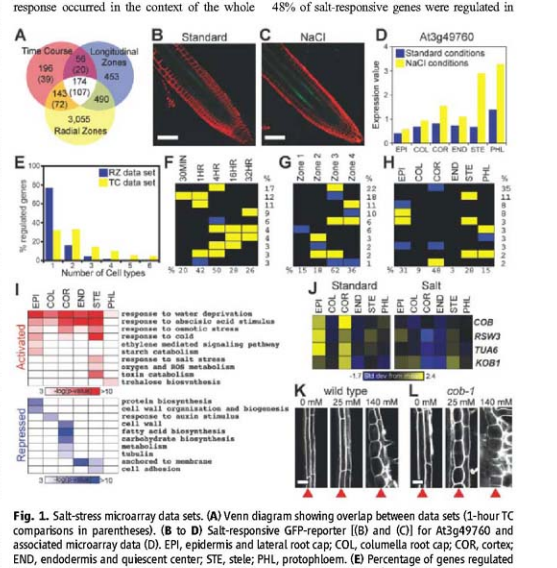

Fig. 1. Salt-stress microarray data sets. **(A)** Venn diagram showing overlap between data sets (1-hour TC comparisons in parentheses). **(B** to **D)** Salt-responsive GFP-reporter [(B) and (C)] for At3g49760 and associated microarray data (D). EPI, epidermis and lateral root cap; COL, columella root cap; COR, cortex; END, endodermis and quiescent center; STE, stele; PHL, protophloem. **(E)** Percentage of genes regulated in one to six cell types identified in the TC and RZ data sets, respectively. **(F** to **H)** Ten most common transcriptional changes in each data set and percent of responsive genes in each experiment (bottom row). Yellow indicates up-regulated genes; blue indicates down-regulated genes. **(I)** Enriched Gene-Ontology categories. **(J)** Expression patterns for cell-shape regulators in response to salt. **(K** and **L)** Cotton cells (arrowheads) swell in response to salt. *cob-1* mutants are hypersensitive to NaCl. Scale bars indicate 50 μm [(B) and (C)] and 30 μm [(K) and (L)].

[1]Department of Biology, Duke University, Durham, NC 27708, USA. [2]Institute for Genome Sciences and Policy Center for Systems Biology, Duke University, Durham, NC 27708, USA. [3]Department of Molecular, Cellular, and Developmental Biology, University of Michigan, Ann Arbor, MI 48109, USA.

*These authors contributed equally to this work.
†Present address: Temasek Lifesciences Laboratory, National University of Singapore, Singapore 117604, Singapore.
‡To whom correspondence should be addressed. E-mail: philip.benfey@duke.edu

the cortex (Fig. 1H), and similar numbers were regulated in the stele (28%) and in the epidermis (31%). Along the longitudinal axis, an increase in salt responsiveness correlates with the beginning of the elongation zone, in which cells begin to acquire their final shape and function (Fig. 1G).

Testing our LZ and RZ data sets for enrichment in Gene-Ontology (*10*) annotations (Fig. 1I, fig. S7, and tables S6 and S7), we found 50 to 82%, respectively, of enriched categories are zone-specific (fig. S8), indicating that salt stress regulates distinct processes on the basis of developmental context. Categories associated with stresses, including abscisic acid (ABA) response, tend to be enriched in multiple cell types, suggesting that most previously characterized stress-response genes are not cell-type–specific.

Salt stress results in radial swelling of the outer tissue layers of roots (Fig. 1K and fig. S9) (*11*), resembling plants with mutations in genes important for cell-wall biogenesis or with reduced tubulin expression. Several of these genes are repressed in the cortex and epidermis, including *COBRA* (*COB*) (*12*), *RADIAL SWELLING3* (*RSW3*) (*13*), *TUBULIN ALPHA-6* (*TUA6*) (*14*), and *KOBITO1* (*KOB1*) (*15*) (Fig. 1J). Gene-Ontology categories associated with these functions are also enriched (Fig. 1I). Consistent with these findings, a hypomorphic allele of *COB* enhances the salt-regulated radial swelling of the cortex, indicating that the expression changes facilitate the cell-shape changes (Fig. 1, K and L, and fig. S9).

We compared cis-element enrichment in the promoters of genes regulated in a zone-specific manner with genes regulated in at least three zones (semiubiquitous responders) for the LZ and RZ data sets, respectively (Fig. 2A and table S8). In the LZ data set, enrichment of many known cis elements, such as drought-responsive element (DRE) (*16*) and ABA-responsive element (ABRE) (*17*, *18*), was observed in both gene sets, whereas enrichment was largely limited to the semiubiquitous gene set in the RZ data set. Thus, although canonical stress-response pathways appear to be active in all cell layers, cell-type–specific responses are distinguishable at the promoter level and probably controlled by other cis elements. This suggests that cell-type–specific salt responses are not simply controlled by a combination of stress- and developmental-regulatory elements in a single promoter.

The plant hormone ABA is known to mediate stress responses, and ABA-response mutants are partly resistant to high salinity (*19*). Strong enrichment of ABRE cis elements in the promoters of semiubiquitous responders suggested that ABA activity is present throughout the root. To test this, we examined the salt responsiveness of hormone-marker genes (*20*). We find enrichment of up-regulated ABA-marker genes in all cell layers of the root (Fig. 2B and table S9) but not for other hormones (fig. S10B). This apparent widespread activity suggested that ABA might primarily mediate semiubiquitous transcriptional responses to salt. We therefore monitored the effects of ABA deficiency on the expression of a set of cell-type–specific, salt-stress–activated genes (*21*, *22*). We find that salt-induced expression is diminished for many of these genes, similar to a collection of semiubiquitous responders also tested (Fig. 2, C and D). Together, these results indicate that ABA regulates cell-type–specific responses to salt stress in a manner independent of characterized ABRE elements.

DRE and its derivatives are bound by a subclass of APETALA2 (AP2)– and ethylene-responsive element-binding protein–type transcription factors, such as *DREB2A* (*23*, *24*). Strong DRE enrichment is detected in genes up-regulated in at least three radial zones (Fig. 2A). Consistent with this, *DREB2A* is expressed in all cell layers under salt-stress conditions (fig. S10C). Recently, potential direct targets of DREB2A have been identified (*25*). These targets tend to be up-regulated by salt in at least three cell types at a higher frequency than expected ($P = 6.5 \times 10^{-6}$, Fig. 2E, and table S10), supporting the hypothesis that the DRE/DREB2A regulatory module primarily controls semiubiquitous responses.

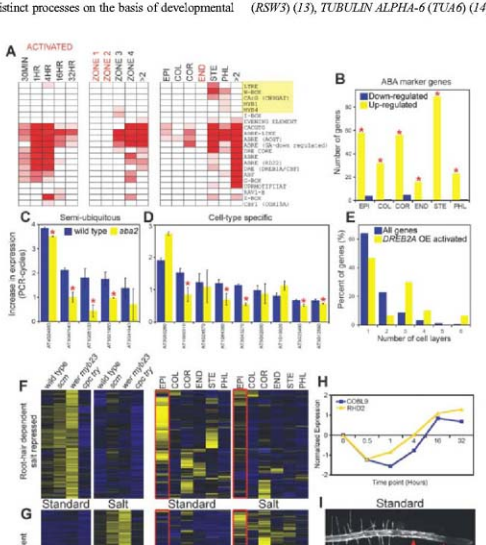

Fig. 2. Regulation of salt responses. **(A)** Enriched known cis-elements. Gene sets in red contain fewer than 50 genes. Shading indicates increasing statistical significance from $P = 1 \times 10^{-3}$ to $P = 1 \times 10^{-10}$; yellow box indicates cell-type–specific enriched cis elements. Figure S10A shows cis elements enriched in salt-repressed gene sets. **(B)** ABA-marker genes are up-regulated and enriched (asterisks, $P < 1 \times 10^{-4}$) in all cell layers. **(C** and **D)** The *aba-2* mutation significantly affects semiubiquitous and cell-type–specific salt-responsive genes (asterisks, $P < 0.05$). **(E)** *DREB2A* overexpression (OE) targets tend to be regulated in multiple cell types by salt. **(F** and **G)** Gene sets regulated by epidermal patterning and salt stress. **(H)** Hair-cell regulators are dynamically expressed in response to salt. **(I** and **J)** Hair-cell outgrowth is transiently suppressed by salt stress. Scale bars, 100 μm [(I) and (J)].

To understand how developmental pathways regulate salt responses, we transcriptionally profiled three mutants that alter cell-fate decisions in the epidermis: *werewolf myb23*, *caprice triptychon* (*26*), and *scrambled* (*27*) (fig. S11, A to D, and table S11). By using less-stringent significance criteria to aid in the identification of cell-type–specific responses, we identified four sets of genes whose activation or repression by salt is dependent on correct epidermal patterning (Fig. 2, F and G, fig. S11, F and G, and table S12). One gene set whose expression is hair-identity–dependent and repressed by salt shows enriched epidermal expression in the RZ data set under standard conditions, indicating that these genes are likely to be hair-cell–specific and salt-responsive (Fig. 2F). Root-hair elongation is inhibited by salt stress (*28*), and we find that many of these repressed genes encode structural components of the cell wall ($P = 1 \times 10^{-8}$) or are involved in trichoblast (hair-cell precursor) differentiation ($P = 1 \times 10^{-4}$). Several of these genes, such as *COBL9* (*29*) and *ROOT HAIR DEFECTIVE2* (*RHD2*) (*30*), show fluctuating expression in the TC data set (Fig. 2H). By quantifying trichoblast cells that failed to form hairs, we were able to track the effects of salt stress on hair development. Hair outgrowth was initially suppressed by salt stress, then resumed after 8 hours of treatment (Fig. 2, I and J, and fig. S11E). Thus, the response of roots is not static but changes over time, potentially as a result of adaptation.

Unexpectedly, 51% of the genes whose expression is affected by salt and epidermal patterning are exclusively regulated in nonepidermal cell types, based on the RZ data set (table S12). Thus, cell-fate decisions may have nonautonomous effects on responses in other cell layers. We also identified 47 genes that respond most dramatically in hairless *caprice triptychon* mutants, indicating that a component of the variation in response is a direct outcome of changes in cell identity and not solely the effects of enhanced salt absorption in genetic backgrounds that develop hairs (fig. S11, F and G, and table S12).

To determine whether the trends we observed for salt stress hold for other environmental stimuli, we generated TC, LZ, and RZ data sets for roots exposed to iron-deficient media (–Fe, tables S1 and S2; control experiments described in SOM). On the basis of the TC data, we performed the LZ and RZ profiling at 24 hours. Iron is a necessary micronutrient and is used in diverse processes from photosynthesis to metabolism. Similar to the salt stress data set, increasing numbers of differentially expressed genes were detected with increasing spatial resolution [at 24 hours: TC, 111 genes; LZ, 142 genes; and RZ, 1318 genes] (Fig. 3A). Most genes are regulated in a zone-specific manner (Fig. 3, B to D, and fig. S12, A and B). Unlike salt stress, iron deprivation elicited the strongest transcriptional response after 24 hours of treatment in LZ 4 (85%) and in the stele (36%), where iron is predominantly stored in seeds and circulated in adult plants (*31*) (Fig. 3, E to G, and fig. S12D). Putative and known genes encoding iron transporter, chelator, storage, metabolic, and regulatory proteins responded in a cell-type–specific manner (Fig. 3H and table S18) (*32*, *33*). The stele response was enriched for generalized stress-responsive genes and suggests that iron deficiency may be sensed internally (Fig. 3I). Consistent with known roles in nutrient absorption, genes activated in the epidermis were enriched for metal-ion transport and nicotianamine (metal chelator) biosynthesis (Fig. 3I, fig. S12A, and table S7). Additionally, cell-wall biogenesis and organization genes, such as the proline-rich extensins associated with root-hair morphogenesis (*29*), were down-regulated in epidermal cells and may explain the observed changes in root-hair morphology (Fig. 3, J and K) (*34*).

A comparison of the two RZ data sets revealed that 20% of salt-responsive genes also responded to iron deprivation (Fig. 4B and table S15). Of these, about half are scored with similar transcriptional changes across all five cell types (Fig. 4A). We initially hypothesized that semi-ubiquitous salt-responsive genes would be most likely to encompass a general stress response;

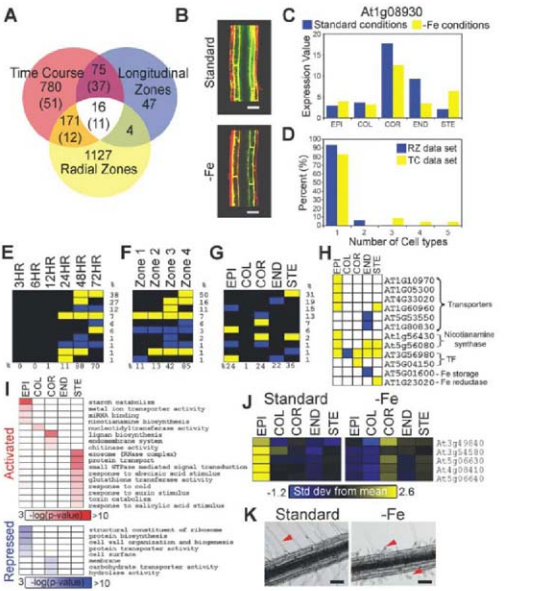

Fig. 3. Iron-deficiency microarray data sets. **(A)** Venn diagram showing overlap between data sets (1-hour TC comparisons in parentheses). **(B)** Iron-deficiency responsive GFP reporter (At1g08930) and associated microarray data **(C)**. **(D)** Percentage of genes regulated in one to six cell types identified in the TC and RZ data sets, respectively. **(E to G)** Ten most common transcriptional changes in each data set and percent of the total responsive genes in each experiment (bottom row). Yellow indicates up-regulated genes; blue indicates down-regulated genes. **(H)** Regulation of putative and known iron-deprivation response genes. Yellow indicates up-regulated genes; blue indicates down-regulated genes (At5g53550, $FDR = 2.7 \times 10^{-5}$). **(I)** Enriched Gene-Ontology categories. miRNA, microRNA; RNase, ribonuclease; GTPase, guanosine triphosphatase. **(J)** Expression patterns for cell-wall biogenesis genes in response to iron deprivation (At3g49840, At3g54580, At4g08410, At5g06630, and At5g06640). **(K)** Root hairs are shorter and misshapen (arrows) in response to iron deprivation. Scale bars, 50 μm [(B)and (K)].

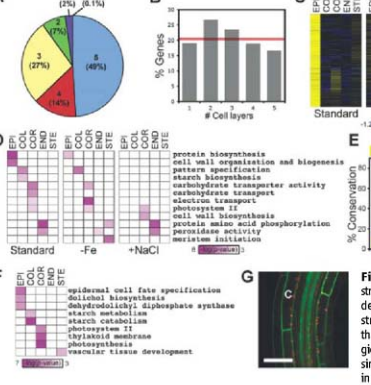

Fig. 4. Comparison of stresses. **(A)** Percent of iron-deprivation– and salt-stress–coregulated genes that exhibit identical (region 5) or completely dissimilar (region 0) regulation in the RZ data set. **(B)** Percent of salt-stress–responsive genes that are also iron-deprivation responsive and the number of cell layers in which those genes respond under salt stress. Overall overlap is 20% (red line). **(C)** Super cluster (no. 406). Figure S13 lists other super clusters. **(D)** Gene-Ontology categories enriched in gene sets with environment-dependent cell-type–specific expression. **(E)** Percent conservation of cell-type–specific gene sets comparing standard conditions with stress gene sets, respectively. **(F)** Gene-Ontology categories enriched in gene sets with environment-independent cell-type–specific expression. **(G)** Chloroplast enrichment in the cortex (*c*). Chloroplasts also accumulate in the pericycle, which was not specifically profiled in these experiments. Scale bar, 50 μm.

however, genes responsive to salt in all five layers are the least likely to be coregulated by iron deprivation, indicating greater environmental specificity for these genes (Fig. 4B). This suggests that cell-type–specific biological processes are common targets for stress regulation, whereas responses occurring in all cells must be finely tuned for specific stimuli. To better understand shared responses, we used the Affinity-Propagation clustering algorithm (*35*) to identify gene sets that coclustered in the iron-deprivation and salt-stress data sets (super clusters, table S15). The largest set of coregulated genes displayed concerted down-regulation in the epidermis and encoded genes important for protein biosynthesis (Fig. 4C and fig. S13A). Both stresses result in reduced root length (figs. S1, A to C, and S12C); this super cluster may represent a common stress module associated with growth suppression.

Previously we have shown that under standard conditions, many biological functions are regulated in a cell-type–specific manner (*6*, *36*). On comparison of expression under standard conditions with these two stresses, we find that only 15% of cell-type–specific biological functions enriched under standard conditions are conserved (Fig. 4D, fig. S13, E and F, and table S16). Thus, the majority of a cell type's unique physiology is environment-dependent. Although the percent of genes that exhibited stable expression patterns between standard conditions and each stress varied for most cell types, the epidermis consistently showed the least conservation (13 to 15%) (Fig. 4E). This trend holds despite the epidermis not being the most responsive cell type for either stress and suggests the functions that define this layer are particularly dependent on environmental constraints.

We identified 244 genes that are cell-type–specific and whose expression pattern does not substantially change with either stress (table S16). Enriched Gene-Ontology categories are consistent with known functions, and we discovered chloroplast accumulation as a novel feature of the cortex in light-grown roots (Fig. 4, F and G). Additionally, this gene set is enriched for many known regulators of cell identity (table S17), suggesting that a small set of core regulators maintain cell identity independent of environmental fluctuations.

Our results reveal that the transcriptional state of a cell is largely a reaction to environmental conditions that are regulated by a smaller core set of genes that stably determines cell identity. The use of environmental stimuli combined with cell- and developmental-stage–specific profiling will enable the identification of high-confidence transcriptional modules, an important first step in modeling transcriptional networks in multicellular organisms.

References and Notes

1. T. J. Flowers, A. Garcia, M. Koyama, A. R. Yeo, *Acta Physiol. Plant.* **19**, 427 (1997).
2. E. Kiegle, C. A. Moore, J. Haseloff, M. A. Tester, M. R. Knight, *Plant J.* **23**, 267 (2000).
3. S. Ma, H. J. Bohnert, *Genome Biol.* **8**, R49 (2007).
4. Material and methods are available on *Science* Online.
5. B. Scheres, P. Benfey, L. Dolan, in *The Arabidopsis Book*, C. R. Somerville, E. M. Meyerowitz, Eds. (American Society of Plant Biologists, Rockville, MD, 2002), pp. 1–18.
6. K. Birnbaum *et al.*, *Science* **302**, 1956 (2003).
7. K. Birnbaum *et al.*, *Nat. Methods* **2**, 615 (2005).
8. J. Y. Lee *et al.*, *Proc. Natl. Acad. Sci. U.S.A.* **103**, 6055 (2006).
9. D. L. Mace *et al.*, *Bioinformatics* **22**, 6323 (2006).
10. M. Ashburner *et al.*, *Nat. Genet.* **25**, 25 (2000).
11. S. Burssens *et al.*, *Planta* **211**, 632 (2000).
12. G. Schindelman *et al.*, *Genes Dev.* **15**, 1115 (2001).
13. J. E. Burn *et al.*, *Plant J.* **32**, 949 (2002).
14. Y. Bao, B. Kost, N. H. Chua, *Plant J.* **28**, 145 (2001).
15. S. Pagant *et al.*, *Plant Cell* **14**, 2001 (2002).
16. K. Yamaguchi-Shinozaki, K. Shinozaki, *Plant Cell* **6**, 251 (1994).
17. J. Mundy, K. Yamaguchi-Shinozaki, N. H. Chua, *Proc. Natl. Acad. Sci. U.S.A.* **87**, 1406 (1990).
18. W. R. Marcotte Jr., S. H. Russell, R. S. Quatrano, *Plant Cell* **1**, 969 (1989).
19. P. Achard *et al.*, *Science* **311**, 91 (2006).
20. J. L. Nemhauser, F. Hong, J. Chory, *Cell* **126**, 467 (2006).
21. M. Gonzalez-Guzman *et al.*, *Plant Cell* **14**, 1833 (2002).
22. E. Nambara, H. Kawaide, Y. Kamiya, S. Naito, *Plant Cell Physiol.* **39**, 853 (1998).
23. Q. Liu *et al.*, *Plant Cell* **10**, 1391 (1998).
24. Y. Sakuma *et al.*, *Plant Cell* **18**, 1292 (2006).
25. Y. Sakuma *et al.*, *Proc. Natl. Acad. Sci. U.S.A.* **103**, 18822 (2006).
26. S. Schuellmann *et al.*, *EMBO J.* **21**, 5036 (2002).
27. S. H. Kwak, R. Shen, J. Schiefelbein, *Science* **307**, 1111 (2005).
28. S. J. Halperin, S. Gilroy, J. P. Lynch, *J. Exp. Bot.* **54**, 1269 (2003).
29. M. A. Jones, M. J. Raymond, N. Smirnoff, *Plant J.* **45**, 83 (2006).
30. J. Foreman *et al.*, *Nature* **422**, 442 (2003).
31. S. A. Kim *et al.*, *Science* **314**, 1295 (2006).
32. S. A. Kim, M. L. Guerinot, *FEBS Lett.* **581**, 2273 (2007).
33. H. Y. Wang *et al.*, *Planta* **226**, 897 (2007).
34. M. Muller, W. Schmidt, *Plant Physiol.* **134**, 409 (2004).
35. B. J. Frey, D. Dueck, *Science* **315**, 972 (2007).
36. S. M. Brady *et al.*, *Science* **318**, 801 (2007).

37. We thank D. Orlando for writing the R-script used for running the affinity propagation clustering algorithm; A. Pillai, D. McClay, D. Sherwood, and members of the Benfey lab for reviewing this manuscript. J.R.D. is supported by a Ruth Kirschstein National Research Service Award postdoctoral fellowship. T.A.L. by an NSF Minority Postdoctoral Research Fellowship, and S.M.B. by a Natural Sciences and Engineering Research Council postdoctoral fellowship. Funding to J.S. is provided by an NSF Al2010 grant (no. 0723493). This work was largely funded by an NSF AT2010 grant (no. 0618304) to P.N.B. The authors have declared that no competing interests exist. The National Center for Biotechnology Information Gene Expression Omnibus accession numbers for new microarray data discussed in this manuscript are GSE8787, GSE7642, GSE7641, GSE7639, GSE7636, and GSE10576.

Supporting Online Material

www.sciencemag.org/cgi/content/full/320/5878/942/DC1
Materials and Methods
SOM Text
Figs. S1 to S13
Tables S1 to S18
References

5 December 2007; accepted 19 March 2008
10.1126/science.1153795

Early Forebrain Wiring: Genetic Dissection Using Conditional *Celsr3* Mutant Mice

Libing Zhou,[1] Isabelle Bar,[2]* Younès Achouri,[1] Kenneth Campbell,[3] Olivier De Backer,[2] Jean M. Hebert,[4] Kevin Jones,[5] Nicoletta Kessaris,[6] Catherine Lambert de Rouvroit,[2] Dennis O'Leary,[7] William D. Richardson,[6] Andre M. Goffinet,[1] Fadel Tissir[1]†

Development of axonal tracts requires interactions between growth cones and the environment. Tracts such as the anterior commissure and internal capsule are defective in mice with null mutation of *Celsr3*. We generated a conditional *Celsr3* allele, allowing regional inactivation. Inactivation in telencephalon, ventral forebrain, or cortex demonstrated essential roles for Celsr3 in neurons that project axons to the anterior commissure and subcerebral targets, as well as in cells that guide axons through the internal capsule. When Celsr3 was inactivated in cortex, subcerebral projections failed to grow, yet corticothalamic axons developed normally, indicating that besides guidepost cells, additional Celsr3-independent cues can assist their progression. These observations provide in vivo evidence that Celsr3-mediated interactions between axons and guidepost cells govern axonal tract formation in mammals.

Formation of axonal tracts is essential for brain wiring, and several cues, such as extracellular molecules, guidepost cells, and fiber-to-fiber interactions, guide growing axons to their targets (*1*). We showed previously that the anterior commissure (AC) and the internal capsule (IC) are defective in constitutive *Celsr3* mutant mice (*2*). *Celsr1*, *Celsr2*, *Celsr3* are homologous to *Drosophila flamingo/starry night* (*Fmi/stan*) (*3*, *4*), which collaborates with *Frizzled* and *Van Gogh* to regulate planar cell polarity (PCP) and neurite development. Celsr proteins are seven-pass transmembrane cadherins and are thought to mediate cell adhesion via homophilic interactions. Celsr3 is expressed in postmigratory neurons in cortex, ventral telencephalon, olfactory structures, and thalamus during development and progressively down-regulated during maturation (*5*).

To probe forebrain wiring, we generated a conditional mutant allele that allows inactivation of *Celsr3* by crosses with mice that express the Cre recombinase in region-specific manners (*6*). This allele was produced by flanking exons 19 to 27, deletion of which generates a null allele (*2*), with *loxP* sites ("floxed" allele, *Celsr3f*). Mice with regional inactivation were produced by crossing double heterozygous males (*Celsr3+/−;Cre/+*) with homozygous *Celsr3f/f* females. *Celsr3* inactivation requires Cre-mediated modification of one floxed allele only, thereby increasing efficiency. To facilitate reading, we use the shorthand "|": for example, *Celsr3|Foxg1* is short for *Celsr3f/−;Foxg1-Cre/+*. Cre-expressing strains were crossed with *ROSA26R* mice (*7*) to verify that Cre activation proceeded as described. Inactivation was further confirmed by in situ hybridization with a probe complementary to exons 19 to 27 that allows detection of intact *Celsr3* mRNA only and by Western blot (fig. S1). Control animals were double heterozygotes, e.g., *Celsr3f/+;Foxg1-Cre/+*.

We first examined the role of Celsr3 during formation of the AC. In *Celsr3|Foxg1* mice in which Celsr3 is inactivated in the telencephalon (*8*), the AC was absent (Fig. 1, A, B, D, and E). It was also drastically affected in *Celsr3|Emx1* mice that express Cre in olfactory structures and neocortex (*9*). Diminutive bundles originating from olfactory nuclei ran caudally and turned, but never crossed the midline, as confirmed by injecting 1,1′-dioctadecyl-3,3,3′,3′-tetramethylindocarbocyanine perchlorate (DiI) in the olfactory bulb (Fig. 1, C and F). This phenotype could reflect the kinetics of Cre activation: Axonal growth from olfactory nuclei may be initiated before a full inactivation of Celsr3 is achieved. In *Celsr3|Emx1* mice, *Celsr3* mRNA is absent from the olfactory and the temporal neurons of origin of the AC but present in the cells located along the pathway. Thus, normal Celsr3 activity is likely required cell-autonomously in the neurons of origin of the AC. In all other crosses, namely *Celsr3|Gsh2*, *Celsr3|Nkx2.1*, double *Celsr3|(Gsh2* and *Nkx2.1)*, and *Celsr|Dlx5/6*, that express Cre in large sectors of basal telencephalon but not in olfactory nuclei nor temporal cortex (*10*, *11*), the AC developed normally. This suggests that Celsr3 expression may not be required in cells along the AC pathway. Alternatively, functionally

[1]Developmental Neurobiology, Université Catholique de Louvain, 1200 Bruxelles, Belgique. [2]Facultés Universitaires Notre-Dame de la Paix, 5000 Namur, Belgique. [3]Division of Developmental Biology, Children's Hospital Research Foundation, Cincinnati, OH 45229, USA. [4]Albert Einstein College of Medicine, Bronx, NY 10461, USA. [5]University of Colorado, Boulder, CO 80309, USA. [6]University College London, London WC1E 6AE, UK. [7]Salk Institute, La Jolla, CA 92037, USA.

*Present address: Université Libre de Bruxelles, 1050 Bruxelles, Belgique.

†To whom correspondence should be addressed. E-mail: fadel.tissir@uclouvain.be

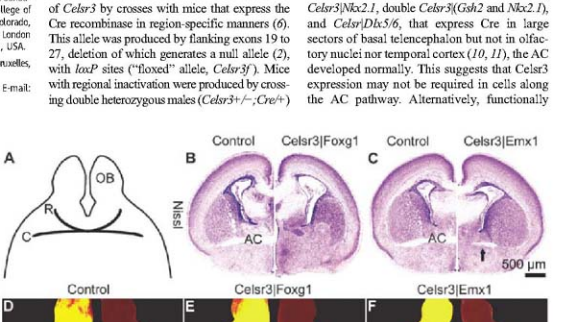

Fig. 1. Celsr3 expression is required intrinsically in neurons of origin of the AC. **(A)** Schematic representation of the AC, composed of a rostral component (R) that contains commissural axons connecting olfactory nuclei and a caudal component (C) made of axons that connect temporal lobes. OB indicates olfactory bulb. **(B** and **C)** Montages of coronal sections at the level of the AC in newborn animals. The control phenotype is shown on the left side, and the right side shows *Celsr3|Foxg1* (B) and *Celsr3|Emx1* (C) mice. Note the rudiment of AC in *Celsr3|Emx1* mice (arrow in C). **(D** to **F)** Horizontal sections at birth day (P0) after DiI injection in control (D), *Celsr3|Foxg1* (E), and *Celsr3|Emx1* mice (F). Arrows in (C) and (F) point to rudiments of AC that never cross the midline.

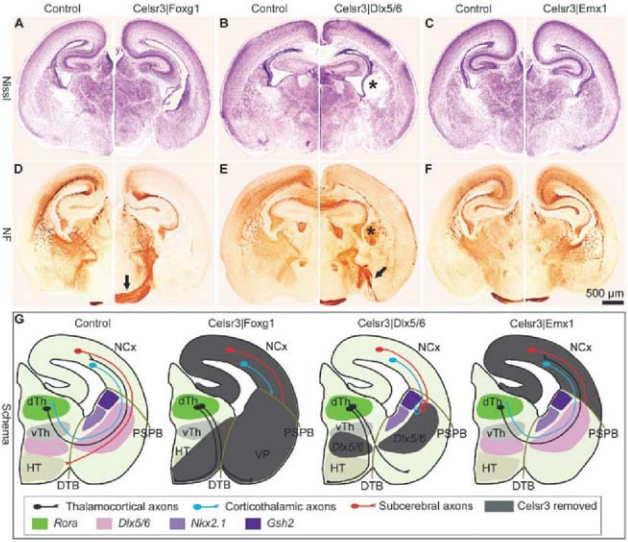

Fig. 2. Region-specific Celsr3 inactivation affects development of the IC in different manners. (**A** to **F**) Montages of P0 sections stained with Cresyl violet [(A) to (C)] or neurofilament antibody (NF) [(D) to (F)]. The IC is fully defective in *Celsr3|Foxg1* mice in which some thalamic axons cross to the contralateral diencephalon [arrow in (D)]. In *Celsr3|Dlx5/6* mice, the IC does not form, but cortical axons stall and form a mass at the level of the striatum [asterisks in (B) and (E)], whereas thalamic fibers are misrouted to the amygdala [arrow in (E)]. In *Celsr3|Emx1* mice, the IC is present and thalamocortical connections are similar to that in normal mice [(C) and (F)]. (**G**) Schematic summary of the IC phenotypes in the various mice used, in relation to areas of Celsr3 inactivation (gray) and expression of markers (*Dlx5/6*, *Gsh2*, *Nkx2.1*, and *Rora*). dTh and vTh, dorsal and ventral thalamus; HT, hypothalamus; VP, ventral pallidum; NCx, neocortex; PSPB, pallial subpallial boundary; and DTB, diencephalon telencephalon border.

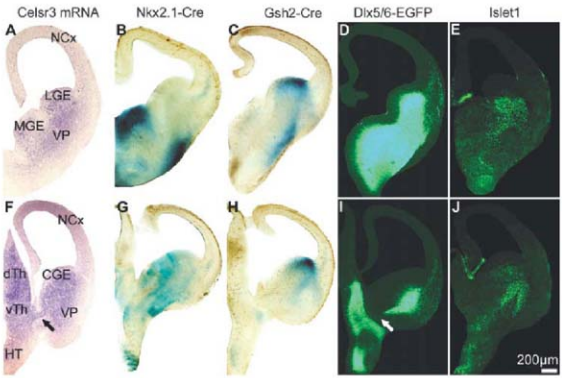

Fig. 3. The IC corridor expresses *Celsr3*, *Dlx5/6*, and *Islet1* and is flanked with expression of *Nkx2.1* and *Gsh2*. Coronal sections at rostral (**A** to **E**) and caudal levels (**F** to **J**) of the forebrain at E12.5, showing expression of *Celsr3* [(A) and (F), in situ hybridization], activation of the LacZ reporter in *ROSA26R*\|*Nkx2.1* mice [(B) and (G)] and *ROSA26R*\|*Gsh2* mice [(C) and (H)], expression of Dlx5/6 [(D) and (I), EGFP in the transgene], and expression of Islet1 [(E) and (J), immunohistochemistry]. A central corridor is characterized by high levels of Celsr3, Dlx5/6, and Islet1, and low levels of LacZ. Arrows in (F) and (I) indicate a *Celsr3*-positive, *Dlx5/6*-negative zone that could explain partial growth of TCA in *Celsr3|Dlx5/6* mice. CGE, LGE, and MGE, caudal, lateral, and medial ganglionic eminences.

relevant cells in intermediate regions may have escaped Celsr3 inactivation, because *Gsh2-*, *Nkx2.1-*, and *Dlx5/6-Cre* mice do not express Cre strongly in the medial region where AC axons cross the midline. We favor the latter interpretation because it fits with the observations on the IC described below.

We next investigated the function of Celsr3 during development of the three components of the IC, namely corticothalamic axons (CTA), thalamocortical axons (TCA), and subcerebral projections [terminology of Molyneaux *et al.* (*12*)]. In *Celsr3*|*Foxg1* mice, despite normal Celsr3 expression in dorsal thalamus, all three components were defective (Fig. 2, A and D). No thalamic fibers turned toward the striatum, and no thalamic neurons were labeled after DiI injection in cortex. Reciprocally, injection of DiI in thalamus did not label cortical neurons but stained thalamic axons that ran into the basal forebrain or crossed the midline ventrally, like in constitutive *Celsr3* and *Fzd3* mutants (*2*, *13*) (fig. S2). With use of focal DiI injections in the basal forebrain at embryonic day 13.5 (E13.5), we found that early thalamic fibers reached the medial ganglionic eminence in normal but not in *Celsr3*$^{-/-}$ mice. In contrast, in both genotypes, corticofugal fibers crossed the pallial subpallial boundary and reached the lateral ganglionic eminence at E13.5 (fig. S3). Thus, Celsr3 is required for the early growth of TCA, but not CTA, toward ventral telencephalon.

The three components of the IC were also defective in *Celsr3*|*Dlx5/6* mice that express Cre in the ventral forebrain (*11*) (Fig. 2, B and E). A subset of TCA managed an incomplete turning at the diencephalon-telencephalon border but then ran aberrantly through the pallidum and amygdala. Corticofugal fibers crossed the pallial-subpallial boundary and entered the lateral part of the basal forebrain. However, they failed to progress and spiraled in a disorderly manner, forming an abnormal mass that filled most of the dorsal striatum and protruded in the lateral ventricle (Fig. 2E). After DiI injections in cortex and thalamus, no labeling of thalamic or cortical cells was observed, confirming that both TCA and CTA were defective (fig. S2). Similarly, no subcerebral projections formed, as shown by absence of corticospinal tract (CST) (fig. S4). Thus, Celsr3 expression by *Dlx5/6*-positive cells is required for progression of TCA, CTA, and subcerebral projections through the ventral telencephalon. Partial progression of CTA through the pallial subpial boundary in *Celsr3*|*Dlx5/6* but not in *Celsr3*|*Foxg1* mice may reflect Celsr3-mediated fiber-to-fiber interactions among CTA, in which Celsr3 is expressed, or interactions between CTA and *Celsr3*-positive, *Dlx5/6*-negative cells. Similarly, the partial turning of TCA in *Celsr3*|*Dlx5/6* mice may reflect interactions with *Celsr3*-positive, *Dlx5/6*-negative cells.

To define which subset of *Dlx5/6*-positive cells could qualify as guidepost cells, we used *Gsh2-Cre* and *Nkx2.1-Cre* mice that express Cre in the lateral and medial ganglionic eminences, respectively. In *Celsr3*|*Gsh2*, *Celsr3*|*Nkx2.1*, and double *Celsr3*|*Gsh2-Nkx2.1* mice, all components of the IC developed normally (fig. S5). This showed that a sufficient number of *Celsr3*-expressing guidepost cells along the IC originate from *Nkx2.1*- and *Gsh2*-negative precursors. We compared the distribution of Celsr3 (in situ hybridization), Nkx2.1 and Gsh2 (LacZ histochemistry and immunohistochemistry), Dlx5/6 [enhanced green fluorescent protein (EGFP) reporter], and Islet1 (immunohistochemistry) at E12.5, before any fiber growth in the ventral telencephalon, and at E14.5, when the IC begins to form. At E12.5 (Fig. 3), Celsr3 expression was very similar to that of Dlx5/6, with maximal signal along the ganglionic eminences where Islet1 was also present (compare Fig. 3, D and E, to A). Expression of *LacZ* in *ROSA26R*|*Nkx2.1* and *ROSA26R*|*Gsh2* mice was strong in large sectors of the ganglionic eminences and in the striatal mantle but low in the intermediate region where expression of *Celsr3* and *Dlx5/6* was maximal. At E14.5 (fig. S6), zones of *Gsh2* and *Nkx2.1* expression flanked axonal bundles of the incipient IC, whereas Islet1-expressing cells were in close contact with axonal tracts, in the region of highest Dlx5/6 signal and minimal Gsh2 and Nkx2.1 signal. These observations suggest that Celsr3 is required in basal forebrain guidepost cells that are positive for Dlx5/6 and possibly Islet1 and that are derived from *Nkx2.1-Cre*– and *Gsh2-Cre*–negative precursors.

To test whether Celsr3 is required intrinsically for progression of corticofugal axons, we studied *Celsr3*|*Emx1* mice, in which Celsr3 is inactivated early in the cortical anlage (*9*) (fig. S1). In those mice, subcerebral projections such as CST were defective. In crosses with Thy1–yellow fluorescent protein (YFP) transgenic mice (*14*), the CST was clearly defined in control mice but absent in *Celsr3*|*Emx1* mice in which the number of cortical layer 5 neurons was dramatically reduced (Fig. 4). After injections of Fluoro-Gold (Biotum, Incorporated, Haywood, CA) in the spinal cord, cells were labeled in the hindbrain, red nucleus, and layer 5 in normal mice but only in the hindbrain and red nucleus, and not in layer 5, in *Celsr3*|*Emx1* mice (fig. S7). Thus, Celsr3 is required, presumably cell autonomously, in the neurons of origin of subcerebral axons, like in those of the AC.

In contrast to subcerebral projections, CTA and TCA developed normally in *Celsr3*|*Emx1* mice (Fig. 2). At E14.5, fibers from dorsal thalamus turned at the diencephalon-telencephalon border and progressed along the ganglionic eminences before passing the pallial subpallial boundary and growing toward the cortex, similar to fibers of control mice. Injections of DiI in the cortex and thalamus resulted in labeling of thalamic and cortical neurons, respectively (fig. S2). To assess the cortical distribution of TCA, we studied cortical barrels by using cytochrome oxidase and Nissl staining of parietal cortex. As shown in fig. S8, barrels failed to form in mice that had no TCA, such as *Celsr3*|*Foxg1* and *Celsr3*|*Dlx5/6* mice, and developed normally in *Celsr3*|*Emx1* mice, indicating normal TCA mapping. Thus, inactivation of Celsr3 in CTA did not prevent them from navigating to the thalamus,

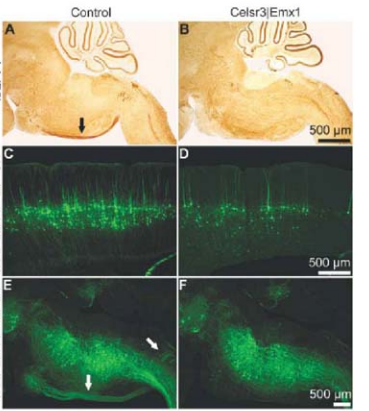

Fig. 4. The corticospinal tract is defective in *Celsr3*|*Emx1* mice. Comparison of control [**(A)**, **(C)**, and **(E)**] and *Celsr3*|*Emx1* [**(B)**, **(D)**, and **(F)**] mice. In sagittal sections at P6 stained with an antibody against the L1 molecule (**A**) and (**B**), corticospinal axons are labeled in control [arrow in (**A**)] but not in the mutant ventral hindbrain. Crosses were carried out with Thy1-YFP mice, a transgene that labels neurons in cortical layer 5 and corticospinal axons (**C**) to (**F**). At P20, layer 5 is well populated in control mice (**C**), and the corticospinal tract is clearly defined [arrows in (**E**)], whereas cortical layer 5 is very diminutive (**D**) and no corticospinal axons are detected in the hindbrain (**F**) of *Celsr3*|*Emx1* mice.

nor did it perturb the growth and cortical mapping of TCA.

Why would Celsr3 be required in AC and subcerebral axons but not in CTA? First, a few subplate cells could escape Celsr3 inactivation in *Celsr3|Emx1* mice and provide pioneering axons to thalamus (*15*, *16*). However, Celsr3 is inactivated early in the cortex in those mice (fig. S1), making this rather unlikely. Second, other Celsr proteins may act redundantly with Celsr3 in CTA neurons and mediate their interactions with *Celsr3*-positive guidepost cells. Alternatively, normal *Celsr3* expression in dorsal thalamus and basal forebrain in *Celsr3|Emx1* mice allows progression of TCA, which could encounter *Celsr3*-deficient CTA and help them travel to the thalamus, as predicted by the "handshake hypothesis" (*17*). *Celsr3|Rora* mice were produced to inactivate Celsr3 in dorsal thalamic nuclei and thereby assess their role in TCA growth. The IC developed normally in those mice, indicating a situation reciprocal to that in *Celsr3|Emx1* mice. However, studies of *ROSA26R|Rora* mice showed that *Cre* expression was restricted to a subset of dorsal thalamic cells. Thus being unable to test the function of Celsr3 in thalamic neurons in vivo, we addressed the question using explant cultures. We co-cultured explants from normal or Celsr3-mutant thalamus that expressed the GFP transgene ubiquitously (*18*) with explants of normal ventral diencephalons at E13.5. As shown in fig. S9, normal dorsal thalamic axons were repelled by explants from ventral diencephalon (32/57 cases) (*19*). However, almost no repulsive activity was detected for *Celsr3*-defective thalamic axons (4/34 cases; $P < 0.01$, χ^2), suggesting that *Celsr3* expression in TCA was required for their response to ventral diencephalic cues. Thus, *Celsr3* expression is probably necessary both in TCA and in cells along their pathway (*Celsr3|Dlx5/6* mice).

Our results have implications for the mechanisms of brain wiring and the function of Celsr3. Demonstrated in invertebrates (*20*), a role of guidepost cells in axonal navigation in mammals has been repeatedly proposed (*21*–*24*). Our results demonstrate that they indeed play a crucial function that requires Celsr3 expression (the role of other molecules implicated in thalamocortical and CST fiber nagivation is discussed briefly in SOM). Altogether, our data indicate that Celsr3 is required both in axons and guidepost cells, consistent with its mediating homophilic interactions. Normal CTA development in *Celsr3|Emx1* mice indicates that Celsr3-independent cues are also involved in their growth. Candidate mechanisms are CTA-TCA fiber interactions like the handshake (*17*, *21*), fiber-fiber interactions between CTA and pioneer subplate axons (*15*, *16*), and adhesion of Celsr3 in guidepost cells with other Celsr molecules present in growth cones. Furthermore, *Celsr3|Emx1* mice provide a unique model to study how subcerebral projections segregate from CTA when they reach the medial aspect of the IC en route to the cerebral peduncles, an important developmental event that hitherto received little attention.

In *Drosophila* wing cells, symmetrically expressed Fmi/stan proteins are thought to undergo homophilic interactions, bringing distal and proximal cell membranes in contact and thereby fostering signaling by asymmetrically located Frizzled on the distal and Van Gogh on the proximal side (*25*). Axonal anomalies in *Celsr3* and *Fzd3* mutant mice are similar (*13*), suggesting that corresponding proteins also act together in mice (*25*). Moreover, *Fzd3* and *Vangl2* are co-expressed with *Celsr3* in postmigratory neurons (*26*). Like in the fly, Celsr3 expressed on the membranes of growth cones and guidepost cells may promote adhesion and allow Fzd3 and Vangl2 to interact and signal. This model predicts that the expression and action of Fzd3 and Vangl2 should be asymmetric, one in axons and the other in guidepost cells. Conditional Fzd3 and Vangl2 alleles should allow testing that model further.

References and Notes

1. M. Tessier-Lavigne, *Harvey Lect.* **98**, 103 (2002).
2. F. Tissir, I. Bar, Y. Jossin, A. M. Goffinet, *Nat. Neurosci.* **8**, 451 (2005).
3. T. Usui *et al.*, *Cell* **98**, 585 (1999).
4. J. Chae *et al.*, *Development* **126**, 5421 (1999).
5. F. Tissir, O. De-Backer, A. M. Goffinet, C. Lambert de Rouvroit, *Mech. Dev.* **112**, 157 (2002).
6. Materials and methods are available on *Science* Online.
7. P. Soriano, *Nat. Genet.* **21**, 70 (1999).
8. J. M. Hebert, S. K. McConnell, *Dev. Biol.* **222**, 296 (2000).
9. J. A. Gorski *et al.*, *J. Neurosci.* **22**, 6309 (2002).
10. N. Kessaris *et al.*, *Nat. Neurosci.* **9**, 173 (2006).
11. J. Stenman, H. Toresson, K. Campbell, *J. Neurosci.* **23**, 167 (2003).
12. B. J. Molyneaux, P. Arlotta, J. R. Menezes, J. D. Macklis, *Nat. Rev. Neurosci.* **8**, 427 (2007).
13. Y. Wang, N. Thekdi, P. M. Smallwood, J. P. Macke, J. Nathans, *J. Neurosci.* **22**, 8563 (2002).
14. G. Feng *et al.*, *Neuron* **28**, 41 (2000).
15. A. Ghosh, A. Antonini, S. K. McConnell, C. J. Shatz, *Nature* **347**, 179 (1990).
16. S. K. McConnell, A. Ghosh, C. J. Shatz, *Science* **245**, 978 (1989).
17. Z. Molnar, C. Blakemore, *Nature* **351**, 475 (1991).
18. M. Okabe, M. Ikawa, K. Kominami, T. Nakanishi, Y. Nishimune, *FEBS Lett.* **407**, 313 (1997).
19. J. E. Braisted, R. Tuttle, D. O'Leary, *Dev. Biol.* **208**, 430 (1999).
20. D. Bentley, M. Caudy, *Nature* **304**, 62 (1983).
21. R. F. Hevner, E. Miyashita-Lin, J. L. Rubenstein, *J. Comp. Neurol.* **447**, 8 (2002).
22. J. Mitrofanis, R. W. Guillery, *Trends Neurosci.* **16**, 240 (1993).
23. G. Lopez-Bendito *et al.*, *Cell* **125**, 127 (2006).
24. R. Tuttle, Y. Nakagawa, J. E. Johnson, D. D. O'Leary, *Development* **126**, 1903 (1999).
25. D. Strutt, H. Strutt, *Dev. Biol.* **302**, 181 (2007).
26. F. Tissir, A. M. Goffinet, *Eur. J. Neurosci.* **23**, 597 (2006).

27. We thank V. Bonte, I. Lambermont, and E. Paitre for technical assistance; G. Hamard for help with embryonic stem cell injections; M. Okabe for GFP mice; F. G. Rathjen for antibodies against L1; P. Soriano for *ROSA26R* mice; and L. Nguyen, A. Stoykova, and P. Vanderhaeghen for help or discussion. This work was supported by grants Actions de recherches concertées (ARC-3861, FRFC 2.4504.01, FRSM 3.4501.07, and FRSM 3.4529.03; by Interuniversity Poles of Attraction (ISTC, PAI p6/20); and by the Fondation Médicale Reine Elisabeth, all from Belgium. F.T. is a Research Associate of the Fonds National de la Recherche Scientifique.

Supporting Online Material

www.sciencemag.org/cgi/content/full/320/5878/946/DC1
Materials and Methods
SOM Text
Figs. S1 to S9
Table S1
References

15 January 2008; accepted 18 April 2008
10.1126/science.1155244

cAMP-Dependent Signaling as a Core Component of the Mammalian Circadian Pacemaker

John S. O'Neill,[1]* Elizabeth S. Maywood,[1] Johanna E. Chesham,[1] Joseph S. Takahashi,[2] Michael H. Hastings[1]†

The mammalian circadian clockwork is modeled as transcriptional and posttranslational feedback loops, whereby circadian genes are periodically suppressed by their protein products. We show that adenosine 3′,5′-monophosphate (cAMP) signaling constitutes an additional, bona fide component of the oscillatory network. cAMP signaling is rhythmic and sustains the transcriptional loop of the suprachiasmatic nucleus, determining canonical pacemaker properties of amplitude, phase, and period. This role is general and is evident in peripheral mammalian tissues and cell lines, which reveals an unanticipated point of circadian regulation in mammals qualitatively different from the existing transcriptional feedback model. We propose that daily activation of cAMP signaling, driven by the transcriptional oscillator, in turn sustains progression of transcriptional rhythms. In this way, clock output constitutes an input to subsequent cycles.

The suprachiasmatic nuclei (SCN) of the hypothalamus are the principal circadian pacemaker in mammals, driving the sleep-wake cycle and coordinating subordinate clocks in other tissues (*1*). Disturbed circadian timing can have a major negative impact on human health (*2*). The molecular clockwork within the SCN has been modeled as a combination of

transcriptional and posttranslational negative-feedback loops (*3*), whereby protein products of *Period* and *Cryptochrome* genes periodically suppress their own expression (*4*). It is unclear how long-term, high-amplitude oscillations with a daily period are maintained, not least because transcriptional feedback loops are typically less precise than the oscillation of the circadian clock and oscillate at a higher frequency than one cycle per day (*5*). Moreover, recombinant cyanobacterial proteins can sustain circadian cycles of autophosphorylation in vitro, in the absence of transcription (*6*), and intracellular signaling molecules cyclic adenosine diphosphate–ribose (cADPR) and Ca^{2+} are essential regulators of circadian oscillation in *Arabidopsis* and *Drosophila* (*7*, *8*). This indicates that transcriptional mechanisms may not be the sole, or principal, arbiter of circadian pacemaking (*9*, *10*). We show that the transcriptional feedback loops of the SCN are sustained by cytoplasmic adenosine 3′,5′-monophosphate (cAMP) signaling, which determines their canonical properties of amplitude, phase, and period. This extends the concept of the mammalian pacemaker beyond transcriptional feedback to incorporate its integration with rhythmic cAMP-mediated cytoplasmic signaling.

We tracked the molecular oscillations of the SCN as circadian emission of bioluminescence by organotypical slices from transgenic mouse brain. Rhythmic luciferase activity controlled by the *Per1* promoter (*Per1::luciferase*) revealed circadian transcription, and a fusion protein of mPER2 and LUCIFERASE (mPER2::LUC) reported circadian protein synthesis rhythms. Under these conditions, the cAMP content of the SCN was circadian (Fig. 1A) and accompanied by a circadian cycle in activity of cAMP response element (CRE) sequences reported by a *CRE::luciferase* adenovirus (Fig. 1B). In molluscs, birds, and the mammalian SCN, cAMP is implicated in entrainment or maintenance of clocks, or both, or mediation of clock output (*11*–*13*). It has not been considered as part of the core oscillator (*14*). If the cAMP-mediated rhythm of CRE activity is necessary for SCN pacemaking, its suppression should compromise circadian gene expression. We treated SCN slices with MDL-12,330A (MDL), a potent, irreversible inhibitor of adenylyl cyclase (AC) (*15*) to reduce concentrations of cAMP to basal levels (Fig. 1A). MDL rapidly suppressed circadian *CRE::luciferase* activity, presumably through loss of cAMP-dependent activation of CRE sequences (fig. S1A), and caused a dose-dependent decrease in the amplitude of cycles of circadian transcription and protein synthesis observed with *mPer1::luciferase* and mPER2::LUC (Fig. 1C and fig. S1, B and C). Damping was reversible over several days and not an artifact of the bioluminescent reporters, because MDL also suppressed *mPer1*-dependent circadian transcription reported by green fluorescent protein (fig. S1D). Video imaging of mPER2::LUC expression showed that MDL (2.5 μM) rapidly suppressed cellular circadian gene expression to barely detectable levels (Fig. 1D). Prolonged exposure to MDL (1.0 μM) suppressed and desynchronized the transcriptional cycles of SCN cells (Fig. 1E). Pharmacological inactivation of AC therefore mimicked the effect of pertussis toxin (*16*) and loss of the gene encoding the vasoactive intestinal peptide receptor 2 (*Vip2r*), an activator of AC within the SCN (*17*). MDL also reduced cAMP to undetectable levels in NIH 3T3 fibroblast cultures (fig. S2, A and B) and suppressed circadian transcriptional cycling revealed by a *Bmal1::luc* reporter (*3*) (fig. S2, C to E). MDL had no effect, however, on luciferase expression from NIH 3T3 cells transfected with a control, noncircadian (CMV, cytomegalovirus) promoter (fig. S2F).

If cAMP sustains the clock, interference with cAMP effectors should compromise pacemaking. Treatment of brain slices with inhibitors of cAMP-dependent protein kinase had no effect, however, on circadian gene expression in the SCN (fig. S3). cAMP also acts through hyperpolarizing cyclic nucleotide–gated ion (HCN) channels (*18*) and through the guanine nucleotide–exchange factors Epac1 and Epac2 (Epac, exchange protein directly activated by cAMP) (*19*).

[1]Medical Research Council (MRC) Laboratory of Molecular Biology, Hills Road, Cambridge CB2 0QH, UK. [2]Howard Hughes Medical Institute, Department of Neurobiology and Physiology, Northwestern University, 2205 Tech Drive, Evanston, IL 60208–3520, USA.

*Present address: Center for Systems Biology at Edinburgh, University of Edinburgh, Edinburgh EH9 3JU, UK.

†To whom correspondence should be addressed. E-mail: mha@mrc-lmb.cam.ac.uk

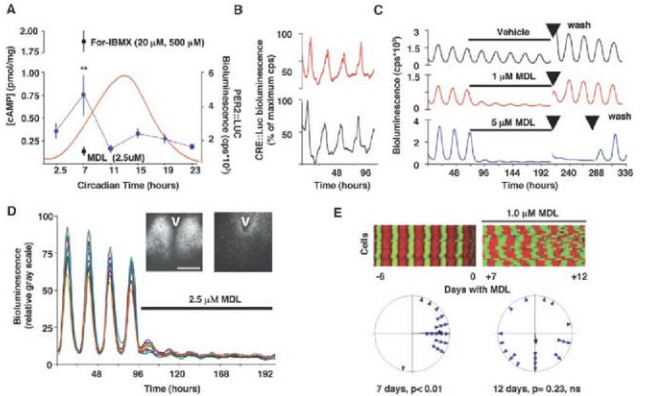

Fig. 1. Damped and desynchronized cellular circadian gene expression in SCN after suppression of cAMP and CRE rhythms. **(A)** Circadian oscillation of cAMP concentration (blue) and PER2::LUC bioluminescence (red), as well as cAMP concentration in SCN slices treated with MDL-12,330A (MDL) or with forskolin plus IBMX. [**$P < 0.01$ versus other samples, by analysis of variance (ANOVA) and post hoc Duncan's multiple-range test.] **(B)** Circadian oscillation of CRE activity in two representative SCN slices reported by *CRE::luciferase* adenovirus. **(C)** Reversible, dose-dependent suppression of SCN PER2::LUC expression by MDL. Arrows indicate medium changes. **(D)** Effect of MDL on PER2::LUC expression in individual SCN neurons ($n = 20$), bioluminescence expressed as relative gray-scale units (0 to 255 pixel intensity). Videomicrographs illustrate distribution of PER2::LUC expression before (left) and during (right) treatment with MDL. V, third ventricle. Scale bar, 500 μm. **(E)** Desynchronization of cellular pacemakers of SCN revealed by (top) raster plots and (bottom) Rayleigh plots of PER2::LUC oscillations of 20 representative SCN neurons before and after addition of MDL. Data are representative of three or more slices.

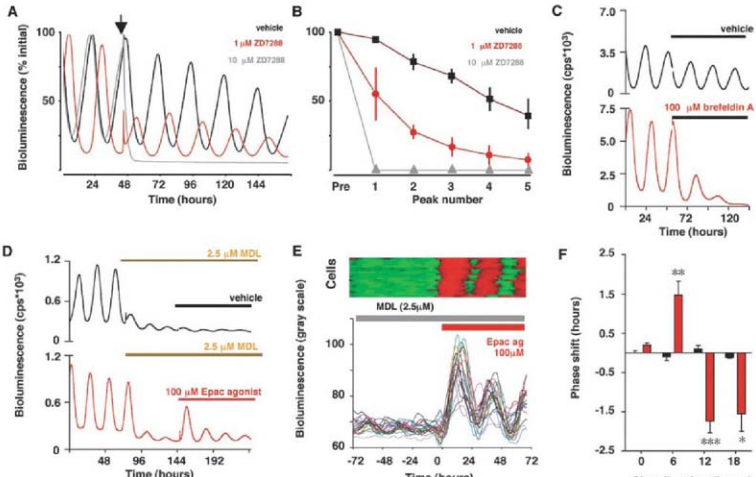

Fig. 2. Influence of effectors of cAMP signaling on SCN circadian pacemaking. **(A)** Effect of HCN channel blocker ZD7288 (arrow) on SCN mPER2::LUC circadian gene expression. **(B)** Damping of peak bioluminescence in SCN slices treated with vehicle or ZD7288 (Pre, pretreatment; means ± SEM, $n \geq 4$). **(C)** Brefeldin A suppresses circadian gene expression in PER2::LUC SCN. **(D)** Transient reactivation of MDL-suppressed circadian PER2::LUC expression in SCN slices by Sp-8-CPT-2′-*O*-Me-cAMPS. **(E)** Acute activation of cellular circadian gene expression (expressed as relative gray-scale units) by Epac agonist in presence of MDL, illustrated by raster (top) and graphical plots (bottom) of 20 representative cells. **(F)** Phase shifts of SCN circadian PER2::LUC bioluminescence rhythm by Epac agonist (Sp-8-CPT-2′-*O*-Me-cAMP, red) but not vehicle (black) (means ± SEM, $n \geq 3$ per time point; $^{**}P < 0.01$ versus vehicle, by ANOVA and Bonferroni test).

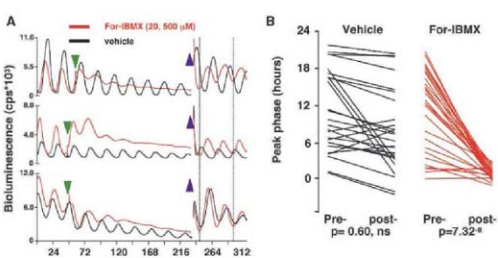

Fig. 3. Alterations in the phase of the SCN oscillator after acute transitions in cAMP concentrations. **(A)** PER2::LUC bioluminescence rhythms from SCN treated with vehicle or forskolin and IBMX (green arrowhead), followed by washout (blue arrowheads). Dotted lines highlight synchrony of For-IBMX–treated slices, but not control slices, after washout. **(B)** Phases of PER2::LUC rhythms in individual SCN immediately before (pre-) and 4 days after (post-) washout of vehicle or For-IBMX. Removal of For-IBMX caused resynchronization, driving slices to a common phase, regardless of phase before washout.

The irreversible HCN channel blocker ZD7288, which would be expected to hyperpolarize the neuronal membrane, dose-dependently damped circadian gene expression in the SCN (Fig. 2, A and B). This is consistent with disruption of transcriptional feedback rhythms by other manipulations that hyperpolarize clock neurons (*17*, *20*, *21*). Brefeldin A, applied at a dose that antagonizes Epac but does not affect synaptic transmission (*22*), also rapidly and chronically suppressed SCN pacemaking (Fig. 2C and fig. S4A). Thus, circadian pacemaking is sustained by cAMP effectors, as well as by AC activity. Direct activation of the effectors might compensate, therefore, for inactivation of AC by MDL. A hydrolysis-resistant Epac agonist [8-(4-chlorophenylthio)-2′-*O*-methyladenosine-3′,5′-cyclic monophosphorothioate, Sp-isomer, Sp-8-CPT-2′-*O*-Me-cAMPS] (Fig. 2D and fig. S4B) transiently activated oscillations in transcriptional activity in SCN treated with MDL. An agonist active on both Epac and cAMP-dependent protein kinase (PKA), namely, Sp-8-CPT-cAMPS, also transiently activated circadian gene expression, whereas an

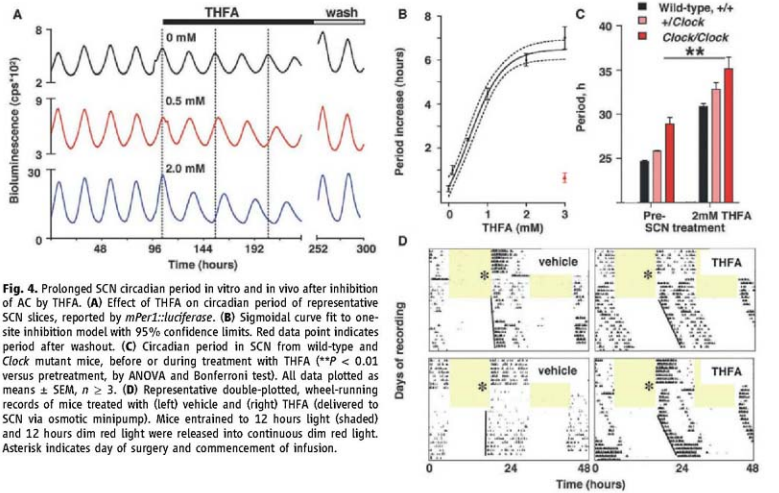

Fig. 4. Prolonged SCN circadian period in vitro and in vivo after inhibition of AC by THFA. **(A)** Effect of THFA on circadian period of representative SCN slices, reported by *mPer1::luciferase*. **(B)** Sigmoidal curve fit to one-site inhibition model with 95% confidence limits. Red data point indicates period after washout. **(C)** Circadian period in SCN from wild-type and *Clock* mutant mice, before or during treatment with THFA (**$P < 0.01$ versus pretreatment, by ANOVA and Bonferroni test). All data plotted as means ± SEM, $n \geq 3$. **(D)** Representative double-plotted, wheel-running records of mice treated with (left) vehicle and (right) THFA (delivered to SCN via osmotic minipump). Mice entrained to 12 hours light (shaded) and 12 hours dim red light were released into continuous dim red light. Asterisk indicates day of surgery and commencement of infusion.

agonist specific for PKA (6-Bnz-cAMP) had no effect (fig. S4B). Video imaging showed that Epac agonist synchronously activated circadian gene expression in individual SCN cells (Fig. 2E). The transcriptional cycles induced by Epac agonism damped rapidly in the presence of MDL, however, which demonstrated that, when cAMP concentrations were permanently suppressed, the reactivated transcriptional feedback loops were not self-sustaining.

Epac can lead to activation of the transcription factor CRE-binding protein (CREB) by phosphorylation (*23*), and so CRE sequences in *Per1* and *Per2* are likely points of integration between Epac and the core loop. An Epac agonist acutely triggered CREB phosphorylation (fig. S4C) and *CRE::luciferase* activity (increase ± SEM: vehicle, 1.9% ± 0.7%; Epac agonist, 38.4% ± 13.0%; $n = 4$) in SCN slices treated with MDL. If Epac activity were rate-limiting during the normal circadian cycle, acute activation should reset the oscillator, and indeed, a short-acting, hydrolyzable Epac agonist (Sp-8-CPT-2′-*O*-Me-cAMP) phase-shifted SCN slices (Fig. 2F). As with cAMP agonists (*13*), treatment of slices with Epac agonist during the circadian day advanced the SCN. The dependence of circadian gene expression on cAMP mediators Epac1 and Epac2 and HCN confirms the necessary contribution of cAMP signaling in sustaining the SCN pacemaker.

If circadian cAMP signaling is an intrinsic part of the pacemaker, feeding back into the transcriptional loops rather than being solely an output, it should determine their temporally specific parameters of phase and period. To test this, we decoupled cAMP concentrations from the transcriptional oscillator by treating SCN slices with forskolin (For), the activator of AC, and the cAMP phosphodiestease inhibitor 3-isobutyl-1-methylxanthine (IBMX). This chronically elevated cAMP levels (Fig. 1A) and acutely increased mPER2::LUC activity (Fig. 3A). Previously asynchronous SCN slices were resynchronized, an effect inconsistent with cAMP signaling acting solely as an output (fig. S5A). Continued exposure of slices to For-IBMX elevated the circadian nadir of mPER2::LUC expression, damping amplitude and definition of the circadian profile of the slice and of individual cells across the SCN (Fig. 3A and fig. S5, B and C). With sustained elevation of cAMP concentrations, the imposed synchrony between free-running slices dissipated (fig. S5D).

After 5 to 7 days of treatment with For-IBMX, we acutely reduced cAMP concentrations by transferring slices to fresh medium. This was done as a "wedge" experiment (*24*, *25*), such that the reduction of cAMP concentrations was imposed at different phases of the ongoing oscillations of different slices. If cAMP signals constitute part of the pacemaker and not solely its output, the enforced decline in cAMP concentrations would set the transcriptional oscillator to a new unique phase. Consequently, the gene expression rhythms of all slices would be synchronized, regardless of their phase before washout. Washout did not synchronize vehicle-treated SCN (Fig. 3B and fig. S5D). In contrast, washout resynchronized SCN previously treated with For-IBMX to a common phase distinct from that of control slices. Note that the extrapolated phase of peak PER2::LUC activity occurred about 39 ± 11 min after the time of washout, which is consistent with the delay of about 1 hour between the circadian minimum of cAMP content and peak PER2::LUC activity in SCN slices (Fig. 1A). Hence, the behavior of the transcriptional loop was determined by acute changes in cAMP signaling, decoupled pharmacologically from that loop. As with protein synthesis (*25*), these results identify cAMP as a component of the SCN oscillator.

Finally, if cAMP signaling is an integral component of the SCN pacemaker, altering the rate of cAMP synthesis should affect circadian period. 9-(Tetrahydro-2-furyl)-adenine (THFA) is a noncompetitive AC inhibitor (*15*) that slows the rate of G_s-stimulated cAMP synthesis, which attenuates peak concentrations (fig. S2, A and B). THFA dose-dependently increased the period of circadian pacemaking in the SCN, from 24 to 31 hours (Fig. 4, A and B), with rapid reversal

upon washout. Rhythm amplitude decreased at higher concentrations of THFA (fig. S6A). Imaging of individual cells revealed that THFA increased period in neurons across the SCN (fig. S6B). Other noncompetitive inhibitors also lengthened SCN period (fig. S6C). The effect of THFA was additive to that of the *Clock* mutation (Fig. 4C), which suggests THFA acts in addition to, and independently of, E-box–mediated transactivation by CLOCK and BMAL1. Further, THFA acted additively with inhibition of c-Jun N-terminal kinase (JNK), by generating unusually long periods of 36 hours (fig. S6, D and E). THFA also lengthened the period of circadian oscillators in peripheral tissues from mPER2::LUC mice and fibroblasts transfected with *Bmal1::luc* reporter (fig. S7, A to D). Note that THFA lengthened the circadian period of wheel-running when delivered continuously and directly to the SCN of mice via intracerebral cannulae (Fig. 4D and fig. S7E). The differential circadian effects of AC inhibitors, damping versus period-lengthening by MDL and THFA, respectively, reflect their particular actions on cAMP kinetics. The current results therefore suggest that noncompetitive inhibitors, such as THFA, might be of therapeutic value in patients with acute (jet lag, shift work) or maintained [familial advanced sleep phase syndrome (*26*)] acceleration of circadian period.

We conclude that circadian pacemaking in mammals is sustained, and its canonical properties of amplitude, phase, and period are determined by a reciprocal interplay in which transcriptional and posttranslational feedback loops drive rhythms of cAMP signaling and that dynamic changes in cAMP signaling, in turn, regulate transcriptional cycles. Thus, output from the current cycle constitutes an input into subsequent cycles. The interdependence between nuclear and cytoplasmic oscillator elements we describe for cAMP also occurs in the case of Ca^{2+} and cADPR (*7*, *8*), which highlights an important newly recognized common logic to circadian pacemaking in widely divergent taxa.

References and Notes

1. S. M. Reppert, D. R. Weaver, *Nature* **418**, 935 (2002).
2. M. H. Hastings, A. B. Reddy, E. S. Maywood, *Nat. Rev. Neurosci.* **4**, 649 (2003).
3. H. R. Ueda *et al.*, *Nat. Genet.* **37**, 187 (2005).
4. T. K. Sato *et al.*, *Nat. Genet.* **38**, 312 (2006).
5. H. Hirata *et al.*, *Science* **298**, 840 (2002).
6. M. Nakajima *et al.*, *Science* **308**, 414 (2005).
7. A. N. Dodd *et al.*, *Science* **318**, 1789 (2007).
8. M. C. Harrisingh, Y. Wu, G. A. Lnenicka, M. N. Nitabach, *J. Neurosci.* **27**, 12489 (2007).
9. P. L. Lakin-Thomas, *J. Biol. Rhythms* **21**, 83 (2006).
10. Y. Fan, A. Hida, D. A. Anderson, M. Izumo, C. H. Johnson, *Curr. Biol.* **17**, 1091 (2007).
11. A. Eskin, J. S. Takahashi, *Science* **220**, 82 (1983).
12. J. S. Takahashi, M. Zatz, *Science* **217**, 1104 (1982).
13. R. A. Prosser, M. U. Gillette, *J. Neurosci.* **9**, 1073 (1989).
14. S. S. Nikaido, J. S. Takahashi, *Neuron* **3**, 609 (1989).
15. C. Lippe, C. Ardizzone, *Comp. Biochem. Physiol. C* **99**, 209 (1991).
16. S. J. Aton, J. E. Huettner, M. Straume, E. D. Herzog, *Proc. Natl. Acad. Sci. U.S.A.* **103**, 19188 (2006).
17. E. S. Maywood *et al.*, *Curr. Biol.* **16**, 599 (2006).
18. T. Rosenbaum, S. E. Gordon, *Neuron* **42**, 193 (2004).
19. J. de Rooij *et al.*, *Nature* **396**, 474 (1998).
20. M. N. Nitabach, J. Blau, T. C. Holmes, *Cell* **109**, 485 (2002).
21. G. B. Lundkvist, Y. Kwak, E. K. Davis, H. Tei, G. D. Block, *J. Neurosci.* **25**, 7682 (2005).
22. C. C. Huang, K. S. Hsu, *Mol. Pharmacol.* **69**, 846 (2006).
23. G. X. Shi, H. Rehmann, D. A. Andres, *Mol. Cell. Biol.* **26**, 9136 (2006).
24. B. D. Aronson, K. A. Johnson, J. J. Loros, J. C. Dunlap, *Science* **263**, 1578 (1994).
25. S. Yamaguchi *et al.*, *Science* **302**, 1408 (2003).
26. Y. Xu *et al.*, *Nature* **434**, 640 (2005).

27. We thank T. Butcher for technical support; S. R. Williams, C. P. Kyriacou, and G. Churchill for discussion; and H. Okamura (Kyoto, Japan) and H. Ueda (RIKEN, Japan) for reagents. Funded by the MRC and Biotechnology and Biological Sciences Research Council, UK. J.S.T. is an investigator of the Howard Hughes Medical Institute. The authors have no competing financial interests.

Supporting Online Material

www.sciencemag.org/cgi/content/full/320/5878/949/DC1
Materials and Methods
Figs. S1 to S7
References

2 November 2007; accepted 5 March 2008
10.1126/science.1152506

New Products

Well Freeze-Drying System

The VirTis 96 Well Freeze Drying System for high throughput applications combines a choice of glass or plastic vials, set in an aluminum vial holder. The solid aluminum 96-well vial holders provide efficient and even heat distribution to ensure fast and consistent freeze-drying results for every sample. A range of glass-vial sizes is available. The new fluted LyoCap 96 Well CapMat Stoppers enable samples to be quickly freeze-dried and then sealed under vacuum, inert gas, or filtered air after the lyophilization cycle is complete. In traditional 96-well freeze-drying systems, samples in the wells around the plate edges tend to dry more quickly, but the VirTis sytem eliminates this effect. The system's effectiveness means scientists have an alternative to storing sensitive or heat-labile samples at low temperatures.

Genevac
For example +44-1473-240000
www.genevac.com

Yeast RNA Purification

The MasterPure Yeast RNA Purification Kit provides all the reagents needed to purify RNA from various yeast cell types, including Candida, Saccharomyces, Schizosaccharomyces, and from filamentous fungi, such as Aspergillus. The kit makes use of a rapid desalting process to remove contaminating macromolecules, avoiding toxic organic solvents, bead beating, and spheroplasting. The resulting MasterPure RNA is of higher quality than that obtained from bead-beating and is suitable for gene expression analysis.

Epicentre Biotechnologies
For information 800-284-8474
www.EpiBio.com

Basement Membrane Extract

The PathClear Basement Membrane Extract (BME) can be used for promotion and maintenance of a differentiated phenotype in a variety of cell cultures, including primary epithelial cells, endothelial cells, and smooth muscle cells. It has been used in angiogenesis assays, in tumor cell invasion assays, and as a vehicle to augment the tumorgenicity of tumor cells injected in nude mice. The PathClear designation means that in addition to standard sterility, endotoxin, and mouse antibody production testing, the BME is tested by polymerase chain reaction and is clear of a battery of 31 pathogens. Each lot is rigorously qualified in biological performance assays. Available in reduced growth factor form, with and without phenol red, PathClear BME is expected to be of special interest for in vivo murine research and other work requiring BME free from viruses, bacteria, and mycoplasma.

Trevigen
For information 800-873-8443
www.trevigen.com

Low Volume Absorbance Applications

The Infinite 200 NanoQuant is a multimode microplate reader developed for absorbance applications with low volumes. It is available with Tecan's quad4 monochromators, which provide high wavelength accuracy for endpoint measurements over the entire spectral range. It is also available with new 260 nm or 280 nm filters with an ultraviolet-stable coating that provide exact central wavelengths and narrower bandwidths. It can detect DNA concentrations as low as 1 ng/µl. It is suitable for a broad range of applications, including DNA and RNA quantitation and quality control. It offers sensitivity, multiplexing capability, and format flexibility from 6-well to 384-well microplates as well as half-area plates and the new NanoQuant plate for low concentration and sample volumes. The new NanoQuant plate contains a special quartz optic for each of the 16 samples it holds. It offers quick and easy cleaning to reduce the risk of cross contamination. The NanoQuant can be upgraded with additional detection modes.

Tecan
For information +41 44 922 81 11
www.tecan.com

Multifrequency Fluorometer

The MF2 (Multi-Frequency Fluorometer) performs faster fluorescence lifetime measurements, providing previously unattainable insight into the molecular behavior of cells, nanodevices, and other research materials. By grouping multiple frequencies into one high frequency waveform and greatly expanding the available frequency range, the instrument decreases the time it takes to measure a fluorescence lifetime from minutes to milliseconds, a 10,000-fold change.

Horiba Jobin Yvon
For information 800-446-7422
www.horiba.com

Filter Plates

An addition to the MultiScreen family, the MultiScreenHTS+ filter plates are for radiometric kinase and G protein–coupled receptor assays. These filter plates have a mesh backing to create uniformly flowing wells to improve washing efficiency. The new plate design reduces overall nonspecific binding and reduces variability in both background and signal intensities. The filter plates allow for higher throughput, greater assay sensitivity, and detection flexibility.

Millipore
For information 800-548-7853
www.millipore.com

Rodent Respiration Monitoring

The Oxylet System is designed for monitoring respiratory metabolism in rodents. Through use of an indirect calorimetry system, the Oxylet monitors carbon dioxide production, oxygen consumption, and respiratory ratio. It can be scaled up to monitor 32 animals simultaneously. Each animal chamber has an independent flow meter, so one system can accommodate multiple species at the same time. It is suitable for studies of obesity, diabetes, athletic exercise training, and other respiratory-challenging conditions.

Harvard Apparatus
For information 800-272-2775
www.harvardapparatus.com

Electronically submit your new product description or product literature information! Go to **www.sciencemag.org/products/newproducts.dtl** for more information.

Newly offered instrumentation, apparatus, and laboratory materials of interest to researchers in all disciplines in academic, industrial, and governmental organizations are featured in this space. Emphasis is given to purpose, chief characteristics, and availabilty of products and materials. Endorsement by *Science* or AAAS of any products or materials mentioned is not implied. Additional information may be obtained from the manufacturer or supplier.